https://doi.org/10.15388/vu.thesis.995
https://orcid.org/0009-0007-0061-7173

VILNIUS UNIVERSITY
CENTER FOR PHYSICAL SCIENCES AND TECHNOLOGY

Sapargali Pazylbek

Synthesis and Investigation of Various Undoped and Ion-Doped Calcium Phosphates

DOCTORAL DISSERTATION

Natural Sciences,
Chemistry (N 003)

VILNIUS 2026

The dissertation was prepared between 2022 and 2026 at Vilnius University.

Academic Supervisor – Prof. Dr. Aleksej Žarkov (Vilnius University, Natural Sciences, Chemistry, N 003).

This Doctoral Dissertation will be Defended in a Public/Closed Meeting of the Dissertation Defence Panel:

Chairman – Habil. Dr. Rimantas Ramanauskas (Center for Physical Sciences and Technology, Natural Sciences, Chemistry, N 003).
Members:
Prof. Dr. Justina Gaidukevič (Vilnius University, Natural Sciences, Chemistry, N 003),
Assoc. Prof. Dr. Anton Popov (Vilnius University, Natural Sciences, Chemistry, N 003),
Prof. Dr. Vida Vičkačkaitė (Vilnius University, Natural Sciences, Chemistry, N 003),
Dr. Virgīnija Vītola (Institute of Solid State Physics, University of Latvia Natural Sciences, Physics, N 002).

The dissertation shall be defended at a public meeting of the Dissertation Defence Panel at 14:00 on 23rd October 2026 in Inorganic Chemistry Auditorium of the Faculty of Chemistry and Geosciences, Vilnius University.
Address: Naugarduko st. 24, LT – 03225, Vilnius, Lithuania
Tel. +37052193105; e-mail: info@chgf.vu.lt

https://doi.org/10.15388/vu.thesis.995
https://orcid.org/0009-0007-0061-7173

VILNIAUS UNIVERSITETAS
FIZINIŲ IR TECHNOLOGIJOS MOKSLŲ CENTRAS

Sapargali Pazylbek

Įvairių nelegiruotų ir jonais legiruotų kalcio fosfatų sintezė ir tyrimas

DAKTARO DISERTACIJA

Gamtos mokslai,
Chemija (N 003)

VILNIUS 2026

Disertacija rengta 2022–2026 metais Vilniaus universitete.

Mokslinis vadovas – Prof. dr. Aleksej Žarkov (Vilniaus universitetas, gamtos mokslai, chemija, N 003).

Gynimo taryba:
Pirmininkas – habil. dr. Rimantas Ramanauskas (Fizinių ir technologijos mokslų centras, gamtos mokslai, chemija, N 003).
Nariai:
prof. dr. Justina Gaidukevič (Vilniaus universitetas, gamtos mokslai, chemija, N 003),
doc. dr. Anton Popov (Vilniaus universitetas, gamtos mokslai, chemija, N 003),
prof. dr. Vida Vičkačkaitė (Vilniaus universitetas, gamtos mokslai, chemija, N 003),
dr. Virgīnija Vītola (Kietojo kūno fizikos institutas, Latvijos universitetas, gamtos mokslai, fizika, N 002).

Disertacija ginama viešame Gynimo tarybos posėdyje 2026 m. spalio mėn. 23 d. 14:00 val. Vilniaus Universiteto Chemijos ir geomokslų fakulteto Neorganinės chemijos auditorijoje (141 aud.).
Adresas: Naugarduko g. 24, LT – 03225, Vilnius, Lietuva.
Tel. +37052193105; el. paštas info@chgf.vu.lt

TABLE OF CONTENTS

LIST OF ABBREVIATIONS 7

INTRODUCTION 8

1. LITERATURE SURVEY 11

1.1. Calcium phosphates 11

1.1.1. $Ca_5(PO_4)_3Cl$ and Ca_2PO_4Cl 13

1.1.2. $Ca_2P_2O_7$ 16

1.1.3. β-$Ca_3(PO_4)_2$ 18

1.1.4. α-$Ca_3(PO_4)_2$ 22

1.2. Calcium phosphate-based phosphors 24

1.2.1. Cr^{3+}-based phosphors 26

1.2.2. Eu^{2+}-based phosphors 28

1.2.3. Mn^{2+}-based phosphors 30

2. EXPERIMENTAL 32

2.1. Materials and reagents 32

2.2. Synthesis of $Ca_5(PO_4)_3Cl$ and Ca_2PO_4Cl 32

2.3. Synthesis of Cr^{3+}-activated β-$Ca_3(PO_4)_2$ 33

2.4. Synthesis of Eu^{2+}-doped α-$Ca_3(PO_4)_2$ 34

2.5. Synthesis of Mn^{2+}-doped α-$Ca_2P_2O_7$ 34

2.6. Characterization 34

3. RESULTS AND DISCUSSION 36

3.1. Synthesis and morphological control of $Ca_5(PO_4)_3Cl$ and Ca_2PO_4Cl *via* the phase transformation of amorphous calcium phosphate in molten chlorides 36

3.2. Luminescent properties of near-infrared-emitting Cr^{3+}-activated beta-$Ca_3(PO_4)_2$ 43

3.3. Tunable broadband visible emission achieved by phase transformation-driven self-reduction of Eu^{3+} to Eu^{2+} in calcium phosphate matrix 49

3.4. Luminescence and electron–hole-trapping centers in α-$Ca_2P_2O_7$:Mn 55

CONCLUSIONS 63

REFERENCES 65
SANTRAUKA 89
CURRICULUM VITAE 102
ACKNOWLEDGEMENTS 104
LIST OF PUBLICATIONS 105
PUBLICATION REPRINTS 106
1st publication 106
2nd publication 115
3rd publication 124
4th publication 135

LIST OF ABBREVIATIONS

ACP – amorphous calcium phosphate;

CP – Calcium phosphate;

ClAp – calcium chlorapatite, $Ca_5(PO_4)_3Cl$;

CPP – calcium pyrophosphate, $Ca_2P_2O_7$;

CPC – calcium phosphate cement;

CDHA – calcium-deficient hydroxyapatite;

DCPD – dicalcium phosphate dihydrate, $CaHPO_4 \cdot 2H_2O$;

EDX – energy dispersive X-ray spectroscopy;

EPR – electron paramagnetic resonance;

FTIR – Fourier transform infrared spectroscopy;

FWHM – Full Width at Half Maximum;

HA – hydroxyapatite;

ICP-OES – inductively coupled plasma optical emission spectrometry;

LED –light-emitting diode;

MCPM – monocalcium phosphate monohydrate;

NIR – near-infrared;

OCP – octacalcium phosphate;

PLE – photoluminescence excitation;

PL – photoluminescence;

SEM – scanning electron microscopy;

TCP – tricalcium phosphate, $Ca_3(PO_4)_2$;

UV – ultraviolet;

VUV – vacuum ultraviolet;

WLED – white light-emitting diode;

XRD – X-ray diffraction.

INTRODUCTION

Phosphate-based matrices are extensively employed in the development of luminescent materials through doping with rare-earth or transition-metal ions. The interest in this class of materials arises from several factors, including strong and broad ultraviolet (UV) absorption, structural diversity, and the possibility of structural tailoring. Among the most extensively studied phosphate subgroups are apatites, pyrophosphates, orthophosphates (MPO_4, where M denotes a trivalent ion), and whitlockite-type structures [1- 3]. Additionally, ion doping can be considered a way to modify the physical, chemical, and biological properties of biocompatible phosphates. This allows to combine biocompatibility with substitution-induced properties, resulting in the application of these materials in new areas, such as various imaging modalities [4, 5].

Calcium phosphates (CPs) represent an important sub-family of phosphate-based materials and have attracted considerable attention due to their wide range of applications not only in optical materials [6], but also in medicine and bone regeneration [7], catalysis [8], sorption of heavy metals [9], and many others [10]. CPs can be classified by many parameters, including crystal structure, Ca-to-P ratio, and the presence of other structural species (e.g., OH^-, CO_3^{2-}, Cl^-, F^-) [11]. Compositional and structural features of CPs give rise to their distinct chemical and physical properties [12]. Given the variety of CP phases, specific synthetic approaches are required to selectively synthesize specific compounds.

While some CPs can be easily synthesized by a direct precipitation from aqueous solutions or solid-state reaction, some metastable phases can be obtained only through the phase transformation processes from the less thermodynamically stable CPs [13]. Basically, the phase transformation approach comprises two routes: (I) dry, thermally induced phase transformations at elevated temperatures; and (II) phase conversions in aqueous media. Thermally-induced phase transformations of different CP phases suggest the thermal treatment of the starting material at elevated temperatures. The Ca/P ratio in starting materials and final products is usually expected to be identical [14, 15]. For instance, Ca-deficient hydroxyapatite ($Ca_9(PO_4)_4(HPO_4)_2OH$) with the Ca/P ratio of 1.5:1 at elevated temperatures converts to beta-tricalcium phosphate ($Ca_3(PO_4)_2$) [16]. The same behavior is expected for amorphous CP, a metastable and highly reactive member of the CP family, which can be used as a precursor for the synthesis of other phosphate-based materials [17]. Nevertheless, in some specific cases, the phase conversion between different CPs can occur with a drastic change in the

Ca/P ratio. Moreover, reactions in molten salts can yield completely different products due to the reaction with flux components.

The aim of this study was to synthesize various undoped and ion-doped CP phases and investigate their structural, morphological, and optical properties.

The objectives of this study:

- To investigate the influence of synthesis parameters on the selective synthesis of $Ca_5(PO_4)_3Cl$ and Ca_2PO_4Cl from ACP in molten chlorides;
- To synthesize Cr^{3+}-doped β-$Ca_3(PO_4)_2$ and investigate its optical properties;
- To synthesize Eu^{2+}-doped α-$Ca_3(PO_4)_2$ through the phase conversion from Eu^{3+}-doped $CaHPO_4{\cdot}2H_2O$ (DCPD) and investigate its optical properties;
- To synthesize Mn^{2+}-doped α-$Ca_2P_2O_7$ and investigate its optical properties.

Relevance and scientific novelty

The relevance of this dissertation is related to the development of controllable synthetic approaches for CP materials with tailored phase composition, morphology, oxidation state of dopants, and luminescent properties. Particular attention is paid to phase-transformation processes, which offer opportunities to obtain CP phases and functional properties that are difficult to achieve *via* conventional synthesis routes.

The scientific novelty of the dissertation consists of the systematic investigation of phase transformations and ion-doping effects in several CP systems. For the first time, phase transformations of ACP in molten chlorides were systematically investigated, enabling selective formation of $Ca_5(PO_4)_3Cl$ and Ca_2PO_4Cl and control of $Ca_5(PO_4)_3Cl$ particle morphology. For the first time, the incorporation and luminescent behavior of Cr^{3+} ions in β-$Ca_3(PO_4)_2$ were systematically investigated, revealing multiple Cr^{3+}-related centers and broadband near-infrared emission. A phase-transformation route enabling efficient reduction of Eu^{3+} to Eu^{2+} in α-$Ca_3(PO_4)_2$ was demonstrated for the first time, resulting in excitation-dependent broadband visible emission associated with Eu^{2+} ions in different local environments. In addition, for the first time, irradiation-induced electron-hole trapping states and associated luminescence processes in Mn^{2+}-doped α-$Ca_2P_2O_7$ were investigated over a broad excitation-energy range.

Statements to be defended

1. The phase transformation of ACP in molten KCl–$CaCl_2$ can be directed toward the selective formation of $Ca_5(PO_4)_3Cl$ or Ca_2PO_4Cl by changing the chemical composition of the flux, while the $CaCl_2$ content also strongly influences the anisotropic growth and morphology of $Ca_5(PO_4)_3Cl$ particles.
2. Cr^{3+} ions can be incorporated into the β-$Ca_3(PO_4)_2$ structure up to a limited substitution level, producing multiple Cr^{3+}-related centers and broadband near-infrared emission centered at approximately 760 nm.
3. Thermally-induced transformation of Eu^{3+}-doped $CaHPO_4 \cdot 2H_2O$ in vacuum leads simultaneously to the formation of α-$Ca_3(PO_4)_2$ and reduction of Eu^{3+} to Eu^{2+}; the occurrence of Eu^{2+} ions in different local environments results in excitation-dependent broadband visible emission.
4. Irradiation of Mn^{2+}-doped α-$Ca_2P_2O_7$ produces additional radiative states at approximately 2.95 and 3.1 eV, associated with electron-hole trapping and charge-transfer processes involving Mn-related and pyrophosphate-related centers.

1. LITERATURE SURVEY

1.1. Calcium phosphates

Calcium phosphates (CPs) comprise a diverse group of inorganic compounds primarily consisting of calcium and phosphate ions. Owing to their widespread natural occurrence and their essential role in biological systems, these materials have attracted extensive attention in geology, chemistry, biology, and biomedical research [11, 18- 21]. The physicochemical characteristics of calcium phosphates- including solubility, crystallinity, phase stability, and resorption behavior- are strongly influenced by their chemical composition, crystal structure, and synthesis methodology. As a result, specific CP phases can be selected based on the requirements of particular applications. Depending on the synthesis and processing conditions, CPs can be produced in multiple amorphous and crystalline forms, each exhibiting their specific properties (Table 1) [22].

Table 1. Calcium orthophosphate phases and their principal properties [22].

Formula	**Compound**	**Ca/P** molar ratio	**Solubility** [-log Ks]	**Solubility** at 25 °C (g/L)	**pH** stability range in aqueous solutions at
$Ca(H_2PO_4)_2$	Monocalcium phosphate anhydrous (MCPA or MCP)	0.5	1.1	~17	Stable at high temperatures
$Ca(H_2PO_4)_2 \cdot H_2O$	Monocalcium phosphate monohydrate (MCPM)	0.5	1.1	~18	0.0–2.0
$CaHPO_4 \cdot 2H_2O$	Dicalcium phosphate dihydrate DCPD)	1.0	6.59	~0.088	2.0–6.0
$Ca_2P_2O_7$	Calcium pyrophosphate (CPP)	1.0	18.5	~0.0001	6.0–9.0
$Ca_xH_y(PO_4)_z \cdot nH_2O$, n=3–4.5;5%–20% H_2O	Amorphous calcium phosphates (ACPs)	1.2–2.2	Can't be measured precisely	Can't be measured precisely	~5–12 Always metastable
$Ca_8(HPO_4)_2(PO_4)_4 \cdot 5H_2O$	Octacalcium phosphate (OCP)	1.33	96.6	~0.0081	5.5–7.0
α-$Ca_3(PO_4)_2$	α -Tricalcium phosphate (α-TCP)	1.5	25.5	~0.0025	Can't be precipitated from aqueous solutions
β-$Ca_3(PO_4)_2$	β-Tricalcium phosphate (β-TCP)	1.5	28.9	~0.0005	Can't be precipitated from aqueous solutions
$Ca_{10}(PO_4)_6(OH)_2$	Hydroxyapatite (HA or OHAp)	1.67	116.8	~0.0003	9.5–12

CPs are a diverse group of materials extensively studied for their relevance in biomedical and technological applications. Among them, hydroxyapatite (HA) has received the greatest attention due to its close structural and chemical similarity to the mineral phase of human bone and teeth, making it the material of choice for bone substitutes, implant coatings, and advanced biomedical systems such as drug delivery and hyperthermia-related applications [23, 24]. Beyond biomedicine, HA is also employed in environmental, catalytic, and dental care applications. Additional nonbiomedical applications include its use as an environmentally friendly filler, a sorbent for hazardous elements, a catalyst or catalyst support, and a UV-protective additive.

Dicalcium phosphate dihydrate (DCPD) is another biologically relevant phase, often associated with pathological calcifications and considered a transient phase in bone mineralization and enamel dissolution processes [25]. In biomedical practice, DCPD is mainly used in self-setting calcium phosphate cements and tooth remineralization systems [26]. Its applications extend beyond medicine to agriculture, food and feed supplementation, flame-retardant formulations, and glass production.

Octacalcium phosphate (OCP) is widely recognized as a precursor of apatitic biominerals in vivo and has therefore attracted significant interest as a bone substitute material. Its favorable biocompatibility, osteoconductivity, and relatively high resorption rate allow gradual replacement by newly formed bone tissue [27, 28].

Amorphous calcium phosphates (ACPs), characterized by the absence of long-range crystalline order and high solubility, are commonly used in self-setting CPs systems and composite biomaterials for dental and surgical applications [17, 29]. Additionally, ACPs find use in various nonbiomedical applications, including food processing, pharmaceutical formulations, and glass and ceramic manufacturing [30].

In contrast, monocalcium phosphate monohydrate (MCPM) does not occur in biological mineralization due to its high acidity and solubility; however, it plays a crucial role as a reactive component in self-hardening calcium phosphate cements [31- 33].

Nanoscale CP systems have attracted considerable attention due to their exceptional multifunctionality arising from size-dependent effects. These materials combine excellent biological compatibility with the ability to actively stimulate bone formation, while maintaining sufficient structural integrity and precisely adjustable degradation profiles. In addition, nanosized CPs exhibit pronounced binding capabilities toward genetic materials, including small interfering RNA, microRNA, and plasmid DNA, as well as

high loading efficiency for diverse classes of anticancer and therapeutic drugs, such as paclitaxel, carboplatin, doxorubicin, gefitinib, and cisplatin [34- 36]. As a result, CP nanostructures represent a highly versatile platform not only for bone tissue engineering and regenerative medicine, but also for advanced drug delivery systems, nanocarriers, and multifunctional therapeutic applications [37].

1.1.1. $Ca_5(PO_4)_3Cl$ and Ca_2PO_4Cl

Calcium chlorapatite ($Ca_5(PO_4)_3Cl$, ClAp) belongs to the apatite family and crystallizes in a hexagonal lattice characterized by the space group $P6_3/m$ [37, 38]. Its crystal framework comprises two crystallographically distinct cationic sites, commonly denoted as M1 and M2, which differ markedly in their coordination environments. The M1 sites are coordinated by nine oxygen atoms, whereas the M2 sites are coordinated by six oxygen atoms from the phosphate groups, along with two chloride ions aligned along the crystallographic *c*-axis (Fig. 1). Phosphate units form rigid PO_4 tetrahedra, which constitute the backbone of the apatite structure. Owing to the comparatively larger size and lower symmetry of the Ca2 sites, these positions preferentially accommodate larger substituent ions, including trivalent rare-earth cations, thereby enabling effective lattice modification and functional tuning [39, 40].

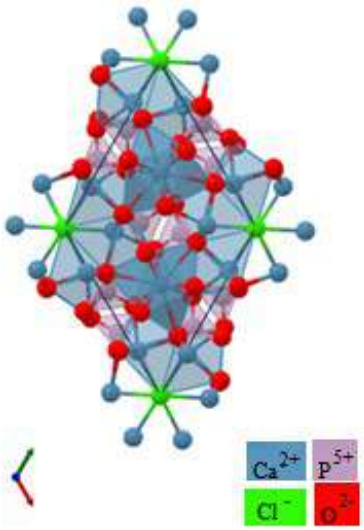

Fig. 1. The crystal structure of $Ca_5(PO_4)_3Cl$ [40].

The physicochemical properties of ClAp nanocrystals are strongly dependent on parameters such as particle size, size distribution, and morphological characteristics, which can be deliberately tailored during synthesis. A wide range of synthetic strategies has been developed for the preparation of ClAp nanoparticles, encompassing dry and wet chemical routes, high-temperature processes, and hybrid approaches [41]. Commonly employed techniques include solid-state reactions [42- 44], mechanochemical processing [45], precipitation-based methods [46], pyrolysis [47], hydrothermal and aqueous colloidal synthesis [44, 48, 49], microwave-assisted routes [50], sol–gel processing [51], solution combustion [52], and other wet chemical methodologies [53].

In addition to its biomedical relevance, chlorapatite has emerged as a multifunctional material of considerable interest in environmental and energy-related applications. Its crystal framework exhibits a strong capacity for the sequestration of hazardous heavy-metal species, including Pb^{2+} and Cd^{2+}, through coupled ion-exchange and dissolution– reprecipitation processes, resulting in the stabilization of these elements within thermodynamically robust metal–phosphate matrix [54]. Moreover, the $Ca_5(PO_4)_3Cl$ lattice provides a structurally adaptable host for rare-earth activators, thereby enabling its use in advanced luminescent and optical systems [55].

Owing to its exceptional chemical stability and structural tolerance toward the incorporation of halogens and actinide species, chlorapatite has also been widely recognized as a viable ceramic matrix for the long-term immobilization of radioactive waste [56, 57]. In parallel, this mineral phase plays a critical role in geological and geochemical investigations, where it serves as a sensitive archive for halogen and volatile element distributions in magmatic environments, providing valuable insights into melt evolution and degassing processes [58].

Ca_2PO_4Cl crystallizes in an orthorhombic lattice belonging to the *Pbcm* space group and contains four formula units per unit cell. The refined lattice parameters are $a = 6.1850$ Å, $b = 6.983$ Å, and $c = 10.816$ Å [59]. Structurally, Ca_2PO_4Cl adopts the spodiosite-type framework [60], which accommodates divalent cations at two crystallographically nonequivalent sites characterized by C_2 and C_s site symmetries. Both cationic sites exhibit eightfold coordination, consisting of six oxygen atoms and two chloride ions; however, they differ in coordination polyhedron dimensions. The C_s site represents the larger coordination environment, with average Ca–O and Ca–Cl bond lengths of approximately 2.50 Å and 2.89 Å, respectively, whereas the more compact C_2 site is characterized by shorter average distances of about 2.46 Å (Ca–O)

and 2.81 Å (Ca–Cl) [61]. The crystal structure of Ca_2PO_4Cl and the coordination environments of Ca^{2+} ions are illustrated schematically in Fig. 2.

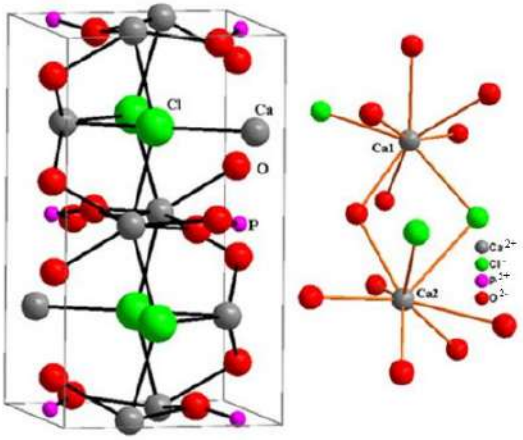

Fig. 2. Crystal structure of Ca_2PO_4Cl and coordination spheres of Ca^{2+} [60].

Rare-earth-activated Ca_2PO_4Cl phosphors (RE= Eu^{2+}, Dy^{3+}, Ce^{3+}) are typically synthesized using high-temperature solid-state methods, which enable efficient incorporation of activator ions into the host lattice and yield materials with good phase purity and optical performance [62]. Among them, Eu^{2+}-doped Ca_2PO_4Cl has been extensively investigated as an intense blue-emitting phosphor for near-UV–excited solid-state lighting applications due to its high luminescence efficiency and favorable thermal stability [59]. When combined with green- and red-emitting phosphors in white LED (WLED) architectures, $Ca_2PO_4Cl:Eu^{2+}$ enables the generation of high-quality white light with a high color rendering index ($R_a \approx 93$) [63]. Moreover, co-doping strategies, such as the introduction of Mn^{2+} ions, allow effective modulation of the emission toward warm white light, further broadening the applicability of Ca_2PO_4Cl-based phosphors in energy-efficient lighting systems [64].

Beyond optoelectronic applications, Ca_2PO_4Cl has also been identified as a chemically stable phosphorus-containing phase formed during battery recycling processes under molten-salt conditions, highlighting its relevance in high-temperature materials chemistry and sustainable resource recovery.

1.1.2. $Ca_2P_2O_7$

Calcium pyrophosphate ($Ca_2P_2O_7$, CPP) belongs to the CPs family. In this material the anionic sublattice is composed of pyrophosphate groups ($P_2O_7^{4-}$), formed by two corner-sharing PO_4 tetrahedra linked through a bridging oxygen atom. In recent years, CPP has attracted growing interest as a functional biomaterial due to its favorable combination of properties, including high bioresorbability, controlled solubility, excellent osteoconductivity, adequate mechanical performance, and good biocompatibility [65- 67].

Beyond biomedical relevance, CPP and its hydrated derivatives are involved in a variety of technological applications and natural processes. CPP is commonly employed as a mild abrasive component in toothpaste formulations [68, 69] and has been proposed as an enamel-repair agent for the treatment of dentin hypersensitivity [70]. In addition, it is utilized as a functional additive in phosphate-based bone cements for orthopedic applications [71] and has also been investigated as a host matrix for luminescent activators [72].

From a crystal-chemical perspective, pyrophosphates with the general formula $M(II)_2P_2O_7$, where M(II) denotes a divalent metal cation, exhibit several distinct structure types. Representative examples include the potassium dichromate-type structure ($K_2Cr_2O_7$) [73] and the thortveitite-type structure ($Sc_2Si_2O_7$) [74]. The adopted structure type is strongly governed by the ionic radius of the divalent cation: compounds containing cations larger than approximately 0.97 Å preferentially crystallize in the dichromate-type arrangement, whereas smaller cations favor the thortveitite-type framework. These two structural motifs differ primarily in the conformation of the pyrophosphate anion, which adopts an eclipsed configuration in the dichromate-type structure and a staggered configuration in the thortveitite-type structure [75]. Correspondingly, the P–O–P bond angle typically ranges from 120 to 135° in dichromate-type pyrophosphates and from 140 to 180° in thortveitite-type compounds [76].

CPP exhibits pronounced polymorphism and is known to crystallize in three distinct forms: γ-CPP, β-CPP, and the high-temperature α-CPP phase. The α-polymorph is metastable and undergoes a reversible transformation to the thermodynamically stable β-phase upon cooling [77, 78]. X-ray diffraction investigations have demonstrated that the formation of these polymorphs is strongly dependent on the thermal treatment conditions, particularly the firing temperature applied during synthesis [79]:

γ-$Ca_2P_2O_7$ (270-430 °C)

↓

β-$Ca_2P_2O_7$ (750-850 °C)

↓

α-$Ca_2P_2O_7$ (1140-1220 °C)

↓

T_{melt} of **$Ca_2P_2O_7$** (1353-1365 °C)

The lattice parameters corresponding to the three crystallographic modifications of CPP are summarized in Table 2 [80]. The γ-CPP adopts a triclinic crystal system, whereas β-CPP crystallizes in a tetragonal symmetry. In contrast, the high-temperature α-CPP phase is characterized by a monoclinic crystal structure. In all three polymorphs, the pyrophosphate anions exhibit predominantly eclipsed conformations; however, notable variations in the P–O–P bridging angle are observed. Specifically, the P–O–-P angle amounts to approximately 138° in β-CPP, 130° in α-CPP, and 134.1° in γ-CPP. Representative crystal structures of the γ-, α-, and β-CPP phases are depicted in Fig. 3 [80].

Table 2. Crystal structure parameters of γ-, β- and α- CPP [79, 80].

Unit cell parameters							
CPP	**a (Å)**	**b (Å)**	**c (Å)**	**β (°)**	**Space group**	**Z**	**$\rho_{calcul.}$ (g/cm^3)**
γ	6.666	6.722	6.737	87.763	$\overline{P}_1$	2	3.095
β	6.684	6.684	24.144	90	$P4_1$	8	3.129
α	12.66	8.542	5.315	90.3	$P2_1/n$	4	2.950

Previous studies have shown that the incorporation of β-CPP into biomaterials and bioceramics can substantially enhance their mechanical performance and degradation behavior [81]. In particularly Lee *et al.* [82] reported that β-CPP-based implants outperform HA counterparts as bone graft substitutes, exhibiting superior osteoconductivity alongside accelerated bioresorption and biodegradation. Beyond biomedical applications, β-CPP has also attracted attention in diverse functional fields, including water purification [83], catalytic processes [84], and electrical and electronic systems [85]. Furthermore, owing to its structurally adaptable host lattice, CPP has been extensively explored for photo- and thermoluminescent applications through the incorporation of various dopants, enabling effective tuning of its optical response [86].

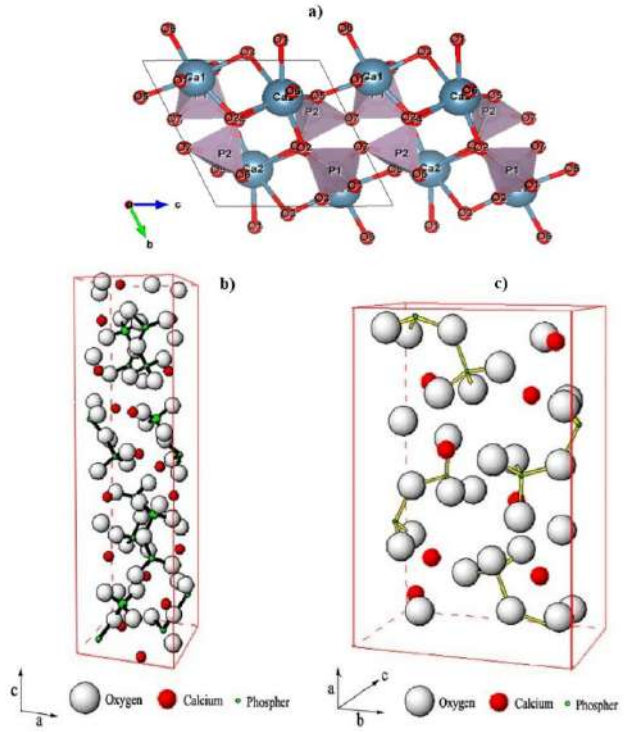

Fig. 3. The crystal structures of (a) γ-, (b) β- and (c) α-CPP [79, 80].

A variety of synthetic approaches have been developed for the preparation of CPP, such as conventional solid-state reactions, wet chemical precipitation, and sol–gel techniques [87]. Among these, solid-state synthesis via the thermal dehydration of calcium hydrogen phosphate remains the most widely adopted route, primarily due to its procedural simplicity and capability to yield phase-pure products [88]. Alternatively, wet chemical and sol–gel methods provide enhanced compositional uniformity and allow finer control over particle size and morphology, which is particularly advantageous for biomedical applications [89]. Moreover, β-CPP can be synthesized using the liquid flame spray technique. This method is characterisized by extremely short synthesis times and offers key advantages such as scalability, reproducibility, continuous operation, tunability and relatively low production cost, making it highly attractive for large-scale material fabrication [90].

1.1.3. β-$Ca_3(PO_4)_2$

Beta tricalcium phosphate (TCP, $Ca_3(PO_4)_2$) represents the thermodynamically stable low-temperature modification within the CaO–P_2O_5 phase diagram. This compound is ideally characterized by a Ca/P molar

ratio of 1.5 and a theoretical density of 3.17 $g \cdot cm^{-3}$ [91]. Among TCP polymorphs, β-TCP has gained particular prominence as a biocompatible material for bone regeneration, where it is employed either as a bulk bone substitute or as a coating for orthopedic and dental implants, similarly to apatite-based materials [92]. In addition, TCP serves as an important precursor phase in the synthesis of apatites, enabling controlled phase transformation and compositional tuning [93]. A key feature distinguishing β-TCP from HA is its significantly higher aqueous solubility, which is approximately twice that of HA, resulting in enhanced bioresorption kinetics [94].

From a biological standpoint, TCP functions as a resorbable, temporary bone space filler. Upon implantation, it interacts with physiological fluids and gradually converts into HA through a dissolution–reprecipitation mechanism, thereby facilitating bone remodeling and integration according to the following reaction:

$$4Ca_3(PO_4)_2 + 2H_2O \rightarrow Ca_{10}(PO_4)_6(OH)_2\ (\text{surface}) + 2Ca^{2+} + 2HPO_4^{2-} \quad (1)$$

The kinetics of TCP dissolution are strongly influenced by the local chemical environment; in particular, an increase in solution pH leads to a reduction in reaction rate while simultaneously enhancing TCP solubility. From a theoretical perspective, resorbable TCP represents an ideal implant material, as it undergoes gradual degradation in vivo and is progressively replaced by newly formed biological tissue. This transformation promotes true tissue regeneration rather than passive material substitution, thereby mitigating interfacial stability issues commonly associated with permanent implants [95, 96].

A wide range of synthetic strategies has been reported for the preparation of β-TCP, including wet-chemical routes [97, 98], conventional solid-state reactions [99, 100], microwave-assisted synthesis [101, 102], and sol–gel processing [103, 104], employing various calcium and phosphate precursors [105]. Notably, β-TCP has been successfully produced using both synthetic and naturally derived calcium sources. Synthetic precursors typically include inorganic calcium salts such as calcium nitrate ($Ca(NO_3)_2$), calcium hydroxide ($Ca(OH)_2$), and chemically synthesized calcium oxide (CaO) [87]. In contrast, natural calcium sources are often obtained from $CaCO_3$-rich biogenic waste materials, including mollusk shells, e.g. green mussel shells (*Perna viridis*) [106], rangia clam shells [107], and pearl oyster shells [108]), chicken eggshells [109], limestone [110], and coral-derived materials [111].

In solid-state synthesis, maximizing the reactive surface area of the starting materials is a critical factor governing phase formation and reaction efficiency. β-TCP can be produced through the reaction of calcium-rich

compounds– such as $CaCO_3$ [112], HA [113], or $Ca(OH)_2$ with hosphate-containing precursors including $CaHPO_4$, $CaHPO_4 \cdot 2H_2O$, $Ca_2P_2O_7$ (CPP), or $(NH_4)_2HPO_4$ [114]. The most commonly employed starting powders and their corresponding overall reactions leading to TCP formation are summarized below:

$$CaCO_{3\,(s)} + 2CaHPO_{4\,(s)} \rightarrow Ca_3(PO_4)_{2\,(s)} + CO_{2\,(g)} + H_2O_{\,(g)}\ [115,116] \quad (2)$$

$$CaCO_{3\,(s)} + Ca_2P_2O_{7\,(s)} \rightarrow \alpha\text{-}Ca_3(PO_4)_{2\,(s)} + CO_{2\,(g)}\ [117, 118] \quad (3)$$

$$3CaCO_{3\,(s)} + 2NH_4H_2PO_{4\,(s)} \rightarrow Ca_3(PO_4)_{2(s)} + 3H_2O_{\,(g)} +$$

$$+ 3CO_{2(g)} + 2NH_{3(g)}\ [117,119] \quad (4)$$

$$Ca_{10}(PO_4)_6(OH)_{2\,(s)} + 2CaHPO_{4\,(s)} \rightarrow 4Ca_3(PO_4)_{2\,(s)} + 2H_2O_{(g)}\ [120] \quad (5)$$

During solid-state synthesis, compositional inhomogeneity may arise, often leading to the unintended formation of secondary phases such as HA or β-CPP. To suppress the appearance of these impurity phases, multistep thermal treatment protocols are commonly employed, combined with repeated grinding to increase the effective surface area and improve interdiffusion between reactants. A critical factor in such reactions is strict control of the Ca/P molar ratio, which must be carefully adjusted to closely match the stoichiometry of the targeted TCP phase, as deviations readily promote the formation of competing CP [121].

An alternative and widely adopted approach for TCP synthesis involves thermal transformation from ACP [122] or calcium-deficient HA (CDHA). Upon heat treatment at approximately 800 °C these precursor phases undergo controlled phase conversion to TCP. Compared with conventional solid-state reactions, this route offers substantially improved chemical homogeneity and phase purity, resulting in a more uniform final product with reduced risk of secondary phase formation [123].

$$Ca_9(HPO_4)(PO_4)5OH \rightarrow 3\beta\text{-}Ca_3(PO_4)_2 + H_2O \quad (6)$$

Among the polymorphic forms of TCP, the β-phase is thermodynamically stable at ambient conditions and is generally favored over the high-temperature α-modification, which exists in the temperature range of approximately 1180–1400 °C. This preference arises from the superior biocompatibility, enhanced mechanical performance, and reduced dissolution kinetics exhibited by β-TCP, making it more suitable for biomedical applications [124].

Crystallographically, β-TCP adopts a trigonal (rhombohedral) structure that is commonly described using a hexagonal setting and belongs to the space group *R3c*, with $Z = 21$. The refined lattice parameters were determined to be $a = b = 10.431 \pm 0.007$ Å, $c = 37.376 \pm 0.020$ Å, with interaxial angles $\alpha = \beta = 90°$ and $\gamma = 120°$, corresponding to a unit cell volume of 3521.55 ± 6.322 Å^3 [125, 126].

The crystal structure of β-TCP (Fig. 4), can be rationalized in terms of columnar arrangements extending along the *c*-axis. One type of column is composed of alternating layers of P(1), Ca(4), and Ca(5), while a second column type comprises stacked layers of Ca(1), Ca(2), Ca(3), P(2), and P(3). Within the unit cell, each column of the first type is surrounded by six columns of the second type, whereas each column of the second type is typically coordinated by two columns of the first type [127].

The crystal framework of β-TCP is characterized by a high degree of compositional flexibility, allowing partial substitution of calcium ions by a wide range of metal cations. In particular, TCP readily accommodates small divalent transition-metal ions such as Mg^{2+}, Mn^{2+}, Fe^{2+}/Fe^{3+}, Ni^{2+}, Co^{2+}, Cu^{2+}, and Zn^{2+} [103, 128], as well as larger alkaline-earth cations including Ba^{2+} and Sr^{2+} [129]. Among these dopants, magnesium incorporation is especially effective in stabilizing the β-TCP structure and modifying its physicochemical properties [130].

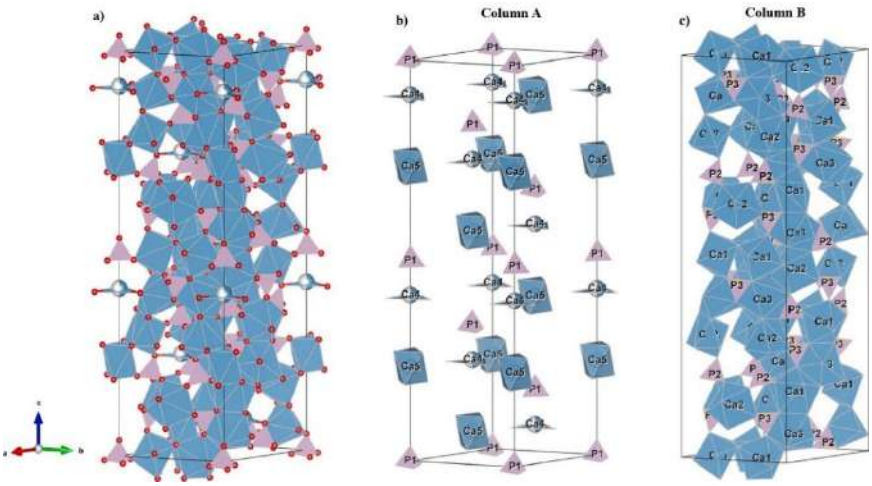

Fig. 4. The crystal structure of β-TCP. a) the hexagonal unit cell along the *c* axis. The unit cell composed of b) column A with parallel layers of P1–Ca4–Ca5 and c) column B with parallel layers of Ca1–Ca2–Ca3–P2–P3 along the c axis [127].

Systematic investigations by Enderle [131] and Araujo *et al.* [132] have addressed the substitution limits of Mg^{2+} for Ca^{2+} in β-TCP. Their results indicate that up to approximately 15 mol% of the calcium sites can be replaced by magnesium without destabilizing the β-TCP lattice, highlighting the significant substitutional tolerance of this structure and its potential for property tailoring through controlled doping.

1.1.4. α-$Ca_3(PO_4)_2$

Alpha-tricalcium phosphate (α-TCP, $Ca_3(PO_4)_2$) has attracted considerable interest owing to a combination of properties that are particularly advantageous for biomedical applications. These include its high solubility in aqueous environments, the ability to undergo hydration reactions at physiological pH, and the subsequent formation of CDHA upon setting. This phase transformation results in a material with pronounced bioresorbability, closely mimicking the natural bone remodeling process.

The synthesis of α-TCP requires high-temperature treatment of CP precursors with a calcium-to-phosphorus (Ca/P) ratio close to 1.50, corresponding to the stoichiometric composition of TCP [133]. Commonly employed precursors include ACP, CDHA, and β-TCP. The choice of precursor, together with the applied synthesis conditions, plays a decisive role in determining the characteristics of the resulting α-TCP powder, including phase purity, crystallinity, crystallite size, Ca/P ratio, and specific surface area [134, 135].

The available synthetic strategies for α-TCP preparation can be broadly grouped into three main categories: solid-state reactions, wet-chemical routes, and alternative or non-conventional methods, as summarized in Table 3 [136]. Each approach offers distinct advantages with respect to compositional control, homogeneity, and scalability.

From a crystallographic perspective, the structure of α-TCP has a strong similarity to that of the mineral glaserite ($K_3Na(SO_4)_2$), as initially reported in 1972. This structural connection was later validated and analyzed in depth by Mathew *et al.* in 1977 [137], and further improved by Yashima and Sakai [138]. These studies indicate that α-TCP crystallizes within the monoclinic crystal system and falls under the space group $P2_1/a$, having unit cell parameters a= 12.85 Å, b= 27.35 Å, c= 15.22 Å, and a monoclinic angle β= 126.35°. Thermodynamically, the α-TCP phase is stable at high temperatures in the range of approximately 1125–1430 °C [139] and can be retained as a metastable phase at room temperature under suitable cooling conditions [140]. The corresponding crystallographic characteristics include a unit cell volume

of 4.31(6) nm^3, 24 formula units per unit cell (Z= 24), a volume per formula unit of 0.18(6) nm^3, and a theoretical density of 2.86 $g \cdot cm^{-3}$ [141].

Table 3. Main methods to synthesize α-TCP [136].

Method and initial reagents	**Calcium phosphate precursor**				
Solid-state reaction					
$CaCO_3$+$CaHPO_4$ $CaCO_3$+ γ- $CaHPO_4$ $CaCO_3$+ $NH_4H_2PO_4$ $Ca_{10}(PO_4)_6(OH)_2$+ $CaHPO_4$	→	β-TCP		→	α-TCP
Wet chemical reaction					
$Ca(OH)_2$+ H_3PO_4 $Ca(NO_3)_2$+ H_3PO_4	→	CDHA	→ β-TCP	→	α-TCP
$CaCl_2$+ $(NH_4)H\,PO_4$	↗ ↘				
$CaCl_2$+ H_3PO_4	→	ACP		→	α-TCP
Alternative methods					
Hydrothermal Sol-gel	→	CDHA	→ β-TCP	→	α-TCP
Flame spray pyrolysis	→	ACP		→	α-TCP
Combustion synthesis	→	Calcium phosphate mixtures		→	α-TCP

A key feature of α-TCP is its pronounced chemical reactivity in aqueous environments, where it readily undergoes hydration and transforms into poorly crystalline HA with a Ca/P molar ratio of 1.50. This transformation underlies its widespread use as the primary reactive phase in apatite-based CP cements (CPCs). Owing to this hydration-driven conversion, α-TCP exhibits excellent biocompatibility and a higher biodegradation rate compared with β-TCP. Importantly, the phase purity of TCP strongly influences the biological response of the final material, as structural differences between TCP polymorphs directly affect solubility, reactivity, and resorption behavior. In this context, the higher aqueous solubility of α-TCP relative to its β counterpart accounts for its enhanced reactivity and bioresorbability, enabling its conversion into CDHA, which is crystallographically, chemically, and morphologically closer to the mineral phase of natural bone [142, 143, 144].

From a structural perspective, the α-TCP lattice can be described in terms of columnar arrangements of calcium and phosphate units extending along the [001] crystallographic direction. Two distinct types of columns are present: calcium-only columns (denoted as C–C) and mixed calcium–phosphate columns (C–A) (Fig. 5). Each C–C column is surrounded by six C–A columns,

while each C–A column is in turn coordinated by an alternating arrangement of C–C and C–A columns, resulting in a highly ordered three-dimensional network. Notably, the C–C columns deviate significantly from linearity, reflecting the intrinsic structural distortion of the α-TCP lattice [139].

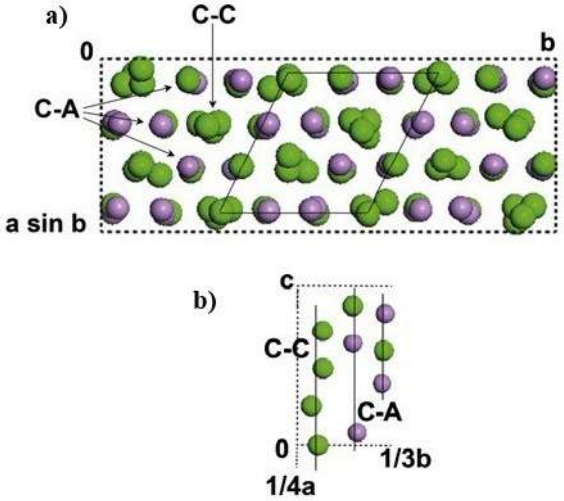

Fig. 5. a) Schematic representation and b) fractional projections of the α-TCP. Ca^{2+}, green; P^{5+}, magenta; O^{2-} has not been represented for the sake of clarity. C-C, cation- cation column; C-A, cation- anion column [139].

A structural relationship between α-TCP and HA can be established by considering a subcell embedded within the α-TCP unit cell. In this analogy, the hydroxyl columns characteristic of HA may conceptually replace the C–C columns located at the cell corners. Correspondingly, the Ca–PO_4 columns in hydroxyapatite can be viewed as highly distorted analogues of the C–A columns found in α-TCP. This crystallographic similarity provides a structural basis for the facile transformation of α-TCP into apatite phases during hydration and cement setting reactions [145].

1.2. Calcium phosphate-based phosphors

CP-based materials constitute a versatile class of inorganic compounds that have emerged as highly attractive host lattices for luminescent phosphors. Their appeal arises from a favorable combination of chemical robustness, structural adaptability, low toxicity, and abundant availability. A key advantage of these materials lies in their ability to incorporate a wide variety of optically active dopants, including rare-earth RE^{3+} ions and divalent

transition-metal ions, while maintaining crystallographic integrity and minimizing lattice strain.

Compared to conventional oxide or sulfide phosphor hosts, CPs offer a unique balance of high thermal stability and relatively low phonon energies, which effectively suppress non-radiative relaxation pathways and enhance emission efficiency. Consequently, CP-based phosphors have been intensively explored for a broad spectrum of applications, ranging from solid-state lighting and bioimaging to persistent luminescence and radiation dosimetry (Fig. 6) [146-148].

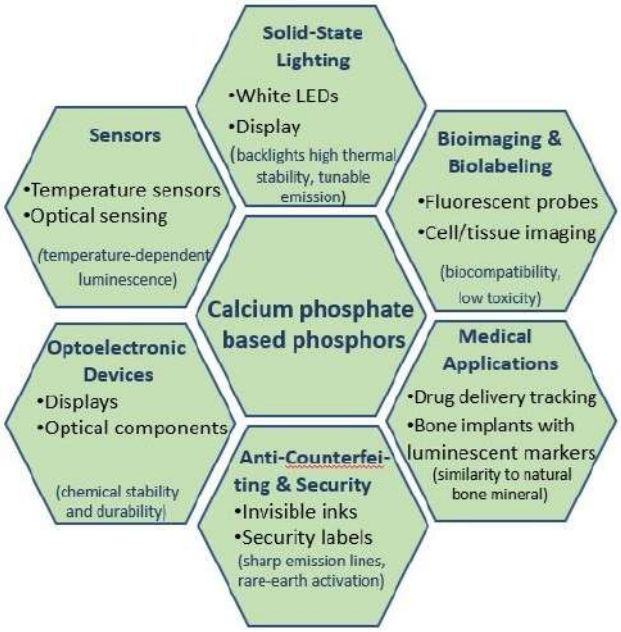

Fig. 6. Applications of CP-based phosphors [148].

Among phosphate hosts, calcium-containing compounds are of particular significance due to their close compositional and structural similarity to the mineral phase of human bone and teeth. These characteristics render them especially promising for medical radiation dosimetry applications [24, 25]. Several CP-based phosphors, including $Ca_2P_2O_7:Ce^{3+},Tb^{3+}$, $Ca_9La(PO_4)_5(SiO_4)F_2$, and $LiCaPO_4$, exhibit intense thermoluminescence response even at low radiation doses, highlighting their suitability for low-dose detection and monitoring [149-152].

In addition, $ABPO_4$-type phosphors (where *A* and *B* denote monovalent and divalent cations, respectively) such as $KCaPO_4:Dy^{3+}$, $NaCaPO_4:Dy^{3+}$, and $LiCaPO_4:Eu^{2+}$ demonstrate excellent thermoluminescent and

photoluminescent performance, making them attractive for both dosimetric and optical applications [153-155]. The apatite family of CPs has likewise been extensively investigated owing to its strong photoluminescence characteristics and compatibility with light-emitting diode (LED) technologies [156]. Furthermore, rare-earth–activated alkali and alkaline-earth phosphates with the general composition $NaMPO_4$ (M = Mg, Ca, Sr, Ba) are regarded as highly efficient phosphor hosts due to their wide band gaps, strong PO_4^{3-} absorption in the vacuum ultraviolet (VUV) region, excellent chemical and thermal stability, and favorable dopant incorporation enabled by close ionic radius matching [157].

Among $NaMPO_4$-based hosts, Eu^{3+}-doped $NaCaPO_4$ exhibits the most intense red emission and is therefore considered a promising phosphor for white LED applications. This behavior is attributed to the close ionic size match between Ca^{2+} and Eu^{3+}, which enables efficient lattice substitution and suppresses non-radiative losses, as further evidenced by the prolonged $^5D_0$ excited-state lifetime compared to other $NaMPO_4:Eu^{3+}$ systems (M = Mg, Sr, Ba) [158].

1.2.1. Cr^{3+}-based phosphors

Cr^{3+}-activated phosphors have recently emerged as a prominent class of near-infrared (NIR) emitters, primarily due to their efficient excitation under blue-light irradiation and their pronounced spectral tunability. This tunable emission behavior originates from the unique $3d^3$ electronic configuration of Cr^{3+} ions, which renders their luminescence highly sensitive to the crystal-field environment imposed by the host lattice. Consequently, a broad range of Cr^{3+}-doped materials exhibiting broadband NIR emission in the range of approximately 780–1100 nm has been successfully developed through rational host selection and crystal-field engineering.

Phosphate-, borate-, and garnet-type host matrices are particularly attractive for Cr^{3+} activation, as they combine favorable optical characteristics with high chemical durability, thermal stability, and cost-effectiveness. In this context, $AlPO_4$-based hosts have drawn attention owing to their wide operational temperature window and structural robustness, making $AlPO_4:Cr^{3+}$ a promising deep-red to NIR phosphor for horticultural lighting applications. Similarly, Cr^{3+}-doped borate compounds offer additional advantages, including non-toxicity, chemical stability, and low material consumption, which are highly desirable for scalable industrial production. [159-161].

From an application perspective, the broad absorption bands of Cr^{3+} ions extending across the UV–visible region enable efficient pumping by UV and blue LED chips, while the resulting NIR emission overlaps well with the absorption bands of plant photoreceptors. This spectral compatibility, together with the excellent thermal stability provided by rigid host lattices, particularly garnet-type structures, positions Cr^{3+}-activated phosphors as highly promising candidates for next-generation LED-based plant growth and pc-LED technologies [162].

The absorption bands of Cr^{3+} ions span the ultraviolet to visible spectral region, enabling efficient excitation by UV and blue LED chips. At the same time, the corresponding emission bands overlap well with the absorption spectra of key plant photosensitizing pigments, namely phytochrome red and phytochrome far-red, which explains the extensive interest in Cr^{3+}-activated phosphors for LED-based plant growth lighting [163]. In addition to the choice of activator ion, the host lattice plays a decisive role in determining the luminescent performance of these phosphors. In this respect, garnet-type structures, characterized by high lattice rigidity and excellent thermal stability, are regarded as particularly suitable host matrices [164].

From a crystal-field perspective, Cr^{3+} ions ($3d^3$ electronic configuration) are typically stabilized in octahedral or near-octahedral coordination environments in doped solids. Under weak crystal-field conditions, the lowest excited state corresponds to the quartet $^4T_2$ ($t_{2g}^2e_g^1$) level, which retains the same spin multiplicity as the $^4A_2$ (t_{2g}^3) ground state. In contrast, under moderate to strong crystal fields, the lowest excited state becomes the ^2E (t_{2g}^3) level, which shares the same orbital occupation as the ground state but differs in spin multiplicity. Additional higher-energy doublet and quartet ligand-field states are also present.

As a consequence of this electronic structure, Cr^{3+} ions exhibit intense visible absorption bands associated with spin-allowed ligand-field transitions from the $^4A_2$ ground state to the $^4T_2$ ($t_{2g}^2e_g^1$), $^4T_1$ ($t_{2g}^2e_g^1$), and $^4T_1$ ($t_{2g}^2e_g^1$), excited states. Furthermore, weak yet sharp spectral features extending into the NIR region arise from spin-forbidden transitions, primarily the $^4A_2 \rightarrow {}^2E$ transition, as well as transitions to other higher-lying doublet states. Notably, the $^4A_2 \rightarrow {}^4T_2$ transition involves electron promotion into antibonding e_g orbitals, leading to a pronounced elongation of the metal–ligand bond length. In contrast, the $^4A_2 \rightarrow {}^2E$ transition is a spin-flip process and is therefore accompanied by minimal geometrical relaxation relative to the ground state, as schematically illustrated in the configurational coordinate diagram (Fig. 7) [165].

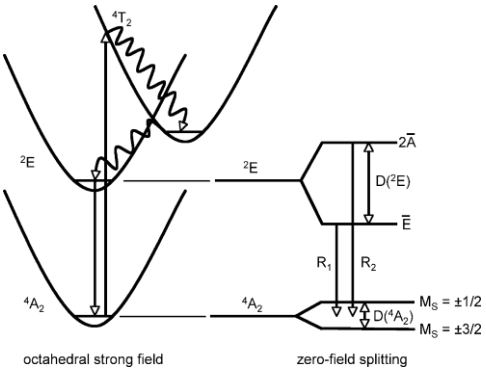

Fig. 7. The Scheme of the ground state and the lowest excited ligand-field states of Cr^{3+} in a moderate to strong octahedral ligand field (left) and the zero-field splittings resulting from a trigonal distortion and spin-orbit coupling (right)[165].

1.2.2. Eu^{2+}-based phosphors

Divalent europium (Eu^{2+}) is widely recognized as one of the most efficient luminescent activators in inorganic solid-state phosphors [166, 167]. For the free Eu^{2+} ion, a large energy separation exists between the $4f^7$ ground-state configuration and the lowest $4f^65d^1$ excited state, amounting to approximately 4.216 eV (~34 000 cm^{-1}) [168]. Upon incorporation into a crystalline host lattice, the energetic position of the Eu^{2+} 5d levels becomes strongly host dependent. As schematically illustrated in Fig. 8, interactions with the surrounding lattice induce both a centroid shift (ε_c) and a crystal-field splitting (ε_{cfs}) of the 5d states, collectively referred to as the spectroscopic red shift D(A), and activation energy ΔE from the lowest 5d level to the bottom of the conduction band are indicated [169].

The excitation characteristics of Eu^{2+}-activated phosphors are governed primarily by the magnitude of the centroid shift and the crystal-field splitting, whereas the emission properties are determined by the lowest 5d excited state in combination with the Stokes shift, ΔS(A). The Stokes shift originates from lattice relaxation effects associated with strong electron-phonon coupling following optical excitation of the 5d electron and is therefore also highly sensitive to the host crystal environment [170]. Consequently, by rational modification of the host lattice, such as altering its crystal structure, coordination environment, or bonding characteristics, it is possible to systematically tune the centroid shift, crystal-field splitting, and Stokes shift. This tunability provides an effective strategy for controlling both the

photoluminescence excitation (PLE) and photoluminescence (PL) behavior of Eu^{2+}-activated phosphors.

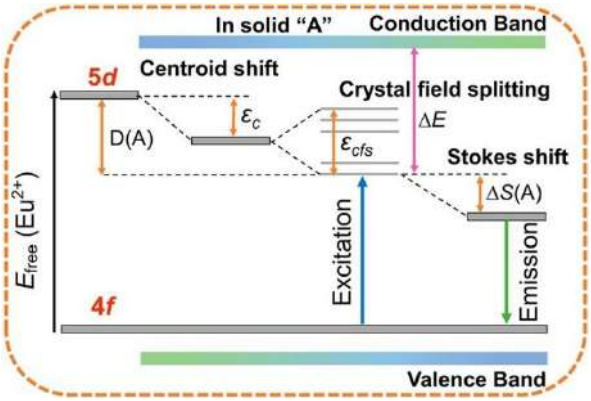

Fig. 8 Crystal-field–induced modifications of the Eu^{2+} 5d energy levels in an inorganic host lattice [169].

Multicolor Eu^{2+}-activated phosphors satisfy key requirements for advanced lighting applications, including appropriate emission wavelength and bandwidth, high quantum efficiency, excellent thermal and chemical stability, and cost-effective fabrication (Fig. 9) [171].

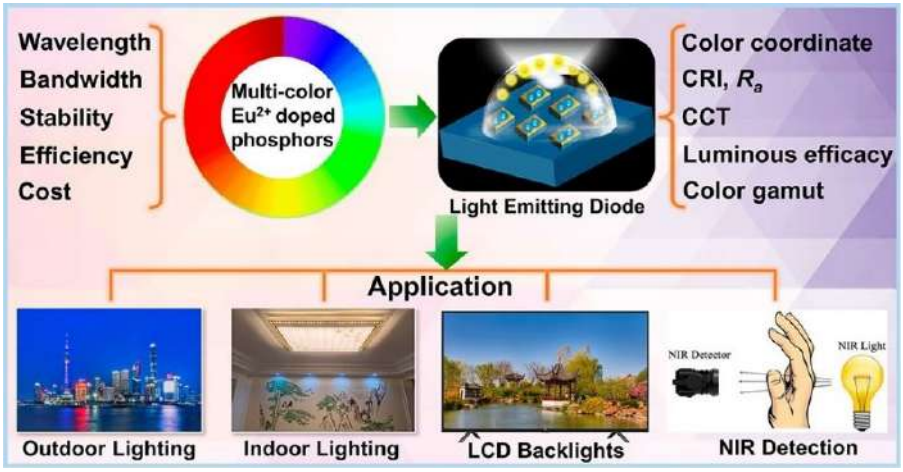

Fig. 9. Relationship between the emission properties of Eu^{2+}-doped phosphors and their LED applications [171].

Phosphate-based phosphors are widely recognized as an important class of luminescent materials owing to their excellent thermal stability, high emission efficiency, and the possibility of synthesis at relatively low

temperatures [172]. Within this family, Eu^{2+}-activated $ABPO_4$ compounds have attracted considerable attention as efficient blue-emitting phosphors under near-ultraviolet excitation. Representative examples such as $KSrPO_4:Eu^{2+}$, $KBaPO_4:Eu^{2+}$, and $LiCaPO_4:Eu^{2+}$ exhibit strong luminescence, high quantum efficiency, and good resistance to thermal quenching. These favorable characteristics render Eu^{2+}-doped $ABPO_4$ phosphors promising candidates for application in phosphor-converted WLEDs [173].

A variety of synthesis routes have been developed for the preparation of inorganic phosphor powders, including conventional solid-state reactions, solution-based techniques, combustion synthesis, and polymer-assisted methods such as polyethylene glycol-mediated processing. The choice of synthesis strategy plays a crucial role in determining the phase purity, particle morphology, and luminescent performance of the resulting phosphor materials.

1.2.3. Mn^{2+}-based phosphors

Manganese ions (Mn^{2+}) are widely employed as luminescent activators owing to their low toxicity, high photochemical, thermal, and chemical stability, as well as cost effectiveness [174, 175]. With a half-filled $3d^5$ electronic configuration, Mn^{2+}-doped phosphors exhibit emission arising from parity-forbidden d–d transitions, typically assigned to the $^4T_1 \rightarrow {}^6A_1$ transition. Although such transitions are strictly forbidden for free ions, they become partially allowed in crystalline hosts due to lattice-induced crystal-field effects and symmetry breaking.

The emission color of Mn^{2+} is highly sensitive to the local crystal field strength and coordination environment: weak crystal fields and tetrahedral coordination favor green emission, whereas strong crystal fields and octahedral coordination lead to orange or deep-red emission. These parity-relaxed transitions are characterized by long decay lifetimes in the millisecond range, making Mn^{2+}-activated phosphors particularly suitable for applications in fluorescent lamps, display devices, and white light-emitting diodes [176].

The spectral diversity characteristic of Mn^{2+}-activated phosphors is illustrated in the upper panel of Fig. 10, while the corresponding crystal-field splitting of the excited energy levels for octahedrally coordinated Mn^{2+} ($3d^5$) is depicted in the lower panel. The PL and PLE spectra shown in Fig. 10 originate from representative Mn^{2+}-doped hosts, including CaF_2, $Ba_2Si_5N_8$, and Mg_2GeO_4. In all cases, the observed emission is assigned to the $^4T_{1g}(^4G) \rightarrow {}^6A_{1g}(^6S)$ transition, whereas the lowest-energy excitation band corresponds to the reverse $^6A_{1g}(^6S) \rightarrow {}^4T_{1g}(^4G)$ transition [177].

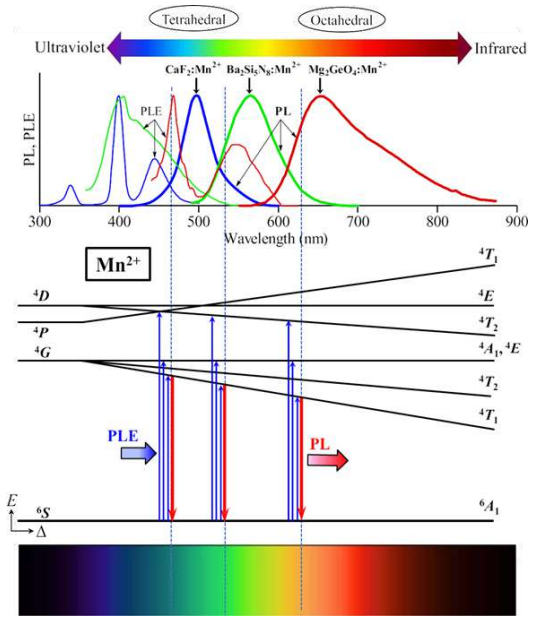

Fig. 10. Crystal-field splitting scheme for the electronic energy levels of Mn^{2+} ion in a phosphor material (Δ= crystal-field splitting parameter) [177].

Due to the spin- and parity-forbidden nature of these transitions, Mn^{2+} exhibits inherently low oscillator strength and pronounced temperature dependence of its luminescence intensity. Consequently, efficient sensitization mechanisms are often required to enhance Mn^{2+} emission, which is a critical consideration for its practical implementation in phosphor-based devices.

Mn^{2+} is widely recognized as an efficient luminescent activator across a broad range of host materials, including oxides, phosphates, nitrides, oxynitrides, chalcogenides, halides, as well as organic-inorganic hybrid systems [178]. Owing to its versatile emission behavior and good chemical stability, Mn^{2+}-activated phosphors have been extensively explored for solid-state lighting applications. For example, Zhang *et al.* reported $ZnAl_2O_4$:Mn phosphors synthesized via a sol-gel route, exhibiting intense green emission under blue LED excitation and demonstrating strong potential for white LED devices [179]. Subsequently, Menon *et al.* observed green emission centered at 523 nm from Mn^{2+}-doped Zn_2SnO_4 prepared by a conventional solid-state reaction method [180]. In addition, Su *et al.* successfully fabricated γ-AlON:Mn^{2+},Mg^{2+} phosphors using a co-precipitation precursor approach, achieving narrow-band green emission suitable for high-color-purity lighting applications [181].

2. EXPERIMENTAL

2.1. Materials and reagents

Calcium nitrate tetrahydrate ($Ca(NO_3)_2 \cdot 4H_2O$, ≥99%, Carl Roth), diammonium hydrogen phosphate ($(NH_4)_2HPO_4$, ≥98%, Carl Roth), ammonia solution (NH_4OH, 25%, Carl Roth), lithium chloride (LiCl, ≥98.5%, Roth), sodium chloride (NaCl, >99.8%, Carl Roth), potassium chloride (KCl, >99%, Carl Roth) and calcium chloride ($CaCl_2$, ≥94%, Carl Roth) and chromium (III) nitrate nonahydrate ($Cr(NO_3)_3 \cdot 9H_2O$, 98%, Alfa Aesar), europium(III) nitrate hexahydrate ($Eu(NO_3)_3 \cdot 6H_2O$, 99.9%, Acros Organics), manganese(II) nitrate tetrahydrate ($Mn(NO_3)_2 \cdot 4H_2O$, 98%, Alfa Aesar) were used as starting materials.

2.2. Synthesis of $Ca_5(PO_4)_3Cl$ and Ca_2PO_4Cl

Initial ACP powder (Ca/P= 1.5) was synthesized according to the previously reported procedure [122] using calcium nitrate tetrahydrate ($Ca(NO_3)_2 \cdot 4H_2O$) and diammonium hydrogen phosphate ($(NH_4)_2HPO_4$) as starting materials. Briefly, an appropriate amount of $(NH_4)_2HPO_4$ was dissolved in deionized water to obtain a 0.5M solution, to which a concentrated ammonia solution (NH_4OH, 25%) was added under a constant mixing to adjust the pH value to 10. Next, an aqueous 0.75M solution of calcium nitrate was rapidly added to the above mixture, resulting in the formation of white precipitates. The obtained precipitates were aged in the reaction mixture for 10 min, vacuum filtered, washed with deionized water and isopropanol, and dried at 50 °C overnight.

Lithium chloride (LiCl), sodium chloride (NaCl), potassium chloride (KCl) and calcium chloride ($CaCl_2$) were used for the molten salt synthesis. For the reactions in molten salts, the as-prepared ACP was mixed with an appropriate amount of selected salts in an agate mortar, transferred into an alumina crucible and annealed in a muffle furnace at certain temperature for different periods of time. The temperature, annealing time and ACP to flux weight ratio were chosen individually for different experiments. After the reaction, the obtained products were washed with a hot deionized water in order to remove the salts. The residual products were dried in an oven at 100 °C. The reaction scheme is presented in Fig. 11.

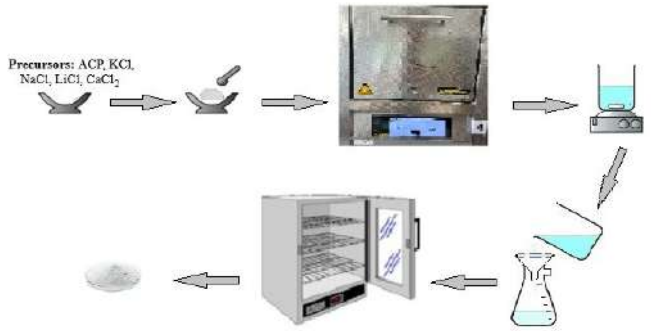

Fig. 11. Molten salt reaction scheme.

2.3. Synthesis of Cr^{3+}-activated β-$Ca_3(PO_4)_2$

β-TCP powders substituted with Cr^{3+} ions were synthesized by a wet co-precipitation method followed by high-temperature annealing according to a slightly modified previously reported procedure [182, 183]. The substitution level (0.1, 0.5, 1.0, 2.0, and 5.0 mol%) is given with respect to Ca^{2+} ions. Appropriate amounts of $Ca(NO_3)_2 \cdot 4H_2O$ and $Cr(NO_3)_3 \cdot 9H_2O$ were dissolved in deionized water to obtain a solution with a total concentration of metal ions of 0.75M. In parallel, $(NH_4)_2HPO_4$ was dissolved in deionized water in a separate beaker to obtain a 0.5M solution, to which concentrated ammonia solution (NH_4OH, 25%) was added to adjust the pH to 10. Next, a solution containing metal nitrates was rapidly added to the $(NH_4)_2HPO_4$ solution, leading to the formation of precipitates. The obtained precipitates were aged for 10 min, vacuum-filtered, washed with deionized water, and dried in an oven overnight. Dry powders were ground in an agate mortar and annealed in a muffle furnace in air at 1100 °C for 5 h at a heating rate of 5 °C min^{-1}. The reaction scheme is presented in Fig. 12.

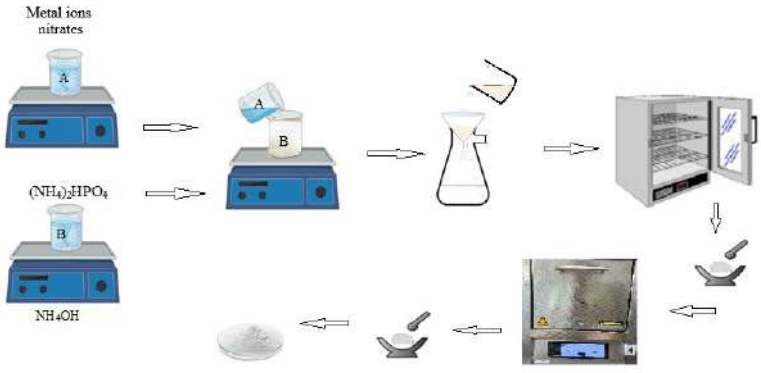

Fig. 12. Synthesis scheme of a wet co-precipitation method.

2.4. Synthesis of Eu^{2+}-doped α-$Ca_3(PO_4)_2$

The starting Eu^{3+}-doped DCPD powder was synthesized by wet co-precipitation method modifying previously reported procedure [184, 185]. First, the metal nitrates were dissolved in deionized water, resulting in a 0.8M solution, where the Eu-substitution level was adjusted as 0.1 mol% with respect to Ca^{2+} ions. The $(NH_4)_2HPO_4$ solution of the same concentration was prepared in parallel. The solution containing phosphate ions was rapidly poured into the solution of metal ions under constant stirring, forming white precipitates. The as-prepared precipitates were aged in the reaction mixture for 5 min; afterward, vacuum filtered, washed with deionized water and dried in an oven at 50 °C overnight. For the synthesis of Eu-doped α-TCP, the as-prepared precipitates were annealed in a tube furnace in a vacuum ($7.8 \cdot 10^{-2}$ mbar) at 1300 °C for 24 h. After the annealing procedure, the furnace was cooled down naturally.

2.5. Synthesis of Mn^{2+}-doped α-$Ca_2P_2O_7$

The synthesis of undoped and Mn-doped CPP polymorphs was performed by wet co-precipitation method [185]. Firstly, 0.8M Ca^{2+} and Mn^{2+} nitrates solution was prepared by dissolving metal salts in deionized water. Mn-substitution level was chosen as 1 mol% with respect to Ca^{2+} ions. $(NH_4)_2HPO_4$ solution of the same concentration was prepared in a separate beaker. Next, the solution containing phosphate ions was rapidly added to the solution of metal ions under constant mixing on a magnetic stirrer, resulting in precipitates' formation. The obtained precipitates were aged in the reaction mixture for 5 min while stirring, afterward filtered, washed with deionized water, and dried in an oven at 50 °C overnight. The obtained precipitates were annealed at 1200 °C, with a heating rate of 5 °C/min and a holding time of 10 minutes.

2.6. Characterization

Powder X-ray diffraction (XRD) analysis was performed using a Rigaku MiniFlex II diffractometer (Cu-Kα, λ = 1.5419 Å) working in Bragg-Brentano (θ/2θ) geometry. The data were collected within the 10–60° 2θ range with a step of 0.02° and a scanning speed of 5°/min.

Fourier transform infrared spectra (FTIR) were recorded in the range of 4000–400 cm^{-1} using a Bruker ALPHA-FTIR spectrometer.

The morphological features of synthesized powder were analyzed by scanning electron microscopy (SEM) using a Hitachi SU-70 microscope.

The chromium content in the synthesized products was determined by inductively coupled plasma optical emission spectrometry (ICP-OES) using a Perkin-Elmer Optima 7000DV spectrometer. The samples prior to analysis were dissolved in 5% nitric acid (HNO_3, Rotipuran® Supra 69%, Roth) and diluted to an appropriate volume.

A Bruker ELEXSYS-II E500 CW-EPR spectrometer was used for electron paramagnetic resonance (EPR) analysis of the samples. The spectra acquisition settings were as follows: room temperature, 9.833 GHz microwave frequency, 10 mW microwave power, and 0.4 mT magnetic field modulation amplitude.

The PLE and PL spectra were measured using the Edinburgh Instruments FLS980 spectrometer equipped with double excitation and emission monochromators, a 450 W Xe arc lamp, a cooled (−20 °C) single-photon counting photomultiplier (Hamamatsu R928P), and mirror optics for the powder samples. Emission spectra were recorded using a 0.5 nm emission slit width, a 3.5 nm excitation slit width, a step size of 0.5 nm, an integration time of 0.2 s, and averaged over three repetitions. Excitation spectra were acquired using a 1.5 nm emission slit width, a 0.5 nm excitation slit width, the same step size and integration time, and also averaged over three repetitions. The PL spectra were corrected by a correction file obtained from a tungsten incandescent lamp certified by NPL (National Physics Laboratory, UK). The PLE spectra were corrected by a reference detector. PL decay curves were measured using the same Edinburgh Instruments FLS980 spectrometer. A 405 nm pulsed laser diode (Edinburgh Instruments, EPL-405) was used as the excitation source.

Measurements of emission and excitation spectra in the spectral range from 6.2 eV to 12.4 eV (100–200 nm) were carried out using a vacuum monochromator assembled according to the Seiya-Namioka scheme with a recording monochromator Solar M-266 (Belarus) and a PMT detector Hamamatsu H11890 -01 (Japan). A hydrogen lamp is used for excitation in the VUV range of the spectrum. Cooling up to 15 K is provided by a cryostat with helium cooling equipment of a closed cycle.

3. RESULTS AND DISCUSSION

3.1. Synthesis and morphological control of $Ca_5(PO_4)_3Cl$ and Ca_2PO_4Cl *via* the phase transformation of amorphous calcium phosphate in molten chlorides

In order to investigate the influence of chemical composition of the molten salt on the phase purity and morphology of the product, a series of reactions was performed using a fixed amount of ACP and varying ratio of KCl and $CaCl_2$. The XRD patterns of the obtained products are depicted in Fig. 13. Evidently, the composition of the molten salts strongly influenced the crystal structure of the product. Single-phase ClAp was obtained from the K-rich mixtures down to the KCl/$CaCl_2$ ratio of 6:4. It is also seen that increasing $CaCl_2$ content obviously changes the intensity ratio of the diffraction peaks.

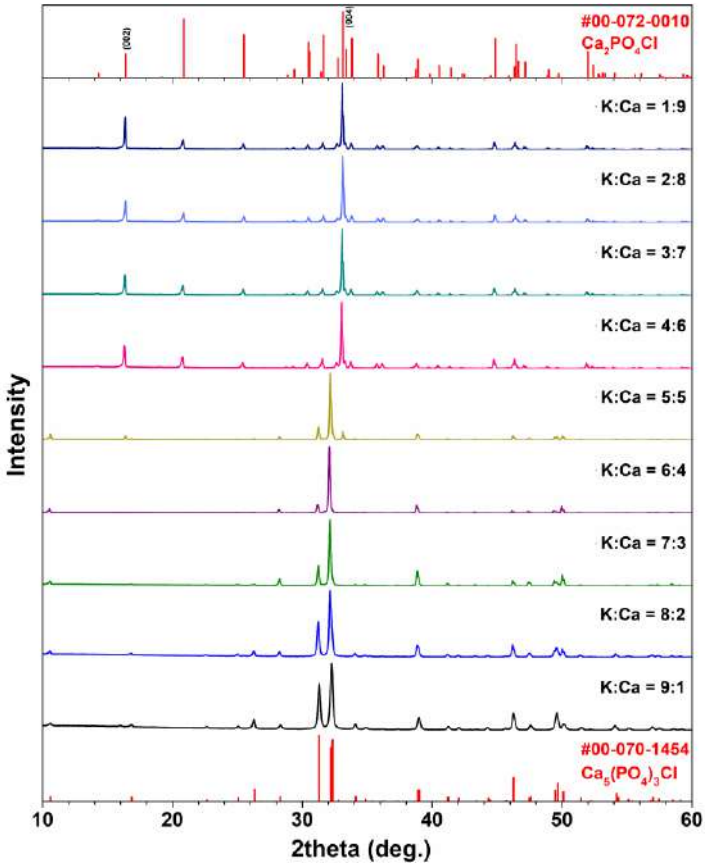

Fig. 13. XRD patterns of the synthesis products obtained after the treatment of ACP in the mixtures of KCl and $CaCl_2$ mixed in different molar proportions (T= 750 °C, ACP/flux= 1:2, t= 5 h).

The XRD patterns of the samples obtained from the fluxes with high Ca content (30 and 40 mol%) are obviously dominated by the diffraction peak centered at ca. 32.2°. Such a behavior suggests an anisotropic growth of ClAp particles, resulting in the appearance of preferred orientation observed in the XRD patterns. When the KCl/$CaCl_2$ ratio reached 5:5, the major phase in the obtained product was still ClAp; however, neighboring Ca_2PO_4Cl phase was also observed indicating the formation of biphasic product. With higher amount of $CaCl_2$, exclusively Ca_2PO_4Cl was formed; there were no even traces of other crystalline phases. All the observed XRD patterns of single-phase Ca_2PO_4Cl possessed preferred orientation with an expressed diffraction peaks corresponding to (002) and (004) planes.

FTIR spectra of the obtained series were recorded in order to supplement the results of XRD analysis. The spectral region in the range from 1500 to 400 cm^{-1} is given in Fig. 14 as representative for the phosphate-related absorption bands. There were no bands associated with phosphate vibrations in the rest region up to 4000 cm^{-1}.

The spectra of the samples prepared in K-rich media (KCl/$CaCl_2$ ratio from 9:1 to 6:4) exhibit few absorption bands. The absorption bands located in the range from approximately 1130 to 930 cm^{-1} correspond to asymmetric stretching mode (ν_3) and symmetric stretching mode (ν_1) of the P-O bonds in PO_4 tetrahedra. The bands observed in the region from 630 to 530 cm^{-1} and the band centered at 473 cm^{-1} are ascribed to the ν_4 and ν_2 bending modes of the O–P–O bonds of the phosphate group, respectively [186]. The FTIR spectrum of the sample obtained from the KCl $CaCl_2$ = 5:5 exhibit the same shape as observed for the single-phase ClAp confirming that ClAp is the major phase. Obvious change in the positions and the shape of absorption bands is seen, when powders synthesized in Ca rich media ($CaCl_2$ percentage from 60 mol% and higher). The absorption bands corresponding to the ν_4 mode are obviously shifted to lower wavenumber region; while the band ascribed to the ν_2 mode in ClAp disappeared. The shape of the Ca_2PO_4Cl spectrum matches well with that of previously reported in the literature [187]. The band centered at ca. 875 cm^{-1} is most probably indicates the presence of carbonates [188]. A closer look also allows to see the bands representing the C–O bonds of carbonate groups at ca. 1485 cm^{-1}. The amount of carbonates is associated with the presence of $CaCl_2$ in the flux. Increasing the percentage of $CaCl_2$ in the KCl $CaCl_2$ mixture led to the increase of the amount of carbonates in the obtained product.

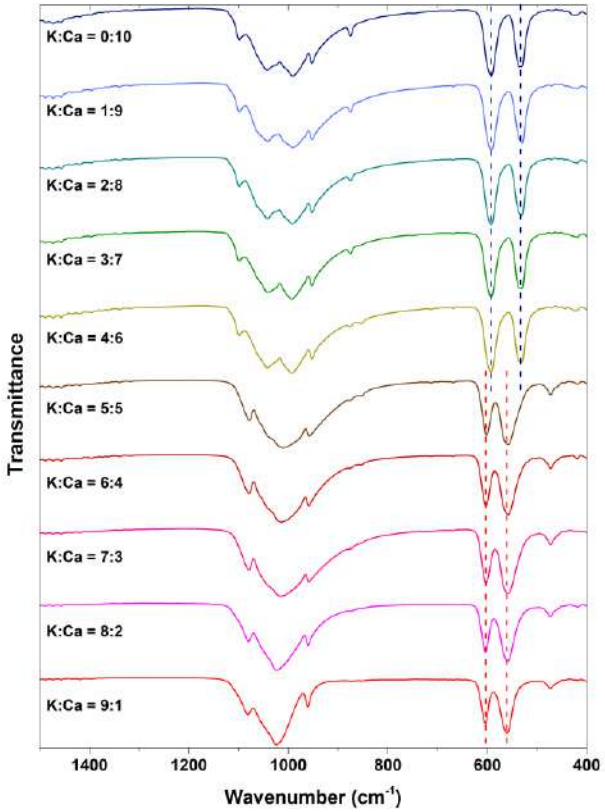

Fig. 14. FTIR spectra of the synthesis products obtained after the treatment of ACP in the mixtures of KCl and $CaCl_2$ mixed in different molar proportions (T = 750 °C, ACP/flux = 1:2, t = 5 h).

The SEM images of the samples obtained in the KCl $CaCl_2$ mixtures of different compositions are shown in Fig. 15. Evidently, the composition of the synthesis medium strongly influences the morphology of the products both in terms of size and shape of the particles. ClAp obtained in the mixtures with KCl/$CaCl_2$ ratio of 9:1 and 8:2 consisted mostly of agglomerated sub-micrometer particles possessing a nearly spherical shape; however, a closer look reveals the presence of the particles of polygonal rod-like shape. Increasing the $CaCl_2$ percentage up to 30 mol% resulted in the drastic change in the morphology. Resulting polydisperse powders consisted of hexagonal rods of micrometric dimensions covered by smaller particles. The KCl/$CaCl_2$ ratio of 6:4 resulted in the reduced number of small particles; the obtained rod-like particles were more uniform. Further increase in $CaCl_2$ fraction up to 50% led to the obvious change in the aspect ratio of the rods due to the reduction of the length. The products obtained in the Ca-rich mixtures exhibited different morphology consisting of the square prism-like particles of

micrometric dimensions. This correlates well with the phase transformation from ClAp to Ca_2PO_4Cl. It can be concluded that the presence of $CaCl_2$ in the flux promotes the crystal growth of ClAp significantly; moreover, it facilitates the anisotropic growth along the c-axis, resulting in the formation of hexagonally-shaped rods. However, the influence of this parameter is limited due to the formation of Ca_2PO_4Cl in $CaCl_2$-rich fluxes. At the same time, the crystals of Ca_2PO_4Cl do not tend to grow anisotropically, which probably associated with the peculiarities of their crystal structure.

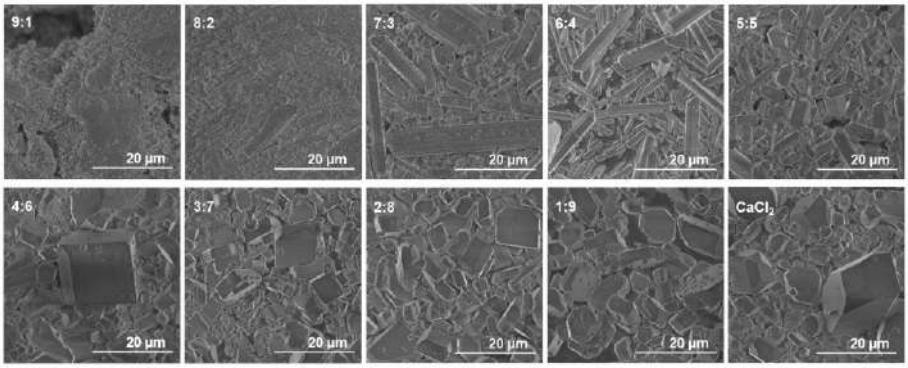

Fig. 15. SEM micrographs of the synthesis products obtained after the treatment of ACP in the mixtures of KCl and $CaCl_2$ mixed in different molar proportions (for K:Ca ratio from 9:1 to 1:9 T = 750 °C, ACP/flux= 1:2, t=5 h; for $CaCl_2$ T= 800 °C).

In order to study the influence of the ACP-to-flux ratio on the phase purity and morphology of ClAp powders, a series of powders was synthesized varying the ACP-to-flux mass ratio from 1:1 to 1:10. For this experiment two different mixtures of salts with the KCl/$CaCl_2$ ratios of 9:1 and 6:4 were employed. The XRD patterns clearly demonstrate that single-phase ClAp was obtained in all cases regardless of the ACP-to-flux ratio and chemical composition of the flux. While the phase purity was not affected by the composition and weight fraction of the salts, the morphology of ClAp was influenced significantly. The SEM images reflecting the influence of ACP-to-flux ratio on the morphology of ClAp powders are given in Fig. 16.

The effect was more pronounced for the KCl/$CaCl_2$ ratio of 9:1. Evidently, the relatively high concentration of ACP resulted in the formation of small particles (Figs. 16a,b). In this case the powders consisted of nearly spherical particles of sub-micrometer dimensions. In more diluted sample with ACP-to-flux ratio of 1:4 (Fig. 16c) the formation of microrods was evident; however; the small particles still remained dominating. Further

dilution of the reaction mixture up to ACP-to-flux ratio of 1:10 led to the increased number of microrods and the reduced number of small particles; however, their presence was still evident. Overall, it can be concluded that the size of the particles can be tuned by the content of ACP in the initial reaction mixture. By contrast, when the flux with the $KCl/CaCl_2$ ratio of 6:4 was used for the synthesis, the effect of ACP concentration was rather minor; the microrods were formed in all cases (Figs. 16e-h). This observation indicates, that synergistic effect of $CaCl_2$ in the flux (Fig. 15) and the ACP-to-flux ratio on the anisotropic crystal growth is not achievable.

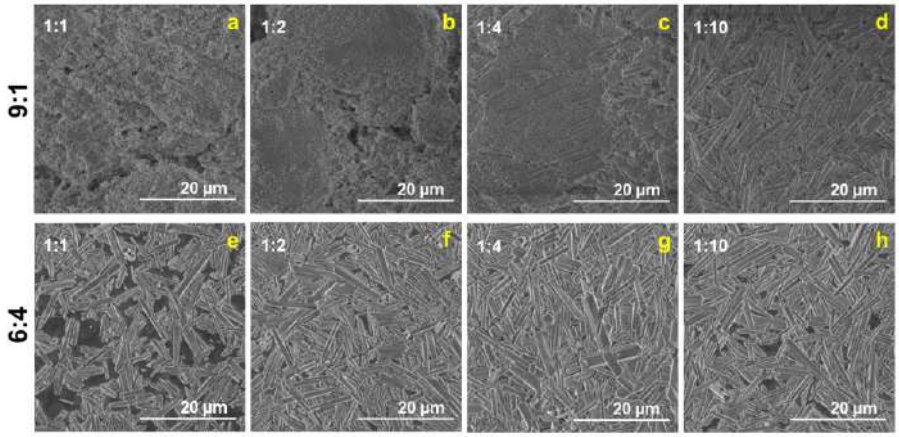

Fig. 16**.** SEM micrographs of ClAp powders obtained after the treatment of ACP with different amounts molten salts, when $KCl/CaCl_2$ ratio is 9:1 (a-d) and 6:4 (e-h); ACP/flux ratio is 1:1 (a, e); 1:2 (b, f); 1:4 (c, g); and 1:10 (d, h) (T=750 °C, t=5 h).

The reaction time in the range from 1 to 48 h did not affect the phase purity of the samples obtained in the flux of $KCl/CaCl_2$=6:4 at 750 °C. The XRD patterns clearly show that ClAp was obtained in all cases. This indicates that single-phase ClAp can be obtained in a time-efficient manner in just 1 h. Fig. 17 illustrates the influence of the reaction time on the morphology of ClAp powders. As seen, the duration did not have a significant effect. In all cases the synthesized ClAp powders possessed the morphology of microrods.

Finally, the influence of the reaction temperature on the phase purity and morphological features of ClAp was investigated in the range from 750 °C to 1200 °C. The XRD patterns of the synthesized products clearly demonstrate the formation of ClAp. Taking into account the previously mentioned results of the XRD analysis, it can be concluded that the phase composition of the product is influenced exceptionally by the chemical composition of the flux,

whereas other synthesis parameters such as temperature or time did not demonstrate any effect. Unlike the phase composition, the morphology of ClAp was determined to be strongly dependent on the temperature (Fig. 18). Increasing the temperature resulted in the formation of larger particles with noticeably lower aspect ratio.

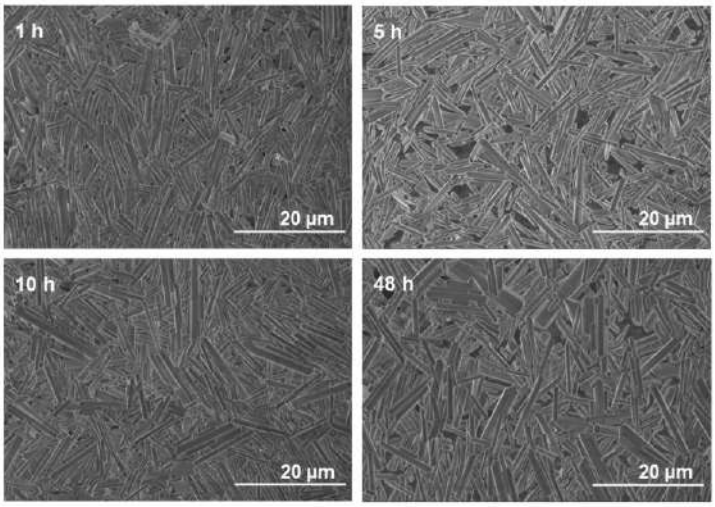

Fig. 17. SEM micrographs of ClAp powders obtained after the treatment of ACP with molten salts for different periods of time: 1 h (a); 5 h (b); 10 h (c); 48 h (d) (T=750 °C, KCl/$CaCl_2$=6:4, ACP/flux=1:10).

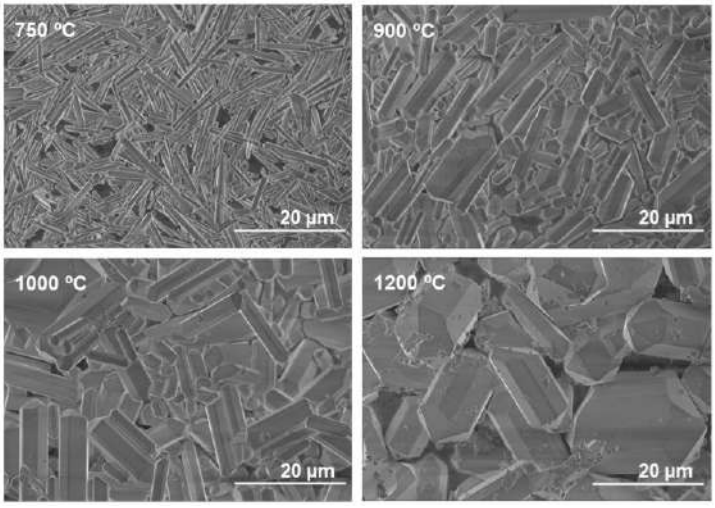

Fig. 18. SEM micrographs of ClAp powders obtained after the treatment of ACP with molten salts at different temperatures: 750 °C (a); 900 °C (b); 1000 °C (c); 1200 °C(d); (KCl/$CaCl_2$= 6:4, ACP/flux= 1:10, t= 5 h).

It is known that both natural and synthetic apatites are able to adopt other ions including monovalent alkali metal ions [189]. Since in our study the synthesis of ClAp was performed in the presence of high amount of K^+ ions, the K-doping is a reasonable concern. The EDX analysis was performed in order to check the presence of K^+ ions in the synthesized samples; the representative spectrum is depicted in Fig. 19. It is seen that all the observed signals attribute to the elements constituting ClAp crystal structure, namely, Ca, P, O and Cl; there were no signals ascribed to K^+ ions. The absence of K^+ correlate well with the results obtained in single-salt flux, where biphasic product was obtained due to the inability of K^+ ions to compensate the deficiency of Ca. The extra signal attributed to Al arise from the sample holder. The calculated Ca/P ratio was very close to that of stoichiometric ClAp (1.67). Other elements were manually eliminated from these calculations; the sum of Ca and P atoms was assumed as 100%.

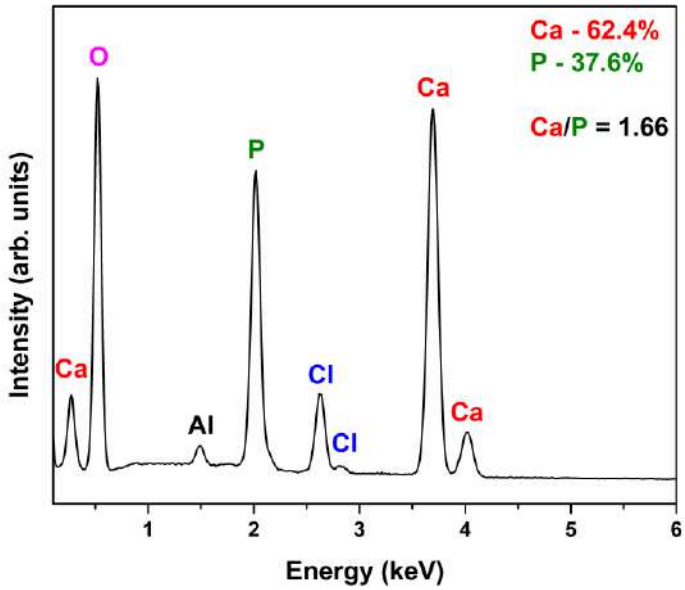

Fig. 19. EDX spectrum of ClAp (ACP/flux= 1:10, T= 1200 °C, t=5 h).

Summarizing the obtained results, it can be concluded that in molten chlorides ACP can be selectively converted to ClAp or Ca_2PO_4Cl using an appropriate chloride salts. The proposed synthetic approach is simple and time-efficient, moreover, it allows to control the morphology of resulting products.

3.2. Luminescent properties of near-infrared-emitting Cr^{3+}-activated beta-$Ca_3(PO_4)_2$

The XRD patterns of the resulting products are shown in Fig. 20a. The major β-TCP phase was obtained for all samples regardless of the Cr content. All diffraction peaks match very well with the standard of rhombohedral $Ca_3(PO_4)_2$ with *R*3c space group (#00-070-2065). A minor impurity phase was detected in the sample with the highest Cr content (5 mol%). This secondary phase was identified as Cr_2O_3 (#00-038-1479). The XRD patterns of the powders with lower Cr content did not reveal the presence of this impurity. This observation indicates that under the selected synthetic conditions, the amount of Cr^{3+} ions that can be incorporated into the β-TCP crystal structure is limited. Although some previous study have reported significantly higher Cr^{3+} substitution level ($Ca_9Cr(PO_4)_7$, i.e. 10 mol% with respect to Ca ions), it should be noted that this material was synthesized from a melt in the Cs_2O–CaO–Cr_2O_3 system using a polyphosphate flux [190]. To the best of our knowledge, there have been no other reports on the synthesis of this material. Alshemary et al. reported the synthesis of Cr^{3+}-doped β-TCP by microwave-assisted wet precipitation method [191]; however, Cr_2O_3 impurity was also detected starting from the Cr^{3+} substitution level of 4 mol%.

The FTIR spectra of Cr^{3+}-doped β-TCP samples are depicted in Fig. 20b. The spectral range from 1400 to 400 cm^{-1} was chosen as a representative, because there are no absorption bands in the spectrum of β-TCP in other regions. The spectrum of the undoped sample exhibited absorption bands characteristic of phosphate groups in the β-TCP crystal structure. The bands located in the range of ca. 1150–990 cm^{-1} were assigned to the phosphate ν_3 stretching mode, while the two bands centered at 970 and 940 cm^{-1} were ascribed to the ν_1 vibrational mode. The bands at 640–500 cm^{-1} were ascribed to the ν_4 bending mode, and the weak absorption band centered at approximately 434 cm^{-1} corresponded to the ν_2 mode [192]. The shape of the spectra changed slightly with increasing Cr^{3+} content. Two absorption bands centered at 901 and 864 cm^{-1} were clearly visible for the samples with Cr content of 1 mol% and higher. There are not enough data in the literature on Cr^{3+}-doped β-TCP for comparison; however; it is known that doping with trivalent ions, such as Fe^{3+} or Ga^{3+}, changes the shape of FTIR spectrum of β-TCP [128, 182, 193, 194]. Additional absorption bands at ~865 cm^{-1} were observed for both dopants. According to Mellier et al. [194], the substitution of Ca^{2+} with trivalent ions leads to significant changes in the local environment of the phosphate sites. This results in stronger splitting and the appearance of

new absorption bands. The appearance of these absorption bands confirms that Cr^{3+} ions are introduced into the β-TCP crystal lattice.

The EPR spectra presented in Fig. 20c reveal the concentration-dependent incorporation of Cr^{3+} ions into the investigated β-TCP series. In the undoped sample, a minor signal from Mn^{2+} ions, commonly found as impurities in CP materials [195], is observed. As the Cr^{3+} concentration increases, two prominent signals appear: an asymmetric low-field component at around 160 mT (g_{eff} = 4.46), and a symmetric line at 356 mT (g_{eff} = 1.97). EPR signal positions are governed by the magnitude of the zero-field splitting (ZFS) of the $^4A_2$ ground state of Cr^{3+}, typically spanning a broad magnetic field range in various crystalline and amorphous hosts [196-200]. Within the investigated concentration range, the double-integrated intensity of the low-field component increased proportionally with the Cr concentration. However, variations in the relative intensities of the low-field and g_{eff}= 1.97 components across different samples indicate the presence of multiple Cr^{3+}-related centers.

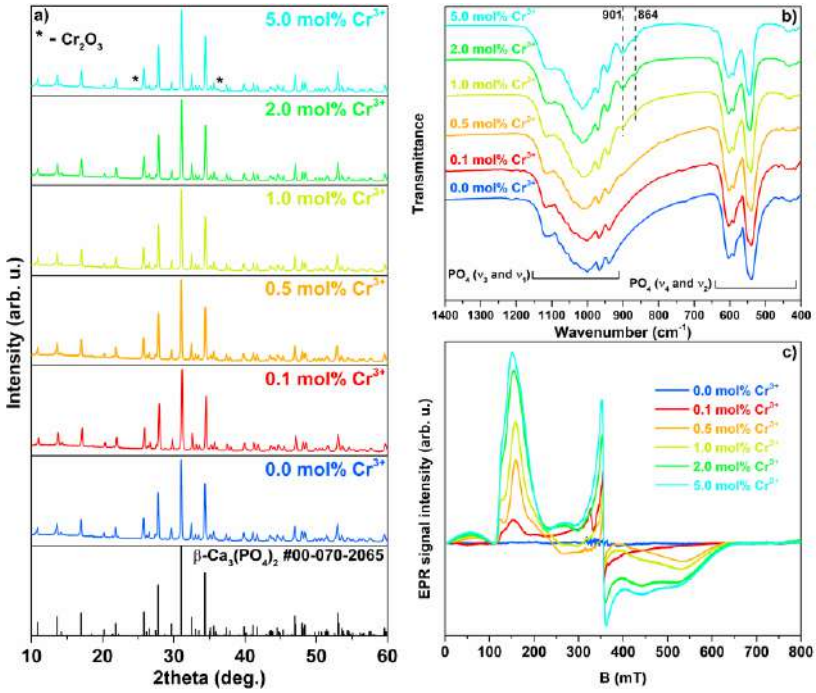

Fig. 20. (a) XRD patterns; (b) FTIR spectra; and (c) EPR spectra of β-TCP with various Cr^{3+} content.

A discussion of the local environment of Cr^{3+} ions in β-TCP can be initiated based on experimental powder EPR spectra and available literature data. Similar spectra (coexistence of low-field and g_{eff}= 1.97 components)

have been reported for various Cr-doped glass systems [196-198]. In these studies, the low-field component was attributed to isolated Cr^{3+} centers in distorted octahedral sites, whereas the interpretation of the high-field component was ambiguous. Cr^{3+} ions preferentially occupy crystallographic positions, providing a 6-fold coordinated environment. Five cation sites, Ca(1)-Ca(5), are available in the β-TCP structure for substitution with transition metal ions.; Of these, Ca(5) is coordinated by 6 ligands [141]. The substitution of Ca^{2+} sites by Cr^{3+} ions necessitates charge compensation, suggesting that multiple Cr^{3+} centers could arise from the same crystallographic site, but with different defects, such as cation vacancies, in the vicinity. Such a complicated case would likely result in broad EPR spectra due to overlapping signals from different environments, as observed in the present study. It should be mentioned, that according to Zatovsky et al. in the crystal structure of $Ca_9Cr(PO_4)_7$ the coordination of Cr^{3+} ions is slightly distorted octahedral [190], which corresponds to the Ca(5) site.

The SEM images of the synthesized β-TCP powders are given in Fig. 21. Evidently, the grain size strongly depends on the concentration of Cr^{3+} ions. In the case of undoped TCP, relatively large grains of approximately 2-4 μm were formed; however, the presence of 0.1 mol% of Cr^{3+} obviously reduced the grain size to 1-2.5 μm. In the case of 5 mol% Cr^{3+}, the grain growth was retarded even more, and the powders consisted of relatively small elongated particles of undefined shape necked to each other.

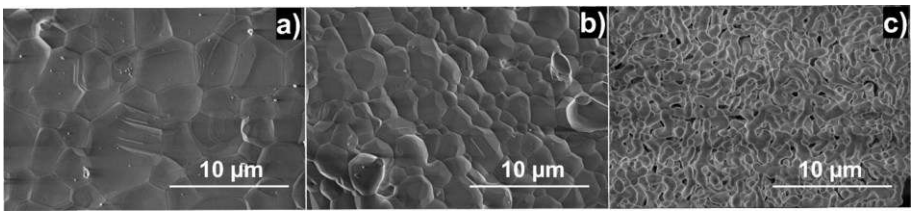

Fig. 21. SEM images of β-TCP with (a) 0 mol% Cr^{3+}; (b) 0.1 mol% Cr^{3+}; and (c) 5 mol% Cr^{3+}.

The well-known disadvantage of the co-precipitation method is the challenge in controlling the chemical composition; therefore, elemental analysis of the synthesis products is an obligatory part of the characterization. The results of ICP-OES analysis of the Cr^{3+}-doped samples are summarized in Table 4. The determined Cr content in the synthesized powders was in good agreement with the theoretical values. The only exception is the sample with the highest Cr concentration, where the determined value was approximately 20% lower than the nominal value.

Table 4. Results of the elemental analysis performed by ICP-OES.

Sample	Theoretical Cr/(Cr+Ca) ratio, mol%	Determined Cr/(Cr+ Ca) ratio, mol%
TCP: 0.1% Cr^{3+}	0.100	0.101
TCP: 0.5% Cr^{3+}	0.500	0.507
TCP: 1.0% Cr^{3+}	1.00	0.976
TCP: 2.0% Cr^{3+}	2.00	2.01
TCP: 5.0% Cr^{3+}	5.00	3.94

Fig. 22 shows the photoluminescence (PL) excitation and emission spectra of the β-TCP: Cr^{3+} samples. Three Cr^{3+} typical excitation bands were detected for all samples, with maxima at approximately 300, 450, and 640 nm. These bands were attributed to the intra-*3d* spin-allowed optical transitions of Cr^{3+}: $^4A_2(^4F) \rightarrow {}^4T_1(^4P)$ at 300 nm; $^4A_2(^4F) \rightarrow {}^4T_1(^4F)$ at 450 nm, and $^4A_2(^4F) \rightarrow {}^4T_2(^4F)$ at 640 nm [201, 202]. The positions of the Cr^{3+} 3d energy levels are strongly affected by the crystal field surrounding the Cr^{3+} ion. Therefore, small changes in the lattice, such as increased Cr^{3+} doping concentration and subsequent generation of defects required for charge compensation, can lead to changes in the spectral features [203]. In the case of the β-TCP: Cr^{3+} samples, a redshift for the 450 nm excitation band with increased Cr^{3+} concentration was observed.

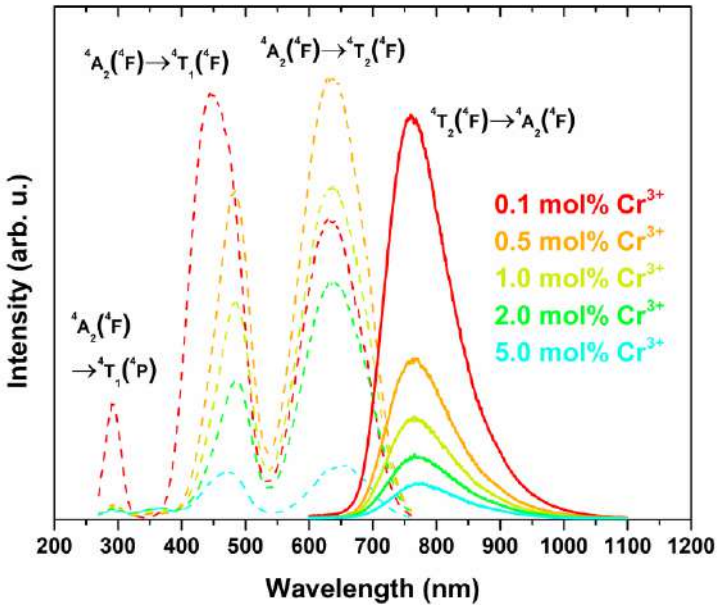

Fig. 22. Excitation (dashed lines) and emission (solid lines) spectra of the β-TCP with various Cr^{3+} concentrations (λ_{em}=790 nm; λ_{ex}= 450 nm).

To gain insight into the interelectronic transitions occurring in d-orbitals, Tanabe-Sugano diagrams are typically employed [204, 205]. These diagrams illustrate the energy levels of transition metal ions with respect to the crystal field strength (Dq) and Racah parameter (B). Fig. 23b demonstrates a simplified Tanabe-Sugano diagram that elucidates the energy levels of a Cr^{3+} ion in octahedral coordination. Thus, the redshift of the $^4A_2(^4F) \rightarrow {}^4T_1(^4F)$ transition should be expected in the case of decreasing crystal-field strength. Furthermore, when excited at 450 nm, all samples can be characterized by a broad near-infrared luminescence band in the 680–900 nm range, originating from the spin-allowed $^4T_2(^4F) \rightarrow {}^4A_2(^4F)$ optical transition typical of Cr^{3+} ions in a relatively weak crystal field [206]. The best PL intensity was achieved for the 0.1 mol% Cr^{3+} sample, most likely due to concentration quenching at higher Cr^{3+} concentrations.

For the 0.1 mol% sample, a series of temperature-dependent measurements of the PL spectra in the 77−500 K range was carried out. The results are shown in Fig. 23a. The two primary observations are as follows: first, there is strong thermal quenching with increasing temperature; second, at low-temperature conditions (77 and 100 K), not only the previously discussed broad Cr^{3+} PL band but also a narrow band related to the spin-forbidden $^2E(^2G) \rightarrow {}^4A_2(^4F)$ optical transition emerges. In general, the appearance of this band is a sign of Cr^{3+} ions under strong crystal field conditions. In the Tanabe-Sugano diagram for the d^3 electron configuration (Fig. 23b), the crystal field is considered weak if $Dq/B < 2.3$ and strong if $Dq/B > 2.3$. In the case of $Dq/B \approx 2.3$, an intermediate crystal field can be assumed, and there should be thermal equilibrium between the $^2E(^2G)$ and $^4T_2(^4F)$ states, leading to the broadband and narrow-band emission of Cr^{3+}.

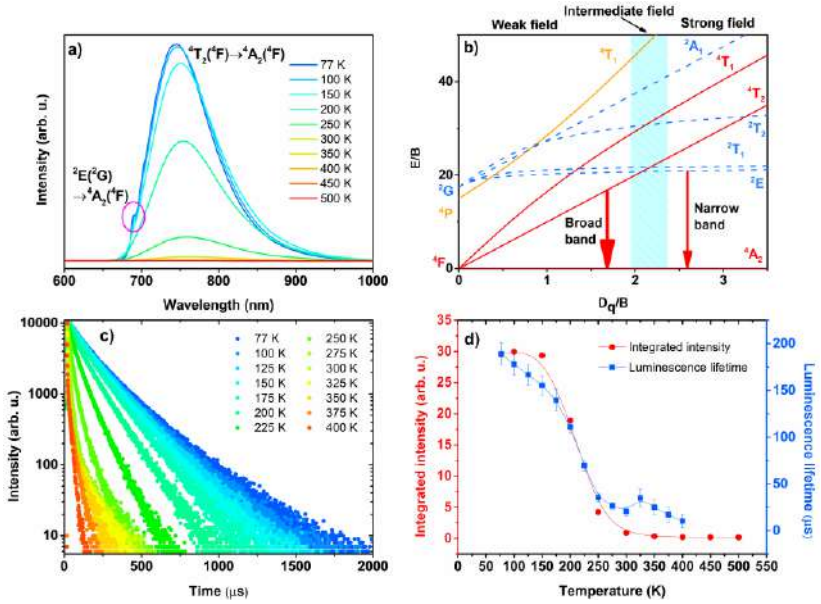

Fig. 23. (a) Temperature-dependent emission spectra of the 0.1 mol% Cr^{3+} β-TCP sample (λ_{ex} = 450 nm); (b) simplified Tanabe-Sugano diagram for d^3 ion in octahedral site symmetry; (c) temperature-dependent decay curves (λ_{ex}= 450 nm, λ_{em}= 765 nm) and (d) temperature dependence of the intensity and luminescence lifetime of the 0.1 mol% Cr^{3+} β-TCP sample.

Therefore, in the low-temperature range, Cr^{3+} ions in the β-TCP host are considered to be in an intermediate crystal field. However, when the temperature rises above 100 K, the crystal field weakens due to the thermal expansion of the lattice, and only the $^4T_2(^4F) \rightarrow {}^4A_2(^4F)$ transition appears in the spectra. This effect has been previously reported by several authors [207, 208]. On the other hand, the disappearance of narrowband PL could also be explained by thermal activation from the $^2E(^2G)$ to $^4T_2(^4F)$ states, as has been proven in similar materials [209] or as a combination of both of these effects.

As for thermal quenching – considering the effect of the lattice vibration with increased temperature, a thermally activated quenching process of the $^4T_2(^4F)$ state via a nonradiative relaxation process to the $^4A_2(^4F)$ ground state is expected [210, 159]. Additionally, the decay kinetics of the Cr^{3+} PL (λ_{em}=765 nm) at different temperatures were measured, as shown in Fig. 23c. As is typical for the case of increasing nonradiative relaxation contribution to the PL mechanism, the luminescence lifetime decreases with temperature from 189 μs at 77 K to 20.6 and 10.2 μs at 300 and 400 K, respectively (Fig. 23d).

3.3. Tunable broadband visible emission achieved by phase transformation-driven self-reduction of Eu^{3+} to Eu^{2+} in calcium phosphate matrix

The XRD pattern of the material annealed in a vacuum at 1300 °C is given in Fig. 24. Evidently, the phase transformation to α-TCP occurred. The diffraction peaks matched very well with the standard XRD data of monoclinic $Ca_3(PO_4)_2$ (#00-070-0364). Such transformation indicates the evaporation of phosphate species and formation of the CP phase with a significantly higher Ca/P ratio (Ca/P= 1.5:1). The SEM image (inset of Fig. 24) demonstrates the formation of monoliths with undefined shape and size varying in a microscopic range, which is typical for α-TCP prepared at high temperature [183].

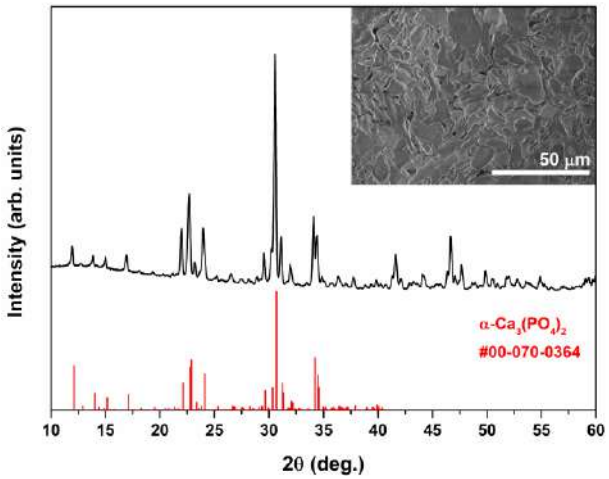

Fig. 24. XRD pattern of Eu-doped α-TCP obtained after annealing of Eu-doped DCPD in vacuum at 1300 °C. Inset: corresponding SEM micrograph.

The normalized PLE spectra of Eu-doped α-TCP for 475 and 610 nm emission are shown in Fig. 25a. When monitored at λ_{em}= 475 nm, a broad band is seen, which is assigned to the $4f^7 \rightarrow 4f^6 5d^1$ transition of Eu^{2+} ions; however, for λ_{em}= 610 nm the shape of the PLE spectrum changed significantly. The difference in the shape of the PLE spectra suggests that Eu^{2+} ions occupy at least 2 different sites. The sharp lines are associated with the presence of a minor Eu^{3+} amount and indicate an incomplete reduction. These lines originate from $^7F_0 \rightarrow {}^5D_4$ (ca. 361.5 nm), $^7F_0 \rightarrow {}^5G_2$ (ca. 368.5 nm), $^7F_0 \rightarrow {}^5L_6$ (ca. 393 nm), $^7F_0 \rightarrow {}^5D_2$ (ca. 464 nm), $^7F_0 \rightarrow {}^5D_1$ (ca. 525 nm), and $^7F_1 \rightarrow {}^5D_1$ (ca. 532 nm) intraconfigurational $[Xe]4f^6 \rightarrow [Xe]4f^6$ transitions of Eu^{3+} ions [211].

The PL spectrum obtained under 285 nm excitation exhibited a single broadband emission centered at 470 nm with a FWHM of 94 nm (4068 cm^{-1}), which is attributed to the $4f^65d^1 \rightarrow 4f^7$ transition typical of Eu^{2+} (Figure 25b). The emission spectrum covers the entire range of visible light, while the asymmetric shape of the emission also suggests the presence of Eu^{2+} in multiple sites. In mixed-valent Eu-doped materials, the emission can be tuned by varying the excitation wavelength, which allows the observation of the emission of exclusively Eu^{2+} or Eu^{3+} ions or control of the intensity ratio of simultaneous emission [212-214]. Such an effect allowing for direct control of the luminescence color is achieved due to the overlap in the excitation spectra of Eu^{2+} and Eu^{3+} within the range of 250–450 nm [215]. Therefore, we also recorded the PL spectrum under an excitation wavelength of 393 nm. The emission lines associated with Eu^{3+} can be seen at ca. 590 nm ($^5D_0 \rightarrow {}^7F_1$), 610 nm ($^5D_0 \rightarrow {}^7F_2$), and 700 nm ($^5D_0 \rightarrow {}^7F_4$); however, the emission spectrum is still dominated by the broadband emission of Eu^{2+}. The Eu^{2+} emission maximum was red-shifted to 503 nm, and a significant increase in the FWHM value to 142 nm (5268 cm^{-1}) was observed. Considering these spectral changes, we investigated the dependence of emission spectra on the excitation wavelength, systematically changing λ_{ex} from 250 to 420 nm with a step of 10 nm (Fig. 25c). This variation allowed the emission spectra tuning in terms of emission maximum and FWHM (Fig. 25d). Two opposite trends were observed depending on the excitation wavelength: the increase of the excitation wavelength from 250 to 310 nm led to the blue shift accompanied by the narrowing of the emission band, while in the range from 310 to 420 nm, the effect was opposite. Summarizing, under specific excitation, the emission maximum can be shifted from 467 to 517 nm, and FWHM values can be varied from 87 to 142 nm. Yu *et al*. [214]. previously achieved similar spectral tuning in Eu^{2+}/Eu^{3+}-doped Ba_2InTaO_6. The authors associated the observed shift with the occupation of different crystallographic sites by Eu^{2+} ions. The observed dependence of the CIE 1931 chromaticity coordinates on excitation wavelength was nearly linear (Fig. 25e), shifting from a blue to greenish-yellow region as the excitation wavelength increased from 310 to 420 nm. Under specific excitation, a near-white emission can be obtained, demonstrating a color-adjustable emission. Fig. 25f shows the PL emission decay curve of Eu-doped α-TCP when the specimen was excited at 405 nm, and emission was monitored at 475 nm. A two-exponential PL decay was observed with fast (τ= 0.16 μs) and slow (τ= 1.35 μs) components. The calculated effective PL lifetime value (τ_{eff}) was 1.27 μs. It has been previously reported that the appearance of the fast component could be linked to nonradiative energy migration between Eu^{2+} ions [216].

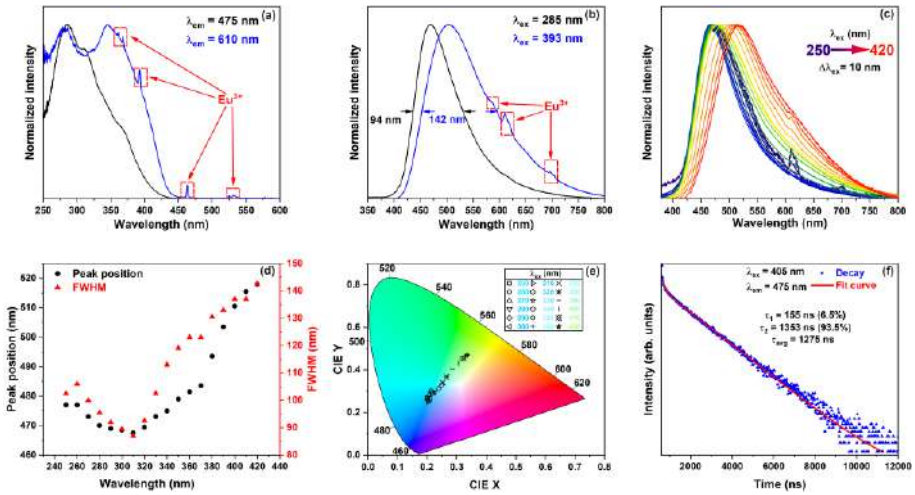

Fig. 25. Normalized PLE (λ_{em}=475 and 610 nm) spectra (a); normalized PL (λ_{ex}= 285 and 393 nm) spectra (b); normalized PL spectra obtained under different excitation wavelengths (c); dependence of emission maximum and FWHM on excitation wavelength (d); dependence of the CIE 1931 chromaticity coordinates on excitation wavelength (e); and decay curve (λ_{ex}= 405 nm and λ_{em} = 475 nm) (f) for Eu-doped α-TCP.

The mechanism of Eu^{3+} self-reduction in the phosphates of divalent metals is usually explained by the formation of cationic vacancies due to substitution with aliovalent Eu^{3+} ions [217,218]. Negatively charged vacancies act as electron donors and reduce Eu^{3+} ions to the divalent state, further protected from the oxidizing air atmosphere by the phosphate framework. In our case, such a mechanism is reasonably accepted; however, during the transformation of CPP to α-TCP in a vacuum, the charged phosphate species are evaporated, which also could influence the oxidation state of Eu ions in the matrix. Some reports on the Eu partial self-reduction in α-TCP synthesized by solid-state reaction are known [217, 219, 220]. The comparison of the emission spectra under 393 nm revealed that we achieved a significantly higher degree of reduction, which could be associated with the peculiarities of the synthetic approach.

The Eu-doped DCPD precursor was also annealed in air at an identical temperature for comparison. The XRD analysis revealed that the major crystalline phase was α-CPP, which indicates that the Ca/P ratio in the as-prepared and annealed materials is nearly the same. A negligible amount of β-TCP was also identified as an impurity. The formation of α-CPP was expected since α-CPP is assumed to be a high-temperature CPP polymorph, and an annealing procedure was performed above the β- to α-CPP phase transition

temperature [185]. The PL spectrum of this sample is dominated by sharp emission lines originating from Eu^{3+}, indicating that Eu ions mainly exist in the +3 oxidation state. Nevertheless, the emission band centered at ca. 412nm was also observed, suggesting that the minor amount of Eu ions was reduced during the annealing. Previously, Doat et al. [221]. reported the partial stabilization of Eu^{2+} ions in α-CPP synthesized in air atmosphere and thermally quenched in liquid nitrogen. The emission band aroused from Eu^{2+} was observed at 415 nm, which agrees well with our results.

Temperature-dependent PL spectra of Eu-doped α-TCP obtained under excitation wavelengths of 285 and 393 nm are depicted in Fig. 26. Under 285 nm excitation, the PL spectra changed in terms of intensity, spectral shape, and emission maximum (Fig. 26a). At 77 K, two emission peaks centered at 457 and 505 nm are clearly seen; however, with an increase in temperature, the spectral shape transforms into an asymmetric single-peak band. The position of emission maximum was nearly stable at 470 nm in the temperature range from 150 to 350 K, followed by a red shift at higher temperatures. The FWHM value exhibited a multidirectional trend depending on the temperature: in the range from 77 to 300 K, it decreased, while in the range from 300 to 450 K, it increased (Fig. 26b). The maximum value of 114.5 nm (4761 cm^{-1}) was determined at 77 K. A nearly linear thermal quenching of integrated intensity was observed (Fig. 26b). At 400 K the integrated emission intensity constituted 51% of that at 300 K. The relatively strong thermal quenching of emission might be caused by thermal ionization (photoionization), thermally activated crossover to the ground state, multiphonon-relaxation, energy transfer to quenching centers [222-224]. The occurring thermal quenching might limit the phosphor from the high-temperature applications. The CIE chromaticity coordinates were located in the cyan-white region (Fig. 26c).

In the case of 393 nm excitation, the emission spectra obtained were significantly broader (Fig. 26). The FWHM value demonstrated a decreasing trend in the temperature range from 77 to 350 K and nearly stabilized at higher temperatures (Fig. 26e). The highest value of 282 nm (8942 cm^{-1}) was also observed at 77 K. For the calculations of FWHM, only the emission of Eu^{2+} ions was involved; the emission of Eu^{3+} was ignored. The diversified dependence of FWHM values for both excitation wavelengths could be associated with the different behavior of Eu^{2+} ions occupying particular sites in the crystal lattice. The emission intensity decreased with the increasing temperature owing to the non-radiative decay at higher temperatures. The observed decrease was also nearly linear; in this case, at 400 K, it constituted 49% of that at 300 K. The thermal quenching in the red region was more

pronounced, which is reflected in the gradual shift of CIE chromaticity coordinates from orange to greenish-white (Fig. 26f).

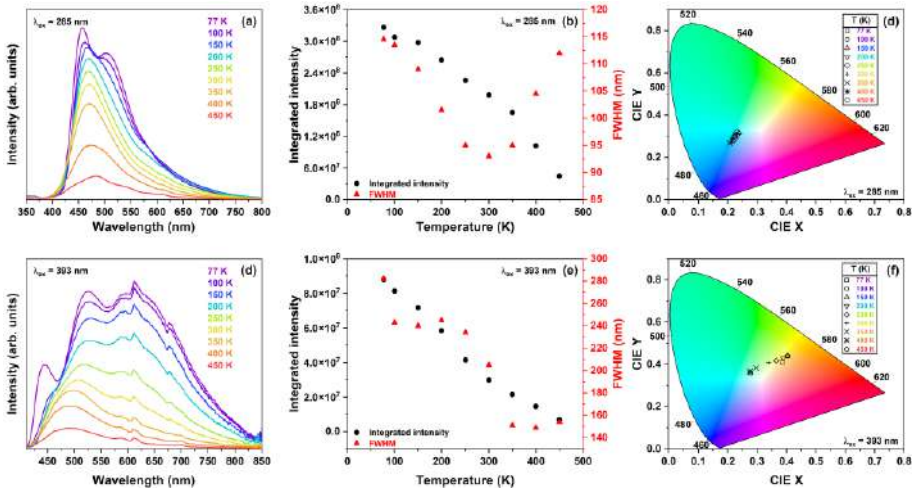

Fig. 26. Temperature-dependent PL spectra (a, c); dependence of the CIE 1931 chromaticity coordinates on temperature (b, e); dependence of integrated emission intensity and FWHM on temperature (c, f) for Eu-doped α-TCP excited with 285 nm (a, b, c) and 393 nm (d, e, f).

The deconvolution of broadband emission spectra with multiple peaks could ascribe the spectra components to the Eu^{2+} ions occupying specific crystallographic sites. For instance, such an approach was demonstrated by Liao *et al.* [225], who investigated the PL spectra of Eu^{2+}-doped $Rb_{0.5}K_{1.5}CaPO_4(F, Cl)$. The authors concluded that there are 3 suitable sites for Eu^{2+} substitution in the analyzed crystal structure; consequently, 3 components of the PL spectrum were specifically ascribed. In our case, the determination of Ca sites occupied by Eu^{2+} ions is extremely challenging due to the peculiarities of α-TCP crystal structure. This compound crystallizes in a monoclinic crystal structure with $P2_1/a$ space group having 18 inequivalent crystallographic Ca sites [226]. Considering the doping level investigated in this work, the commonly employed Rietveld refinement of the XRD data do not seem to be a reliable tool for determining the Eu^{2+} position in the crystal lattice.

The theoretical work by Matsunaga *et al*. investigated the thermodynamic equilibrium between TCP polymorphs substituted with divalent cations having different sizes [101]. One of the investigated ions was Sr^{2+}. Taking into account the nearly identical ionic radii of Eu^{2+} and Sr^{2+}[227] a simplified assumption can be made that the behavior of Eu^{2+} in the considered crystal

structure could be identical to that of Sr^{2+}. It was shown that 4 specific Ca sites in the α-TCP structure are energetically more favorable for Sr^{2+}. The lowest defect formation energies of Sr^{2+} are in Ca-5 (CN= 7), Ca-8 (CN= 7), Ca-14 (CN= 7), and Ca-17 (CN= 7) positions, having polyhedron volumes of 19.9, 19.9, 17.2, and 20.0 $Å^3$, respectively [226].

The fitting of emission spectra obtained at 77 and 300 K under 285 and 393 nm excitation is shown in Fig. 27. Regardless of the excitation wavelength and temperature, all spectra can be fitted with 3 sub-spectra corresponding to Eu^{2+} ions in at least 3 different environments. Another approach to ascribe the sub-spectra proposed by van Uitert considers the calculations involving the coordination number, radius of the cation replaced by Eu^{2+}, and electron affinity of anion atoms [228]. In the case of α-TCP:Eu^{2+}, there is only one type of cations and anions in the matrix. If we assume the abovementioned calculations by Matsunaga *et al.* [101] for Eu^{2+}, the coordination number for all four positions is also the same. Thus, further investigation is needed to attribute the emission of Eu^{2+} centers to specific crystallographic sites.

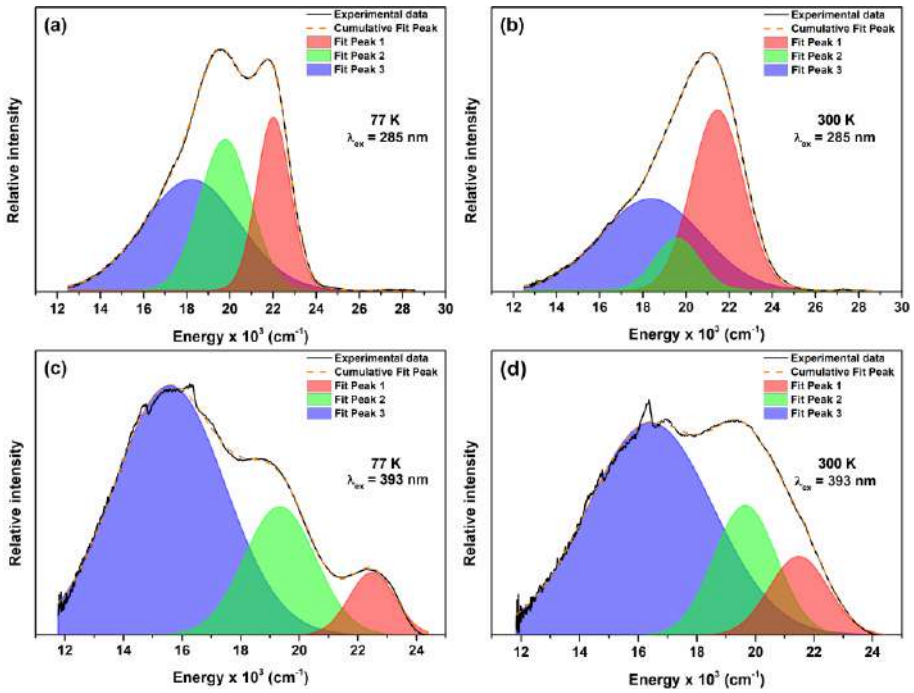

Fig. 27. PL spectra and Gaussian fitting curves of Eu-doped α-TCP for λ_{ex}= 285 nm (a, b) and λ_{ex}= 393 nm (c, d) at 77 K (a, c) and 300 K (b, d).

3.4. Luminescence and electron-hole-trapping centers in α-$Ca_2P_2O_7$:Mn

The crystallinity and purity of the synthesized powders were assessed using XRD analysis. The XRD pattern of the $Ca_2P_2O_7$ sample doped with Mn, after annealing at 1200 °C, is depicted in Fig. 28. The diffraction peaks closely match the standard pattern for α- $Ca_2P_2O_7$ (PDF #073-0440), confirming the successful formation of the target material. A minor presence of the adjacent phase, α-$Ca_3(PO_4)_2$, was also observed, likely resulting from the evaporation of phosphate particles during the process.

The morphological characteristics of the synthesized powders were examined through SEM. Representative SEM images of the Mn doped $Ca_2P_2O_7$ sample, displayed in Fig. 29, reveal that the powders are composed of a mix of plate-like and irregularly shaped particles. Notably, the plate-like particles exhibit grains ranging in size from micrometers to sub-micrometers.

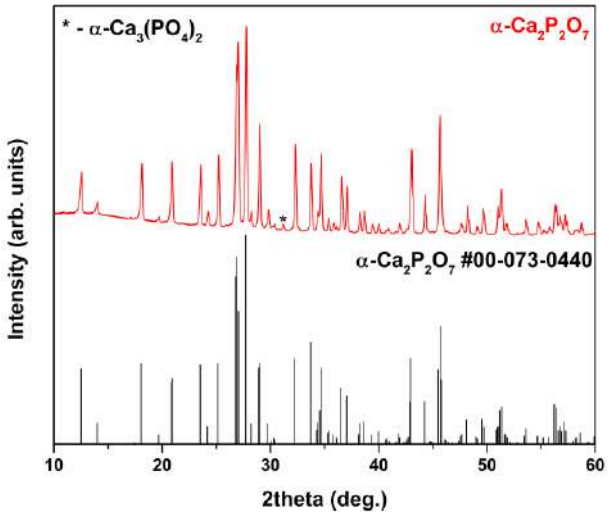

Fig. 28. XRD pattern of α-$Ca_2P_2O_7$: Mn powder.

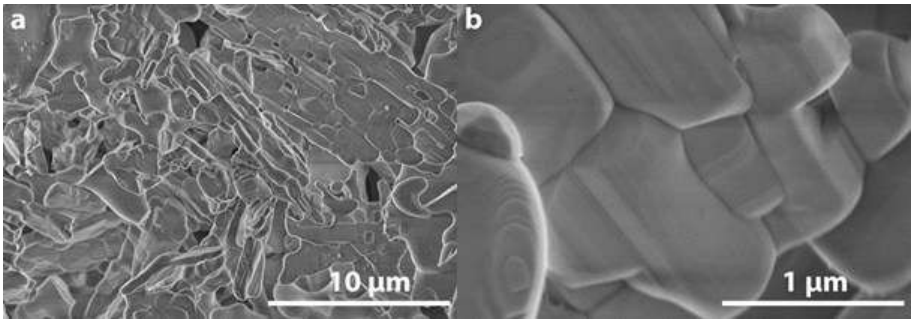

Fig. 29. SEM images of α-$Ca_2P_2O_7$:Mn powder at different magnifications.

In Fig. 30, the emission spectrum of the $Ca_2P_2O_7$:Mn phosphor, upon irradiation with 6.2 eV photons at 300 K, is depicted as curve 1. Additionally, the emission spectrum measured at 77 K in a cryostat, following excitation with 6.2 eV (200 nm) photons, is shown as curve 2. The analysis of Fig. 30a reveals that at 300 K, there is an intracenter emission band at 2.06 eV (602 nm), attributed to the Mn^{2+} ion within the phosphor, alongside with the emergence of new emission bands at 3.06 eV (405 nm) and 2.92 eV (425 nm). Notably, at 77 K, the Mn^{2+} emission band markedly diminishes, whereas the intensity of the newly observed emission bands experiences a 1.5-fold increase.

In Fig. 30b, the excitation spectrum for the main intracenter emission of Mn^{2+} at 2.06 eV (602 nm), 300 K (curve 1), and 77 K (curve 2) is presented. The analysis of the graph indicates that at 77 K, the emission band is excited at discrete energies of approximately 2.5 eV (496 nm), 3.0 eV (413 nm), 3.5 eV (354 nm), 4.0 eV (310 nm), 4.5 eV (275 nm), and within the range of 6.2 to 5.0 eV. Conversely, at 300 K, these emission bands also occur but exhibit lower intensity, particularly within the narrower range of 4.0 eV (310 nm) to 4.5 eV (275 nm).

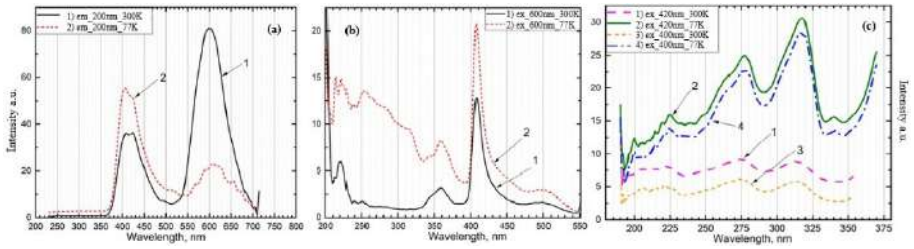

Fig. 30. a)Emission spectra of the $Ca_2P_2O_7$:Mn phosphor upon excitation with 6.2 eV (200 nm) photons (1 - at 300 K, 2 - at 77 K). b) Excitation spectra of the intracenter emission for the 2.06 eV (602 nm) band. c) Excitation spectra of the pre-irradiated phosphor: 1 - for the emission band at 2.92 eV (425 nm) at 300 K; 2 - for the emission band at 2.92 eV (425 nm) at 77 K; 3 - for the emission band at 3.06 eV (405 nm) at 300 K; 4 - for the emission band at 3.06 eV (405 nm) at 77 K.

In Fig. 30c, the excitation spectra for the newly identified bands at 3.06 eV (405 nm) and 2.92 eV (425 nm), following pre-irradiation of the phosphor at 6.2 eV (200 nm), are displayed a t b oth 300 K a nd 77 K. Excitation bands a re identified within the ranges of 3.94-4.0 eV (310-314 nm), 4.5-4.6 eV (269-275 nm), and broadly from 6.2 eV (200 nm) to 5.5 eV (225 nm). Notably, these bands are prominently observed at 77 K, indicating a stronger response

to excitation at this lower temperature. Conversely, at 300 K, these same bands manifest as weak excitation bands, suggesting a diminished excitation efficiency at higher temperatures.

When measuring the excitation spectra for the intracenter emission of the Mn^{2+} ion at 2.06 eV (602 nm), emission bands similar to those identified by authors in [229] were observed at 2.5 eV (496 nm), 3.1 eV (400 nm), 3.0 eV (413 nm), and between 3.5 eV (354 nm) and 3.6 eV (344 nm). Additionally, alongside the main intracenter emission at 2.06 eV (602 nm) for Mn^{2+}, the excitation spectrum revealed bands for the newly identified emissions at 3.06 eV (405 nm) and 2.92 eV (419 nm), specifically within the ranges of 3.94–4.0 eV (310-314 nm) and 4.5-4.6 eV (269-275 nm). Furthermore, excitation bands at 5.0 eV (248 nm) and 5.64 eV (220 nm) were also detected. Consequently, these newly emerged emission bands are excited by photon energies of 3.94-4.0 eV (310-314 nm), 4.5–4.6 eV (269-275 nm), 5.0 eV (248 nm), and 5.64 eV (220 nm).

The experimental results highlight the following processes occurring in the $Ca_2P_2O_7$:Mn phosphor upon excitation with 6.2 eV (200 nm) ultraviolet photons:

1. The occurrence of impurity intracenter emissions at 2.06 eV (600 nm) from the Mn^{2+} ion, observable at both 300 K and 77 K.
2. The generation of new induced recombination emissions at 2.95 eV (420 nm) and 3.1 eV (400 nm), resulting from charge transfer between excited matrix anions and impurities, specifically between (O^{2-}–Mn^{2+}) and O^{2-}–$(P_2O_7)^{4-}$.

To further elucidate the characteristics of the intracenter emission at 600 nm and the newly induced emissions, the excitation spectra of these emissions were meticulously measured. Intracenter emissions at 2.06 eV (600 nm) were excited:

- at 3.65 eV (340 nm) and 3.4 eV (335 nm) as shown by the authors [230] corresponding to intra-center excitations of the Mn^{2+} ion.
- at 5.64 eV (220 nm) and 4.96 eV (251 nm) because of charge transfer from the excited anion to impurities and neighboring anions (O^{2-}–Mn^{2+}) and O^{2-}– $(P_2O_7)^{4-}$.
- ~2.5 eV (496 nm) excitation of trap centers near the Mn^{2+} ion.
- 4.0 eV (310 nm) and 4.5 eV (275 nm) emissions arising in the transparency region of the $Ca_2P_2O_7$:Mn matrix.

The newly created induced emissions at 2.95 eV (496 nm) and 3.1 eV (400 nm) are excited at photon energies of 4.0 eV (310 nm) and 4.5 eV (275 nm), as well as in the spectral range of 4.96 eV (256 nm) and 5.64 eV (220

nm), where these new induced emissions are mainly created at low temperatures of 77 K.

Next, to clarify the correlation between the above-mentioned regularities with the processes in the pure matrix $Ca_2P_2O_7$, similar experimental studies on the $Ca_2P_2O_7$ phosphor were conducted.

- When the pure $Ca_2P_2O_7$ phosphor was excited with photon energies ranging from 5.9 to 6.2 eV (200-210 nm), emissions at 2.95 eV (420 nm) and 3.1 eV (400 nm) were detected at both 77 K and 300 K.
- These induced emissions are excited at photon energies of 4.0 eV (310 nm) and 4.5 eV (275 nm) in the transparency region of the pure $Ca_2P_2O_7$ matrix, more intensively at 77 K.

The main question of these studies is the formation of induced or combined radiative states in pure and doped phosphors in the same manner, as a result of charge transfer from the matrix to impurities and neighboring anions (O^{2-}–Mn^{2+}) and O^{2-}–$(P_2O_7)^{4-}$. As a result, intrinsic and impurity electron trapping centers Mn^{+} and $(P_2O_7)^{5-}$- complementary to hole trapping centers $(P_2O_7)^{3-}$ near Mn^{2+} impurities are formed. During the excitation of the anion $(P_2O_7)^{4-}$ due to the charge transfer of Mn^{2+} impurities Mn^{+} should be created, and the hole component $(P_2O_7)^{3-}$ is mainly localized near Mn^{2+} impurities.

Table 5. Emission spectra data.

Sample	Tempera-ture	Excitation energy	Emission peaks	Interpre-tation
$Ca_2P_2O_7$-Mn	300 K	6.2 eV (200 nm)	2.06 eV (600 nm), 3.06 eV (405 nm), 2.92 eV (425 nm)	Mn^{2+}
	77 K		2.06 eV (600 nm)- low intensity 3.06 eV (405 nm), 2.92 eV (425 nm)– high intensity	Mn^{2+}
$Ca_2P_2O_7$	300 K	6.2 eV (200 nm)	2.92 eV (425 nm), 3.06 eV (405 nm),	matrix
		5.64 eV (220 nm)	2.92 eV (425 nm), 3.06 eV (405 nm),	matrix
	77 K	6.2 eV(200 nm)	2.92 eV (425 nm), 3.06 eV (405 nm),	matrix
		5.64 eV (220 nm)	2.92 eV (425 nm), 3.06 eV (405 nm),	matrix

It is assumed that similar induced and combined radiative states at 2.95 eV (420 nm) and 3.1 eV (400 nm) should be created upon trapping free electrons and holes by Mn^{2+} impurities and $(P_2O_7)^{4-}$ anions. We conducted experimental research in the vacuum ultraviolet spectral range from 12.4 eV

(100 nm) to 4.96 eV (250 nm), where free electron-hole pairs are created. When irradiated with photons with energies of 8.26 eV (150 nm) and 7.75 eV (160 nm) at temperatures of 300 K and 15 K, intracenter emissions of Mn^{2+} at 2.15 eV (577 nm) and new induced or combined radiative states at 2.95 eV (420 nm) and 3.1 eV (400 nm) are created. Impurity emissions of Mn^{2+} at photon energies of 8.0 eV (155 nm) are excited by free electrons. It is known that the band gap of $CaBPO_5$ and $LiCaPO_4$ phosphors are 8.26 eV (150 nm) and 7.65 eV (162 nm), respectively [231].

The primary focus of these studies is to understand the formation of induced or combined radiative states in both pure and doped phosphors, facilitated by charge transfer from the matrix to impurities and neighboring anions, specifically O^{2-}–Mn^{2+} and O^{2-}–$(P_2O_7)^{4-}$. This process results in the formation of intrinsic and impurity electron trapping centers (Mn^{+} and $(P_2O_7)^{5-}$) that complement hole trapping centers $(P_2O_7)^{3-}$ located near Mn^{2+} impurities. It is proposed that during the excitation of the anion $(P_2O_7)^{4-}$, charge transfer from Mn^{2+} impurities should lead to the creation of Mn^{+}, with the hole component $(P_2O_7)^{3-}$. primarily localized near Mn^{2+} impurities. Consequently, it is hypothesized that similar induced and combined radiative states at 2.95 eV (420 nm) and 3.1 eV (400 nm) are formed by the trapping of free electrons and holes by Mn^{2+} impurities and $(P_2O_7)^{4-}$ anions.

The estimated band gap of $Ca_2P_2O_7$ is approximately 8.0 eV (155 nm). Thus, the new combined radiative states are created as a result of charge transfer from the excited ion P_2O_7 to Mn^{2+} impurities and ions $(P_2O_7)^{4-}$.

These radiative states are generated when electrons are captured by impurities and intrinsic centers, specifically through the reactions $Mn^{2+}+e^{-} \rightarrow Mn^{+}$ and $(P_2O_7)^{4-} + e^{-} \rightarrow (P_2O_7)^{5-}$. This results in the formation of impurity $Mn^{+} + (P_2O_7)^{3-}$ and intrinsic $(P_2O_7)^{5-}$ - $(P_2O_7)^{3-}$ electron-hole trapping centers. The trapping of electrons by Mn^{2+} ions and $(P_2O_7)^{4-}$ anions leads to the creation of these specific centers, facilitating the observed radiative states

Table 6. Excitation spectra data.

Sample	Tempera-ture	Emission peaks	Excitation energy	Interpre-tation
$Ca_2P_2O_7$-Mn	300 K	2.06 eV (600 nm)	4.0-4.5 eV (275 – 310 nm)	Mn^{2+}
	77 K	2.06 eV (600 nm)	2.5 eV (496 nm), 3.0 eV (413 nm), 3.5 eV (354 nm), 4.0 eV (310 nm), 4.5 eV (275 nm), 5.0 – 6.2 eV (200 –248 nm)	Mn^{2+}

Sample	Tempera-ture	Emission peaks	Excitation energy	Interpre-tation
	300 K	3.06 eV (405nm), 2.92 eV (425nm)	3.94 - 4.0 eV (310 – 314 nm), 4.5 – 4.6 eV (269– 275 nm), 5.5-6.2 eV (200 –225 nm) – weak intensity	matrix
	77 K	3.06 eV (405nm) 2.92 eV (425nm)	3.94 – 4.0 eV (310 – 314 nm), 4.5 – 4.6 eV (269 – 275 nm), 5.5 – 6.2 eV (200 – 225 nm) – strong intensity	
$Ca_2P_2O_7$	300 K	2.92 eV (425nm), 3.06 eV (405nm)	3.94 – 4.0 eV (310 – 314 nm), 4.5 – 4.6 eV (269 – 275 nm), 5.64 eV (220 nm).	matrix
	77 K	2.92 eV (425 nm), 3.06 eV (405nm)	3.94 – 4.0 eV (310 – 314 nm), 4.5 – 4.6 eV (269 – 275 nm), 5.64 eV (220 nm).	

The temperature-dependent measurements of the new radiative states at 2.95 eV (420 nm) and 3.1 eV (400 nm) reveal a distinct pattern: their intensity steadily decreases from 77 K to 250 K, experiences a surge between 250 K and 300 K, and then undergoes a sharp decline from 300 K to 400 K. Concurrently, the intensity of the intracenter emission at 2.06 eV Mn^{2+} shows a slight decrease over the same temperature range, followed by a significant increase between 370 K and 450 K.

The experimental results confirm the temperature dependence of the intensity for the newly induced emissions at 2.95 eV (420 nm) and 3.1 eV (400 nm). Notably, the efficiency of generating these induced emissions at lower temperatures, specifically at 15 K and 77 K, is found to be twice as high compared to that at higher temperatures ranging from 300 K to 350 K.

The observed temperature-dependent behavior of the radiative states at 2.95 eV (420 nm) and 3.1 eV (400 nm), particularly the flaring up and subsequent rapid decrease in intensity between 250 K and 300 K, can be attributed to ionization processes: $Mn^{+} \rightarrow Mn^{2+}+e^{-}$; $(P_2O_7)^{3-} \rightarrow (P_2O_7)^{4-}+e^{-}$. This ionization leads to the generation of free electrons in the conduction band, which then recombine with localized holes near the Mn^{2+} impurity, specifically $(P_2O_7)^{3-}$ The energy released during this recombination is transferred to the impurities, resulting in an observed increase in the intensity of intracenter emission at 2.06 eV (600 nm) for Mn^{2+}. Consequently, this process facilitates energy transfer from the matrix to the impurities. In analogous research conducted by authors [232] on $KSrPO_4$-Eu^{3+}, electron ionization from the Eu^{2+} ion into the conduction band was observed with an activation energy of 0.4 eV, illustrating a similar charge transfer mechanism.

The decrease in the intensity of the combined radiative state of 2.92 eV (425 nm) and 3.0 eV (413 nm) is associated with the decay of electron trapping centers and the implementation of electron recombination with a hole trapping center, which is confirmed by the appearance of thermoluminescence peaks in this temperature range in the irradiated phosphor $Ca_2P_2O_7$-Mn at 80 K. The presence of TL peaks confirms the formation of electron and hole trapping centers during irradiation with UV (6.2 eV(200 nm)) photons.

The formation of induced or combined radiative states, which include the electronic configurations of electron-hole trapping centers Mn^+- $(P_2O_7)^{3-}$ and $(P_2O_7)^{5-}$-$(P_2O_7)^{3-}$, is supported by experimental evidence. Specifically, new induced emissions at 2.95 eV (420 nm) and 3.1 eV (400 nm), stimulated by the irradiation of trapping centers, are excited at photon energies of 4.0 eV (310 nm) and 4.5 eV (275 nm) within the transparency region of the matrix.

The experimental evidence solidly supports that induced states arise from the electronic configurations of both intrinsic and impurity trapping centers. Specifically, the radiative decay and relaxation processes involving the excited state Mn^+-$(P_2O_7)^{3-}$ commence from a singular energy level as the temperature increases. This behavior underscores the dynamic interaction between these trapping centers under thermal variation. Fig. 31 presents a model illustrating the presumed arrangement of electronic and hole trapping centers, providing a visual representation of these complex interactions.

Here is the explanation of the model describing electronic transitions in irradiated $Ca_2P_2O_7$-Mn at temperatures of 300 K and 77 K.

At a temperature of 300 K, irradiated $Ca_2P_2O_7$ with photons of 6.2 eV (200 nm) generates electron-hole pairs $e^+(P_2O_7)^{3-}e^-$. Upon the transition from $6A_1$ to $4T_1$ in the Mn^{2+} ion, an emission band occurs at 2.06 eV (600 nm). At temperatures of 77 K and 300 K, a free electron occurs:

Upon capture by Mn^{2+} impurities: $Mn^{2+}+e^- \rightarrow Mn^+$;

Upon capture by the matrix anions $(P_2O_7)^{4-}+ e^- \rightarrow (P_2O_7)^{5-}$.

As a result, electronic Mn^+ and hole $(P_2O_7)^{3-}$ capture centers arise, i.e., Mn^+ - $(P_2O_7)^{3-}$. Hybrid or combined electronic states arise beneath the conduction band, consisting of the electronic state Mn^+ and $(P_2O_7)^{5-}$.

Parallel to this process, a hole localized above the valence band near the ground state of the Mn^+ ion is localized above the valence band $(P_2O_7)^{3-}$. Due to the anisotropic nature of the compound, the holes formed with unpaired electrons in different crystallographic directions localize above the valence band ceiling at different energy positions $(P_2O_7)^{3-}$(a) and $(P_2O_7)^{3-}$ (b).

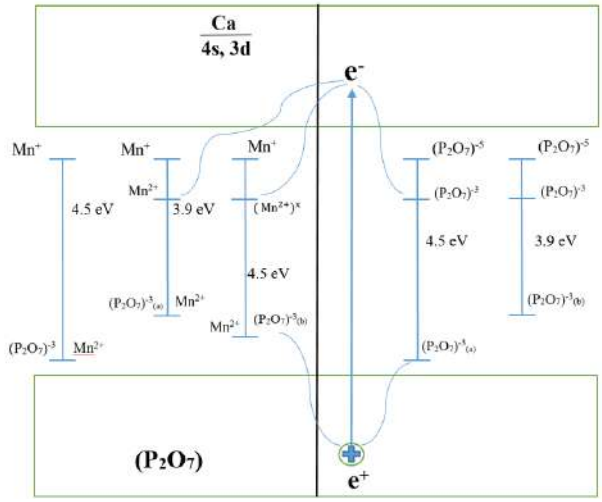

Fig. 31. Model depicting the arrangement of electronic and hole trapping centers.

CONCLUSIONS

1. The phase conversion of ACP in different molten chlorides was investigated in detail. The chemical composition of the molten salts, the heat-treatment temperature, and the ACP-to-flux ratio were determined as the main factors influencing the phase purity and morphological features of the products. It was shown that the phase-selective synthesis of single-phase $Ca_5(PO_4)_3Cl$ or Ca_2PO_4Cl can be achieved by adjusting the composition of KCl–$CaCl_2$ flux. The KCl-rich fluxes led to the formation of $Ca_5(PO_4)_3Cl$, while the Ca-rich fluxes resulted in the formation of Ca_2PO_4Cl. The morphology of $Ca_5(PO_4)_3Cl$ powders can be controlled by varying the KCl/$CaCl_2$ ratio in the flux as well. The $CaCl_2$-rich fluxes promoted the anisotropic growth of $Ca_5(PO_4)_3Cl$ crystals, resulting in the formation of monodispersed hexagonally-shaped microrods. Whereas anisotropic growth was observed at relatively low temperature (750 °C), the increase of the reaction temperature up to 1200 °C significantly reduced this effect.
2. Cr^{3+}-doped β-TCP powders were successfully synthesized by a wet co-precipitation method followed by high-temperature treatment. The dissolution of Cr^{3+} ions in the β-TCP crystal structure is limited. Single-phase materials were obtained with a doping level of up to 2 mol%, whereas the secondary Cr_2O_3 phase was detected with a 5 mol% doping level. EPR spectroscopy revealed multiple Cr^{3+}-related centers, which most likely arise from the same crystallographic site but with different defects in the vicinity. All Cr^{3+}-doped β-TCP powders exhibited broadband emission with a maximum at 760 nm. The highest intensity was achieved for the 0.1 mol% Cr^{3+} sample, most likely due to concentration quenching at higher Cr^{3+} concentrations.
3. Eu^{2+}-doped α-TCP was successfully synthesized via a phase transformation of Eu^{3+}-doped DCPD. The phase conversion, accompanied by a reduction of Eu^{3+} to Eu^{2+}, was achieved by annealing the starting material at 1300 °C in a vacuum. The initial Ca/P ratio of 1 : 1 characteristic of DCPD changed to ca. 1.5 : 1 due to the selective evaporation of phosphate species. The obtained material exhibited a broadband emission covering the entire visible spectrum. The emission tunability was achieved by varying the excitation wavelength, resulting in the shift of the emission maximum and FWHM values ranging from 87 to 142 nm at room temperature. The broadband emission was achieved due to the multi-site occupancy of Eu^{2+} ions in a complex α-TCP matrix. Deconvolution of the emission spectra indicated that Eu^{2+} ions occupy at least 3 inequivalent crystallographic sites. The high degree of reduction and multi-site occupancy of Eu^{2+} ions in α-TCP achieved

by the selected synthetic approach opens new possibilities for the development of color-tunable broadband phosphors.

4. $Ca_2P_2O_7$ powder doped with 1 mol% of Mn^{2+} ions was successfully synthesized by a wet co-precipitation method followed by high-temperature treatment. The mechanisms of formation of induced intrinsic and impurity radiative states, consisting of intrinsic and impurity electron-hole trapping center states, were investigated using thermoactivation and vacuum-ultraviolet spectroscopy in irradiated $Ca_2P_2O_7:Mn^{2+}$ and undoped $Ca_2P_2O_7$. In irradiated $Ca_2P_2O_7:Mn^{2+}$ phosphors, new induced emissions at 2.95 eV (420 nm) and 3.1 eV (400 nm) have been detected. The new radiative states result from charge transfer from the $(P_2O_7)^{4-}$ ion to the Mn^{2+} impurities.

REFERENCES

[1] X. Pan, Y. Jian, N. An, R.-J. Xie, S. Ke, Z. Li, H. Wang, C. Lin, Y. Zhuang, J. Zhou, L. Mei, L. Liao, Innovations in phosphate phosphors: Bridging structure-property gaps for enhanced luminescence, Coordination Chemistry Reviews, 528, 2025, 216407,
(https://doi.org/10.1016/j.ccr.2024.216407).
[2] H. Liu, L. Liao, X. Pan, K. Su, P. Shuai, Z. Yan, Q. Guo, L. Mei, Recent research progress of luminescent materials with apatite structure: A review, Open Ceramics, 10, 2022, 100251,
(https://doi.org/10.1016/j.oceram.2022.100251).
[3] I.V. Nikiforov, D.V. Deyneko, D.A. Spassky, B.I. Lazoryak, S. M. Aksenov, Whitlockite-Type Structure as a Matrix for Optical Materials: Synthesis and Characterization of Novel TM-SM Co-Doped Phosphate $Ca_9Gd(PO_4)_7$, a Single-Phase White Light Phosphors, Minerals, 12, 2022, 76, (https://doi.org/10.3390/min12010076).
[4] C. Qi, J. Lin, L.-H. Fu, P. Huang, Calcium-based biomaterials for diagnosis, treatment, and theranostics, Chem. Soc. Rev., 47 (2), 2018, 357-403,
(https://doi.org/10.1039/C6CS00746E).
[5] M. Gu, W. Li, L. Jiang, X. Li, Recent progress of rare earth doped hydroxyapatite nanoparticles: luminescence properties, synthesis and biomedical applications, Acta Biomater., 148, 2022, 22- 43,
(https://doi.org/10.1016/j.actbio.2022.06.006).
[6] J. Qiao, J. Zhao, Z. Xia, A review on the Eu^{2+} doped β-$Ca_3(PO_4)_2$-type phosphors and the sites occupancy for photoluminescence tuning, Opt. Mater. X, 1, 2019, 100019,
(https://doi.org/10.1016/j.omx.2019.100019).
[7] W. Habraken, P. Habibovic, M. Epple, M. Bohner, Calcium phosphates in biomedical applications: materials for the future?, Mater. Today, 19(2), 2016, 69-87,
(https://doi.org/10.1016/j.mattod.2015.10.008).
[8] H. Yook, J. Hwang, W. Yeo, J. Bang, J. Kim, T.Y. Kim, J.S. Choi, J.W. Han, Design Strategies for Hydroxyapatite-Based Materials to Enhance Their Catalytic Performance and Applicability, Adv. Mater., 35(43), 2023, 2204938,
(https://doi.org/10.1002/adma.202204938).
[9] L. Sinusaite, A. Antuzevics, A.I. Popov, U. Rogulis, M. Misevicius, A. Katelnikovas, A. Kareiva, A. Zarkov, Synthesis and luminescent properties of Mn-doped alpha-tricalcium phosphate, Ceram. Int., 47(4), 2021, 5335-5340,

(https://doi.org/10.1016/j.ceramint.2020.10.114).
[10] B. Parra-Torrejón, M. Salvachúa-de la Fuente, M.J. Giménez-Bañón, J.D. Moreno-Olivares, D.F. Paladines-Quezada, J.A. Bleda-Sánchez, R. Gil-Muñoz, G.B. Ramírez-Rodríguez, J.M. Delgado-López, Amorphous vs. nanocrystalline calcium phosphate as efficient nanocarriers of elicitors in vineyards, CrystEngComm, 25(16), 2023, 2372-2378, (https://doi.org/10.1039/D3CE00185G).
[11] S.V. Dorozhkin, M. Epple, Biological and medical significance of calcium phosphates, Angew. Chem., 41(17), 2002, 3130-3146, (https://doi.org/10.1002/1521-3773(20020902)41:17%3C3130::AID-ANIE3130%3E3.0.CO;2-1).
[12] S.V. Dorozhkin, Calcium Orthophosphate ($CaPO_4$)-Based Bioceramics: Preparation, Properties, and Applications, Coatings, 12(10), 2022, 1380, (https://doi.org/10.3390/coatings12101380).
[13] D. Griesiute, A. Kizalaite, A. Dubnika, V. Klimavicius, V. Kalendra, V. Tyrpekl, S.H. Cho, T. Goto, T. Sekino, A. Zarkov, A copper-containing analog of the biomineral whitlockite: dissolution–precipitation synthesis, structural and biological properties, Dalton Trans., 53(4), 2024, 1722-1734, (https://doi.org/10.1039/D3DT03756H).
[14] D. Griesiute, E. Raudonyte-Svirbutaviciene, A. Kareiva, A. Zarkov, The influence of annealing conditions on the Ca/P ratio and phase transformations in bulk calcium phosphates, CrystEngComm, 24(6), 2022, 1166-1170, (https://doi.org/10.1039/D1CE01625C).
[15] N. Döbelin, Y. Maazouz, R. Heuberger, M. Bohner, A. A. Armstrong, A. J. Wagoner Johnson, C. Wanner, A thermodynamic approach to surface modification of calcium phosphate implants by phosphate evaporation and condensation, J. Eur. Ceram. Soc., 40(15), 2020, 6095-6106, (https://doi.org/10.1016/j.jeurceramsoc.2020.07.028).
[16] L. Sinusaite, I. Grigoraviciute-Puroniene, A. Popov, K. Ishikawa, A. Kareiva, A. Zarkov, Controllable synthesis of tricalcium phosphate (TCP) polymorphs by wet precipitation: Effect of washing procedure, Ceram. Int., 45(9), 2019, 12423-12428, (https://doi.org/10.1016/j.ceramint.2019.03.174).
[17] C. Combes, C. Rey, Amorphous calcium phosphates: Synthesis, properties and uses in biomaterials, Acta Biomater., 6(9), 2010, 3362-3378, (https://doi.org/10.1016/j.actbio.2010.02.017).
[18] S.V. Dorozhkin, A detailed history of calcium orthophosphates from 1770s till 1950, Mater. Sci. Eng. C, 33(6), 2013, 3085–3110, (https://doi.org/10.1016/j.msec.2013.04.002).

[19] S. Bose, S. Tarafder, Calcium phosphate ceramic systems in growth factor and drug delivery for bone tissue engineering, Acta Biomaterialia, 8(4), 2012, 1401-1421,
(https://doi.org/10.1016/j.actbio.2011.11.017).
[20] M. Canillas, P. Pena, A.H. de Aza, M.A. Rodríguez, Calcium phosphates for biomedical applications, Bol. De. la Soc. Esp. De. Ceram., 56, 2017, 91-112,
(https://doi.org/10.1016/j.bsecv.2017.05.001).
[21] Y. Cai, R.Tang, Calcium phosphate nanoparticles in bio mineralization and biomaterials, J. Mater. Chem., 18, 2008, 3775-3787,
(https://doi.org/10.1039/B805407J).
[22] R. Drevet, J. Fauré, H. Benhayoune, Bioactive Calcium Phosphate Coatings for Bone Implant Applications, Coatings, 13(6), 2023, 1091,
(https://doi.org/10.3390/coatings13061091).
[23]. S. Gautam, D. Bhatnagar, D. Bansal, H. Batra, N. Goyal, Recent advancements in nanomaterials for biomedical implants, Biomedical Engineering Advances, 3, 2022, 100029, (https://doi.org/10.1016/j.bea.2022.100029).
[24] W. Suchanek, M. Yoshimura, Processing and properties of hydroxyapatite-based biomaterials for use as hard tissuereplacement implants, J. Mater. Res., 13, 1998, 94-117,
(https://doi.org/10.1557/JMR.1998.0015).
[25] S.V. Dorozhkin, Self-setting calcium orthophosphate ($CaPO_4$) for mulations and their biomedical applications, Adv. Nano-Bio. Mater. Dev., 3, 2019, 321–421.
[26] S.V. Dorozhkin, Calcium orthophosphates in dentistry, J Mater Sci: Mater Med., 24, 2013, 1335-1363,
(https://doi.org/10.1007/s10856-013-4898-1).
[27] O. Suzuki, Octacalcium phosphate (OCP)-based bone substitute materials, Jpn. Dent. Sci. Rev., 49, 2013, 58- 71,
(https://doi.org/10.1016/j.jdsr.2013.01.001).
[28] M. Kakei, T. Sakae, M. Yoshikawa, Electron microscopy of octa calcium phosphate in the dental calculus, J. Electron Microsc. (Tokyo), 58, 2009, 393-398,
(https://doi.org/10.1093/jmicro/dfp034).
[29] S.V. Dorozhkin, Amorphous calcium (ortho)phosphates, Acta Biomaterialia, 6(12), 2010, 4457-4475,
(https://doi.org/10.1016/j.actbio.2010.06.031).
[30] S.V. Dorozhkin, Amorphous calcium orthophosphates: nature, chemistry and biomedical applications, Int. J. Mater. Chem., 2(1), 2012, 19- 46,

(https://doi.org/10.5923/J.IJMC.20120201.04).
[31] R.M. Khashaba, M.M. Moussa, Ch. Koch, A.R. Jurgensen, D.M. Missimer, R.L. Rutherford, N.B. Chutkan, J.L. Borke, Preparation, Physical-Chemical Characterization, and Cytocompatibility of Polymeric Calcium Phosphate Cements, Int. J. Biomater., 2011, 467641,
(https://doi.org/10.1155/2011/467641).
[32] O. Bermúdez, M.G Boltong, F.C.M Driessens, J.A. Planell, Optimization of a calcium orthophosphate cement formulation occurring in the combination of mono calcium phosphate monohydrate with calcium oxide. J. Mater. Sci. Mater. Med., 5, 1994, 67-71,
(https://doi.org/10.1007/BF00121693).
[33] Z. Huan, J.Chang, Novel bioactive composite bone cements based on the β-tricalcium phosphate-mono calcium phosphate monohydrate composite cement system, Acta Biomater., 5(4), 2009, 1253-64, (https://doi.org/10.1016/j.actbio.2008.10.006).
[34] V. Sokolova, M .Epple, Biological and Medical Applications of Calcium Phosphate Nanoparticles, Chem. Eur. J., 27, 2021, 7471-1488,
(https://doi.org/10.1002/chem.202005257).
[35] T.J. Levingstone, S. Herbaj, J. Redmond, H.O. McCarthy, N.J. Dunne, Calcium Phosphate Nanoparticles-Based Systems for RNAiDelivery: Applications in Bone Tissue Regeneration, Nanomaterials, 10(1), 2020, 146,
(https://doi.org/10.3390/nano10010146).
[36] C. Qiu, Y. Wu, Q. Guo, Q. Shi, J. Zhang, Y. Meng, F. Xia, J. Wang, Preparation and application of calcium phosphate nanocarriers in drug delivery, Mater. Today Biol., 17, 2022, 100501,
(https://doi.org/10.1016/j.mtbio.2022.100501).
[37] H. Jena, B.K. Maji, R. Asuvathraman, K.V.G. Kutty, Synthesis and thermal characterization of glass bonded Ca-chlorapatite matrices for pyrochemical chloride waste immobilization. Journal of Non-Crystalline Solids, 358, 2012, 1681-1686,
(https://doi.org/10.1016/j.jnoncrysol.2012.05.002).
[38] A. Durugkar, S. Tamboli, N.S. Dhoble, S.J. Dhoble, Novel photoluminescence properties of Eu^{3+} doped chlorapatite phosphor synthesized via sol-gel method. Materials Research Bulletin, 97, 2018, 466-472,
(https://doi.org/10.1016/j.materresbull.2017.09.043).
[39] M.H. Hwang, Y.J. Kim, S.H. Jung, S.H. Han, Preparation and Luminescent Characterization of $M_5(PO_4)_3Cl$ (M: Sr, Ca) Chlorapatites by a Solid-state Reaction Method, Synthesis and Reactivity in Inorganic and Metal-Organic Chemistry, 38(3), 2008, 307-311,

(https://doi.org/10.1080/15533170802023528).
[40] C.-X. Li, Y.-H. Duan, W.-C. Hu, Electronic structure, elastic anisotropy, thermal conductivity and optical properties of calcium apatite $Ca_5(PO_4)_3X$ (X=F, Cl or Br), J. Alloys Compd., 619, 2015, 66-77,
(https://doi.org/10.1016/j.jallcom.2014.09.022).
[41] M. Ganjali, S. Pourhashem, M. Mozafari, The effect of heat-treatment on the structural characteristics of nanocrystalline chlorapatite particles synthesized via an in situ wet-chemical route, Ceram. Int., 41(10), 2015, 13100-13104,
(https://doi.org/10.1016/j.ceramint.2015.07.020).
[42] N.J. Flora, K.W. Hamilton, R.W. Schaeffer, C.H. Yoder, A Comparative Study of the Synthesis of Calcium, Strontium, Barium, Cadmium, and Lead Apatites in Aqueous Solution, Synthesis and Reactivity in inorganic and metal-organic chemistry, 34(3), 2001, 503-521,
(https://doi.org/10.1081/SIM-120030437).
[43]. X. Xu, X. Yu, L. Mao, S.P. Yang, Z. Peng, Preparation and photoluminescence of Bi^{3+}-doped strontium chlorapatite nano-phosphor, J. Matter. Let., 58(29), 2004, 3665-3668,
(https://doi.org/10.1016/j.matlet.2004.04.037).
[44] P. Ptáček, Synthetic Phase with the Structure of Apatite, IntechOpen, 2016,
(https://doi.org/10.5772/62212).
[45] A. Ito, Y. Otsuka, M. Takeuchi, H. Tanaka, Mechanochemical synthesis of chloroapatite and its characterization by powder X-ray diffractometory and attenuated total reflection-infrared spectroscopy, Colloid Polym. Sci., 295(10), 2017, 2010-2018,
(https://doi.org/10.1007/s00396-017-4177-7).
[46] R.T. Maske, A.N. Yerpude, S.J. Dhoble, Wet chemical synthesis of Sm^{3+} doped $Ca_{10}(PO_4)_6Cl_2$ phosphor for w-LED application, Mater. Lett. X, 19, 2023, 100214,
(https://doi.org/10.1016/j.mlblux.2023.100214).
[47] W.-N. Wang, F. Iskandar, K. Okuyama, Yu Shinomiya, Rapid Synthesis of Non-Aggregated Fine Chloroapatite Blue Phosphor Powders with High Quantum Efficiency, Adv. Mater., 20, 2008, 3422–3426,
(https://doi.org/10.1002/adma.200800415).
[48] M. Nabiyouni, H. Zhou, S.B. Bhaduri, Microwave assisted solution combustion synthesis (MASCS) of europium (Eu) doped chlorapatite nanowhiskers, Mater. Lett., 2013, 108, 54-57,
(https://doi.org/10.1016/j.matlet.2013.06.089).

[49]. J. Zhao, Z. Wang, Zhi Tang, M. Hui, Sh. Yin, Facile preparation of apatite nanostructures and their potential application in water treatment, Desalination and Water Treatment, 306, 2023, 189–198, (https://doi.org/10.5004/dwt.2023.29838).
[50] R. Pazik, J.-M. Nedelec, R.J. Wiglusz, Preferential site substitution of Eu^{3+} ions in $Ca_{10}(PO_4)_6Cl_2$ nanoparticles obtained using microwave stimulated wet chemistry technique, CrystEngComm, 16, 2014, 5308–5318, (https://doi.org/10.1039/C4CE00197D).
[51] R.V Tikale, A. D Koparkar, A.R Kadam, S J Dhoble, Structural and Photoluminescent Investigation of Eu^{3+} Doped $Ca_5(PO_4)_3Cl$ Chloropatite Phosphor by Modified Pechini Method: Crystal Structure and Judd-ofelt Description of Radiative Properties, J. Fluoresc., 35, 2025, 7771–7783, (https://doi.org/10.1007/s10895-024-04127-4).
[52] A. Varma, A.S. Mukasyan, A.S. Rogachev, K.V. Manukyan, Solution Combustion Synthesis of Nanoscale Materials, Chem. Rev., 116, 2016, 14493-14586, (https://doi.org/10.1021/acs.chemrev.6b00279).
[53] T. White, C. Ferraris, J. Kim, S. Madhavi, Apatite – An Adaptive Framework Structure, Mineralogy & Geochemistry, 57, 2005, 307-401, (https://doi.org/10.2138/rmg.2005.57.10).
[54] J. Wan, C. Zhang, G. Zeng, D. Huang, L. Hu, C. Huang, H. Wu, L. Wang, Synthesis and evaluation of a new class of stabilized nano-chlorapatite for Pb immobilization in sediment, J. Hazard. Mater., 320, 2016, 278-288, (https://doi.org/10.1016/j.jhazmat.2016.08.038)
[55] Z. Zhang, J. Wang, M. Zhang, Q. Zhang, Q. Su, The energy transfer from Eu^{2+} to Tb^{3+} in calcium chlorapatite phosphor and its potential application in LEDs, Appl. Phys. B, 91 (3), 2008, 529–537, (https://doi.org/10.1007/s00340-008-3035-1).
[56] R. C. Ewing, Nuclear waste forms for actinides, Proc. Natl. Acad. Sci. USA, 96(7), 1999, 3432-3439, (https://doi.org/10.1073/pnas.96.7.3432).
[57] G.R. Lumpkin, Ceramic Waste Forms for Actinides, Elements, 2(6), 2006, 365–372, (https://doi.org/10.2113/gselements.2.6.365).
[58] J.M. Hughes, J. Rakovan, The Crystal Structure of Apatite, $Ca_5(PO_4)_3$(F, OH, Cl), Reviews in Mineralogy and Geochemistry, 48(1), 2002, 1-12, (https://doi.org/10.2138/rmg.2002.48.1).
[59] Y.C. Chiu, W.-R. Liu, C.-K. Chang, C.-C. Liao, Y.-T. Yeh, S.-M. Jang, T.-M. Chen, Ca_2PO_4Cl: Eu^{2+}: an intense near-ultraviolet converting blue phosphor for white light-emitting diodes, J. Mater. Chem., 20, 2010, 1755,

(https://doi.org/10.1039/B920610H).
[60] W. Chen, A. Zhou, Cation-tunable blue phosphor $Ca_2PO_4Cl:Eu^{2+}$: enhancive emission and site occupancy, Luminescence, 31(3), 2016, 808–812, (https://doi.org/10.1002/bio.3027).
[61] Materials Data on Ca_2PClO_4 by Materials Project, United States: N. p., 2020, (https://doi.org/10.17188/1267727).
[62] P. Li, Z. Wang, Z. Yang, Q. Guo, Tunable blue–green emission phosphor $Ca_2PO_4Cl:Ce^{3+},Tb^{3+}$: Luminescence and energy transfer, Opt. Commun., 332, 2014, 83–88,
(https://doi.org/10.1016/j.optcom.2014.06.037).
[63]. P. Li, Zh.Wang, Zh. Yang, Q. Guo, A novel,warm, white light-emitting phosphor $Ca_2PO_4Cl:Eu^{2+}$, Mn^{2+} for white LEDs, J. Mater. Chem. C, 2, 2014, 7823-7829,
(https://doi.org/10.1039/C4TC01055H).
[64] Z. Wang, P. Li, Q. Guo, Z. Yang, Luminescence and energy transfer of tunable emission phosphor $Ca_2PO_4Cl:Ce^{3+},Mn^{2+}$. Spectrochim. Acta Part A Mol. Biomol. Spectrosc., 137, 2015, 871–876,
(https://doi.org/10.1016/j.saa.2014.09.023).
[65] D.C. Bassett, T.E. Robinson, R.J. Hill, L.M. Grover, J.E. Barralet, Self-assembled calcium pyrophosphate nanostructures for targeted molecular delivery, Biomater. Adv., 140, 2022, 213086,
(https://doi.org/10.1016/j.bioadv.2022.213086).
[66] T. Safronova, A. Kiselev, I. Selezneva, T. Shatalova, Y. Lukina, Y. Filippov, O. Toshev, S. Tikhonova, O. Antonova, A. Knotko, Bioceramics based on β-calcium pyrophosphate, Materials, 15, 2022, 3105,
(https://doi.org/10.3390/ma15093105).
[67] A.D. Anastasiou, M. Nerantzaki, A.P. Brown, A. Jha, D.N. Bikiaris, Drug loading capacity of microporous β-pyrophosphate crystals, Mater. Des., 168, 2019, 107661,
(https://doi.org/10.1016/j.matdes.2019.107661).
[68] R. W. Broge, R. J. Grabenstetter, Calcium Pyrophosphate Abrasive and Dentifrice Containing the Same. U.S. Patent 2,876,168, 1959. Application No. 604,972.
[69] H. C. Schweizer, Beta Phase Calcium Pyrophosphate Dentifrice Abrasives and Methods for Their Preparation U.S. Patent 3,112,247, 1963. Application No. 169,098.
[70] A. D. Anastasiou, S. Strafford, O. Posada-Estefan, C.L. Thomson, S.A. Hussain, T.J. Edwards, M. Malinowski, N. Hondow, N. K. Metzger, C.T.A. Brown, M.N. Routledge, A.P. Brown, M.S. Duggal, A. Jha, β-pyrophosphate:

A potential biomaterial for dental applications, Mater. Sci. Eng. C, 75, 2017, 885–894,
(https://doi.org/10.1016/j.msec.2017.02.116).
[71] T. Kitsugi, T.Yamamuro,T. Nakamura, S. Kotani, T. Kokubo, H. Takeuchi, Four calcium phosphate ceramics as bone substitutes for non-weight-bearing. Biomaterials, 14(3), 1993, 216-224,
(https://doi.org/10.1016/0142-9612(93)90026-X).
[72] P.W. Ranby, D.H. Mash, S.T. Henderson, The investigation of new phosphors, with particular reference to the pyrophosphates, Br. J. Appl. Phys., 6, 1955, S18,
(https://doi.org/10.1088/0508-3443/6/S4/307).
[73] R.L. Carter, C.E. Bricker, Comparison of the vibrational spectra of $K_2Cr_2O_7$, $Rb_2Cr_2O_7$ and $Cs_2Cr_2O_7$, Spectrochimica Acta Part A: Molecular Spectroscopy, 29(2), 1973, 253-262,
(https://doi.org/10.1016/0584-8539(73)80069-8).
[74] M.D. Alba, A.I. Becerro, P. Chain, A. Escudero, T. Gonzalez-Carrascosa, Getting more out of $X_2T_2O_7$ compounds with thortveitite structure: The bond-valence model, J. Solid State Chem., 181, 2008, 340–344,
(https://doi.org/10.1016/j.jssc.2007.11.027).
[75] I. D. Brown, C. Calvo, The crystal chemistry of large cation dichromates, pyrophosphates, and related compounds with stoichiometry $X_2Y_2O_7$, J. Solid State Chem., 1(2), 1970, 173–179,
(https://doi.org/10.1016/0022-4596(70)90010-1).
[76] P. Gras, N. Ratel-Ramond, S. Teychéné, C. Rey, E. Elkaim, B. Biscans, S. Sarda, C. Combes, Structure of the calcium pyrophosphate monohydrate phase ($Ca_2P_2O_7 \cdot H_2O$): towards understanding the dehydration process in calcium pyrophosphate hydrates, Acta Crystallogr. Sect. C, 70, 2014, 862-866,
(https://doi.org/10.1107/S2053229614017446).
[77] C. Calvo, Crystal structure of alpha-calcium pyrophosphate, Inorg. Chem., 7(7), 1968, 1345–1351,
(https://doi.org/10.1021/ic50065a019).
[78] G. Berend, A.J. Hegedüs, Thermoanalytische untersuchung von sekundärem calciumphosphatdihydrat. Thermochim. Acta, 11, 1975, 367-379,
(https://doi.org/10.1016/0040-6031(75)80004-9).
[79] W. Sauskojus, Jan K. Wied, C.F. Litterscheid, M. Mangstl, J. Schmedt auf der Günne, Crystal Structure of γ-$Ca_2P_2O_7$, Z. Anorg. Allg. Chem., 648(21), 2022, e202200196,
(https://doi.org/10.1002/zaac.202200196).

[80] J.-J. Bian, D.-W. Kim, K.-S. Hong, Phase transformation and sintering behavior of $Ca_2P_2O_7$, Materials Letters. 58 (3-4), 2004, 347-351, (https://doi.org/10.1016/S0167-577X(03)00498-1).
[81] I. Chrysafi, E. Kontonasaki, A.D. Anastasiou, D. Patsiaoura, L. Papadopoulou, G. Vourlias, E. Vouvoudi, D. Bikiaris, Mechanical and thermal properties of PMMA resin composites for interim fixed prostheses reinforced with calcium β-pyrophosphate, J. Mech. Behav. Biomed. Mater. 112, 2020, 104094, (https://doi. org/10.1016/j.jmbbm.2020.104094).
[82] K.-S. Lee, H.-S. Han, Y.-C. Kim, J.H. Lo Han, H. Seung, H.-S. Lee, J.-S. Chang, D.-H. Lee, Evaluation of porous β-calcium pyrophosphate as bioresorbable bone graft substitute material, Mater. Res. Innov., 19, 2015, 86-90, (https://doi.org/10.1179/1433075X14Y.0000000215).
[83] D. Griesiute, J. Gaidukevic, A. Zarkov, A. Kareiva, Synthesis of β-$Ca_2P_2O_7$ as an adsorbent for the removal of heavy metals from water, Sustainability. 13 (2021) 7859, (https://doi.org/10.3390/su13147859).
[84] V.C. Ghantani, M.K. Dongare, S.B. Umbarkar, Nonstoichiometric calcium pyrophosphate: a highly efficient and selective catalyst for dehydration of lactic acid to acrylic acid, RSC Adv., 4, 2014, 33319–33326, (https://doi.org/10.1039/C4RA06429A).
[85] R. Baitahe, C. Sronsri, S. Thompho, K. Chaiseeda, N. Montri, B. Boonchom, Correlation between structure, chromaticity, and dielectric properties of calcium copper pyrophosphates, $Ca_{2-x}Cu_xP_2O_7$, Sci. Rep., 12, 2022, 6869, (https://doi.org/10.1038/s41598-022-11056-4).
[86] K.K. Gupta, S. Dhoble, A.R. Krupski, Facile synthesis and thermoluminescence properties of nano bio-ceramic β-$Ca_2P_2O_7$: Dy phosphor irradiated with 75 meV C^{6+} ion beam, Sci. Rep., 10, 2020, 21203, (https://doi.org/10.1038/s41598-020-78365-4).
[87] S. Raynaud , E.Champion, D.Bernache-Assollant, P.Thomas, Calcium phosphate apatites with variable Ca/P atomic ratio I. Synthesis, characterisation and thermal stability of powders, Biomaterials, 23(4), 2002, 1065–1072, (https://doi.org/10.1016/s0142-9612(01)00218-6).
[88] K. Tõnsuaadu, K.A. Gross, L. Plūduma, M. Veiderma, A review on the thermal stability of calcium apatites, J. Therm. Anal. Calorim., 110, 2012. 647- 659, (https://doi.org/10.1007/s10973-011-1877-y).

[89] M. Bohner, Calcium orthophosphates in medicine: from ceramics to calcium phosphate cements, Injury, 31, 2000, 37-47,
(https://doi.org/10.1016/S0020-1383(00)80022-4).
[90] A. Charmforoushan, M. Sorvali , J. M. Makela, Fast-facile synthesis of single-phase nanocrystalline β-$Ca_2P_2O_7$ powder by an aerosol synthesis method, Powder Technology, 434, 2024, 119342,
(https://doi.org/10.1016/j.powtec.2023.119342).
[91] B. Mirhadi, B. Mehdikhani, N. Askari, Synthesis of nano-sized β-tricalcium phosphate via wet precipitation. Process. Appl. Ceram., 5 (4), 2011, 193–198,
(https://doi.org/10.2298/PAC1104193M).
[92] M. Bohner, B.L.G. Santoni, N. Dobelin, β-tricalcium phosphate for bone substitution: synthesis and properties, Acta Biomater., 113, 2020, 23- 41,
(https://doi.org/10.1016/j.actbio.2020.06.022).
[93] S.C. Liou, S.Y. Chen, Transformation mechanism of different chemically precipitated apatitic precursors into β-tricalcium phosphate upon calcination, Biomaterials, 23, 2002, 4541–4547,
(https://doi.org/10.1016/S0142-9612(02)00198-9).
[94] A.C. Tas, F. Korkusuz, M. Timucin, N. Akkas, An Investigation of the Chemical Synthesis and High-Temperature Sintering Behaviour of Calcium Hydroxyapatite (HA) and Tricalcium Phosphate (TCP) Bioceramics, J. Mater. Sci. Mater. Med., 8, 1997, 91–96,
(https://doi.org/10.1023/a:1018506800033).
[95] Z. Sheikh, Mohamed-Nur Abdallah, A. A. Hanafi, S. Misbahuddin , H. Rashid, M. Glogauer, Mechanisms of in Vivo Degradation and Resorption of Calcium Phosphate Based Biomaterials, Materials, 8(11), 2015, 7913-7925,
(https://doi.org/10.3390/ma8115430).
[96] R. A. Horowitz, Z. Mazor, C. Foitzik, H. Prasad, M. Rohrer, A. Palti, β-tricalcium phosphate as bone substitute material: properties and clinical applications, J. Osseointegr., 2(2), 2010, 61-68,
(https://doi.org/10.23805/jo.2010.02.02.04).
[97] S. Tkachenko, M.Horynová, M. Casas-Luna, S. Diaz-de-la-Torre, K. Dvořák, L. Čelko, J. Kaiser, E. B. Montufar, Strength and fracture mechanism of iron reinforced tricalcium phosphate cement fabricated by spark plasma sintering, J. Mech. Behav. Biomed. Mater., 81, 2018, 16-25,
(https://doi.org/10.1016/j.jmbbm.2018.02.016).
[98] M. Gallo, B.Le Gars Santoni, T. Douillard, F. Zhang, L. Gremillard, S. Dolder, W. Hofstetter, S. Meille, M. Bohner, J. Chevalier, S. Tadier, Effect of grain orientation and magnesium doping on β-tricalcium phosphate resorption behavior, Acta Biomater., 89, 2019, 391-402,

(https://doi.org/10.1016/j.actbio.2019.02.045).
[99] M. Frasnelli, A. Pedranz; M. Biesuz, S. Dirè, V.M. Sglavo, Flash sintering of Mg-doped tricalcium phosphate (TCP) nanopowders, J. Eur. Ceram. Soc., 39, 2019, 3883-3892,
(https://doi.org/10.1016/j.jeurceramsoc.2019.05.007).
[100] S. Kannan, I.A.F. Lemos, J.H.G. Rocha, J.M.F. Ferreira, Synthesis and characterization of magnesium substituted biphasic mixtures of controlled hydroxyapatite/β-tricalcium phosphate ratios, J. Solid State Chem., 178, 2005, 3190–3196,
(https://doi.org/10.1016/j.jssc.2005.08.003).
[101] K. Matsunaga, T. Kubota, K. Toyoura, A. Nakamura, First-principles calculations of divalent substitution of Ca^{2+} in tricalcium phosphates, Acta Biomater., 23, 2015, 329–337,
(https://doi.org/10.1016/j.actbio.2015.05.014).
[102] L. Sinusaite, A.M. Renner, M.B. Schütz, A. Antuzevics, U. Rogulis, I. Grigoraviciute-Puroniene, S. Mathur, A. Zarkov, Effect of Mn doping on the low-temperature synthesis of tricalcium phosphate (TCP) polymorphs. J. Eur. Ceram. Soc., 39, 2019, 3257-3263,
(https://doi.org/10.1016/j.jeurceramsoc.2019.03.057).
[103] A. Altomare, R. Rizzi, M. Rossi, A. El Khouri, M. Elaatmani,V. Paterlini, G.D. Ventura, F. Capitelli, New $Ca_{2.90}(Me^{2+})_{0.10}(PO_4)_2$ β-tricalcium Phosphates with Me^{2+}= Mn, Ni, Cu: Synthesis, Crystal-Chemistry, and Luminescence Properties, Crystals, 9(6), 2019, 288,
(https://doi.org/10.3390/cryst9060288).
[104] A.A. Belik, V.A. Morozov, S.S. Khasanov, B.I. Lazoryak, Crystal structures of new double calcium and cobalt phosphates, Mater. Res. Bull., 33, 1998, 987–995,
(https://doi.org/10.1016/S0025-5408(98)00083-X).
[105] P. Miranda, E. Saiz, K. Gryn, A.P. Tomsia, Sintering and robocasting of β-tricalcium phosphate scaffolds for orthopaedic applications, Acta Biomaterialia, 2(4), 2006, 457–466,
(https://doi.org/10.1016/j.actbio.2006.02.004).
[106] D. Susanti, R. A. Pradana, Synthesis of β-Tricalcium Phosphate from Green Mussel Shell (Perna viridis) as Calcium Source for Bone Graft. Mater. Sci. Forum, 931, 2018, 377–381.
[107] D. A. Lestari, Y. Setyarini, Synthesis of β-TCP from Rangga Clam Shells as Bone Implant Biomaterial Candidates. J. Rekayasa Proses, 13, 2019, 101–108.

[108] M. Rahayu, A.Setiawan, Sumardi, Synthesis and Characterization of β-Tricalcium Phosphate from Pearl Oyster Shell, IOP Conf. Ser.: Mater. Sci. Eng., 833(1), 2020, 012015.
[109] D. P. Sari, R.Indrati, S.Hartati, Hydroxyapatite Synthesis from Chicken Eggshells via Precipitation Method, J. Bahan Alam Terbarukan, 6(1), 2017, 1–8.
[110] Z. Al-Noamani, M. M. Al-Marsoomi, Preparation and Characterization of Hydroxyapatite from Natural Limestone. J. Eng. Appl. Sci., 14(14), 2019, 4811–4816.
[111] M.N. Ramli, N. Mohamed, M.Z. Abdullah, Synthesis of Hydroxyapatite from Natural Coral. J. Aust. Ceram. Soc., 51(2), 2015, 173–177.
[112] A. Bigi, E. Foresti, M. Gandolfi, M. Gazzano, N. Roveri, Isomorphous substitutions in b-tricalcium phosphate: the different effects of zinc and strontium. J. Inorg. Biochem., 66(4), 1997, 259-265, (https://doi.org/10.1016/S0162-0134(96)00219-X).
[113] F.H. Lin, C.J. Liao, K.-S. Chen, J.-S. Sun, Preparation of high-temperature stabilized beta-tricalcium phosphate by heating deficient hydroxyapatite with $Na_4P_2O_7$ $10H_2O$ addition, Biomaterials, 19, 1998, 1101-1107, (https://doi.org/10.1016/S0142-9612(98)00040-4).
[114] T. Konishi, Low-temperature syntesis of tricalcium phosphate and related materials. Phosphorus Res. Bull., 37, 2021, 011-020. (https://doi.org/10.3363/prb.37.11).
[115] N. Jinlong, Z. Zhenxi, J. Dazong, Investigation of phase evolution during the thermochemical synthesis of tricalcium phosphate, J. Mater. Synth. Process, 9 (5), 2001, 235-240, (https://doi.org/10.1023/A:1015243216516).
[116] G. Cicek, E.A. Aksoy, C. Durucan, N. Hasirci, Alpha-tricalcium phosphate (α- TCP): solid state synthesis from different calcium precursors and the hydraulic reactivity, J. Mater. Sci. Mater. Med., 22 (4), 2011, 809-817, (https://doi.org/10.1007/s10856-011-4283-x).
[117] C. Durucan, P.W. Brown, Reactivity of α-tricalcium phosphate. J. Mater. Sci., 37 (5), 2002, 963-969, (https://doi.org/10.1023/A:1014347814241).
[118] L.A. Vasconcellos, L.A. Dos Santos, Calcium phosphate cement scaffolds with PLGA fibers, Mater. Sci. Eng. C, 33 (3), 2013, 1032-1040, (https://doi.org/10.1016/j.msec.2012.10.019).
[119] X. Wei, O. Ugurlu, M. Akinc, Hydrolysis of α-tricalcium phosphate in simu-lated body fluid and dehydration behavior during the drying process, J. Am. Ceram. Soc., 90 (8), 2007, 2315- 2321,

(https://doi.org/10.1111/j.1551-2916.2007.01682.x).
[120] R. Famery, N. Richard, P. Boch, Preparation of α- and β-tricalcium phosphate ceramics, with and without magnesium addition, Ceram. Int., 20(5), 1994, 327-336,
(https://doi.org/10.1016/0272-8842(94)90050-7).
[121] B. Le Gars Santonia, L. Nigglia, G. A. Sblendorio, D. T. L. Alexander, C. Stähli, P. Bowen, N. Döbelin, M. Bohner, Chemically pure β-tricalcium phosphate powders: Evidence of two crystal structures, J. Eur. Ceram. Soc., 4192), 2021, 1683–1694,
(https://doi.org/10.1016/j.jeurceramsoc.2020.09.055).
[122] L. Sinusaite, A. Kareiva, A. Zarkov, Thermally induced crystallizationand phase evolution of amorphous calcium phosphate substituted with divalent cations having different sizes. Cryst.Growth Des., 21(2), 2021, 1242−1248,
(https://doi.org/10.1021/acs.cgd.0c01534).
[123] I. Grigoraviciute-Puroniene, K. Tsuru, E. Garskaite, Z. Stankeviciute, A. Beganskiene, K. Ishikawa, A. Kareiva, A novel wet polymeric precipitation synthesis method for monophasic β-TCP. Adv. Powder Technol., 28, 2017, 2325–2331,
(https://doi.org/10.1016/j.apt.2017.06.014).
[124] H.-S.Y Ryu, H.-J. Youn, K. S. Hong, B.-S. Chang, C.-K. Lee, S.-S. Chung, An improvement in sintering property of β-tricalcium phosphate by addition of calcium pyrophosphate, Biomaterials, 23(3), 2002, 909-914, (https://doi.org/10.1016/s0142-9612(01)00201-0).
[125] L. Obadia, P. Deniard, B. Alonso, T. Rouillon, S. Jobic, J. Guicheux, M. Julien, D. Massiot, B. Bujoli, J.-M. Bouler, Effect of sodium doping in b-tricalcium phosphate on its structure and properties. Chem. Mater., 18, 2006, 1425-1433,
(https://doi.org/10.1021/cm052135f).
[126] S. Hesaraki, S. Farhangdoust, K. Ahmadi, R. Nemati, M. Khorami, M. Khorami, Phase evaluation and lattice parameters of strontium/magnesium incorporated beta-tricalcium phosphate bioceramics. J. Aust. Ceram. Soc., 48, 2012, 166-172.
[127] S. Elbashir, M. Brostrom, N. Skoglund, Thermodynamic modelling assisted three-stage solid state synthesis of high purity β-$Ca_3(PO_4)_2$. Materials & Design, 238, 2024, 112679,
(https://doi.org/10.1016/j.matdes.2024.112679).
[128] L. Sinusaite, A. Popov, A. Antuzevics, K. Mazeika, D. Baltrunas, J.-C. Yang, J.-L. Horng, S. Shi, T. Sekino, K. Ishikawa, A. Kareiva, A. Zarkov, Fe and Zn co-substituted beta-tricalcium phosphate (β-TCP): Synthesis,

structural, magnetic, mechanical and biological properties. Mater. Sci. Eng. C, 112, 2020, 11091,
(https://doi.org/10.1016/j.msec.2020.110918).
[129] N. Somers, F. Jean, M. Lasgorceix, H. Curto, G. Urruth, A. Thuault, F. Petit, A. Leriche, Influence of dopants on thermal stability and densification of β-tricalcium phosphate powders, Open Ceram., 7, 2021, 100168,
(https://doi.org/10.1016/j.oceram.2021.100168).
[130] S.L.O. Costa, P.F. Silva, G.K.G. Carvalho, Y.B.A. Almeida, J.R.S. Farias, A.S.N. Braga, A brief review of beta tricalcium phosphate (β -TCP) doped with metal ions, Am. J. Eng. Res., 10(8), 2021, 333-344, e-ISSN: 2320-0847.
[131] R. Enderlea, F. G.-Neunhoeffera, M. Göbbels, F. A. Müller, P. Greil, Influence of magnesium doping on the phase transformation temperature of β-TCP ceramics examined by Rietveld refinement, Biomaterials, 26, 2005, 3379–3384,
(https://doi.org/10.1016/j.biomaterials.2004.09.017).
[132] J.C. Araújoa, M.S. Sader, E.L. Moreira, G. de Almeida Soares, Maximum substitution of magnesium for calcium sites in Mg-β-TCP structure determined by X-ray powder diffraction with the Rietveld refinement, Mater. Chem. Phys., 118, 2009, 337–340,
(https://doi.org/10.1016/j.matchemphys.2009.07.064).
[133] L. Sinusaite, A. M. Renner, M. B. Schütz, A. Antuzevics, U. Rogulis, I. Grigoraviciute-Puroniene, S. Mathur, A. Zarkov, Effect of Mn doping on the low-temperature synthesis of tricalcium phosphate (TCP) polymorphs, J. Eur. Ceram. Soc., 39(10), 2019, 3257-3263,
(https://doi.org/10.1016/j.jeurceramsoc.2019.03.057).
[134] J. Kolmas, A. Kaflak, A. Zima, A. Slósarczyk, Alpha-tricalcium phosphate synthesized by two different routes: structural and spectroscopic characterization. Ceram. Int., 41(4), 2015, 5727-5733,
(https://doi.org/10.1016/j.ceramint.2014.12.159).
[135] N. Döbelin, T.J. Brunner, W.J. Stark, M. Fisch, E. Conforto, M. Bohner, Thermal treatment of flame-synthesized amorphous tricalcium phosphate nanoparticles, J. Am. Ceram. Soc., 93(10), 2010, 3455-3463,
(https://doi.org/10.1111/j.1551-2916.2010.03856.x).
[136] M.C. Tronco, J.B. Cassel, L.A. dos Santos, α-TCP-based calcium phosphate cements: A critical review. Acta Biomater., 151, 2022, 70-87,
(https://doi.org/10.1016/j.actbio.2022.08.040).
[137] M. Mathew, L. W. Schroeder, B. Dickens, W. E. Brown, The crystal structure of a $Ca_3(PO_4)_2$. Acta Crystallogr. Sect B, B33, 1977, 1325–33,
(https://doi.org/10.1107/S0567740877006037).

[138] M. Yashima, A.Sakai, High-temperature neutron powder diffraction study of the structural phase transition between α and α' phases in tricalcium phosphate $Ca_3(PO_4)_2$. Chem. Phys. Lett., 372, 2003, 779–83, (https://doi.org/10.1016/S0009-2614(03)00505-0).
[139] R.G. Carrodeguas, S. De Aza, α-Tricalcium phosphate: Synthesis, properties and biomedical applications, Acta Biomater., 7(10), 2011, 3536-3546, (https://doi.org/10.1016/j.actbio.2011.06.019).
[140] J. Duncan, J.F. MacDonald, J.V. Hanna, Y. Shirosaki, S. Hayakawa, A. Osaka, J.M.S. Skakle, I.R. Gibson, The role of the chemical composition of monetite on the synthesis and properties of α-tricalcium phosphate, Mater. Sci. Eng. C, 34, 2014, 123-129, (https://doi.org/10.1016/j.msec.2013.08.038).
[141] M. Yashima, A. Sakai, T. Kamiyama, A. Hoshikawa, Crystal structure analysis of β-tricalcium phosphate $Ca_3(PO_4)_2$ by neutron powder diffraction, J. Solid State Chem., 175, 2003, 272–277, (https://doi.org/10.1016/S0022-4596(03)00279-2).
[142] H. Ji, Z. Huang, Z. Xia, M.S. Molokeev, M. Chen, V.V. Atuchin, M. Fang, Y. Liu, X. Wu, Phase transformation in $Ca_3(PO_4)_2:Eu^{2+}$ via the controlled quenching and increased Eu^{2+} content: identification of new cyan-emitting α- $Ca_3(PO_4)_2:Eu^{2+}$ phosphor, J. Am. Ceram. Soc., 98(10), 2015, 3280-3284, (https://doi.org/10.1111/jace.13787).
[143] D. Correa, A. Almirall, R.G. Carrodeguas, L.A. dos Santos, A.H. De Aza, J. Parra, L. Morejón, J.A. Delgado, α-Tricalcium phosphate cements modified with β-dicalcium silicate and tricalcium aluminate: physicochemical characterization, in vitro bioactivity and cytotoxicity, J. Biomed. Mater. Res. Part B Appl. Bio-mater., 103 (1), 2015, 72–83, (https://doi.org/10.1002/jbm.b.33176).
[144] A.F. Vásquez, S. Domínguez, L.A. Loureiro dos Santos, S. Pina, J. M. F. Ferreira, α-TCP cements prepared by syringe-foaming: Influence of Na_2HPO_4 and surfactant concentration, Mater. Sci. Eng. C, 81, 2017, 148-155, (https://doi.org/10.1016/j.msec.2017.07.056).
[145] O.V. Sinitsyna, A.G.Veresov, V.I. Putlyaev, Y.D. Tretyakov, Synthesis of hydroxyapatite by hydrolysis of α-$Ca_3(PO_4)_2$, Russ. Chem. Bull. 54, 2005, 79–86, (https://doi.org/10.1007/s11172-005-0220-9).
[146] C.B. Palan, N.S. Bajaj, A. Soni, S. Omanwar, A novel $KMgPO_4$: Tb^{3+} (KMPT) phosphor for radiation dosimetry, J. Lumin., 176, 2016, 106-111, (https://doi.org/10.1016/j.jlumin.2016.03.014).

[147] H. Ohtaki, Y. Fukuda, N. Takeuchi, Thermoluminescence in calcium phosphate doped with Dy_2O_3, Radiat. Protect. Dosim.,47 , 1993, 119-122, (https://doi.org/10.1093/oxfordjournals.rpd.a081715).
[148] S. Chand, R. Mehra, V. Chopra, Recent advancements in calcium based phosphate materials for luminescence applications. J. Lum., 252, 2022, 119383,
(https://doi.org/10.1016/j.jlumin.2022.119383).
[149] L.J. Roman, Z.E. Cruz, R.I.B. Lozano, G.J.A.I. Diaz, Thermoluminescence of Cerium and Terbium-Doped Calcium Pyrophosphate, 15 International Symposium on Solid State Dosimetry, Leon, Guanajuato (Mexico), 26-30 Sep, 2015.
[150] R.G. Kunghatkar, V.L. Barai, S.J. Dhoble, Synthesis route dependent characterizations of $CaMgP_2O_7$: Gd^{3+} phosphor, Results Phys., 13, 2019, 102295,
(https://doi.org/10.1016/j.rinp.2019.102295).
[151] C.M. Mehare, Y.R. Parauha, V. Chopra, S. Ray, N.S. Dhoble, C. Ghanty, S.J. Dhoble, Tailoring the luminescent properties of $Ca_9La(PO_4)_5(SiO_4)F_2$:1mol% Eu^{3+} phosphor via doping of chloride, molybdate, vanadate, sulfate, and tungstate ions, J. Mater. Sci. Mater. Electron., 31, 2020, 3426-3440,
(https://doi.org/10.1007/s10854-020-02891-0).
[152] S.D. More, M.N. Meshram, S.P. Wankhede, P.L. Muthal, S.M. Dhopte, S.V. Moharil, Luminescence in $LiCaPO_4$, Phys. B Condens. Matter, 406, 2011, 1178-1181,
(https://doi.org/10.1016/j.physb.2010.12.077).
[153] C. Malik, R.K. Meena, P. Rathi, B. Singh, A. Pandey, Effect of dopant concentration on luminescence properties of a phosphor $KCaPO_4$: Dy, Radiat. Phys. Chem., 168, 2020, 108561,
(https://doi.org/10.1016/j.radphyschem.2019.108561).
[154] K.N. Shinde, S.J. Dhoble, Thermoluminescence and photoluminescence in the $NaCaPO_4$: Dy^{3+} phosphor, Radiat. Protect. Dosim., 152, 2012,463-467, (https://doi.org/10.1093/rpd/ncs074).
[155]. X. Yang, J. Chen, C. Chai, S. Zheng, C. Chen, Near ultraviolet excited white light emitting diode (WLED) based on the blue $LiCaPO_4$: Eu^{2+} phosphor, Optik, 198, 2019, 163238,
(https://doi.org/10.1016/j.ijleo.2019.163238).
[156] P. Mokoena, I. Nagpure, V. Kumar, R.E. Kroon, E.J. Olivier, J.H. Neethling, H.C. Swart, O.M. Ntwaeaborwa, Enhanced UVB emission and analysis of chemical states of $Ca_5(PO_4)_3OH$: Gd^{3+}, Pr^{3+} phosphor prepared by co-precipitation. J. Phys. Chem. Solid.,75, 2014, 998-1003,

(https://doi.org/10.1016/j.jpcs.2014.04.015).
[157] K.N. Shinde, S.J. Dhoble, Optical study of rare earth activated $NaBa_{0.45}Sr_{0.55}PO_4$ phospho, Optik, 123(21), 2012, 1975-1979,
(https://doi.org/10.1016/j.ijleo.2011.09.033).
[158] A. Balakrishna, L. Reddy, O.M. Ntwaeaborwa, H.C. Swart, Remarkable influence of alkaline earth ions on the enhancement of fluorescence from Eu^{3+} ion doped in sodium ortho-phosphate phosphors, J. Mol. Struct., 1203, 2020, 127375,
(https://doi.org/10.1016/j.molstruc.2019.127375).
[159] T. Gao, R. Liu, Y. Liu, X. Chen, X. Ma, Spectral design in Cr^{3+}-doped NIR phosphors via crystal field modulation. J. Lumin., 246, 2022, 118799,
(https://doi.org/10.1016/j.jlumin.2022.118799).
[160] T. M. Trung, N. Tu, N.V. Quang, D.Q. Trung, P.T. Huy, Photoluminescent Properties of Red-emitting $AlPO_4:Cr^{3+}$ Phosphor for Plant Growth LEDs, VNU J. Sci. Math. Phys., 37(3), 2021, 22-31 doi.org/ (https://doi.org/10.25073/2588-1124/vnumap.4617).
[161] T.Y. Gao, W.D. Zhuang, R.H. Liu, Y.H. Liu, X.X. Chen, Design of a broadband NIR phosphor for security-monitoring LED: tunable photoluminescence properties and enhanced thermal stability, Cryst. Growth Des., 20(6), 2020, 3851-3860,
(https://doi.org/10.1021/acs.cgd.0c00154).
[162] D. Duan, S. Yu, Y. Wu, Y. Dong, Q. Shao, J. Jiang, Cr^{3+}-doped far-red phosphors with zero thermal quenching and excellent spectral matching for plant lighting application, J. Am. Ceram. Soc. 107, 2024, 6070-6079,
(https://doi.org/10.1111/jace.19855).
[163] L. Xiaoa, J Ding, X. Li, L. Jiang, X. Wu, A. Wu, Cr^{3+}-doped garnet-type $Ca_3Al_2Ge_3O_{12}$ phosphors with high color purity and high quantum yield for plant growth lighting, Ceram. Int., 50, 2024, 55855-55864,
(https://doi.org/10.1016/j.ceramint.2024.10.467).
[164] Q. Ni, J. Huo, Q. Zhu, J. Zhou, W. Sun, Y. Huang, C. Long, Q. Wang, Efficient CrIII ion governed energy migration for broadband near-infrared emission in $Ca_3Sc_2Ge_3O_{12}$ garnet phosphor, Eur. J. Inorg. Chem., 26 2023, 202300556,
(https://doi.org/10.1002/ejic.202300556).
[165] M. Milos, S. Kairouani, S. Rabaste, A. Hauser, Energy migration with in the ^2E state of Cr^{3+}, Coordination Chemistry Reviews, 252, 2008, 2540–2551,
(https://doi.org/10.1016/j.ccr.2008.04.006).
[166] P. Dorenbos, Energy of the first $4f^7 \rightarrow 4f^6$ 5d transition of Eu^{2+} in inorganic compounds. J. Lumin., 104(4), 2003, 239−260,

(https://doi.org/10.1016/S0022-2313(03)00078-4).
[167] S. X.Wang, Z.Song, Y. Kong, Z. Xia, Q. Liu, Crystal field splitting of $4f^{n-1}5d$-levels of Ce^{3+} and Eu^{2+} in nitride compounds, J. Lumin., 194, 2018, 461−466,
(https://doi.org/10.1016/j.jlumin.2017.10.073).
[168] P. Dorenbos, Relation between Eu^{2+} and Ce^{3+} f ↔ d-transition energies in inorganic compounds, J. Phys. Condens. Matter, 15(27), 2003, 4797−4807, (https://doi.org/10.1088/0953-8984/15/27/311).
[169] P. Dorenbos, f → d transition energies of divalent lanthanides in inorganic compounds. J. Phys.: Condens. Matter, 15(3), 2003, 575-594, (https://doi.org/10.1088/0953-8984/15/3/322).
[170] M. Zhao, Q. Zhang, Z. Xia, Structural Engineering of Eu^{2+}-Doped Silicates Phosphors for LED Applications, Acc. Mater.Res., 1, 2020, 137-145, (https://doi.org/10.1021/accountsmr.0c00014).
[171] N. Yang, Z. Li, J. Liang, W. Huang, Z. Ye, W. He, Y. Tong, J. Shi, Designing of Eu^{2+}-activated single-phase white-emitting phosphor through modifying cationic sites for high color rendering full-spectrum illumination. J. Alloys Compd., 1010, 2025, 177667,
(https://doi.org/10.1016/j.jallcom.2024.177667).
[172] Y.S. Tang, S.F. Hu, C.C. Lin, N.C. Bagkar, R.S. Liu, Thermally Stable Luminescence of $KSrPO_4:Eu^{2+}$ Phosphor for White Light UV Light-Emitting Diodes, Appl. Phys. Lett., 90(15), 2007, 151108,
(https://doi.org/10.1063/1.2721846).
[173] M. E. Hannah, A. P. Piquette, M. Anc, J. McKittrick, J. Talbot, J. Han and K. C. Mishra, A Study of Blue Emitting Phosphors, $ABPO_4:Eu^{2+}$ (A=Li, Na, K; B=Ca, Sr, Ba) for UV LEDs, ECS Transaction, 41(37), 2012, 19-25, (https://doi.org/10.1149/1.3697441).
[174] M. P. Moreiraa, G. D. de Almeida Soares, J. Dentzer, K. Anselme, L. D. de Sena, A. Kuznetsov, E. A. dos Santos, Synthesis of magnesium- and manganese-doped hydroxyapatite structures assisted by the simultaneous incorporation of strontium, Mater. Sci.Eng. C, 61, 2016, 736-743, (https://doi.org/10.1016/j.msec.2016.01.004).
[175] C. Rosticher, B. Viana, T. Maldiney, C. Richard, C. Chanéac, Persistent luminescence of Eu, Mn, Dy doped calcium phosphates for in-vivo optical imaging, J. Lumin., 170, 2016, 460-466,
(https://doi.org/10.1016/j.jlumin.2015.07.024).
[176] Z. Zhang, A. Delsing, P.H. L. Notten, J. Zhao, P. Dorenbos, H.T. Hintzen, Photoluminescence Properties of Red-Emitting Mn^{2+}-Activated $CaAlSiN_3$ Phosphor for White-LEDs, ECS J. Solid State Sci. Technol., 2(4), 2013, R70-R75,

(https://doi.org/10.1149/2.017304jss).
[177] S. Adachi, Review—Mn^{2+}-Based Codopant Phosphor System: Fundamentals and Some Representatives, ECS J. Solid State Sci. Technol., 13, 2024, 126001,
(https://doi.org/10.1149/2162-8777/ad96e2).
[178] S. Adachi, Review—Photoluminescence Spectroscopy of Mn^{2+}-Activated Phosphors: Part II. Some Representative Phosphors, ECS J. Solid State Sci. Technol., 12(12), 2023, 126004,
(https://doi.org/10.1149/2162-8777/ad145d).
[179] D. Zhang, C. Wang, Y. Liu, Q. Shi, W. Wang, Y. Zhai., Green and red photoluminescence from $ZnAl_2O_4$:Mn phosphors prepared by sol–gel method, J. Lumin., 1322012, 1529–1531,
(https://doi.org/10.1016/j.jlumin.2012.01.025).
[180] L.T.T. Vien, N. Tu, D.X. Viet, D.D. Anh, D.H. Nguyen, P.T. Huy, Mn^{2+}- doped Zn_2SnO_4 green phosphor for WLED applications, J. Lumin., 227, 2020, 117522,
(https://doi.org/10.1016/j.jlumin.2020.117522).
[181] Z. Su, Y. Wang, T. Seto, Synthesis of efficient submicron γ-AlON Mn^{2+}, Mg^{2+} phosphors for mini-LEDs by a coprecipitation precursor method, J. Mater. Chem. 12, 2024, 5587-5595,
(https://doi.org/10.1039/D4TC00382A).
[182] D. Griesiute, L. Sinusaite, A. Kizalaite, A. Antuzevics, K. Mazeika, D. Baltrunas, T. Goto, T. Sekino, A. Kareivaa, A. Zarkov, The influence of Fe^{3+} doping on thermally induced crystallization and phase evolution of amorphous calcium phosphate, CrystEngComm, 23(26), 2021, 4627-4637,
(https://doi.org/10.1039/D1CE00371B).
[183] L. Sinusaite, A. Antuzevics, A.I. Popov, U. Rogulis, M. Misevicius, A. Katelnikovas, A. Kareiva, A. Zarkov, Synthesis and luminescent properties of Mn-doped alpha-tricalcium phosphate, Ceram. Int., 47(4), 2021, 5335-5340,
(https://doi.org/10.1016/j.ceramint.2020.10.114).
[184] D. Griesiute, E. Raudonyte-Svirbutaviciene, A. Kareiva and A. Zarkov, The influence of annealing conditions on the Ca/P ratio and phase transformations in bulk calcium phosphates, CrystEngComm, 24, 2022, 1166-1170,
(https://doi.org/10.1039/D1CE01625C).
[185] D. Griesiute, E. Garskaite, A. Antuzevics, V. Klimavicius, V. Balevicius, A. Zarkov, A. Katelnikovas, D. Sandberg and A. Kareiva, Synthesis, structural and luminescent properties of Mn-doped calcium pyrophosphate ($Ca_2P_2O_7$) polymorphs, Sci. Rep., 12, 2022, 7116,
(https://doi.org/10.1038/s41598-022-11337-y).

[186] S. Koutsopoulos, Synthesis and characterization of hydroxyapatite crystals: A review study on the analytical methods, J. Biomed. Mater. Res., 62(4), 2002, 600-612,
(https://doi.org/10.1002/jbm.10280).
[187] O. Livitska, N. Strutynska, O. Livitska, N. Slobodyanik, The alternative approach to the preparation of complex calcium phosphates and their characterization, Func. Mater., 24(3), 2017, 457-462,
(https://doi.org/10.15407/fm24.03.457).
[188] K. Hayashi, R. Kishida, A. Tsuchiya, K. Ishikawa, Transformable Carbonate Apatite Chains as a Novel Type of Bone Graft, Adv. Healthc. Mater., 13(2), 2024, 2303245,
(https://doi.org/10.1002/adhm.202303245).
[189] M. Šupová, Substituted hydroxyapatites for biomedical applications: A review, Ceram. Int., 41(8), 2015, 9203-9231,
(https://doi.org/10.1016/j.ceramint.2015.03.316).
[190] I.V. Zatovsky, N.Y. Strutynska, V.N. Baumer, O.V. Shishkin, N.S. Slobodyanik, The whitlockite-related phosphate $Ca_9Cr(PO_4)_7$, Acta Crystallogr. E, 63(10), 2007, i180-i181,
(https://doi.org/10.1107/S1600536807044765).
[191] A.Z. Alshemary, Y.-F. Goh, I. Shakir, R. Hussain, Synthesis, characterization and optical properties of chromium doped β-Tricalcium phosphate, Ceram. Int., 41(1), 2015, 1663-1669,
(https://doi.org/10.1016/j.ceramint.2014.09.107).
[192] A. Jillavenkatesa, R.A. Condrate Sr., The Infrared and Raman Spectra of β-and α-Tricalcium Phosphate ($Ca_3(PO_4)_2$), Spectrosc. Lett., 31(8), 1998, 1619-1634,
(https://doi.org/10.1080/00387019808007439).
[193] R.K. Singh, M. Srivastava, N.K. Prasad, S. Awasthi, A. Dhayalan, S. Kannan, Iron doped β-Tricalcium phosphate: Synthesis, characterization, hyperthermia effect, biocompatibility and mechanical evaluation, Mater. Sci. Eng. C, 78, 2017, 715-726,
(https://doi.org/10.1016/j.msec.2017.04.130).
[194] C. Mellier, F. Fayon, V. Schnitzler, P. Deniard, M. Allix, S. Quillard, D. Massiot, J.M. Bouler, B. Bujoli, P.Janvier, Characterization and properties of novel gallium-doped calcium phosphate ceramics, Inorg. Chem., 50(17), 2011, 8252-8260,
(https://doi.org/10.1021/ic2007777).
[195] A. Antuzevics, G. Krieke, G. Doke, A. Zarins, L. Avotin, E. Sprugis, J. Stadulis, A. Beganskiene, A. Kareiva, A. Zarkov, Electron paramagnetic

resonance and luminescence spectroscopy of transition metal ion impurities and X-ray-induced radicals in brushite, J. Alloys Compd., 996, 2024, 174779, (https://doi.org/10.1016/j.jallcom.2024.174779).
[196] C.R. Kesavulu, R.P.S. Chakradhar, R.S. Muralidhara, J.L. Rao, R.V. Anavekar, EPR, optical absorption and photoluminescence properties of Cr^{3+} ions in lithium borophosphate glasses, J. Alloys Compd., 496(1), 2010, 75-80, (https://doi.org/10.1016/j.jallcom.2010.02.119).
[197] F.S. De Vicente, F.A. Santos, B.S. Simões, S.T. Dias, M.S. Li, EPR, optical absorption and luminescence studies of Cr^{3+}-doped antimony phosphate glasses, Opt. Mater., 38, 2014, 119-125, (https://doi.org/10.1016/j.optmat.2014.10.012).
[198] K. Kowalska, M. Kuwik, J. Polak, J. Pisarska, W.A. Pisarski, EPR and optical spectroscopy of Cr^{3+} ions in barium gallo-germanate glasses containing B_2O_3/TiO_2, J. Lumin., 245, 2022, 118775, (https://doi.org/10.1016/j.jlumin.2022.118775).
[199] P. Rodionovs, M. Kemere, A. Antuzevics, U. Rogulis, A. Sarakovskis, A. Fedotovs, Multi-site incorporation of Cr^{3+} in $CaAl_{12}O_{19}$, Materialia, 32, 2023, 101927, (https://doi.org/10.1016/j.mtla.2023.101927).
[200] G. Doke, A. Antuzevics, G. Krieke, A. Kalnina, A. Sarakovskis, Novel broadband near-infrared emitting long afterglow phosphor $MgGeO_3$: Cr^{3+}, J. Alloys Compd., 918, 2022, 165768, (https://doi.org/10.1016/j.jallcom.2022.165768).
[201] M. Back, J. Ueda, J. Xu, K. Asami, M.G. Brik, S. Tanabe, Effective Ratiometric Luminescent Thermal Sensor by Cr^{3+}-Doped Mullite $Bi_2Al_4O_9$ with Robust and Reliable Performances, Adv. Opt. Mater., 8(11), 2020, 2000124, (https://doi.org/10.1002/adom.202000124).
[202] Y. Katayama, B. Viana, D. Gourier, J. Xu, S. Tanabe, Photostimulation induced persistent luminescence in $Y_3Al_2Ga_3O_{12}$:Cr^{3+}, Opt. Mater. Express, 6(4), 2016, 1405-1413, (https://doi.org/10.1364/OME.6.001405).
[203] S. Shionoya, W.M. Yen, H. Yamamoto, Phosphor handbook, CRC press, 2018, (https://doi.org/10.1201/9781315222066).
[204] Y. Tanabe, S. Sugano, On the absorption spectra of complex ions. I, J. Phys. Soc. Jpn., 9(5), 1954, 753-766, (https://doi.org/10.1143/JPSJ.9.753).
[205] Y. Tanabe, S. Sugano, On the absorption spectra of complex ions II, J. Phys. Soc. Jpn., 9(5), 1954, 766-779,

(https://doi.org/10.1143/JPSJ.9.766).
[206] M. Back, E. Trave, J. Ueda, S. Tanabe, Ratiometric Optical Thermometer Based on Dual Near-Infrared Emission in Cr^{3+}-Doped Bismuth-Based Gallate Host, Chem. Mater., 28(22), 2016, 8347-8356,
(https://doi.org/10.1021/acs.chemmater.6b03625).
[207] B. Henderson, A. Marshall, M. Yamaga, K.P.O. Donnell, B. Cockayne, The temperature dependence of Cr^{3+} photoluminescence in some garnet crystals, J. Phys. C: Solid State Phys., 21(36), 1988, 6187,
(https://doi.org/10.1088/0022-3719/21/36/018).
[208] M. Yamaga, B. Henderson, K.P. O'Donnell, G. Yue, Temperature dependence of the lifetime of Cr^{3+} luminescence in garnet crystals, Appl. Phys. B, 51(2), 1990, 132-136,
(https://doi.org/10.1007/BF00326013).
[209] J. Ueda, M. Back, M.G. Brik, Y. Zhuang, M. Grinberg, S. Tanabe, Ratiometric optical thermometry using deep red luminescence from $^4T_2$ and ^2E states of Cr^{3+} in $ZnGa_2O_4$ host, Opt. Mater., 85, 2018, 510-516,
(https://doi.org/10.1016/j.optmat.2018.09.013).
[210] M. Back, J. Ueda, H. Nambu, M. Fujita, A. Yamamoto, H. Yoshida, H. Tanaka, M. G. Brik, S. Tanabe, Boltzmann thermometry in Cr^{3+}-doped Ga_2O_3 polymorphs: the structure matters, Adv. Opt. Mater., 9 (9), 2021, 2100033,
(https://doi.org/10.1002/adom.202100033).
[211] Z. Hao, J. Zhang, X. Zhang and X. Wang, $CaSc_2O4:Eu^{3+}$: A tunable full-color emitting phosphor for white light emitting diodes, Opt. Mater., 33, 2011, 355-358,
(https://doi.org/10.1016/j.optmat.2010.09.035).
[212] H. Wang, K. Su, L. Mei, Q. Guo, L. Liao, Vacancy-Enhanced Self-Reduction of Eu in Pyrophosphate Phosphor, Inorg. Chem., 2023, 62(31), 12468-12479,
(https://doi.org/10.1021/acs.inorgchem.3c01656).
[213] X.-Y. Sun, X.-C. Le, Z. Xiao, X. Shi, W.-F. Wang, Z. Hu, Q.-M. Yang, R. Wei and H. Guo, J. Am. Ceram. Soc., 2020, 103(5), 3119-3125.
[214] B. Yu, Y. Li, Y. Wang, N. Li, P. Xiao, D. Liu, L. Geng, Stable Tunable Luminescence of Hetero-valent Eu Ion Activated Ba2InTaO6 Phosphors Synthesized by Defect-Induced Self-Reduction in the Molten-Salt Method, Inorg. Chem., 61, 2022, 2463-2475,
(https://doi.org/10.1021/acs.inorgchem.1c03312).
[215] W. Teng, H. Dong, C. Hu, X. Yang, J. Wang, X. Liang, B. Yang, J. Ru, B. Teng, D. Zhong, Achieving multi-wavelength excitation and multi-color tunable emission in self-reducing phosphor of $Ba_2MgSi_2O_7$: Eu^{2+}/Eu^{3+}, J. Lumin., 269, 2024, 120524,

(https://doi.org/10.1016/j.jlumin.2024.120524).
[216] W. Zhou, J. Han, F. Pan, J. Zhang, Q. Xie, S. Lian, L. Yu and J. Wang, Preparation and Luminescence Properties of Eu^{2+} and Mn^{2+} Coactivated Tricalcium Phosphate Phosphors, J. Am. Ceram. Soc., 97, 2014, 3631-3635, (https://doi.org/10.1111/jace.13198).
[217] C. Tong, Y. Zhu, C. Xu and Y. Li, Preliminary observation of self-reduction of Eu ions in α-$Ca_3(PO_4)_2$ phosphors prepared in air condition, Physica B Condens. Matter, 500, 2016, 20-23, (https://doi.org/10.1016/j.physb.2016.07.026).
[218] M. Peng, Z. Pei, G. Hong and Q. Su, The reduction of Eu^{3+} to Eu^{2+} in $BaMgSiO_4$:Eu prepared in air and the luminescence of $BaMgSiO_4$:Eu^{2+} phosphor, J. Mater. Chem., 13, 2003, 1202-1205, (https://doi.org/10.1039/b211624c).
[219] D. Luo, C. Tong, Y. Zhu, C. Xu and Y. Li, Color tracing in the hydration process of α-$Ca_3(PO_4)_2$:Eu, J. Lumin., 219, 2020, 116863, (https://doi.org/10.1016/j.jlumin.2019.116863).
[220] C. Tong, Y. Zhu, C. Xu, L. Yang and Y. Li, Luminescence properties and color identification of Eu doped $Ca_3(PO_4)_2$ phosphors calcined in air, Physica B Condens. Matter, 521, 2017, 153-157, (https://doi.org/10.1016/j.physb.2017.06.079).
[221] A. Doat, F. Pellé, A. Lebugle, Europium-doped calcium pyrophosphates: Allotropic forms and photoluminescent properties, J. Solid State Chem., 178, 2005, 2354-2362, (https://doi.org/10.1016/j.jssc.2005.05.023).
[222] P. Dorenbos, Thermal quenching of Eu^{2+} 5d–4f luminescence in inorganic compounds, J. Phys. Condens. Matter., 17, 2005, 8103, (https://doi.org/10.1088/0953-8984/17/50/027).
[223] G. Blasse, B. C. Grabmaier, Luminescent Materials, Springer-Verlag, Berlin, Heidelberg, 1994.
[224] W.M. Yen, M.J. Weber, Inorganic phosphors: compositions, preparation and optical properties, CRC press 2004, (https://doi.org/10.1201/9780203506325).
[225] M. Liao, F. Wu, D. Zhu, X. Zhang, H. Dong, Z. Lin, M. Wen, Z. Mu, Towards single broadband white emission in $Rb_{0.5}K_{1.5}CaPO_4$(F, Cl): Eu^{2+} via selective site occupancy engineering for solid-state lighting applications, Chem. Eng. J., 449, 2022, 137801, (https://doi.org/10.1016/j.cej.2022.137801).
[226] M. Yashima, Y. Kawaike, Crystal Structure and Site Preference of Ba-Doped α-Tricalcium Phosphate $(Ca_{1-x}Ba_x)_3(PO_4)_2$ Through High-Resolution

Synchrotron Powder Diffraction (x = 0.05 to 0.15), Chem. Mater., 2007, 19, 3973-3979,
(https://doi.org/10.1021/cm070963y).
[227] R. D. Shannon, Revised effective ionic radii and systematic studies of interatomic distances in halides and chalcogenides, Acta Crystallogr. A, 32, 1976, 751-767,
(https://doi.org/10.1107/S0567739476001551).
[228] L. G. van Uitert, An empirical relation fitting the position in energy of the lower d-band edge for Eu^{2+} or Ce^{3+} in various compounds, J. Lumin., 29, 1984, 1-9,
(https://doi.org/10.1016/S0022-2313(84)90070-X).
[229] A. Lecointre, R.A. Benhamou, A. Bessiére, G. Wallez, M. Elaatmani, B. Viana, Red long-lasting phosphorescence (LLP) in β-TCP type $Ca_{9.5}Mn(PO_4)_7$ compounds, Optical Materials, 34(2), 2011, 376-380,
(https://doi.org/10.1016/j.optmat.2011.05.020).
[230] A. Lecointre, A. Bessière, A.J.J. Bos, P. Dorenbos, B. Viana, S. Jacquart, Designing a red persistent luminescence phosphor: the example of YPO_4: Pr^{3+}, Ln^{3+} (Ln= Nd, Er, Ho, Dy), J. Phys. Chem. C, 115(10), 2011, 4217-4227,
(https://doi.org/10.1021/jp108038v).
[231] B.N. Yussupbekova, T.N. Nurakhmetov, Z.M. Salikhodzha, A. M. Zhunusbekov, A. Z. Kainarbay, D. H. Daurenbekov, K. B. Zhangylyssov, Intrinsic and impurity emission and formation mechanism of trapping centers in $LiKSO_4$-Cu crystals, Nucl. Instrum. Methods Phys. Res., Sect. B, 481, 2020, 19-23,
(https://doi.org/10.1016/j.nimb.2020.07.027).
[232] R.Zhou, L. Lin, C. Liu, P. Dorenbos, Y. Tao, , Y. Huang, H. Liang, Insight into Eu redox and Pr^{3+} 5d emission in $KSrPO_4$ by VRBE scheme construction, Dalton Trans., 47(2), 2018, 306-313,
(https://dx.doi.org/10.1039/c7dt03813e).

SANTRAUKA

ĮVADAS

Fosfatinės matricos plačiai taikomos kuriant liuminescencines medžiagas, aktyvuotas retųjų žemių arba pereinamųjų metalų jonais. Susidomėjimą šia medžiagų klase lemia keletas veiksnių, tarp jų – stipri ir plačiajuostė sugertis ultravioletinėje (UV) srityje, struktūrų įvairovė bei galimybė šias struktūras modifikuoti. Tarp plačiausiai tiriamų fosfatų pogrupių išskiriami apatitinės struktūros fosfatai, pirofosfatai, ortofosfatai (MPO_4, kur M – trivalentis jonas) ir vitlokito tipo struktūros junginiai. Be to, dalinis katijonų pakeitimas fosfatuose gali būti taikomas kaip būdas modifikuoti biosuderinamų fosfatų fizikines, chemines ir biologines savybes. Tai leidžia apjungti biosuderinamumą su katijonų pakeitimo sukeltomis savybėmis ir praplėsti šių medžiagų taikymo sritis, pavyzdžiui, įvairiose vaizdinimo technologijose.

Kalcio fosfatai (CaP) sudaro svarbų fosfatinių medžiagų pogrupį ir sulaukia didelio dėmesio dėl plataus pritaikymo ne tik optinių medžiagų srityje, bet ir medicinoje, kaulų regeneracijoje, katalizėje, sunkiųjų metalų sorbcijoje bei kitose srityse. CaP gali būti klasifikuojami pagal įvairius parametrus, įskaitant kristalinę struktūrą, Ca/P santykį bei kitų struktūrinių grupių buvimą (pvz., OH^-, CO_3^{2-}, Cl^-, F^-). CaP sudėtinės ir struktūrinės ypatybės lemia jų skirtingas chemines ir fizikines savybes. Dėl didelės CaP fazių įvairovės selektyviai konkrečių junginių sintezei reikalingi specifiniai sintezės metodai.

Kai kurie CaP gali būti lengvai susintetinami tiesioginio nusodinimo iš vandeninių tirpalų arba kietafazės reakcijos būdu, tačiau tam tikros metastabilios fazės gali būti gaunamos tik vykstant faziniams virsmams iš termodinamiškai mažiau stabilių CaP. Iš esmės fazinių virsmų metodai skirstomi į du pagrindinius kelius: (I) sausuosius, termiškai indukuotus fazinius virsmus aukštoje temperatūroje ir (II) fazinius virsmus vandeninėje terpėje. Termiškai indukuoti įvairių CaP fazių virsmai vyksta kaitinant pradinę medžiagą aukštoje temperatūroje. Paprastai tikimasi, kad pradinių medžiagų ir galutinių produktų Ca/P santykis išliks nepakitęs. Pavyzdžiui, kalcio deficitinis hidroksiapatitas ($Ca_9(PO_4)_4(HPO_4)_2OH$), kurio Ca/P santykis yra 1,5 : 1, aukštoje temperatūroje virsta β-trikalcio fosfatu ($Ca_3(PO_4)_2$). Panašus elgesys būdingas ir amorfiniam kalcio fosfatui – metastabiliai ir itin reaktyviai CaP šeimos fazei, kuri gali būti naudojama kaip prekursorius kitų fosfatinių medžiagų sintezei. Tačiau tam tikrais atvejais faziniai virsmai tarp skirtingų CaP gali vykti kartu su reikšmingu Ca/P santykio pokyčiu. Be to, reakcijos lydytose druskose dėl sąveikos su lydalo komponentais gali lemti visiškai kitų produktų susidarymą.

Šio darbo tikslas – susintetinti įvairias nelegiruotas bei jonais legiruotas kalcio fosfatų fazes bei ištirti jų struktūrines, morfologines ir optines savybes.

Darbo uždaviniai:

- ištirti sintezės parametrų įtaką selektyviai $Ca_5(PO_4)_3Cl$ ir Ca_2PO_4Cl sintezei iš amorfinio kalcio fosfato lydytuose chloriduose;
- susintetinti Cr^{3+} jonais aktyvuotą β-$Ca_3(PO_4)_2$ ir ištirti jo optines savybes;
- susintetinti Eu^{2+} jonais aktyvuotą α-$Ca_3(PO_4)_2$ vykdant fazinį virsmą iš Eu^{3+} jonais aktyvuoto $CaHPO_4 \cdot 2H_2O$ (DCPD) ir ištirti jo optines savybes;
- susintetinti Mn^{2+} jonais aktyvuotą α-$Ca_2P_2O_7$ ir ištirti jo optines savybes.

METODIKA

Reagentai

Kalcio nitratas tetrahidratas ($Ca(NO_3)_2 \cdot 4H_2O$, ≥99%, Carl Roth), diamonio vandenilio fosfatas ($(NH_4)_2HPO_4$, ≥98%, Carl Roth), amoniako tirpalas (NH_4OH, 25%, Carl Roth), ličio chloridas (LiCl, ≥98.5%, Roth), natrio chloridas (NaCl, >99.8%, Carl Roth), kalio chloridas (KCl, >99%, Carl Roth), kalcio chloridas ($CaCl_2$, ≥94%, Carl Roth), chromo nitratas nonahidratas ($Cr(NO_3)_3 \cdot 9H_2O$, 98%, Alfa Aesar), europio nitratas heksahidratas ($Eu(NO_3)_3 \cdot 6H_2O$, 99.9%, Acros Organics) ir mangano nitratas tetrahidratas ($Mn(NO_3)_2 \cdot 4H_2O$, 98%, Alfa Aesar) buvo naudojami pradinėmis medžiagomis.

$Ca_5(PO_4)_3Cl$ ir Ca_2PO_4Cl sintezė

$Ca_5(PO_4)_3Cl$ ir Ca_2PO_4Cl milteliai buvo sintetinami lydytų druskų metodu. Druskomis buvo naudojami ličio chloridas (LiCl), natrio chloridas (NaCl), kalio chloridas (KCl) ir kalcio chloridas ($CaCl_2$). Reakcijoms druskų lydaluose paruoštas ACP buvo sumaišomas su reikiamu pasirinktos druskos kiekiu agatinėje grūstuvėje, perkeliamas į aliuminio oksido tiglį ir kaitinamas mufelinėje krosnyje nustatytoje temperatūroje tam tikrą laiką. Temperatūra, kaitinimo trukmė bei ACP ir druskų masių santykis buvo parenkami individualiai kiekvienam eksperimentui. Po reakcijos gauti produktai buvo plaunami karštu dejonizuotu vandeniu, siekiant pašalinti druskų likučius. Likę produktai buvo džiovinami 100 °C temperatūroje. Reakcijos schema pateikta 11 paveiksle.

Cr^{3+} jonais legiruoto beta-trikalcio fosfato (β-TCP, β-$Ca_3(PO_4)_2$) sintezė

Cr^{3+} jonais pakeisto β-TCP milteliai buvo susintetinti nusodinimo metodu su tolesniu nuosėdų kaitinimu. Pakeitimo laipsnis (0,1; 0,5; 1,0; 2,0 ir 5,0 mol%) nurodomas Ca^{2+} jonų atžvilgiu. Sintezei reikalingi kiekiai $Ca(NO_3)_2 \cdot 4H_2O$ ir $Cr(NO_3)_3 \cdot 9H_2O$ buvo ištirpinti dejonizuotame vandenyje, siekiant gauti tirpalą, kuriame bendra metalų jonų koncentracija būtų 0,75 M. Tuo pačiu metu atskirame inde dejonizuotame vandenyje buvo ištirpintas $(NH_4)_2HPO_4$, gaunant 0,5 M koncentracijos tirpalą, į kurį buvo pridėta koncentruoto amoniako tirpalo (NH_4OH, 25 %), pH vertei pakelti iki 10. Tuomet metalų nitratų tirpalas buvo greitai supiltas į $(NH_4)_2HPO_4$ tirpalą, dėl ko susidarė nuosėdos. Gautos nuosėdos buvo maišomos reakcijos mišinyje 10 min., filtruojamos, plaunamos dejonizuotu vandeniu ir džiovinamos džiovinimo spintoje per naktį. Išdžiovinti milteliai buvo sutrinami agatinėje grūstuvėje ir kaitinami mufelinėje krosnyje ore 1100 °C temperatūroje 5 val. 5 °C/min kaitinimo greičiu.

Eu^{2+} jonais aktyvuoto alfa-trikalcio fosfato (α-TCP, α-$Ca_3(PO_4)_2$) sintezė

Pradiniai Eu^{3+} jonais legiruoto DCPD milteliai buvo susintetinti nusodinimo metodu. Pirmiausia metalų nitratai buvo ištirpinti dejonizuotame vandenyje, gaunant 0,8 M koncentracijos tirpalą, kuriame Eu pakeitimo laipsnis buvo nustatytas 0,1 mol% Ca^{2+} jonų atžvilgiu. Lygiagrečiai buvo paruoštas tokios pačios koncentracijos $(NH_4)_2HPO_4$ tirpalas. Fosfatų jonų tirpalas, nuolat maišant, buvo greitai supiltas į metalų jonų tirpalą, dėl ko susidarė baltos nuosėdos. Gautos nuosėdos buvo maišomos reakcijos mišinyje 5 min., po to filtruojamos, plaunamos dejonizuotu vandeniu ir džiovinamos 50 °C temperatūroje per naktį. Eu jonais aktyvuoto α-TCP sintezei gautos nuosėdos buvo kaitinamos vamzdinėje krosnyje vakuume ($7,8 \cdot 10^{-2}$ mbar) 1300 °C temperatūroje 24 val. Po kaitinimo krosnis buvo palikta natūraliai atvėsti.

Mn^{2+} jonais legiruoto alfa-kalcio pirofosfato (α-CPP, α-$Ca_2P_2O_7$) sintezė

Nelegiruoto ir Mn^{2+} jonais legiruoto CPP sintezė buvo atlikta nusodinimo metodu. Pirmiausia, ištirpinant metalų druskas dejonizuotame vandenyje, buvo paruoštas 0,8 M koncentracijos Ca^{2+} ir Mn^{2+} nitratų tirpalas. Mn pakeitimo laipsnis buvo pasirinktas 1 mol% Ca^{2+} jonų atžvilgiu. Atskirame inde buvo paruoštas tokios pačios koncentracijos $(NH_4)_2HPO_4$ tirpalas. Tuomet fosfatų jonų turintis tirpalas, nuolat maišant magnetine maišykle, buvo greitai supiltas į metalų jonų tirpalą, dėl ko susidarė nuosėdos. Gautos nuosėdos buvo filtruojamos, plaunamos dejonizuotu vandeniu ir džiovinamos 50 °C temperatūroje per naktį. Toliau nuosėdos buvo kaitinamos 1200 °C temperatūroje 10 min., esant 5 °C/min kaitinimo greičiui.

Siekiant ištirti lydytų druskų cheminės sudėties įtaką produktų faziniam grynumui ir morfologijai, buvo atlikta reakcijų serija naudojant pastovų ACP kiekį ir keičiant KCl bei $CaCl_2$ santykį. Gautų produktų rentgeno spindulių difraktogramos pateiktos 1 paveiksle. Nustatyta, kad lydytų druskų sudėtis stipriai veikia susidarančio produkto kristalinę struktūrą. Vienfazis ClAp buvo gautas K turtinguose mišiniuose iki KCl/$CaCl_2$ santykio 6:4. Taip pat pastebėta, kad didėjantis $CaCl_2$ kiekis reikšmingai keičia difrakcijos smailių intensyvumų santykį.

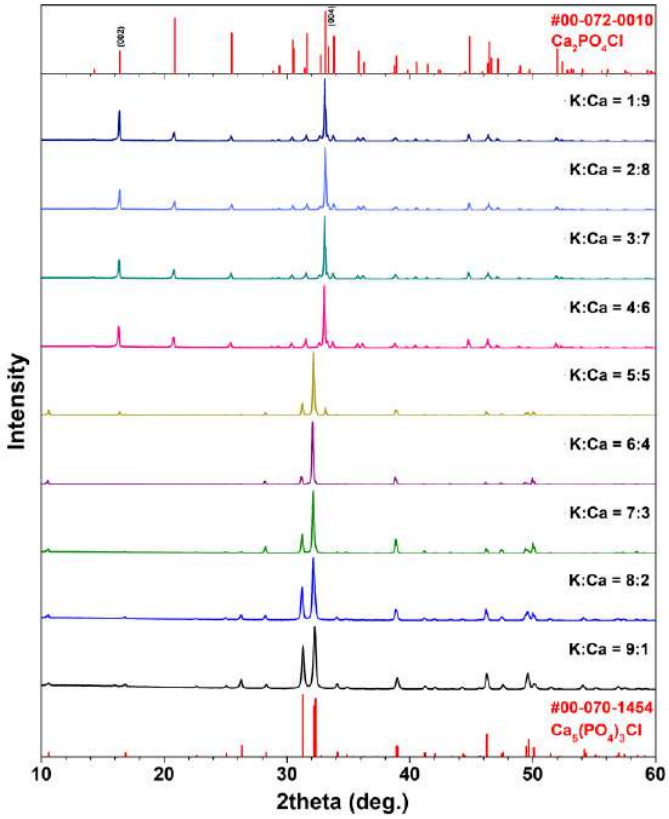

1 pav. Produktų, gautų apdorojant ACP skirtingų molinių santykių KCl ir CaCl2 mišiniuose, rentgeno spindulių difraktogramos (T = 750 °C, ACP/lydalas = 1:2, t = 5 val.).

Mėginių, gautų iš lydalų su dideliu Ca kiekiu (30 ir 40 mol%), difraktogramose vyrauja difrakcijos smailė ties ~32,2°. Toks reiškinys rodo anizotropinį ClAp dalelių augimą, dėl kurio difraktogramose pasireiškia vyraujanti kristalų orientacija. Kai KCl/$CaCl_2$ santykis pasiekė 5:5, pagrindinė

gauto produkto fazė vis dar buvo ClAp, tačiau taip pat buvo stebėta ir gretutinė Ca_2PO_4Cl fazė, rodanti dvifazio produkto susidarymą. Toliau didinant $CaCl_2$ kiekį, susidarė tik Ca_2PO_4Cl fazė be kitų kristalinių fazių priemaišų. Visos vienfazės Ca_2PO_4Cl difraktogramos pasižymėjo preferencine orientacija su ryškiomis difrakcijos smailėmis, atitinkančiomis (002) ir (004) kristalografines plokštumas.

SEM vaizdai mėginių, gautų skirtingos sudėties KCl–$CaCl_2$ mišiniuose, pateikti 2 paveiksle. Nustatyta, kad sintezės terpės sudėtis stipriai veikia produktų morfologiją – tiek dalelių dydį, tiek jų formą. ClAp, gautą mišiniuose, kurių KCl/$CaCl_2$ santykis buvo 9:1 ir 8:2, daugiausia sudarė aglomeruotos submikrometrinės beveik sferinės formos dalelės, tačiau detalesnė analizė atskleidė ir daugiakampės strypelių formos dalelių buvimą. Padidinus $CaCl_2$ kiekį iki 30 mol%, buvo stebėtas ryškus morfologijos pokytis. Susidarę polidispersiniai milteliai buvo sudaryti iš mikrometrinių matmenų heksagoninių strypelių, padengtų smulkesnėmis dalelėmis. Esant KCl/$CaCl_2$ santykiui 6:4, smulkių dalelių kiekis sumažėjo, o strypelių formos dalelės tapo vienodesnės. Toliau didinant $CaCl_2$ kiekį iki 50 %, pastebėtas akivaizdus strypelių ilgio sumažėjimas ir jų geometrinių proporcijų pokytis. Produktai, gauti Ca turtinguose mišiniuose, pasižymėjo kitokia morfologija – juos sudarė mikrometrinių matmenų kvadratinės prizmės formos dalelės. Tai gerai koreliuoja su faziniu virsmu iš ClAp į Ca_2PO_4Cl. Galima teigti, kad $CaCl_2$ buvimas lydale reikšmingai skatina ClAp kristalų padidėjimą bei anizotropinį augimą c ašies kryptimi, dėl ko susidaro heksagoninės formos strypeliai. Tačiau šio parametro įtaka yra ribota dėl Ca_2PO_4Cl fazės formavimosi $CaCl_2$ turtinguose lydaluose. Tuo tarpu Ca_2PO_4Cl kristalai nėra linkę augti anizotropiškai, kas tikriausiai susiję su jų kristalinės struktūros ypatumais.

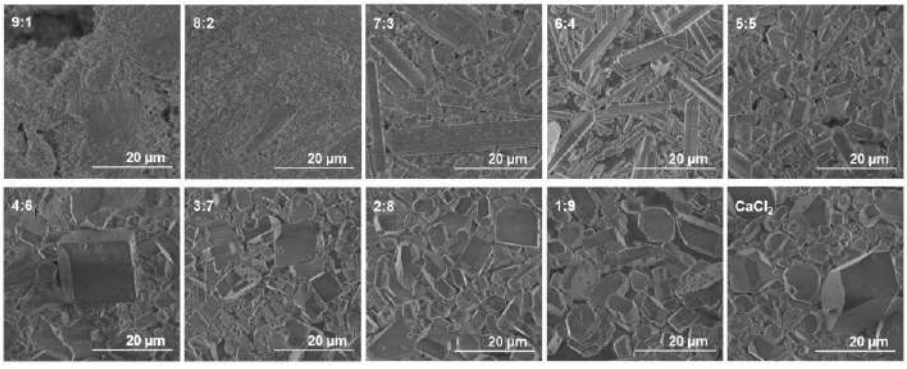

2 pav. Produktų, gautų apdorojant ACP skirtingų molinių santykių KCl ir $CaCl_2$ mišiniuose, SEM vaizdai (K:Ca santykis nuo 9:1 iki 1:9: T = 750 °C, ACP/lydalas = 1:2, t = 5 val.; $CaCl_2$ atveju T = 800 °C).

Cr^{3+} jonais legiruotų β-TCP miltelių rentgeno spindulių difraktogramos pateiktos 3a paveiksle. Nepriklausomai nuo Cr kiekio, visuose mėginiuose susidarė pagrindinė β-TCP fazė. Visos difrakcijos smailės gerai sutapo su romboedrinės $Ca_3(PO_4)_2$ struktūros standartu (*R3c*, #00-070-2065). Mėginyje su didžiausia Cr koncentracija (5 mol%) buvo aptikta nedidelė priemaišinė fazė, identifikuota kaip Cr_2O_3 (#00-038-1479). Mažesnės Cr koncentracijos mėginiuose šios priemaišos nenustatyta. Tai rodo, kad pasirinktomis sintezės sąlygomis Cr^{3+} jonų tirpumas β-TCP kristalinėje gardelėje yra ribotas.

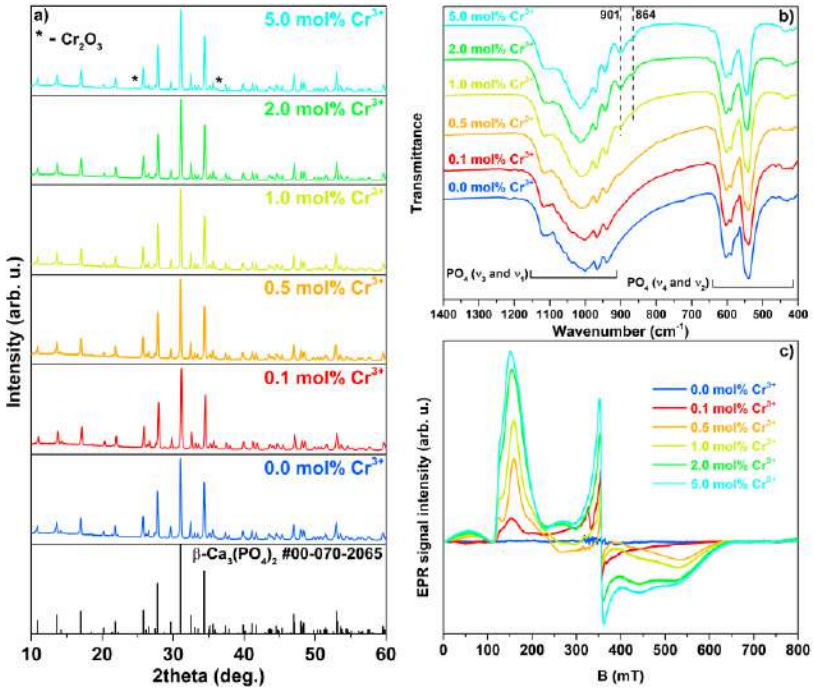

3 pav. β-TCP:Cr^{3+} mėginių rentgeno spindulių difraktogramos (a), FTIR spektrai (b) ir EPR spektrai (c).

Tų pačių mėginių FTIR spektrai pateikti 3b paveiksle. Spektruose stebėtos β-TCP struktūrai būdingos fosfatinių grupių sugerties juostos. Juostos ~1150–990 cm^{-1} srityje priskirtos fosfatų ν_3 virpesiams, o juostos ties 970 ir 940 cm^{-1} – ν_1 virpesiams. Juostos 640–500 cm^{-1} srityje atitiko ν_4 deformacinius virpesius, o silpna sugerties juosta ties ~434 cm^{-1} priskiriama ν_2 virpesiams. Didėjant Cr^{3+} kiekiui, FTIR spektrų forma nežymiai kito. Mėginiuose, kurių Cr kiekis buvo 1 mol% ir didesnis, aiškiai matėsi papildomos sugerties juostos ties 901 ir 864 cm^{-1}. Literatūroje nurodoma, kad trivalenčių jonų, tokių kaip Fe^{3+} ar Ga^{3+}, įterpimas į β-TCP gardelę sukelia lokalinės fosfatinių grupių aplinkos pokyčius ir papildomų sugerties juostų atsiradimą. Todėl šių juostų

atsiradimas patvirtina Cr^{3+} jonų įsiterpimą į β-TCP kristalinę gardelę. EPR spektrai (3c paveikslas) patvirtino Cr^{3+} jonų įsiterpimą į β-TCP mėginių struktūrą. Didėjant Cr^{3+} koncentracijai, atsirado du ryškūs signalai: asimetrinis žemo magnetinio lauko signalas ties ~160 mT ir simetrinis signalas ties 356 mT. Tiriamajame koncentracijų intervale žemo lauko signalo integralinis intensyvumas didėjo proporcingai Cr koncentracijai. Tačiau skirtingų signalų santykinio intensyvumo pokyčiai rodo kelių skirtingų su Cr^{3+} susijusių centrų egzistavimą.

4 paveiksle pateikti β-TCP:Cr^{3+} mėginių fotoliuminescencijos (PL) sužadinimo ir emisijos spektrai. Visuose mėginiuose buvo nustatytos trys Cr^{3+} jonams būdingos sužadinimo juostos, kurių maksimumai yra maždaug ties 300, 450 ir 640 nm. Šios juostos priskirtos Cr^{3+} jonų vidiniams šuoliams: $^4A_2(^4F) \rightarrow {}^4T_1(^4P)$ ties 300 nm, $^4A_2(^4F) \rightarrow {}^4T_1(^4F)$ ties 450 nm ir $^4A_2(^4F) \rightarrow {}^4T_2(^4F)$ ties 640 nm. Cr^{3+} jonų 3d energijos lygmenų padėtis stipriai priklauso nuo kristalinio lauko. Todėl net ir nedideli gardelės pokyčiai, tokie kaip didesnė Cr^{3+} koncentracija ar dėl krūvio kompensacijos susidarantys defektai, gali lemti spektrinius pokyčius. β-TCP:Cr^{3+} mėginiuose, didėjant Cr^{3+} koncentracijai, buvo stebėtas 450 nm žadinimo juostos poslinkis į ilgesnių bangų sritį. Esant 450 nm sužadinimui, visi mėginiai pasižymėjo plačia artimosios infraraudonosios srities liuminescencijos juosta 680–900 nm intervale, kuri atsiranda dėl Cr^{3+} jonams būdingo šuolio $^4T_2(^4F) \rightarrow {}^4A_2(^4F)$, esant santykinai silpnam kristaliniam laukui. Didžiausias emisijos intensyvumas buvo nustatytas 0,1 mol% Cr^{3+} mėginyje, tikriausiai dėl koncentracinio gesinimo esant didesnėms Cr^{3+} koncentracijoms.

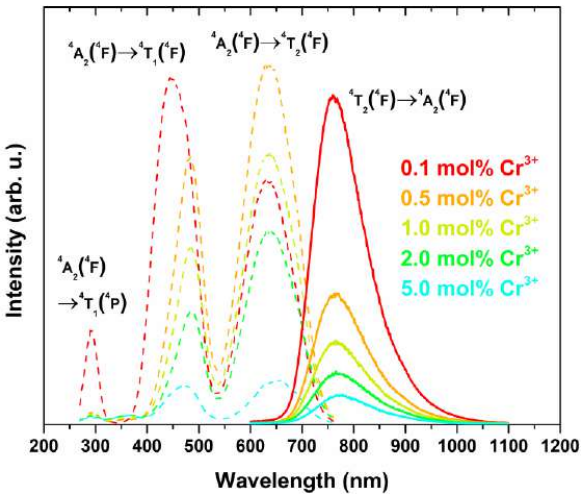

4 pav. β-TCP:Cr^{3+} mėginių sužadinimo (punktyrinės linijos) ir emisijos (vientisos linijos) spektrai (λ_{em} = 790 nm; λ_{ex} = 450 nm).

5 paveiksle pateikta α-TCP:Eu miltelių, iškaitintų vakuume 1300 °C temperatūroje, rentgeno spindulių difraktograma. Difrakcijos smailės gerai sutapo su monoklininės $Ca_3(PO_4)_2$ struktūros standartu (#00-070-0364). Toks virsmas iš DCPD rodo fosfatinių komponentų išgaravimą ir kalcio fosfato fazės, pasižyminčios žymiai didesniu Ca/P santykiu (Ca/P = 1,5:1), susidarymą. SEM vaizdas (5 pav. intarpas) atskleidė netaisyklingos formos ir mikrometrinių matmenų monolitinių dalelių susidarymą, būdingą aukštoje temperatūroje susintetintam α-TCP.

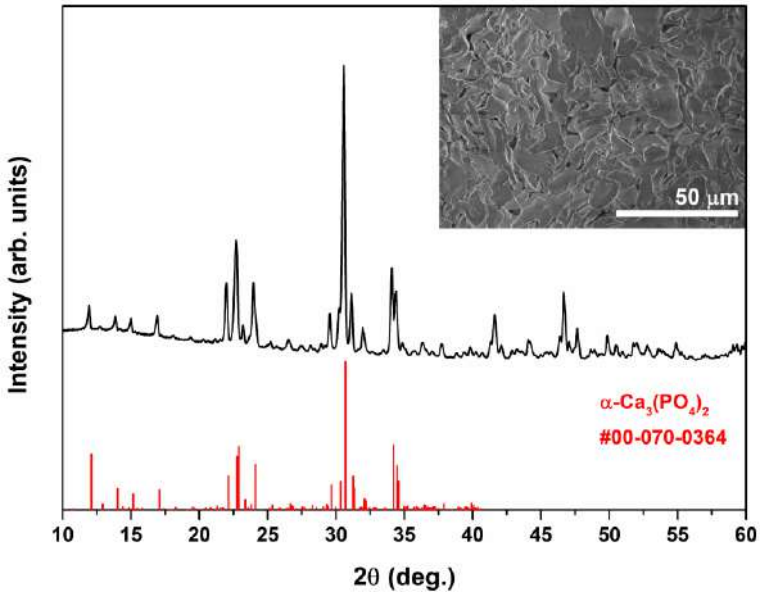

5 pav. α-TCP:Eu miltelių rentgeno spindulių difraktograma. Intarpas – α-TCP:Eu miltelių SEM nuotrauka.

Normalizuoti α-TCP:Eu miltelių PLE spektrai, registruoti ties 475 ir 610 nm emisija, pateikti 6a paveiksle. Registruojant ties λ_{em} = 475 nm, stebima plati juosta, priskirta Eu^{2+} jonų $4f^7 \rightarrow 4f^65d^1$ šuoliui. Tačiau registruojant ties λ_{em} = 610 nm, PLE spektro forma reikšmingai pasikeitė. Šie skirtumai rodo, kad Eu^{2+} jonai užima bent dvi skirtingas kristalografines pozicijas. Spektruose taip pat matomos siauros juostos, susijusios su nedideliu Eu^{3+} kiekiu, rodančiu nepilną Eu jonų redukciją.

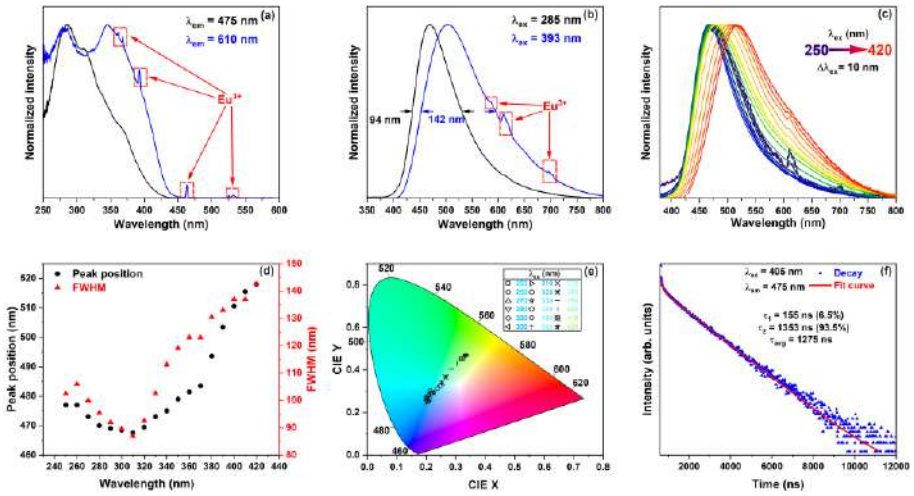

6 pav. α-TCP:Eu miltelių normalizuoti PLE spektrai (λ_{em} = 475 ir 610 nm) (a); normalizuoti PL spektrai (λ_{ex} = 285 ir 393 nm) (b); normalizuoti PL spektrai, gauti esant skirtingiems sužadinimo bangos ilgiams (c); emisijos maksimumo ir puspločio priklausomybė nuo sužadinimo bangos ilgio (d); CIE 1931 chromatiškumo koordinačių priklausomybė nuo sužadinimo bangos ilgio (e); ir gesimo kreivė (λ_{ex} = 405 nm ir λ_{em} = 475 nm) (f).

PL spektras esant 285 nm sužadinimui pasižymėjo viena plačia emisijos juosta, kurios maksimumas buvo ties 470 nm, o puspločio vertė siekė 94 nm. Ši emisija priskiriama Eu^{2+} jonams būdingam $4f^65d^1 \rightarrow 4f^7$ šuoliui (6b pav.). Emisijos spektras apėmė visą regimosios šviesos sritį, o asimetrinė emisijos juostos forma rodo Eu^{2+} jonų buvimą keliose kristalografinėse pozicijose. Mišraus valentingumo Eu aktyvuotose medžiagose emisiją galima reguliuoti keičiant sužadinimo bangos ilgį, taip kontroliuojant Eu^{2+} ir Eu^{3+} emisijų santykį. Šis efektas pasireiškia dėl Eu^{2+} ir Eu^{3+} sužadinimo spektrų persidengimo 250–450 nm srityje. Dėl šios priežasties PL spektras taip pat buvo registruotas sužadinant 393 nm bangos ilgiu. Spektre buvo stebimos Eu^{3+} jonams būdingos emisijos juostos ties ~590 nm, 610 nm ir 700 nm, tačiau spektre vis tiek dominavo plačiajuostė Eu^{2+} emisija, kurios maksimumas pasislinko į 503 nm, o puspločio vertė padidėjo iki 142 nm. Atsižvelgiant į šiuos spektrinius pokyčius, buvo ištirta emisijos spektrų priklausomybė nuo sužadinimo bangos ilgio, sistemingai keičiant λ_{ex} nuo 250 iki 420 nm kas 10 nm (6c pav.). Nustatyta, kad keičiant sužadinimo bangos ilgį galima valdyti emisijos maksimumą ir puspločio vertes (6d pav.). Didinant sužadinimo bangos ilgį nuo 250 iki 310 nm, stebėtas emisijos poslinkis į trumpesnių bangų sritį ir emisijos juostos siaurėjimas, tuo tarpu 310–420 nm intervale buvo stebėtas priešingas efektas. Esant skirtingam sužadinimui, emisijos

maksimumą pavyko pakeisti nuo 467 iki 517 nm, o puspločio vertes – nuo 87 iki 142 nm. CIE 1931 chromatiškumo koordinačių priklausomybė nuo sužadinimo bangos ilgio buvo beveik tiesinė (6e pav.) – didėjant sužadinimo bangos ilgiui nuo 310 iki 420 nm, emisijos spalva kito nuo mėlynos iki žalsvai geltonos srities. Esant tam tikroms sužadinimo sąlygoms buvo gauta artima baltai emisija, rodanti spalviškai reguliuojamos emisijos galimybę. 6f paveiksle pateikta α-TCP:Eu miltelių PL gesimo kreivė, registruota sužadinant 405 nm bangos ilgiu ir stebint emisiją ties 475 nm. Nustatytas dviejų eksponenčių gesimas su greituoju (τ = 0,16 μs) ir lėtuoju (τ = 1,35 μs) komponentais. Apskaičiuota efektyvioji PL gyvavimo trukmė (τ_{eff}) buvo lygi 1,27 μs.

Susintetintų α-$Ca_2P_2O_7$:Mn^{2+} miltelių kristališkumas ir fazinis grynumas buvo įvertinti rentgeno spindulių difrakcijos analize. α-$Ca_2P_2O_7$:Mn^{2+} miltelių, iškaitintų 1200 °C temperatūroje rentgeno spindulių difraktograma pateikta 7 paveiksle. Difrakcijos smailės gerai sutapo su α-$Ca_2P_2O_7$ standartu (PDF #073-0440), patvirtindamos sėkmingą tikslinės medžiagos susidarymą. Taip pat buvo nustatytas nedidelis gretutinės α-$Ca_3(PO_4)_2$ fazės kiekis, kuris, tikėtina, susidarė dėl fosfatinių komponentų išgaravimo.

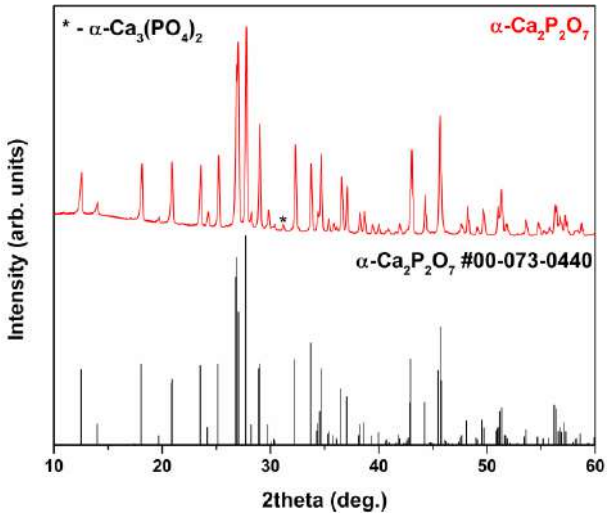

7 pav. α-$Ca_2P_2O_7$:Mn^{2+} miltelių rentgeno spindulių difraktograma.

Susintetintų miltelių morfologinės savybės buvo tirtos SEM metodu. Reprezentatyvūs α-$Ca_2P_2O_7$:Mn^{2+} mėginio SEM vaizdai, pateikti 8 paveiksle, parodė, kad miltelius sudaro plokštelinių ir netaisyklingos formos dalelių mišinys. Plokštelinės formos dalelių grūdelių dydis svyruoja nuo submikrometrinių iki mikrometrinių matmenų.

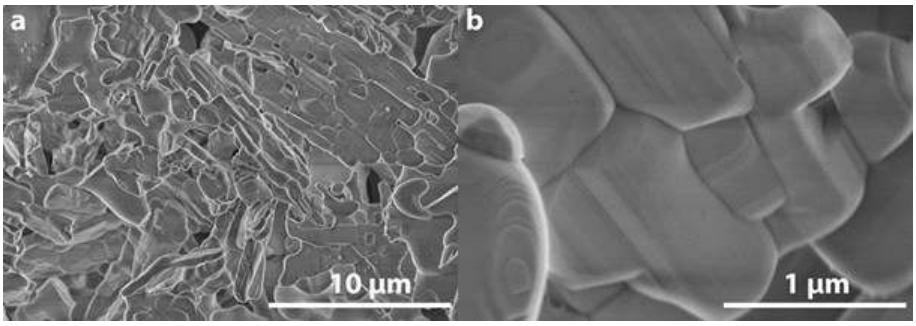

8 pav. α-$Ca_2P_2O_7$:Mn^{2+} miltelių SEM nuotraukos.

9a paveiksle pateikti α-$Ca_2P_2O_7$:Mn^{2+} fosforo emisijos spektrai, registruoti sužadinant 6,2 eV fotonais (200 nm). Kreivė 1 atitinka spektrą, išmatuotą esant 300 K temperatūrai, o kreivė 2 – spektrą, registruotą esant 77 K. Analizuojant 9 paveikslą nustatyta, kad esant 300 K temperatūrai stebima intracentrinė Mn^{2+} jonų emisijos juosta ties 2,06 eV (602 nm) (1 kreivė), kartu pasireiškiant naujoms emisijos juostoms ties 3,06 eV (405 nm) ir 2,92 eV (425 nm) (1 kreivė). Esant 77 K temperatūrai Mn^{2+} emisijos juostos intensyvumas ženkliai sumažėja, tuo tarpu naujai stebimų emisijos juostų intensyvumas padidėja maždaug 1,5 karto. 9b paveiksle pateiktas pagrindinės Mn^{2+} intracentrinės emisijos juostos ties 2,06 eV (602 nm) žadinimo spektras, registruotas esant 300 K (1 kreivė) ir 77 K (2 kreivė) temperatūroms. Spektrų analizė parodė sužadinimo juostas ties 2,5 eV (496 nm), 3,0 eV (413 nm), 3,5 eV (354 nm), 4,0 eV (310 nm), 4,5 eV (275 nm) bei 5,0–6,2 eV srityje. Esant 300 K temperatūrai šios žadinimo juostos taip pat stebimos, tačiau jų intensyvumas yra mažesnis, ypač 4,0–4,5 eV (310–275 nm) srityje. 9c paveiksle pateikti naujai nustatytų emisijos juostų ties 3,06 eV (405 nm) ir 2,92 eV (425 nm) žadinimo spektrai po preliminaraus fosforo apšvitinimo 6,2 eV (200 nm) energijos fotonais, registruoti esant 300 K ir 77 K temperatūroms. Žadinimo juostos nustatytos 3,94–4,0 eV (310–314 nm), 4,5–4,6 eV (269–275 nm) bei plačioje 5,5–6,2 eV (225–200 nm) srityje. Pastebėta, kad šios juostos ypač ryškios esant 77 K temperatūrai, kas rodo stipresnį atsaką į sužadinimą žemoje temperatūroje. Tuo tarpu esant 300 K temperatūrai tos pačios juostos pasireiškia gerokai silpniau, rodydamos sumažėjusį žadinimo efektyvumą aukštesnėje temperatūroje.

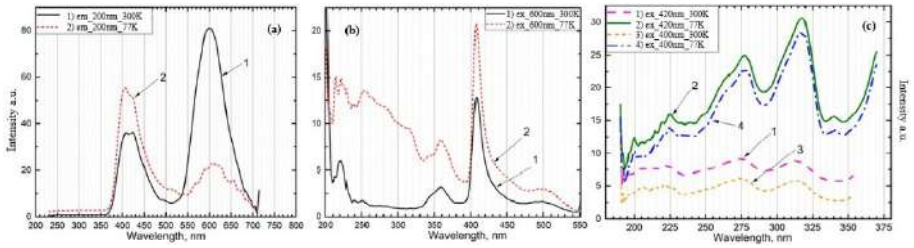

9 pav. α-$Ca_2P_2O_7$:Mn^{2+} fosforo emisijos spektrai, žadinant 6,2 eV (200 nm) fotonais (1 – esant 300 K, 2 – esant 77 K) (a); intracentrinės emisijos sužadinimo spektrai 2,06 eV (602 nm) juostai apšvitintame α-$Ca_2P_2O_7$:Mn^{2+} mėginyje (1 – esant 300 K, 2 – esant 77 K) (b); iš anksto apšvitinto fosforo sužadinimo spektrai: 1 – emisijos juostai ties 2,92 eV (425 nm) esant 300 K; 2 – emisijos juostai ties 2,92 eV (425 nm) esant 77 K; 3 – emisijos juostai ties 3,06 eV (405 nm) esant 300 K; 4 – emisijos juostai ties 3,06 eV (405 nm) esant 77 K (c).

IŠVADOS

1. Detaliai ištirtas amorfinio kalcio fosfato (ACP) fazinių virsmų procesas įvairiuose lydytuose chloriduose. Nustatyta, kad pagrindiniai veiksniai, lemiantys produktų fazinį grynumą ir morfologines savybes, yra lydalų cheminė sudėtis, reakcijos temperatūra bei ACP ir fliuso santykis. Parodyta, kad, keičiant KCl–$CaCl_2$ druskų sudėtį, galima vykdyti faziškai selektyvią vienfazių $Ca_5(PO_4)_3Cl$ arba Ca_2PO_4Cl junginių sintezę. KCl turtingi lydalai skatino $Ca_5(PO_4)_3Cl$ susidarymą, tuo tarpu Ca turtingi lydalai lėmė Ca_2PO_4Cl fazės formavimąsi. Taip pat nustatyta, kad $Ca_5(PO_4)_3Cl$ miltelių morfologiją galima valdyti keičiant KCl/$CaCl_2$ santykį lydale. $CaCl_2$ turtingi lydalai skatino anizotropinį $Ca_5(PO_4)_3Cl$ kristalų augimą, dėl kurio susiformavo monodispersiniai heksagoninės formos mikrostypeliai. Nors anizotropinis augimas buvo stebimas santykinai žemoje temperatūroje (750 °C), reakcijos temperatūrą padidinus iki 1200 °C šis efektas ženkliai sumažėjo.
2. Cr^{3+} jonais aktyvuoto β-TCP milteliai buvo sėkmingai susintetinti taikant nusodinimo metodą ir tolesnį aukštatemperatūrinį apdorojimą. Nustatyta, kad Cr^{3+} jonų tirpumas β-TCP kristalinėje struktūroje yra ribotas. Vienfazės medžiagos buvo gautos esant iki 2 mol% aktyvatoriaus koncentracijai, tuo tarpu, esant 5 mol% koncentracijai, buvo aptikta antrinė Cr_2O_3 fazė. EPR spektroskopijos tyrimai atskleidė kelis su Cr^{3+} susijusius centrus, kurie, tikėtina, susidaro toje pačioje kristalografinėje pozicijoje, tačiau turėjo skirtingas defektų aplinkas. Visi Cr^{3+} aktyvuoti β-TCP junginiai

pasižymėjo plačiajuoste emisija, kurios maksimumas buvo ties 760 nm. Didžiausias emisijos intensyvumas nustatytas 0,1 mol% Cr^{3+} mėginiui, greičiausiai dėl koncentracinio gesinimo esant didesnėms Cr^{3+} koncentracijoms.

3. Eu^{2+} jonais aktyvuotas α-TCP buvo sėkmingai susintetintas vykstant Eu^{3+} aktyvuoto DCPD faziniam virsmui. Fazinis virsmas, lydimas Eu^{3+} saviredukcijos iki Eu^{2+}, buvo įgyvendintas pradinę medžiagą atkaitinant vakuume 1300 °C temperatūroje. DCPD būdingas pradinis Ca/P santykis 1 : 1 pakito iki maždaug 1,5 : 1 dėl selektyvaus fosfatinių komponentų išgaravimo. Gautoji medžiaga pasižymėjo plačiajuoste emisija, apimančia visą regimąjį spektrą. Emisiją galima buvo modifikuoti naudojant skirtingus sužadinimo bangos ilgius; dėl ko kito emisijos maksimumo padėtis ir puspločio (FWHM) vertės, kurios kambario temperatūroje siekė nuo 87 iki 142 nm. Plačiajuostė emisija pasireiškė dėl Eu^{2+} jonų buvimo keliose kristalografinėse pozicijose sudėtingoje α-TCP gardelėje. Emisijos spektrų dekonvoliucija parodė, kad Eu^{2+} jonai užima bent tris nelygiavertes kristalografines pozicijas. Pasirinktas sintezės metodas, leidęs pasiekti didelį Eu^{2+} jonų redukcijos laipsnį ir jų pasiskirstymą keliose kristalografinėse pozicijose α-TCP struktūroje, atveria naujas galimybes spalviškai derinamų plačiajuosčių fosforų kūrimui.

4. 1 mol% Mn^{2+} aktyvuoti $Ca_2P_2O_7$ milteliai buvo sėkmingai susintetinti taikant nusodinimo metodą ir tolesnį aukštatemperatūrinį apdorojimą. Naudojant termoaktyvacijos ir vakuuminės ultravioletinės spektroskopijos metodus apšvitintuose $Ca_2P_2O_7$:Mn^{2+} bei nelegiruotuose $Ca_2P_2O_7$ mėginiuose, ištirti sukeltų vidinių ir priemaišinių spinduliuojančių būsenų, sudarytų iš vidinių ir priemaišinių elektronų–skylių kaupimo centrų, formavimosi mechanizmai. Apšvitintuose $Ca_2P_2O_7$:Mn^{2+} fosforuose nustatytos naujos indukuotos emisijos ties 2,95 eV (420 nm) ir 3,1 eV (400 nm). Šios naujos spinduliuojančios būsenos susidaro dėl krūvio pernašos iš $(P_2O_7)^{4-}$ jonų į Mn^{2+} priemaišinius centrus.

CURRICULUM VITAE

PERSONAL INFORMATION	
Name, Surname: E-mail:	Sapargali Pazylbek

EDUCATION	
1998 – 2002	Bachelor of Physics, E. Buketov Karaganda State University, Karaganda (Kazakhstan)
2002 – 2004	Master of Physics, E. Buketov Karaganda State University, Karaganda
2022 – 2026	PhD studies in Chemistry, Vilnius University

WORK EXPERIENCE	
2006 – 2010	A. Yassawi International Kazakh-Turkish University, Faculty of Natural Sciences, Turkestan, Junior Assistant.
2010 – 2011	The Institute of Nuclear Physics (INP), Almaty, Junior Researcher.
2011 – 2017	L.N. Gumilyov Eurasian National University, Astana, Assistant and Senior Assistant.
2017 – 2022	South Kazakhstan State Pedagogical University, Shymkent, Senior Assistant.

NOTEWORTHY AWARDS	
2022 February – 2022 September	The Scholarship of the President of the Republic of Kazakhstan “Bolashak”, Researcher, Department of Inorganic Chemistry, Vilnius University, Vilnius.
2018 September – 2018 December	Latvian state research scholarship, Researcher, Institute of Solid State Physics, University of Latvia, Riga.
2018 June – 2018 June	Training courses "Computer added desing in microelectronics", "Nanocoating and nanostructures", Technical University of Sofia, Sofia.

2013 November – 2014 April	The Laboratory of Physics of Ionic Crystals, Researcher, Institute of Physics, University of Tartu, Tartu.
2012 September – 2013 June	The "DoRa5" Scholarship, Insitute of Physics, University of Tartu, Tartu.
2012 April – 2014 June	The "DoRa5" Scholarship, Insitute of Physics, University of Tartu, Tartu.
2009 September – 2010 July	Internship as a researcher at the “Radiation Materials Science” Laboratory of the Institute of Nuclear Physics, National Nuclear Center of the Republic of Kazakhstan.

ACKNOWLEDGEMENTS

First and foremost, I would like to express my sincere gratitude to my scientific supervisor, Professor Dr. Aleksej Žarkov, for his invaluable guidance, fruitful scientific discussions, continuous support, and assistance throughout the preparation of this dissertation. His expertise, encouragement, and constructive advice have greatly contributed to the successful completion of this work.

I would also like to extend my deepest appreciation to Academician of the Lithuanian Academy of Sciences, Professor Aivaras Kareiva, for providing me with the opportunity to conduct my research, as well as for his valuable recommendations, support, and encouragement during my scientific journey.

Furthermore, I am sincerely grateful to all the colleagues and friends who participated in my research activities and helped create a friendly, inspiring, and welcoming working environment. In particular, I would like to thank Professor Dr. A. Katelnikovas, Assoc. Prof. Dr. I. Grigoravičiūtė, Professor Dr. A. Antuzevics, Dr. D. Karoblis, Professor N.Nurakhmetov, D. Griesiute, J. Stadulis, Dr. A. Prichodko, D. Vistorskaja, M. Elsheikh, O. Shalkhar, and A. Dastan for their cooperation, insightful discussions, constructive comments, and contributions that helped improve the quality of my research.

I am deeply thankful to everyone whose collaboration, understanding, advice, and support have been an important part of this work and my professional development.

Finally, I would like to express my heartfelt gratitude to my family for their unconditional love, patience, encouragement, and unwavering support throughout my academic journey.

This experience has opened a new scientific path for me, providing opportunities to develop new ideas, establish valuable collaborations, and build lasting friendships. I am truly grateful to all of you for being part of this remarkable journey.

Thank you all very much.

LIST OF PUBLICATIONS

Articles in journals indexed in Claritive Analytics Web of Science database included in the dissertation:

1. **S. Pazylbek**, J. Stadulis, G. Doke, A. Antuzevics, V. Pankratov, G. Merkininkaite, A. Katelnikovas, A. Zarkov, Tunable broadband visible emission achieved by phase transformation-driven self-reduction of Eu^{3+} to Eu^{2+} in a calcium phosphate matrix, *Dalton Transactions* 54(21) **(2025)** 8625-8634.
2. **S. Pazylbek**, J. Stadulis, G. Doke, A. Antuzevics, M. Sandomierski, A. Katelnikovas, C.-Y. Su, H.-W. Fang, A. Zarkov, Luminescent properties of near-infrared-emitting Cr^{3+}-activated beta-$Ca_3(PO_4)_2$, *Optical Materials* 159 **(2025)** 116569.
3. T.N. Nurakhmetov, T.T. Alibay, K.B. Zhangylyssov, A.S. Nurpeissov, **S. Pazylbek**, D. Griesiute, A. Zarkov, A. Kareiva, Luminescence and Electron–Hole-Trapping Centers in α-$Ca_2P_2O_7$-Mn, *Crystals* 14(5) **(2024)** 406.
4. E. Kabasinskas, D. Karoblis, D. Griesiute, E. Raudonyte-Svirbutaviciene, **S. Pazylbek**, R. Lemezis, V. Klimavicius, A. Kareiva, A. Zarkov, Synthesis and morphological control of $Ca_5(PO_4)_3Cl$ and Ca_2PO_4Cl via the phase transformation of amorphous calcium phosphate in molten chlorides, *Ceramics International* 50(10) **(2024)** 16844-16851.

PRESENTATIONS AT CONFERENCES

1. A. Zarkov, S. Bendziute, P. Pazerauskaite, J. Stadulis, **S. Pazylbek**, A. Katelnikovas. Preparation of Eu^{2+}-doped alkaline-earth metal phosphates in air atmosphere. The XIXth Conference of the European Ceramic Society, Aug 31, 2025 – Sep 4, 2025, Dresden, Germany.
2. **S. Pazylbek**, S. Bendziute, J. Stadulis, L. Valeikiene, V. Lisyte, A. Antuzevics, G. Doke, G. Krieke, A. Katelnikovas, A. Zarkov. Tunable Broadband Visible Emission Achieved by Phase Transformation-Driven Self-Reduction of Eu^{3+} to Eu^{2+} in a Calcium Phosphate Matrix. Advanced materials and technologies, 25-29 August 2025, Palanga, Lithuania.
3. A. Zarkov, **S. Pazylbek**, A. Antuzevics, G. Merkininkaite, A. Katelnikovas, A. Kareiva. Phase transformation-driven self-reduction of Eu^{3+} to Eu^{2+} in calcium phosphate matrix, E-MRS 2024 SPRING MEETING, Strasbourg (France), 2024 May 27-31, #00513.
4. E. Kabašinskas, **S. Pazylbek**, V. Klimavičius, D. Griesiūtė, E. Raudonytė-Svirbutavičienė, V. Lisytė, L. Valeikienė, D. Karoblis, A. Žarkov. Synthesis of $Ca_5(PO_4)_3Cl$ microrods via the phase transformation of amorphous calcium phosphate in molten chlorides. ISIPM-11 and FLM2023: 11th International symposium on inorganic phosphate materials, International workshop on forward-looking materials, Venice, Italy, November 22-24, 2023.

1st publication

Synthesis and morphological control of $Ca_5(PO_4)_3Cl$ and Ca_2PO_4Cl via the phase transformation of amorphous calcium phosphate in molten chlorides

E. Kabasinskas, D. Karoblis, D. Griesiute, E. Raudonyte-Svirbutaviciene, **S. Pazylbek**, R. Lemezis, V. Klimavicius, A. Kareiva, A. Zarkov

Ceramics International 50(10) **(2024)** 16844-16851
(https://doi.org/10.1016/j.ceramint.2024.02.157)

Ceramics International 50 (2024) 16844–16851

Contents lists available at ScienceDirect

Ceramics International

journal homepage: www.elsevier.com/locate/ceramint

Synthesis and morphological control of $Ca_5(PO_4)_3Cl$ and Ca_2PO_4Cl *via* the phase transformation of amorphous calcium phosphate in molten chlorides

Erlandas Kabasinskas [a], Dovydas Karoblis [a], Diana Griesiute [a], Eva Raudonyte-Svirbutaviciene [a], Sapargali Pazylbek [a], Rokas Lemezis [b], Vytautas Klimavicius [b], Aivaras Kareiva [a], Aleksej Zarkov [a,*]

[a] Institute of Chemistry, Vilnius University, Naugarduko 24, LT-03225, Vilnius, Lithuania
[b] Institute of Chemical Physics, Vilnius University, Sauletekio 3, LT-10257, Vilnius, Lithuania

ARTICLE INFO

Handling Editor: Dr P. Vincenzini

Keywords:
$Ca_5(PO_4)_3Cl$
Ca_2PO_4Cl
Molten salts
Phase transformation
Amorphous calcium phosphate
Morphology control

ABSTRACT

In the present work, the phase conversion of amorphous calcium phosphate (ACP) in different molten chlorides (LiCl, NaCl, KCl, $CaCl_2$) was investigated in detail. The main synthesis parameters influencing the phase purity and morphological features of the products include the chemical composition of molten salts, the heat treatment temperature and the ACP-to-flux ratio. The selective synthesis of single-phase $Ca_5(PO_4)_3Cl$ or Ca_2PO_4Cl depends on the content of $CaCl_2$ in the reaction medium. The morphology control of $Ca_5(PO_4)_3Cl$ powders was achieved by varying the KCl/$CaCl_2$ ratio in the flux, resulting in the formation of the particles of different size and shape. The KCl-rich fluxes led to the formation of relatively small nearly spherical particles, whereas the $CaCl_2$-rich fluxes promoted an anisotropic growth of the $Ca_5(PO_4)_3Cl$ crystals resulting in the formation of monodispersed hexagonally-shaped microrods. Whereas the anisotropic growth was observed at relatively low temperature (750 °C) the increase of the reaction temperature up to 1200 °C significantly reduced this effect leading to the formation of the particles with obviously low aspect ratio. The phase crystallinity and purity were analyzed using powder X-ray diffraction, FTIR spectroscopy as well as ^{31}P, ^{35}Cl and ^{1}H solid-state NMR. The morphological features and chemical composition of the synthesized products were studied by SEM/EDX analysis.

1. Introduction

Calcium phosphates (CPs) are a family of materials, which are widely used for various applications including medicine and bone regeneration [1], catalysis [2], sorption of heavy metals and organic pollutants [3], development of optical materials [4] and many others [5]. CPs can be classified by many parameters including the crystal structure, the Ca-to-P ratio, and the presence of other structural species (e.g. OH^-, CO_3^{2-}, Cl^-, F^-) [6]. Compositional and structural features of CPs lead to their different chemical and physical properties [7]. Taking into account the variety of CPs phases, some specific synthetic approaches are required for the selective synthesis of particular compounds.

There is a plenty of synthetic approaches employed for the synthesis of various CPs [8]. While some CPs can be easily synthesized by a direct precipitation from aqueous solutions or solid-state reaction, some metastable phases can be obtained only through the phase transformation processes from the less thermodynamically stable CPs [9]. Basically, the phase transformation approach includes two routes: (I) dry thermally induced phase transformations at elevated temperatures and (II) phase conversions in aqueous media. While during the (I) process some volatile species (H_2O, CO_2) can be removed from the initial CP; the bulk Ca/P ratio is expected to be constant, which is not the case only for some specific conditions [10,11]. For example, this route can be used to produce low-temperature γ-$Ca_2P_2O_7$ polymorph from $CaHPO_4 \bullet 2H_2O$ [12]. Upon annealing water is removed from the starting material and a sequence of phase transformations can be observed by increasing the temperature: $CaHPO_4 \bullet 2H_2O \rightarrow CaHPO_4 \rightarrow$ γ-$Ca_2P_2O_7 \rightarrow$ β-$Ca_2P_2O_7 \rightarrow$ α-$Ca_2P_2O_7$. Another commonly employed example is a conversion of calcium-deficient hydroxyapatite (CDHA, $Ca_9(HPO_4)(PO_4)_5OH$, Ca/P = 1.5) to tricalcium phosphate (TCP, $Ca_3(PO_4)_2$) [13].

In the case of phase transformations in aqueous medium, the chemical composition of starting CP can be modified, some functional groups can be attached or lost. The variation in the Ca/P ratio between the starting material and product is also possible due to the dissolution-

* Corresponding author.
E-mail address: aleksej.zarkov@chf.vu.lt (A. Zarkov).

https://doi.org/10.1016/j.ceramint.2024.02.157
Received 27 December 2023; Received in revised form 10 February 2024; Accepted 12 February 2024
Available online 13 February 2024
0272-8842/© 2024 Elsevier Ltd and Techna Group S.r.l. All rights reserved.

precipitation process [14]. One of the representative examples is the transformation of α-TCP to CDHA [15,16].

Remarkable member of the CPs family is amorphous CP (ACP), which is metastable and highly reactive due to its non-crystalline nature [17]. Consequently, ACP can be used as a precursor for the synthesis of other phosphate-based materials. Thermally induced crystallization of ACP with the Ca/P ratio of 1.5:1 is well documented in literature; depending on the annealing temperature it can be converted to α- or β-TCP [18,19]. The phase transformations of ACP in aqueous medium are broadly studied as well. As a result of the dissolution-precipitation reaction it usually transforms to CDHA [20,21]; however, the presence of other ions can considerably change the reaction pathway [3]. Nevertheless, to the best of our knowledge, some aspects of the phase conversions of ACP are still unexplored. For example, the phase transformations of ACP in molten salts or hydroxides. At the same time, molten salt route is well known for its ability to stabilize some metastable phases and to produce the materials at reduced temperature, when compared to the conventional solid-state reaction [22]. Thus, this synthetic approach can result in the formation of unexpected phases with specific morphological features, which could be an important aspect for some applications [23,24].

Calcium chlorapatite (ClAp, $Ca_5(PO_4)_3Cl$) and goryainovite (Ca_2PO_4Cl) are calcium halophosphate minerals occurring in nature [25,26]. Synthetic ClAp found its practical application in purification of water and sediments from heavy metals [27,28], lanthanide-doped ClAp was investigated in terms of optical properties [29–32]. Ca_2PO_4Cl is less studied material, most of the papers are focused on the preparation and investigation of optical properties in lanthanide-doped Ca_2PO_4Cl [33–35]. While for the synthesis of ClAp both wet chemical methods and solid-state reaction can be employed [31,32], the preparation of Ca_2PO_4Cl is most commonly performed by solid-state reaction route [33–35].

The present work is aimed to investigate the phase transformations of ACP in different molten chlorides. The influence of the flux chemical composition, reaction time, temperature, and ACP-to-flux ratio was investigated in detail. Single-phase $Ca_5(PO_4)_3Cl$ and Ca_2PO_4Cl were selectively synthesized under specific conditions. The morphological control of ClAp was achieved by the variation of the composition of molten salts, the reaction temperature and ACP-to-flux ratio.

2. Materials and methods

2.1. Synthesis

Initial ACP powder (Ca/P = 1.5) was synthesized according to the previously reported procedure [18] using calcium nitrate tetrahydrate ($Ca(NO_3)_2{\cdot}4H_2O$, ≥99%, Roth) and diammonium hydrogen phosphate ($(NH_4)_2HPO_4$, ≥98%, Roth) as starting materials. Briefly, an appropriate amount of $(NH_4)_2HPO_4$ was dissolved in deionized water to obtain a 0.5 M solution, to which a concentrated ammonia solution (NH_4OH, 25%, Roth) was added under a constant mixing to adjust the pH value to 10. Next, an aqueous 0.75 M solution of calcium nitrate was rapidly added to the above mixture, resulting in the formation of white precipitates. The obtained precipitates were aged in the reaction mixture for 10 min, vacuum filtered, washed with deionized water and isopropanol, and dried at 50 °C overnight.

Lithium chloride (LiCl, ≥98.5%, Roth), sodium chloride (NaCl, >99.8%, Roth), potassium chloride (KCl, >99%, Roth) and calcium chloride ($CaCl_2$, ≥94%, Roth) were used for the molten salt synthesis. For the reactions in molten salts, the as-prepared ACP was mixed with an appropriate amount of selected salts in an agate mortar, transferred into an alumina crucible and annealed in a muffle furnace at certain temperature for different periods of time. The temperature, annealing time and ACP-to-flux weight ratio were chosen individually for different experiments. After the reaction, the obtained products were washed with a hot deionized water in order to remove the salts. The residual products were dried in an oven at 100 °C.

2.2. Characterization

The powder X-ray diffraction (XRD) analysis of the synthesized powders was performed using a Rigaku MiniFlex II diffractometer ($Cu\text{-}K_\alpha$, λ = 1.5419 Å) working in the Bragg–Brentano (θ/2θ) geometry. The data were collected within the 10–60° 2θ angle range with a speed of 5° min^{-1}. Fourier-transform infrared (FTIR) spectra were obtained in the range of 4000–400 cm^{-1} with a Bruker ALPHA-FTIR spectrometer. The morphology and elemental composition of synthesized specimens was analyzed by scanning electron microscopy (SEM) using a Hitachi SU-70 microscope equipped with energy-dispersive X-ray spectrometer (EDS). Solid-state nuclear magnetic resonance (NMR) experiments were carried out at 9.4 T on a Bruker Avance III HD 400 NMR spectrometer operating at 400.2, 162.0, 39.2 MHz for ^{1}H, ^{31}P and ^{35}Cl, respectively, using a 4 mm double resonance CP MAS probe. The temperature was stabilized at 298 K and 10 kHz MAS was used. For ^{31}P MAS measurements a saturation recovery pulse sequence was employed using saturation pulse train of 20 π/2 pulses followed by 500 s delay. The π/2 excitation pulse was equal to 2.5 μs and 64 scans were accumulated. For ^{1}H MAS measurements pulse sequence with background suppression was used, 128 scans were accumulated, relexation delay was set to 10s. For the ^{35}Cl measurements Hahn-echo pulse sequence was employed using one rotor period as echo delay, 51200 scans were accumulated and 1 s recycle delay was used. Spectra were referenced using ADP (ammonium dihydrogen phosphate, $NH_4H_2PO_4$, δ (^{31}P) = 0.8 ppm), Adamantane ($C_{10}H_{16}$, δ (^{31}P) = 1.85 ppm), sodium chloride (NaCl, δ (^{35}Cl) = 0 ppm) as external standards. Prior to measurements all samples were dried in vacuum ($2\bullet10^{-2}$ mbar) for at least 24 h.

3. Results and discussion

The XRD pattern and SEM image of starting ACP powder are shown in Figs. S1–2. As seen, the XRD pattern does not exhibit any sharp diffraction peaks confirming an amorphous nature of the material. The only observed signal is a broad peak centered at around 30°, which is characteristic of ACP [36]. The SEM image clearly shows that ACP consists of nanosized nearly spherical particles.

Fig. 1 demonstrates the XRD patterns of the synthesis products obtained after the treatment of ACP in different salts.

The difference in the treatment temperature is associated with the melting point of the selected salts. It is seen that the phase composition of the products strongly depends on the nature of chloride salt and the

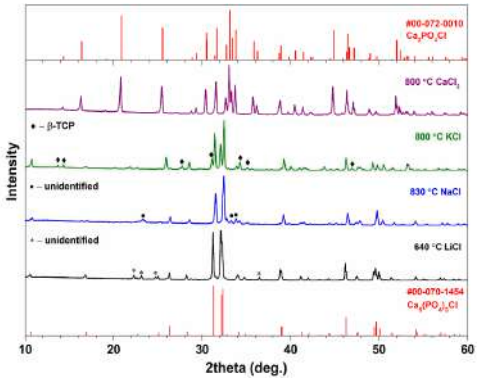

Fig. 1. XRD patterns of the synthesis products obtained after the treatment of ACP in different molten salts (t = 5 h, ACP/flux = 1:2).

treatment temperature. In the case of LiCl and NaCl, the main observed crystalline phase was ClAp; however, the secondary unidentified phase was also detected. The reason of the formation of the secondary phase could be the difference in the Ca/P ratio in starting ACP powders and ClAp. In the former the Ca/P ratio is 1.5:1, while in the latter this ratio is 1.67:1. It can be also concluded that Li and Na cations from the salts do not enter the ClAp structure in significant amount to compensate the charge for the formation of single-phase material. Interestingly, in the case of KCl the obtained product was a mixture of ClAp and β-TCP. The crystal structure of the latter does not contain Cl^- ions, its formation is expected as a result of thermally induced crystallization of ACP (without the presence of molten salts) [36]. Finally, when $CaCl_2$ was used, the resulting product was identified as a single-phase Ca_2PO_4Cl.

In order to check the influence of the presence of Ca ions in the used molten salts, three different mixtures were used as the synthesis media, namely LiCl–$CaCl_2$, NaCl–$CaCl_2$ and KCl–$CaCl_2$. Synthesis temperature and molar composition of the mixtures was chosen based on the eutectic points of the selected mixtures being around 473 °C, 504 °C and 596 °C for 0.65LiCl-0.35$CaCl_2$, 0.48NaCl-0.52$CaCl_2$ and 0.75KCl-0.25$CaCl_2$, respectively. It is worth noting that such a selection of eutectic mixtures leads to the lowest melting temperature; however, the percentage of $CaCl_2$ in these mixtures is different. The XRD patterns of the resulting products are shown in Fig. 2.

Both LiCl–$CaCl_2$ and NaCl–$CaCl_2$ resulted in the formation of phase-pure Ca_2PO_4Cl. All the observed diffraction peaks can be indexed using the standard data of orthorhombic Ca_2PO_4Cl (#00-072-0010); however, the intensity ratio between the peaks in two patterns differs significantly suggesting the formation of the particles of different shape or size. By contrast, after the treatment in KCl–$CaCl_2$, a single-phase ClAp was obtained. ClAp can possess 2 crystal structures: hexagonal with a space group $P6_3/m$ and pseudohexagonal with monoclinic space group $P2_1/b$ [37]. Both these structures are very similar with the main difference in the placement of the halogen ions. In our case all diffraction peaks match very well with the standard XRD data of monoclinic ClAp (#00-070-1454). The formation of phase-pure product confirms the hypothesis that impurity phase observed using a single-salt flux (Fig. 1) is caused by the mismatch of the Ca/P ratio in ACP and ClAp. The addition of $CaCl_2$ compensates the lack of Ca ions serving as a source during the crystallization process. It is worth to note that using only KCl as a flux (Fig. 1) resulted in the formation of hexagonal ClAp (#00-073-1728), which suggests that the formation of particular ClAp polymorph is influenced by the chemical composition of molten salts.

Further experiments were carried out with the KCl–$CaCl_2$ mixture. In order to investigate the influence of chemical composition of the molten salt on the phase purity and morphology of the product, a series of reactions was performed using a fixed amount of ACP and varying ratio of KCl and $CaCl_2$. The XRD patterns of the obtained products are depicted in Fig. 3. Evidently, the composition of the molten salts strongly influenced the crystal structure of the product. Single-phase ClAp was obtained from the K-rich mixtures down to the KCl/$CaCl_2$ ratio of 6:4. It is also seen that increasing $CaCl_2$ content obviously changes the intensity ratio of the diffraction peaks. The XRD patterns of the samples obtained from the fluxes with high Ca content (30 and 40 mol%) are obviously dominated by the diffraction peak centered at ca. 32.2°. Such a behavior suggests an anisotropic growth of ClAp particles, resulting in the appearance of preferred orientation observed in the XRD patterns. When the KCl/$CaCl_2$ ratio reached 5:5, the major phase in the obtained product was still ClAp; however, neighboring Ca_2PO_4Cl phase was also observed indicating the formation of biphasic product. With higher amount of $CaCl_2$, exclusively Ca_2PO_4Cl was formed; there were no even traces of other crystalline phases. All the observed XRD patterns of single-phase Ca_2PO_4Cl possessed preferred orientation with an expressed diffraction peaks corresponding to (002) and (004) planes.

FTIR spectra of the obtained series were recorded in order to supplement the results of XRD analysis. The spectral region in the range from 1500 to 400 cm^{-1} is given in Fig. 4 as representative for the phosphate-related absorption bands. There were no bands associated with phosphate vibrations in the rest region up to 4000 cm^{-1}.

The spectra of the samples prepared in K-rich media (KCl/$CaCl_2$ ratio from 9:1 to 6:4) exhibit few absorption bands. The absorption bands located in the range from approximately 1130 to 930 cm^{-1} correspond to asymmetric stretching mode (ν_3) and symmetric stretching mode (ν_1) of the P–O bonds in PO_4 tetrahedra. The bands observed in the region from 630 to 530 cm^{-1} and the band centered at 473 cm^{-1} are ascribed to the ν_4 and ν_2 bending modes of the O–P–O bonds of the phosphate group, respectively [38]. The FTIR spectrum of the sample obtained from the

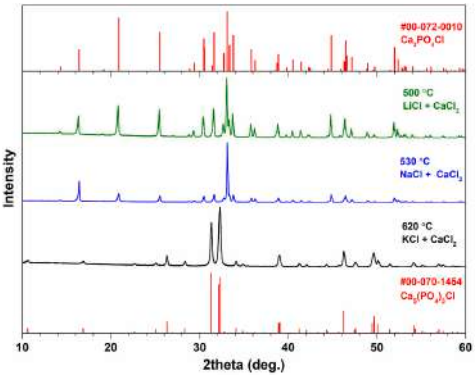

Fig. 2. XRD patterns of the synthesis products obtained after the treatment of ACP in the mixtures of different molten salts (t = 5 h, ACP/flux = 1:2).

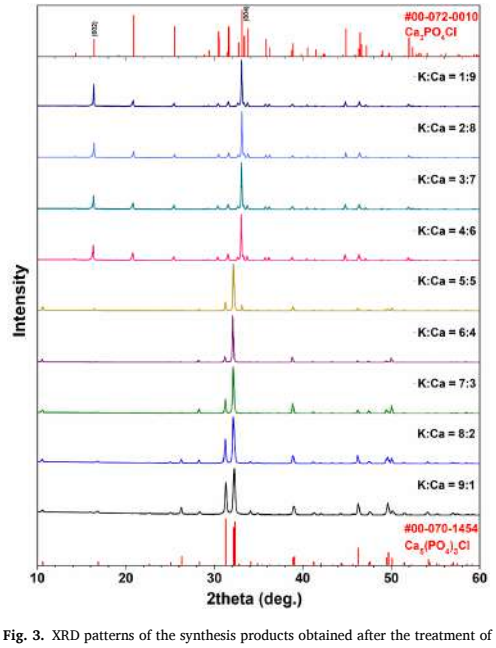

Fig. 3. XRD patterns of the synthesis products obtained after the treatment of ACP in the mixtures of KCl and $CaCl_2$ mixed in different molar proportions (T = 750 °C, ACP/flux = 1:2, t = 5 h).

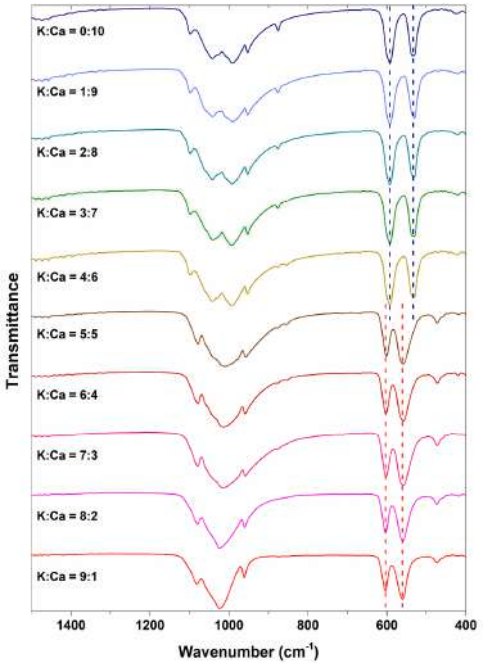

Fig. 4. FTIR spectra of the synthesis products obtained after the treatment of ACP in the mixtures of KCl and $CaCl_2$ mixed in different molar proportions (T = 750 °C, ACP/flux = 1:2, t = 5 h).

KCl–$CaCl_2$ = 5:5 exhibit the same shape as observed for the single-phase ClAp confirming that ClAp is the major phase. Obvious change in the positions and the shape of absorption bands is seen, when powders synthesized in Ca-rich media ($CaCl_2$ percentage from 60 mol% and higher). The absorption bands corresponding to the ν_4 mode are obviously shifted to lower wavenumber region; while the band ascribed to the ν_2 mode in ClAp disappeared. The shape of the Ca_2PO_4Cl spectrum matches well with that of previously reported in the literature [39]. The band centered at ca. 875 cm^{-1} is most probably indicates the presence of carbonates [40]. A closer look also allows to see the bands representing the C–O bonds of carbonate groups at ca. 1485 cm^{-1} (Fig. S3). The amount of carbonates is associated with the presence of $CaCl_2$ in the flux. Increasing the percentage of $CaCl_2$ in the KCl–$CaCl_2$ mixture led to the increase of the amount of carbonates in the obtained product.

The SEM images of the samples obtained in the KCl–$CaCl_2$ mixtures of different compositions are shown in Fig. 5.

Evidently, the composition of the synthesis medium strongly influences the morphology of the products both in terms of size and shape of the particles. ClAp obtained in the mixtures with KCl/$CaCl_2$ ratio of 9:1 and 8:2 consisted mostly of agglomerated sub-micrometer particles possessing a nearly spherical shape; however, a closer look reveals the presence of the particles of polygonal rod-like shape. Increasing the $CaCl_2$ percentage up to 30 mol% resulted in the drastic change in the morphology. Resulting polydisperse powders consisted of hexagonal rods of micrometric dimensions covered by smaller particles. The KCl/$CaCl_2$ ratio of 6:4 resulted in the reduced number of small particles; the obtained rod-like particles were more uniform. Further increase in $CaCl_2$ fraction up to 50% led to the obvious change in the aspect ratio of the rods due to the reduction of the length. The products obtained in the Ca-rich mixtures exhibited different morphology consisting of the square prism-like particles of micrometric dimensions. This correlates well with the phase transformation from ClAp to Ca_2PO_4Cl (see Fig. 3). It can be concluded that the presence of $CaCl_2$ in the flux promotes the crystal growth of ClAp significantly; moreover, it facilitates the anisotropic growth along the *c*-axis, resulting in the formation of hexagonally-shaped rods. However, the influence of this parameter is limited due to the formation of Ca_2PO_4Cl in $CaCl_2$-rich fluxes. At the same time, the crystals of Ca_2PO_4Cl do not tend to grow anisotropically, which probably associated with the peculiarities of their crystal structure.

The selected powders synthesized using different KCl/$CaCl_2$ ratios were also analyzed by solid state NMR; the corresponding spectra are shown in Fig. 6.

The ^{31}P MAS NMR data (Fig. 6a and b) show the formation of pure Ca_2PO_4Cl phase in KCl/$CaCl_2$ mixtures with the ratios of 4:6 and 1:9, namely the single peak centered at 1.7 ppm is detected. The samples obtained in KCl-rich media (KCl/$CaCl_2$ ratios of 9:1 and 6:4) feature the main peak at 1.8 ppm which is attributed to ClAp phase [41], the additional peak at around 3.0 ppm observed for the KCl/$CaCl_2$ = 9:1

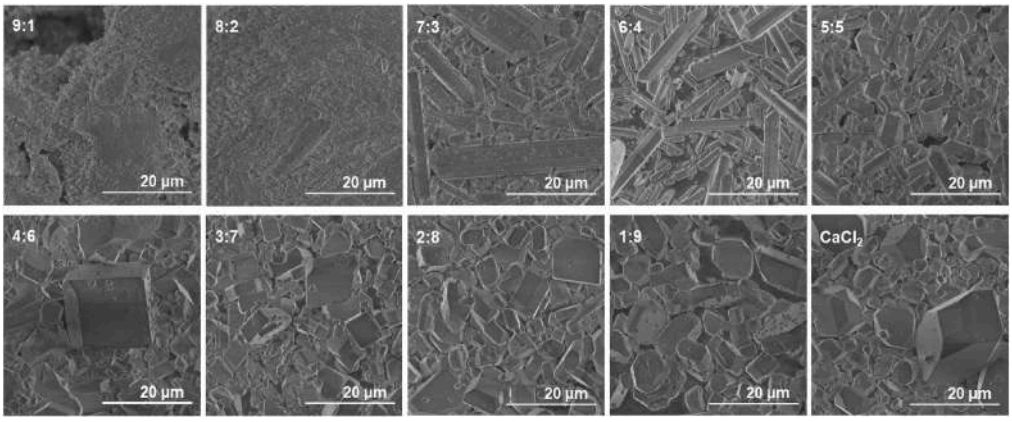

Fig. 5. SEM micrographs of the synthesis products obtained after the treatment of ACP in the mixtures of KCl and $CaCl_2$ mixed in different molar proportions (for K:Ca ratio from 9:1 to 1:9 T = 750 °C, ACP/flux = 1:2, t = 5 h; for $CaCl_2$ T = 800 °C).

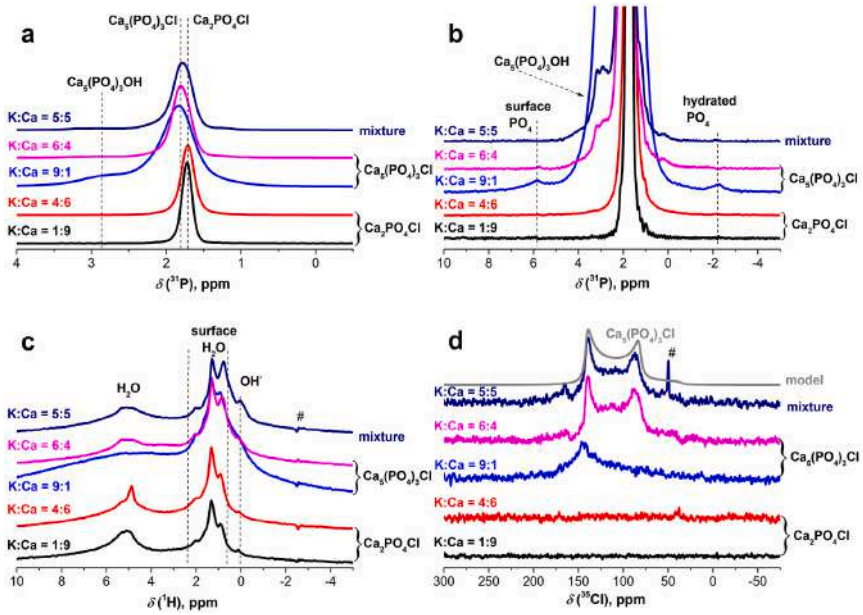

Fig. 6. ^{31}P MAS (a, b), ^{1}H MAS (c) and ^{35}Cl MAS (d) NMR spectra of selected samples obtained after the treatment of ACP in the mixtures of KCl and $CaCl_2$ mixed in different molar proportions (T = 750 °C, ACP/flux = 1:2, t = 5 h). The # denotes the excitation artifact.

sample is assigned to hydroxyapatite ($Ca_5(PO_4)_3OH$) phase [42]. The same peak of much lower intensity (Fig. 6b) is also detected for the rest powders containing ClAp phase (KCl/$CaCl_2$ = 6:4 and 5:5). The presence of $Ca_5(PO_4)_3OH$ could be explained by the fact that the synthesis was performed in air atmosphere and inert conditions were not ensured. Another potentially influencing aspect is the morphology of the samples, namely the sample obtained in KCl/$CaCl_2$ = 9:1 possessed significantly smaller particles and larger surface area in comparison to other samples (Fig. 5), which results in the formation of larger amount of surface-related impurities and defects. This sample also features additional peaks at 5.9 ppm and −2.2 ppm, which are assigned to surface PO_4 and hydrated PO_4 moieties found on the surface of the sample [43]. The sample prepared in KCl/$CaCl_2$ = 5:5, which is a mixture of Ca_2PO_4Cl and ClAp (Fig. 3) also possesses the single peak centered at 1.75 ppm. Unfortunately, due to significant peak width and insufficient difference of chemical shift between the peaks assigned to the different phases, contour separation was not possible.

The structural formulas of the synthesized samples do not contain protons, suggesting that ^{1}H NMR is not beneficial here, though it is not absolutely true, namely it provides insights into the presence of side phases in the samples (Fig. 6c). All studied samples possess peaks at 5.0 ppm, 1.3 ppm and 0.8 ppm, which are assigned to bulk water and water monomers on the surface, respectively. The samples containing $Ca_5(PO_4)_3OH$ side phase (KCl/$CaCl_2$ = 9:1, 6:4 and 5:5) features a peak at 0 ppm assigned to OH^- moiety [42], which corroborates well the ^{31}P data. The sample prepared in KCl/$CaCl_2$ = 9:1 possesses a very broad peak ranging from 10 ppm to 2 ppm, which corresponds to the overlap of physisorbed/chemisorbed water and protonated surface phosphates peaks.

The ^{35}Cl data clearly show the formation of the Cl-containing moiety in the samples containing ClAp species (KCl/$CaCl_2$ = 9:1, 6:4 and 5:5). The spectra corresponding to KCl/$CaCl_2$ = 6:4 and 5:5 samples possess clear quadrupolar lineshape with the following parameters δ_{iso} = 121 ppm, C_Q = 1.7 MHz and η_Q = 0. Similar values were previously reported for highly crystalline ClAp [41]. In contrary, the ClAp sample obtained in KCl/$CaCl_2$ = 9:1 features the line at 145 ppm with a tail towards lower chemical shift range. Lineshapes of such type are the result of a distribution of quadrupolar coupling constants C_Q from a distribution of electronic environments with a relatively small range of chemical shifts. Such observation is logical and explained by much larger surface area of the sample (Fig. 5). Interestingly, single-phase Ca_2PO_4Cl samples do not feature any detectable line in ^{35}Cl spectra. To the best of our knowledge, there is no ^{35}Cl data reported for Ca_2PO_4Cl. Most probably less symmetric chlorine electronic environments in Ca_2PO_4Cl in comparison to $Ca_5(PO_4)_3Cl$ results in very broad linewidths, which are not detectable at current magnetic field using moderate MAS rate.

In order to study the influence of the ACP-to-flux ratio on the phase purity and morphology of ClAp powders, a series of powders was synthesized varying the ACP-to-flux mass ratio from 1:1 to 1:10. For this experiment two different mixtures of salts with the KCl/$CaCl_2$ ratios of 9:1 and 6:4 were employed. The XRD patterns clearly demonstrate that single-phase ClAp was obtained in all cases regardless of the ACP-to-flux ratio and chemical composition of the flux (Fig. S4). While the phase purity was not affected by the composition and weight fraction of the salts, the morphology of ClAp was influenced significantly. The SEM images reflecting the influence of ACP-to-flux ratio on the morphology of ClAp powders are given in Fig. 7.

The effect was more pronounced for the KCl/$CaCl_2$ ratio of 9:1. Evidently, the relatively high concentration of ACP resulted in the formation of small particles (Fig. 7a and b). In this case the powders consisted of nearly spherical particles of sub-micrometer dimensions. In more diluted sample with ACP-to-flux ratio of 1:4 (Fig. 7c) the formation of microrods was evident; however; the small particles still remained dominating. Further dilution of the reaction mixture up to ACP-to-flux ratio of 1:10 led to the increased number of microrods and the reduced number of small particles; however, their presence was still

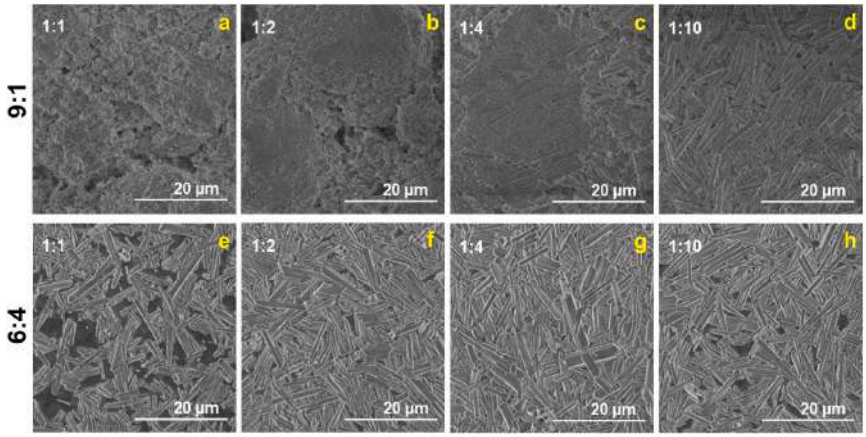

Fig. 7. SEM micrographs of ClAp powders obtained after the treatment of ACP with different amounts molten salts, when $KCl/CaCl_2$ ratio is 9:1 (a–d) and 6:4 (e–h); ACP/flux ratio is 1:1 (a, e); 1:2 (b, f); 1:4 (c, g); and 1:10 (d, h) (T = 750 °C, t = 5 h).

evident. Overall, it can be concluded that the size of the particles can be tuned by the content of ACP in the initial reaction mixture. By contrast, when the flux with the $KCl/CaCl_2$ ratio of 6:4 was used for the synthesis, the effect of ACP concentration was rather minor; the microrods were formed in all cases (Fig. 7e–h). This observation indicates, that synergistic effect of $CaCl_2$ in the flux (see Fig. 5) and the ACP-to-flux ratio on the anisotropic crystal growth is not achievable.

The reaction time in the range from 1 to 48 h did not affect the phase purity of the samples obtained in the flux of $KCl/CaCl_2$ = 6:4 at 750 °C. The XRD patterns clearly show that ClAp was obtained in all cases (Fig. S5). This indicates that single-phase ClAp can be obtained in a time-efficient manner in just 1 h. Fig. 8 illustrates the influence of the reaction time on the morphology of ClAp powders. As seen, the duration did not have a significant effect. In all cases the synthesized ClAp powders possessed the morphology of microrods.

Finally, the influence of the reaction temperature on the phase purity and morphological features of ClAp was investigated in the range from 750 °C to 1200 °C. The XRD patterns of the synthesized products clearly demonstrate the formation of ClAp (Fig. S6). Taking into account the previously mentioned results of the XRD analysis, it can be concluded that the phase composition of the product is influenced exceptionally by the chemical composition of the flux, whereas other synthesis parameters such as temperature or time did not demonstrate any effect. Unlike the phase composition, the morphology of ClAp was determined to be strongly dependent on the temperature (Fig. 9). Increasing the temperature resulted in the formation of larger particles with noticeably lower aspect ratio.

It is known that both natural and synthetic apatites are able to adopt

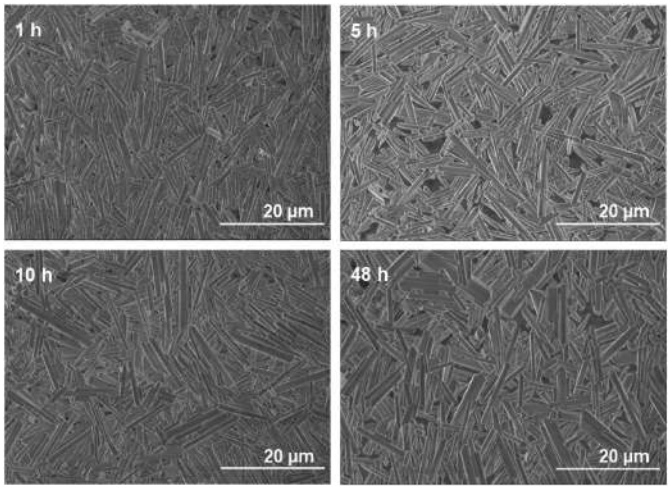

Fig. 8. SEM micrographs of ClAp powders obtained after the treatment of ACP with molten salts for different periods of time: 1 h (a); 5 h (b); 10 h (c); 48 h (d) (T = 750 °C, $KCl/CaCl_2$ = 6:4, ACP/flux = 1:10).

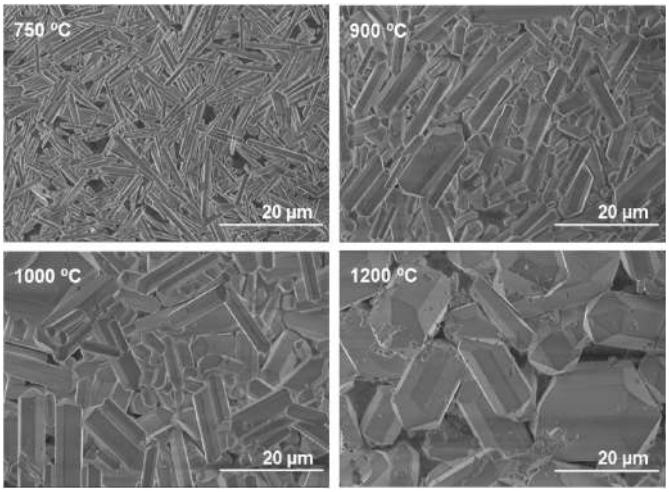

Fig. 9. SEM micrographs of ClAp powders obtained after the treatment of ACP with molten salts at different temperatures: 750 °C (a); 900 °C (b); 1000 °C (c); 1200 °C(d); ($KCl/CaCl_2$ = 6:4, ACP/flux = 1:10, t = 5 h).

other ions including monovalent alkali metal ions [44]. Since in our study the synthesis of ClAp was performed in the presence of high amount of K^+ ions, the K-doping is a reasonable concern. The EDX analysis was performed in order to check the presence of K^+ ions in the synthesized samples; the representative spectrum is depicted in Fig. 10. It is seen that all the observed signals attribute to the elements constituting ClAp crystal structure, namely, Ca, P, O and Cl; there were no signals ascribed to K^+ ions. The absence of K^+ correlate well with the results obtained in single-salt flux, where biphasic product was obtained due to the inability of K^+ ions to compensate the deficiency of Ca (Fig. 1). The extra signal attributed to Al arise from the sample holder. The calculated Ca/P ratio was very close to that of stoichiometric ClAp (1.67). Other elements were manually eliminated from these calculations; the sum of Ca and P atoms was assumed as 100%.

Summarizing the obtained results, it can be concluded that in molten chlorides ACP can be selectively converted to ClAp or Ca_2PO_4Cl using an appropriate chloride salts. The proposed synthetic approach is simple and time-efficient, moreover, it allows to control the morphology of resulting products.

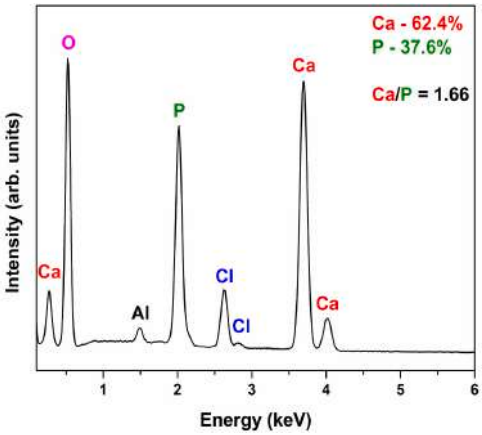

Fig. 10. EDX spectrum of ClAp (ACP/flux = 1:10, T = 1200 °C, t = 5 h).

4. Conclusions

The phase conversion of ACP in different molten chlorides was investigated in detail. The influence of the flux chemical composition, reaction time, temperature and ACP-to-flux ratio was studied. The chemical composition of molten salts, the heat treatment temperature and the ACP-to-flux ratio were determined as the main factors influencing the phase purity and morphological features of the products. It was shown that the phase-selective synthesis of single-phase $Ca_5(PO_4)_3Cl$ or Ca_2PO_4Cl can be achieved by adjusting the composition of $KCl–CaCl_2$ flux. The KCl-rich fluxes led to the formation of $Ca_5(PO_4)_3Cl$, while the Ca-rich fluxes resulted in the formation of Ca_2PO_4Cl. The morphology of $Ca_5(PO_4)_3Cl$ powders can be controlled by varying the $KCl/CaCl_2$ ratio in the flux as well. The $CaCl_2$-rich fluxes promoted the anisotropic growth of $Ca_5(PO_4)_3Cl$ crystals resulting in the formation of monodispersed hexagonally-shaped microrods. Whereas the anisotropic growth was observed at relatively low temperature (750 °C) the increase of the reaction temperature up to 1200 °C significantly reduced this effect.

Declaration of competing interest

The authors declare that they have no known competing financial interests or personal relationships that could have appeared to influence the work reported in this paper.

Acknowledgements

This project has received funding from the Research Council of Lithuania (LMTLT), agreement No S-MIP-23-85.

Appendix A. Supplementary data

Supplementary data to this article can be found online at https://doi.org/10.1016/j.ceramint.2024.02.157.

References

[1] W. Habraken, P. Habibovic, M. Epple, M. Bohner, Calcium phosphates in biomedical applications: materials for the future? Mater. Today 19 (2) (2016) 69–87.

[2] O.V. Zikrata, O.V. Larina, K.V. Valihura, P.I. Kyriienko, D.Y. Balakin, I. Khalakhan, K. Veltruská, A. Krajnc, G. Mali, S.O. Soloviev, S.M. Orlyk, Successive vapor-phase guerbet condensation of ethanol and 1-butanol to 2-Ethyl-1-hexanol over hydroxyapatite catalysts in a flow reactor, ACS Sustain. Chem. Eng. 9 (51) (2021) 17289–17300.

[3] A. Ivanets, A. Zarkov, V. Prozorovich, E. Venhlinskaya, A. Radkevich, J.-C. Yang, E. Papynov, S. Yarusova, A. Kareiva, Effect of Mg^{2+}-, Sr^{2+}-, and Fe^{3+}-substitution on ^{85}Sr and ^{60}Co adsorption on amorphous calcium phosphates: adsorption performance, selectivity, and mechanism, J. Environ. Chem. Eng. 10 (3) (2022) 107425.

[4] L. Sinusaite, A. Antuzevics, A.I. Popov, U. Rogulis, M. Misevicius, A. Katelnikovas, A. Kareiva, A. Zarkov, Synthesis and luminescent properties of Mn-doped alpha-tricalcium phosphate, Ceram. Int. 47 (4) (2021) 5335–5340.

[5] B. Parra-Torrejón, M. Salvachúa-de la Fuente, M.J. Giménez-Bañón, J.D. Moreno-Olivares, D.F. Paladines-Quezada, J.A. Bleda-Sánchez, R. Gil-Muñoz, G.B. Ramírez-Rodríguez, J.M. Delgado-López, Amorphous vs. nanocrystalline calcium phosphate as efficient nanocarriers of elicitors in vineyards, CrystEngComm 25 (16) (2023) 2372–2378.

[6] S.V. Dorozhkin, M. Epple, Biological and medical significance of calcium phosphates, Angew. Chem. 41 (17) (2002) 3130–3146.

[7] S.V. Dorozhkin, Calcium orthophosphate ($CaPO_4$)-based bioceramics: preparation, properties, and applications, Coatings 12 (10) (2022) 1380.

[8] S.V. Dorozhkin, Synthetic amorphous calcium phosphates (ACPs): preparation, structure, properties, and biomedical applications, Biomater. Sci. 9 (23) (2021) 7748–7798.

[9] D. Griesiute, A. Kizalaite, A. Dubnika, V. Klimavicius, V. Kalendra, V. Tyrpekl, S. H. Cho, T. Goto, T. Sekino, A. Zarkov, A copper-containing analog of the biomineral whitlockite: dissolution–precipitation synthesis, structural and biological properties, Dalton Trans. 53 (4) (2024) 1722–1734.

[10] D. Griesiute, E. Raudonyte-Svirbutaviciene, A. Kareiva, A. Zarkov, The influence of annealing conditions on the Ca/P ratio and phase transformations in bulk calcium phosphates, CrystEngComm 24 (6) (2022) 1166–1170.

[11] N. Döbelin, Y. Maazouz, R. Heuberger, M. Bohner, A.A. Armstrong, A.J. Wagoner Johnson, C. Wanner, A thermodynamic approach to surface modification of calcium phosphate implants by phosphate evaporation and condensation, J. Eur. Ceram. Soc. 40 (15) (2020) 6095–6106.

[12] D. Griesiute, E. Garskaite, A. Antuzevics, V. Klimavicius, V. Balevicius, A. Zarkov, A. Katelnikovas, D. Sandberg, A. Kareiva, Synthesis, structural and luminescent properties of Mn-doped calcium pyrophosphate ($Ca_2P_2O_7$) polymorphs, Sci. Rep. 12 (1) (2022) 7116.

[13] L. Sinusaite, I. Grigoraviciute-Puroniene, A. Popov, K. Ishikawa, A. Kareiva, A. Zarkov, Controllable synthesis of tricalcium phosphate (TCP) polymorphs by wet precipitation: effect of washing procedure, Ceram. Int. 45 (9) (2019) 12423–12428.

[14] G. Montes-Hernandez, F. Renard, Nucleation of brushite and hydroxyapatite from amorphous calcium phosphate phases revealed by dynamic in situ Raman spectroscopy, J. Phys. Chem. C 124 (28) (2020) 15302–15311.

[15] L. Sinusaite, A. Popov, E. Raudonyte-Svirbutaviciene, J.-C. Yang, A. Kareiva, A. Zarkov, Effect of Mn doping on hydrolysis of low-temperature synthesized metastable alpha-tricalcium phosphate, Ceram. Int. 47 (9) (2021) 12078–12083.

[16] T. Goto, S. Yin, Y. Asakura, S.H. Cho, T. Sekino, Simultaneous synthesis of hydroxyapatite fibres and β-tricalcium phosphate particles via a water controlled-release solvothermal process, CrystEngComm 25 (14) (2023) 2021–2026.

[17] C. Combes, C. Rey, Amorphous calcium phosphates: synthesis, properties and uses in biomaterials, Acta Biomater. 6 (9) (2010) 3362–3378.

[18] L. Sinusaite, A. Kareiva, A. Zarkov, Thermally induced crystallization and phase evolution of amorphous calcium phosphate substituted with divalent cations having different sizes, Cryst. Growth Des. 21 (2) (2021) 1242–1248.

[19] N. Döbelin, T.J. Brunner, W.J. Stark, M. Fisch, E. Conforto, M. Bohner, Thermal treatment of flame-synthesized amorphous tricalcium phosphate nanoparticles, J. Am. Ceram. Soc. 93 (10) (2010) 3455–3463.

[20] J.A. Stammeier, B. Purgstaller, D. Hippler, V. Mavromatis, M. Dietzel, In-situ Raman spectroscopy of amorphous calcium phosphate to crystalline hydroxyapatite transformation, MethodsX 5 (2018) 1241–1250.

[21] B. Jin, Z. Liu, C. Shao, J. Chen, L. Liu, R. Tang, J.J. De Yoreo, Phase transformation mechanism of amorphous calcium phosphate to hydroxyapatite investigated by liquid-cell transmission electron microscopy, Cryst. Growth Des. 21 (9) (2021) 5126–5134.

[22] D. Karoblis, O.C. Stewart Jr., P. Glaser, S.E. El Jamal, A. Kizalaite, T. Murauskas, A. Zarkov, A. Kareiva, S.L. Stoll, Low-temperature synthesis of magnetic pyrochlores ($R_2Mn_2O_7$, R = Y, Ho–Lu) at ambient pressure and potential for high-entropy oxide synthesis, Inorg. Chem. 62 (27) (2023) 10635–10644.

[23] M. Sadat-Shojai, M. Kalantari-Lalari, M. Asadnia, Synthesis of highly regular dandelion-like hydroxyapatite particles—a Taguchi experimental design approach, CrystEngComm 25 (24) (2023) 3564–3575.

[24] Y.Q. Chen, Y.J. Zhu, Z.Y. Wang, H.P. Yu, Z.C. Xiong, A scalable, low-cost and green strategy for the synthesis of ultralong hydroxyapatite nanowires using peanut oil, CrystEngComm 24 (17) (2022) 3208–3216.

[25] G.Y. Ivanyuk, V.N. Yakovenchuk, Y.A. Pakhomovsky, T.L. Panikorovskii, N. G. Konoplyova, A.V. Bazai, V.N. Bocharov, A.A. Antonov, E.A. Selivanova, Goryainovite, Ca_2PO_4Cl, a new mineral from the Stora Sahavaara iron ore deposit (Norrbotten, Sweden), GFF 139 (1) (2017) 75–82.

[26] J.M. Hughes, M. Cameron, K.D. Crowley, Structural variations in natural F, OH, and Cl apatites, Am. Mineral. 74 (7–8) (1989) 870–876.

[27] Q. Yuan, P. Wang, X. Wang, B. Hu, C. Wang, X. Xing, Nano-chlorapatite modification enhancing cadmium(II) adsorption capacity of crop residue biochars, Sci. Total Environ. 865 (2023) 161097.

[28] R. Deng, X. Zhan, High performance self-assembled nano-chlorapatite in the presence of lactonic sophorolipid for the immobilization of cadmium in polluted sediment, J. Hazard Mater. 445 (2023) 130484.

[29] X. Wen, C. He, B. Wu, X. Huang, Z. Huang, Z. Yin, Y. Liu, M. Fang, X. Wu, X. Min, Molten salt synthesis, growth mechanism, and photoluminescence of rod chlorapatite microcrystallites, CrystEngComm 21 (11) (2019) 1809–1817.

[30] Z. Zhang, J. Wang, M. Zhang, Q. Zhang, Q. Su, The energy transfer from Eu^{2+} to Tb^{3+} in calcium chlorapatite phosphor and its potential application in LEDs, Appl. Phys. B 91 (3) (2008) 529–537.

[31] M.H. Hwang, E.Y. Lee, S.-H. Hong, Y.-B. Sun, Y.J. Kim, Preparation and luminescent properties of $Ca_5(PO_4)_3Cl : Eu^{2+}$ phosphors by a solid-state reaction method, J. Electrochem. Soc. 156 (7) (2009) J185.

[32] R.T. Maske, A.N. Yerpude, S.J. Dhoble, Wet chemical synthesis of Sm^{3+} doped $Ca_{10}(PO_4)_6Cl_2$ phosphor for w-LED application, Mater. Lett. X 19 (2023) 100214.

[33] R.A. Talewar, C.P. Joshi, S.V. Moharil, Sensitization of Nd^{3+} near infrared emission in Ca_2PO_4Cl host, J. Lumin. 197 (2018) 1–6.

[34] Y.-C. Chiu, W.-R. Liu, C.-K. Chang, C.-C. Liao, Y.-T. Yeh, S.-M. Jang, T.-M. Chen, $Ca_2PO_4Cl : Eu^{2+}$: an intense near-ultraviolet converting blue phosphor for white light-emitting diodes, J. Mater. Chem. 20 (9) (2010) 1755–1758.

[35] P. Li, Z. Wang, Z. Yang, Q. Guo, A novel, warm, white light-emitting phosphor $Ca_2PO_4Cl:Eu^{2+}$, Mn^{2+} for white LEDs, J. Mater. Chem. C 2 (37) (2014) 7823–7829.

[36] D. Griesiute, L. Sinusaite, A. Kizalaite, A. Antuzevics, K. Mazeika, D. Baltrunas, T. Goto, T. Sekino, A. Kareiva, A. Zarkov, The influence of Fe^{3+} doping on thermally induced crystallization and phase evolution of amorphous calcium phosphate, CrystEngComm 23 (26) (2021) 4627–4637.

[37] P.E. Mackie, J.C. Elliot, R.A. Young, Monoclinic structure of synthetic $Ca_5(PO_4)_3Cl$, chlorapatite, Acta Crystallogr. B 28 (6) (1972) 1840–1848.

[38] S. Koutsopoulos, Synthesis and characterization of hydroxyapatite crystals: a review study on the analytical methods, J. Biomed. Mater. Res. 62 (4) (2002) 600–612.

[39] O. Livitska, N. Strutynska, O. Livitska, N. Slobodyanik, The alternative approach to the preparation of complex calcium phosphates and their characterization, Functional materials 24 (3) (2017) 457–462.

[40] K. Hayashi, R. Kishida, A. Tsuchiya, K. Ishikawa, Transformable carbonate apatite chains as a novel type of bone graft, Adv. Healthcare Mater. (2024) 2303245.

[41] J.S. Vaughn, D.H. Lindsley, H. Nekvasil, J.M. Hughes, B.L. Phillips, Complex F,Cl apatite solid solution investigated using multinuclear solid-state NMR methods, J. Phys. Chem. C 122 (1) (2018) 530–539.

[42] V. Klimavicius, A. Kareiva, V. Balevicius, Solid-state NMR study of hydroxyapatite containing amorphous phosphate phase and nanostructured hydroxyapatite: cut-off averaging of CP-MAS kinetics and size profiles of spin clusters, J. Phys. Chem. C 118 (49) (2014) 28914–28921.

[43] M. Ben Osman, S. Diallo-Garcia, V. Herledan, D. Brouri, T. Yoshioka, J. Kubo, Y. Millot, G. Costentin, Discrimination of surface and bulk structure of crystalline hydroxyapatite nanoparticles by NMR, J. Phys. Chem. C 119 (40) (2015) 23008–23020.

[44] M. Šupová, Substituted hydroxyapatites for biomedical applications: a review, Ceram. Int. 41 (8) (2015) 9203–9231.

2nd publication

Luminescent properties of near-infrared-emitting Cr^{3+}-activated beta-$Ca_3(PO_4)_2$

S. Pazylbek, J. Stadulis, G. Doke, A. Antuzevics, M. Sandomierski, A. Katelnikovas, C.-Y. Su, H.-W. Fang, A. Zarkov

Optical Materials 159 **(2025)** 116569
(https://doi.org/10.1016/j.optmat.2024.116569)

Optical Materials 159 (2025) 116569



Contents lists available at ScienceDirect

Optical Materials

journal homepage: www.elsevier.com/locate/optmat



Luminescent properties of near-infrared-emitting Cr^{3+}-activated beta-$Ca_3(PO_4)_2$

Sapargali Pazylbek [a], Jonas Stadulis [a], Guna Doke [a,b,**], Andris Antuzevics [a,b], Mariusz Sandomierski [c], Arturas Katelnikovas [a], Chen-Ying Su [d], Hsu-Wei Fang [d], Aleksej Zarkov [a,*]

[a] Institute of Chemistry, Vilnius University, Naugarduko 24, LT-03225, Vilnius, Lithuania
[b] Institute of Solid State Physics, University of Latvia, Kengaraga 8, LV-1063, Riga, Latvia
[c] Institute of Chemical Technology and Engineering, Poznan University of Technology, ul. Berdychowo 4, 60-965, Poznan, Poland
[d] High-Value Biomaterials Research and Commercialization Center, National Taipei University of Technology, Taipei, 10608, Taiwan

ARTICLE INFO

Keywords:
Cr^{3+}-doped TCP
Tricalcium phosphate
Photoluminescence
Thermally stimulated luminescence

ABSTRACT

In this work, a series of Cr^{3+}-doped β-tricalcium phosphate (β-TCP) powders was synthesized by a wet co-precipitation method. It was shown that the dissolution of Cr^{3+} ions in the β-TCP crystal structure is limited, resulting in the formation of a Cr_2O_3 secondary phase at higher substitution levels. The room-temperature and temperature-dependent photoluminescence excitation spectra, emission spectra, and photoluminescence decay curves of the samples were studied. Thermally stimulated luminescence, and afterglow decay spectral measurements were performed as well. All the synthesized materials exhibited broadband photoluminescence in the near-infrared region, ranging from approximately 680 to 900 nm, with a maximum centered at 760 nm. The strongest emission was detected for the sample with a doping level of 0.1 mol% Cr^{3+}. Moreover, for the β-TCP: 0.1 mol% Cr^{3+} sample, the afterglow after irradiation with X-rays can be detected for at least 8 h.

1. Introduction

Calcium phosphates (CPs) are a family of materials that are widely used in various applications, such as medicine [1], catalysis [2], water treatment [3], optical materials [4], etc. One approach used to modify the physical, chemical, and biological properties of biocompatible CPs is the partial substitution of Ca by other metal ions. This allows to combine biocompatibility of CPs with substitution-induced properties, resulting in the application of these materials in new areas, such as various imaging modalities, including fluorescence, magnetic resonance, and multimodal imaging [5,6].

One member of the CPs family is beta-tricalcium phosphate (β-TCP, $Ca_3(PO_4)_2$). This material can be considered as multifunctional. First of all, it is widely used in medicine for the regeneration of hard tissues [7]; however, with appropriate ion doping/substitution, this crystal structure can be successfully employed for the development of luminescent materials [8]. In particular, much attention has been paid to optical materials with β-$Ca_3(PO_4)_2$-type structure and the general formula $Ca_9M(PO_4)_7$, where M is a trivalent ion [4].

β-TCP crystallizes in a rhombohedral crystal structure with R3c space group (#161). The crystal structure of β-TCP contains 5 inequivalent Ca sites and 3 inequivalent P sites, which are arranged in two columns [9]. β-TCP structure can adopt both isovalent and aliovalent ions; this ability was employed in a plenty of works in order to tune biological, optical, magnetic, and other properties of the material [10–12].

Although recent studies have revealed that Cr^{3+} is not an essential trace element in the human body, it can be considered pharmacologically active [13]. At the same time Cr^{3+} ions are widely used for the development of optical materials with emission in the near-infrared region (NIR). Such phosphors can be applied in temperature sensing [14], bioimaging [15], anticounterfeiting [16], night vision [17], etc. Different CP matrices, including calcium hydroxyapatite (HA, $Ca_{10}(PO_4)_6(OH)_2$) and brushite (DCPD, $CaHPO_4 \bullet 2H_2O$), have been previously modified with Cr^{3+} ions [18,19]; however, studies on Cr^{3+}-doped β-TCP are almost absent. A rare exception is the study by Zatovsky et al., who reported the crystal structure of $Ca_9Cr(PO_4)_7$, which

* Corresponding author.
** Corresponding author. Institute of Chemistry, Vilnius University, Naugarduko 24, LT-03225, Vilnius, Lithuania.
E-mail addresses: guna.doke@cfi.lu.lv (G. Doke), aleksej.zarkov@chf.vu.lt (A. Zarkov).

https://doi.org/10.1016/j.optmat.2024.116569
Received 16 November 2024; Received in revised form 10 December 2024; Accepted 12 December 2024
Available online 13 December 2024
0925-3467/© 2024 Elsevier B.V. All rights are reserved, including those for text and data mining, AI training, and similar technologies.

is in fact a heavily Cr^{3+}-doped β-TCP [20]. Another study by Alshemary et al. very briefly investigated the optical properties of β-TCP:Cr^{3+} [21]. However, some reports on the characterization of Cr^{3+}-doped ion-substituted β-$Ca_3(PO_4)_2$ can be found. For instance, Zhao et al. reported the synthesis and optical properties of Cr^{3+}-activated far-red emitting phosphors with β-$Ca_3(PO_4)_2$-type structure, namely $Ca_9M(PO_4)_7$:0.03Cr^{3+} (M = Al, Ga, Sc, In, Lu, Y) [22]. It was shown that all samples, independent of M, exhibited far-red and NIR luminescence, while $Ca_9Ga(PO_4)_7$:Cr^{3+} demonstrated the highest emission intensity. Alawsh et al. recently investigated the thermally stimulated luminescence (TSL) of Cr^{3+}-activated sol-gel derived $Ca_9Al(PO_4)_7$ [23].

The aim of the present work was to synthesize Cr^{3+}-doped β-TCP and investigate its optical properties in terms of photoluminescence and thermally stimulated luminescence. For this purpose, a series of powders with various Cr^{3+} content was synthesized and characterized. Room-temperature and temperature-dependent photoluminescence excitation spectra, emission spectra, and photoluminescence decay curves of the samples were studied. The TSL and afterglow decay spectral measurements were performed as well.

2. Experimental

2.1. Synthesis

β-TCP powders substituted with Cr^{3+} ions were synthesized by a wet co-precipitation method followed by high-temperature annealing according to a slightly modified previously reported procedure [24,25]. The substitution level (0.1, 0.5, 1.0, 2.0, and 5.0 mol%) is given with respect to Ca^{2+} ions. Calcium nitrate tetrahydrate ($Ca(NO_3)_2{\cdot}4H_2O$, ≥99 %, Roth), diammonium hydrogen phosphate ($(NH_4)_2HPO_4$, ≥98 %, Roth) and chromium (III) nitrate nonahydrate ($Cr(NO_3)_3 \bullet 9H_2O$, 98 %, Alfa Aesar) were used as starting materials. Appropriate amounts of $Ca(NO_3)_2{\cdot}4H_2O$ and $Cr(NO_3)_3 \bullet 9H_2O$ were dissolved in deionized water to obtain a solution with a total concentration of metal ions of 0.75 M. In parallel, $(NH_4)_2HPO_4$ was dissolved in deionized water in a separate beaker to obtain a 0.5 M solution, to which concentrated ammonia solution (NH_4OH, 25 %, Roth) was added to adjust the pH to 10. Next, a solution containing metal nitrates was rapidly added to the $(NH_4)_2HPO_4$ solution, leading to the formation of precipitates. The obtained precipitates were aged for 10 min, vacuum-filtered, washed with deionized water, and dried in an oven overnight. Dry powders were ground in an agate mortar and annealed in a muffle furnace in air at 1100 °C for 5 h at a heating rate of 5 °C min^{-1}.

2.2. Characterization

Powder X-ray diffraction (XRD) data of the synthesized powders were obtained using a Rigaku MiniFlex II diffractometer (Cu-K_α, λ = 1.5419 Å) working in the Bragg-Brentano (θ/2θ) geometry. The data were collected within the 10–60° 2θ angle range with a scan speed of 5°/min.

Fourier transform infrared spectra (FTIR) were recorded in the range of 4000–400 cm^{-1} using a Bruker ALPHA-FTIR spectrometer.

The morphology of the synthesized specimens was analyzed via scanning electron microscopy (SEM) using a Hitachi SU-70 microscope.

The chromium content in the synthesized products was determined by inductively coupled plasma optical emission spectrometry (ICP-OES) using a PerkinElmer Optima 7000DV spectrometer. The samples prior to analysis were dissolved in 5 % nitric acid (HNO_3, Rotipuran® Supra 69 %, Roth) and diluted to an appropriate volume.

A Bruker ELEXSYS-II E500 CW-EPR spectrometer was used for electron paramagnetic resonance (EPR) analysis of the samples. The spectra acquisition settings were as follows: room temperature, 9.833 GHz microwave frequency, 10 mW microwave power, and 0.4 mT magnetic field modulation amplitude.

The photoluminescence excitation (PLE) and photoluminescence emission (PL) spectra were measured using the Edinburgh Instruments FLS980 spectrometer equipped with double excitation and emission monochromators, a 450 W Xe arc lamp, a cooled (−20 °C) single-photon counting photomultiplier (Hamamatsu R928P), and mirror optics for the powder samples. The PL spectra were corrected by a correction file obtained from a tungsten incandescent lamp certified by NPL (National Physics Laboratory, UK). The excitation spectra were corrected by reference detector. PL decay curves were measured using the same Edinburgh Instruments FLS980 spectrometer. A Xe μ-flash lamp μF920 was used as the excitation source.

Thermally stimulated luminescence (TSL), and afterglow decay spectral measurements were performed using the Lexsyg research fully automated TSL/OSL reader from Freiberg Instruments GmbH equipped with either a Hamamatsu R13456 photomultiplier tube or a DV420A-BU2 CCD camera coupled with an Andor SR-303i-B spectrometer. An X-ray tube (40 kV, 0.5 mA, W-anode) was used to irradiate the samples. TSL measurements were performed using a linear heating rate of 1 °C/s from room temperature (RT) to 270 °C. Isothermal afterglow decay was measured at 25 °C. To eliminate any effects of the previously stored energy, the samples were preheated to 300 °C before each measurement.

3. Results and discussion

The XRD patterns of the as-precipitated powders are shown in Fig. S1. It is evident that the phase composition of the precipitates strongly depends on the amount of Cr^{3+}. The samples with lower Cr^{3+} content (≤1 mol%) were identified as Cr^{3+}-doped Ca-deficient hydroxyapatite (CDHA), which is in good agreement with previously reported data [26]. A higher amount of Cr^{3+} retards the crystallization process, leading to the formation of nearly or completely amorphous calcium phosphate (ACP). In terms of thermally induced phase evolution, the behavior of both CDHA and ACP with a Ca-to-P ratio of 1.5:1 is nearly identical; at certain temperature both materials transform to β-TCP [26,27]. Indeed, after annealing at 1100 °C, phase conversion occurred, resulting in the formation of Cr^{3+}-doped β-TCP. The XRD patterns of the resulting products are shown in Fig. 1a. The major β-TCP phase was obtained for all samples regardless of the Cr content. All diffraction peaks match very well with the standard of rhombohedral $Ca_3(PO_4)_2$ with R3c space group (#00-070-2065). A minor impurity phase was detected in the sample with the highest Cr content (5 mol%). This secondary phase was identified as Cr_2O_3 (#00-038-1479). The XRD patterns of the powders with lower Cr content did not reveal the presence of this impurity. This observation indicates that under the selected synthetic conditions, the amount of Cr^{3+} ions that can be incorporated into the β-TCP crystal structure is limited. Although some previous study have reported significantly higher Cr^{3+} substitution level ($Ca_9Cr(PO_4)_7$, i.e. 10 mol% with respect to Ca ions), it should be noted that this material was synthesized from a melt in the Cs_2O–CaO–Cr_2O_3 system using a polyphosphate flux [20]. To the best of our knowledge, there have been no other reports on the synthesis of this material. Alshemary et al. reported the synthesis of Cr^{3+}-doped β-TCP by microwave-assisted wet precipitation method [21]; however, Cr_2O_3 impurity was also detected starting from the Cr^{3+} substitution level of 4 mol%.

The FTIR spectra of Cr^{3+}-doped β-TCP samples are depicted in Fig. 1b. The spectral range from 1400 to 400 cm^{-1} was chosen as a representative, because there are no absorption bands in the spectrum of β-TCP in other regions. The spectrum of the undoped sample exhibited absorption bands characteristic of phosphate groups in the β-TCP crystal structure. The bands located in the range of ca. 1150–990 cm^{-1} were assigned to the phosphate ν_3 stretching mode, while the two bands centered at 970 and 940 cm^{-1} were ascribed to the ν_1 vibrational mode. The bands at 640–500 cm^{-1} were ascribed to the ν_4 bending mode, and the weak absorption band centered at approximately 434 cm^{-1} corresponded to the ν_2 mode [28]. The shape of the spectra changed slightly with increasing Cr^{3+} content. Two absorption bands centered at 901 and 864 cm^{-1} were clearly visible for the samples with Cr content of 1 mol%

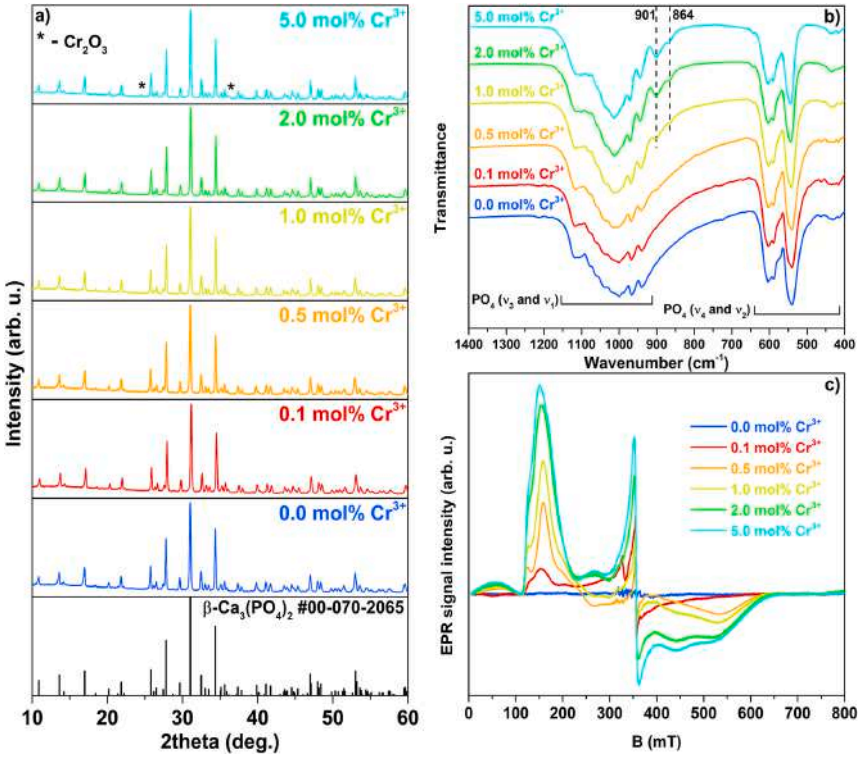

Fig. 1. (a) XRD patterns; (b) FTIR spectra; and (c) EPR spectra of β-TCP with various Cr^{3+} content.

and higher. There are not enough data in the literature on Cr^{3+}-doped β-TCP for comparison; however; it is known that doping with trivalent ions, such as Fe^{3+} or Ga^{3+}, changes the shape of FTIR spectrum of β-TCP [10,24,29,30]. Additional absorption bands at ~865 cm^{-1} were observed for both dopants. According to Mellier et al. [30], the substitution of Ca^{2+} with trivalent ions leads to significant changes in the local environment of the phosphate sites. This results in stronger splitting and the appearance of new absorption bands. The appearance of these absorption bands confirms that Cr^{3+} ions are introduced into the β-TCP crystal lattice.

The EPR spectra presented in Fig. 1c reveal the concentration-dependent incorporation of Cr^{3+} ions into the investigated β-TCP series. In the undoped sample, a minor signal from Mn^{2+} ions, commonly found as impurities in CP materials [31], is observed. As the Cr^{3+} concentration increases, two prominent signals appear: an asymmetric low-field component at around 160 mT (g_{eff} = 4.46), and a symmetric line at 356 mT (g_{eff} = 1.97). EPR signal positions are governed by the magnitude of the zero-field splitting (ZFS) of the $^4A_2$ ground state of Cr^{3+}, typically spanning a broad magnetic field range in various crystalline and amorphous hosts [32–36]. Within the investigated concentration range, the double-integrated intensity of the low-field component increased proportionally with the Cr concentration. However, variations in the relative intensities of the low-field and g_{eff} = 1.97 components across different samples indicate the presence of multiple Cr^{3+}-related centers.

A discussion of the local environment of Cr^{3+} ions in β-TCP can be initiated based on experimental powder EPR spectra and available literature data. Similar spectra (coexistence of low-field and g_{eff} = 1.97 components) have been reported for various Cr-doped glass systems [32–34]. In these studies, the low-field component was attributed to isolated Cr^{3+} centers in distorted octahedral sites, whereas the interpretation of the high-field component was ambiguous. Cr^{3+} ions preferentially occupy crystallographic positions, providing a 6-fold coordinated environment. Five cation sites, Ca(1)–Ca(5), are available in the β-TCP structure for substitution with transition metal ions. Of these, Ca(5) is coordinated by 6 ligands [9]. The substitution of Ca^{2+} sites by Cr^{3+} ions necessitates charge compensation, suggesting that multiple Cr^{3+} centers could arise from the same crystallographic site, but with different defects, such as cation vacancies, in the vicinity. Such a complicated case would likely result in broad EPR spectra due to overlapping signals from different environments, as observed in the present study. It should be mentioned, that according to Zatovsky et al. in the crystal structure of $Ca_9Cr(PO_4)_7$ the coordination of Cr^{3+} ions is slightly distorted octahedral [20], which corresponds to the Ca(5) site.

The SEM images of the synthesized β-TCP powders are given in Fig. 2. Evidently, the grain size strongly depends on the concentration of Cr^{3+} ions. In the case of undoped TCP, relatively large grains of approximately 2–4 μm were formed; however, the presence of 0.1 mol% of Cr^{3+} obviously reduced the grain size to 1–2.5 μm. In the case of 5 mol % Cr^{3+}, the grain growth was retarded even more, and the powders consisted of relatively small elongated particles of undefined shape necked to each other.

The well-known disadvantage of the co-precipitation method is the challenge in controlling the chemical composition; therefore, elemental

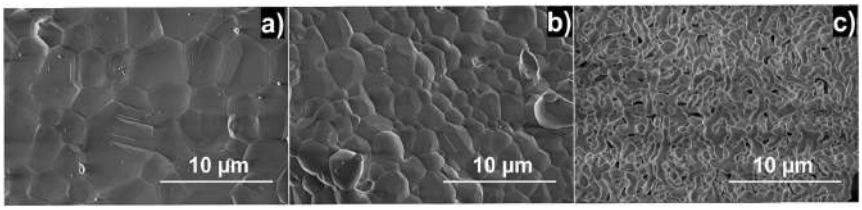

Fig. 2. SEM images of β-TCP with (a) 0 mol% Cr^{3+}; (b) 0.1 mol% Cr^{3+}; and (c) 5 mol% Cr^{3+}.

analysis of the synthesis products is an obligatory part of the characterization. The results of ICP-OES analysis of the Cr^{3+}-doped samples are summarized in Table 1. The determined Cr content in the synthesized powders was in good agreement with the theoretical values. The only exception is the sample with the highest Cr concentration, where the determined value was approximately 20 % lower than the nominal value.

Fig. 3 shows the photoluminescence (PL) excitation and emission spectra of the β-TCP: Cr^{3+} samples. Three Cr^{3+} typical excitation bands were detected for all samples, with maxima at approximately 300, 450, and 640 nm. These bands were attributed to the intra-*3d* spin-allowed optical transitions of Cr^{3+}: $^4A_2(^4F) \rightarrow {}^4T_1(^4P)$ at 300 nm; $^4A_2(^4F) \rightarrow {}^4T_1(^4F)$ at 450 nm, and $^4A_2(^4F) \rightarrow {}^4T_2(^4F)$ at 640 nm [37,38]. The positions of the Cr^{3+} 3d energy levels are strongly affected by the crystal field surrounding the Cr^{3+} ion. Therefore, small changes in the lattice, such as increased Cr^{3+} doping concentration and subsequent generation of defects required for charge compensation, can lead to changes in the spectral features [39]. In the case of the β-TCP: Cr^{3+} samples, a redshift for the 450 nm excitation band with increased Cr^{3+} concentration was observed.

To gain insight into the interelectronic transitions occurring in d-orbitals, Tanabe-Sugano diagrams are typically employed [40,41]. These diagrams illustrate the energy levels of transition metal ions with respect to the crystal field strength (Dq) and Racah parameter (B). Fig. 4b demonstrates a simplified Tanabe-Sugano diagram that elucidates the energy levels of a Cr^{3+} ion in octahedral coordination. Thus, the redshift of the $^4A_2(^4F) \rightarrow {}^4T_1(^4F)$ transition should be expected in the case of decreasing crystal-field strength. Furthermore, when excited at 450 nm, all samples can be characterized by a broad near-infrared luminescence band in the 680–900 nm range, originating from the spin-allowed $^4T_2(^4F) \rightarrow {}^4A_2(^4F)$ optical transition typical of Cr^{3+} ions in a relatively weak crystal field [42]. The best PL intensity was achieved for the 0.1 mol% Cr^{3+} sample, most likely due to concentration quenching at higher Cr^{3+} concentrations.

For the 0.1 mol% sample, a series of temperature-dependent measurements of the PL spectra in the 77−500 K range was carried out. The results are shown in Fig. 4a. The two primary observations are as follows: first, there is strong thermal quenching with increasing temperature; second, at low-temperature conditions (77 and 100 K), not only the

Table 1
Results of the elemental analysis of the samples performed by ICP-OES.

Sample	Theoretical Cr/(Cr + Ca) ratio, mol%	Determined Cr/(Cr + Ca) ratio, mol%
TCP: 0.1 % Cr^{3+}	0.100	0.101
TCP: 0.5 % Cr^{3+}	0.500	0.507
TCP: 1.0 % Cr^{3+}	1.00	0.976
TCP: 2.0 % Cr^{3+}	2.00	2.01
TCP: 5.0 % Cr^{3+}	5.00	3.94

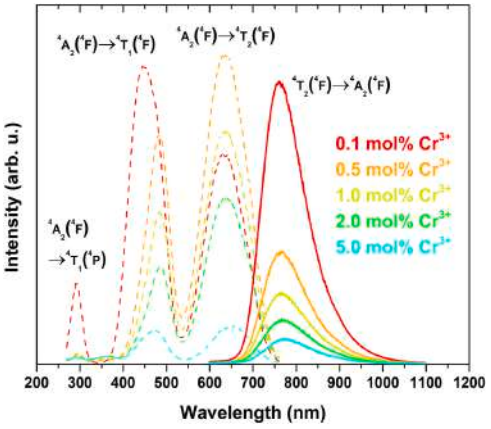

Fig. 3. Excitation (dashed lines) and emission (solid lines) spectra of β-TCP with various Cr^{3+} concentrations (λ_{em} = 790 nm; λ_{ex} = 450 nm).

previously discussed broad Cr^{3+} PL band but also a narrow band related to the spin-forbidden $^2E(^2G) \rightarrow {}^4A_2(^4F)$ optical transition emerges. In general, the appearance of this band is a sign of Cr^{3+} ions under strong crystal field conditions. In the Tanabe-Sugano diagram for the d^3 electron configuration (Fig. 4b), the crystal field is considered weak if Dq/B < 2.3 and strong if Dq/B > 2.3. In the case of Dq/B ≈ 2.3, an intermediate crystal field can be assumed, and there should be thermal equilibrium between the $^2E(^2G)$ and $^4T_2(^4F)$ states, leading to the broadband and narrow-band emission of Cr^{3+}. Therefore, in the low-temperature range, Cr^{3+} ions in the β-TCP host are considered to be in an intermediate crystal field. However, when the temperature rises above 100 K, the crystal field weakens due to the thermal expansion of the lattice, and only the $^4T_2(^4F) \rightarrow {}^4A_2(^4F)$ transition appears in the spectra. This effect has been previously reported by several authors [43,44]. On the other hand, the disappearance of narrowband PL could also be explained by thermal activation from the $^2E(^2G)$ to $^4T_2(^4F)$ states, as has been proven in similar materials [45] or as a combination of both of these effects.

As for thermal quenching – considering the effect of the lattice vibration with increased temperature, a thermally activated quenching process of the $^4T_2(^4F)$ state via a nonradiative relaxation process to the $^4A_2(^4F)$ ground state is expected [14,46]. Additionally, the decay kinetics of the Cr^{3+} PL (λ_{em} = 765 nm) at different temperatures were measured, as shown in Fig. 4c. As is typical for the case of increasing nonradiative relaxation contribution to the PL mechanism, the luminescence lifetime decreases with temperature from 189 μs at 77 K to 20.6 and 10.2 μs at 300 and 400 K, respectively (Fig. 4d).

When certain materials are exposed to ionizing radiation, free charge carriers may be produced. If the material contains appropriate defects,

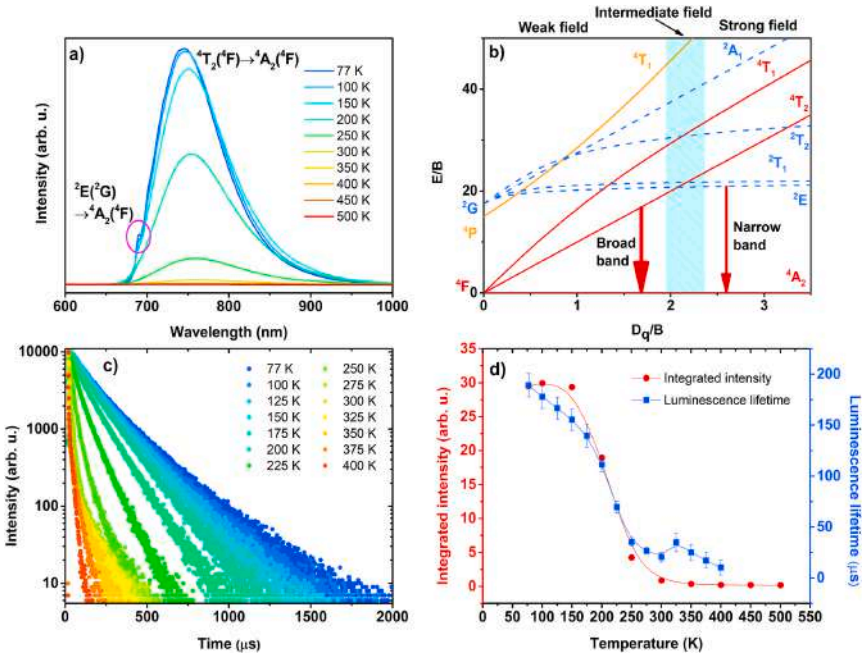

Fig. 4. (a) Temperature-dependent emission spectra of the 0.1 mol% Cr^{3+} β-TCP sample (λ_{ex} = 450 nm); (b) simplified Tanabe-Sugano diagram for d^3 ion in octahedral site symmetry; (c) temperature-dependent decay curves (λ_{ex} = 450 nm, λ_{em} = 765 nm) and (d) temperature dependence of the intensity and luminescence lifetime of the 0.1 mol% Cr^{3+} β-TCP sample.

these charges may become confined within so-called charge traps. Over time, trapped charges are released, typically via the accumulation of thermal energy. However, athermal tunneling has also been reported to be a viable detrapping mechanism [47]. One of the most prevalent techniques for studying trap centers in solids is TSL [48–50].

Cr^{3+}-doped and undoped β-TCP samples were irradiated with X-rays for 3 min, and then the TSL glow curves were measured at a heating rate of 1 °C/s. The results are shown in Fig. 5a. From this, it is evident that Cr^{3+}-doped and undoped samples have fundamentally different filled trap structures. Doped samples have relatively shallow traps with corresponding glow peak maxima around 60–70 °C, and with increasing dopant concentration, the intensity of the TSL signal drastically decreases. However, this is most likely linked to Cr^{3+}-related luminescence concentration quenching, not the defect structure. On the other hand, the undoped sample can be characterized by a broad, relatively weak, and uniform TSL signal from 50 to 170 °C, followed by a high-intensity TSL peak with a maximum at around 220 °C. A slight increase in the high-temperature range for doped samples is related to thermal

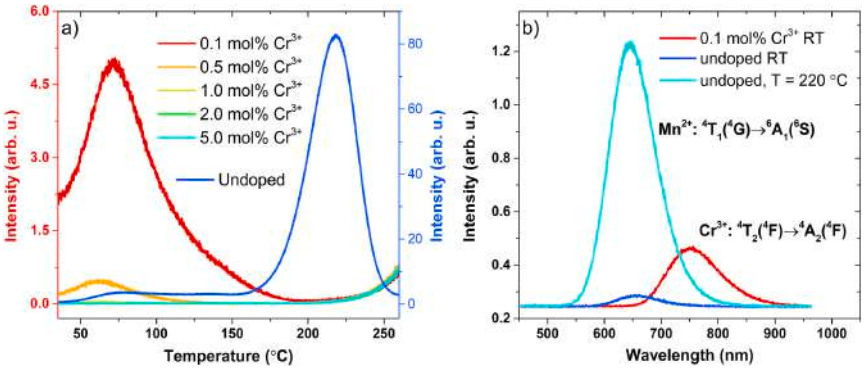

Fig. 5. (a) TSL glow curves of β-TCP samples after irradiation with X-rays for 3 min; (b) spectral response of samples at room temperature (RT) and 220 °C after irradiation with X-rays for 3 min.

radiation. The TSL spectra of the 0.1 mol% Cr^{3+} doped and undoped samples at different temperatures are shown in Fig. 5b. As expected, the Cr^{3+}-doped sample can be characterized by a Cr^{3+} typical broadband near-infrared luminescence band identical to the RT PL band of the same sample, involving the same optical transitions. In the case of the undoped sample, no Cr^{3+} related luminescence bands were detected; however, a broad luminescence band with a maximum at approximately 650 nm was detected at RT and throughout the entire heating range. The band was ascribed to the $^4T_1(^4G) \rightarrow {}^6A_1(^6S)$ optical transition of Mn^{2+} ions, the minor presence of which was already detected by EPR measurements.

To identify the nature of the traps and the trap depth, also known as the activation energy, the T_{max}-T_{stop} method combined with an initial rise analysis (IRA) was utilized. Both methods are well-established and are commonly used in defect research via TSL analysis [48,49,51]. The T_{max}-T_{stop} approach involves measuring multiple TSL curves of the same sample, with each cycle of irradiation and heating followed by preheating to a progressively higher temperature, T_{stop}. On the other hand, the basic principle of IRA assumes that the low-temperature side of the TSL glow peak follows the Arrhenius equation:

$$I(T) = C \bullet \exp\left(-\frac{E_a}{k_B T}\right),$$

where $I(T)$ – intensity as a function of temperature, C – a constant that includes a frequency factor (assumed to be independent of temperature), and T is temperature [52,53]. If $ln(I)$ is plotted as a function of $\frac{1}{k_B T}$, a straight line with a slope of -E_a is obtained to represent the activation energy.

In this study, T_{stop} was increased in 10 °C increments for each measurement. The resulting TSL glow curves are depicted in Fig. 6a for the 0.1 mol% Cr^{3+}-doped sample and in Fig. 6d for the undoped sample. The corresponding IRA plots are shown in Fig. 6b, e, and the obtained activation energy values are shown in Fig. 6c, f.

From the results, it is clear that, in the case of the Cr^{3+}-doped sample, charge traps by their nature can be considered quasi-continuous, as with each increased T_{stop} value, the glow peak maximum (T_{max}) also moves to higher temperatures. The same conclusion can be drawn from the E_a – T_{stop} plot: with each measurement, the activation energy value gradually increased from approximately 0.55 to 0.85 eV. Similarly, for the undoped sample, the first part of the glow curves up to 150 °C can be linked to a quasi-continuous trap depth distribution, with trap depth values from 0.70 to 1.25 eV. In addition, atypical plateau-type TSL bands have been previously interpreted to be related to the thermally assisted tunneling process [54,55]. The deep trap corresponding to the 220 °C glow peak, on the other hand, is a typical example of a discrete trapping center, with T_{max} and E_a values that remain almost constant with increasing T_{stop}. The E_a of this trap was evaluated to be approximately 1.3 eV.

It is established that the best trap depth for excellent persistent luminescence (PersL) performance at RT is around 0.6–0.8 eV [49,52]. Thus, based on the TSL analysis, an afterglow after irradiation with X-rays should be expected from Cr^{3+}-doped and undoped β-TCP samples. Fig. 7 shows PersL decay curves of the 0.1 mol% Cr^{3+}-doped β-TCP sample and undoped β-TCP sample after irradiation for 5 min with X-rays. The PersL spectra throughout all measurement period stayed the same as RT TSL spectra (Fig. 5b), namely, the Cr^{3+} luminescence band in the case of β-TCP: 0.1 mol% Cr^{3+} and Mn^{2+} luminescence band in the case of β-TCP: 0.0 mol% Cr^{3+}. For both samples, afterglow was detected for at least 8 h after the cessation of irradiation.

4. Conclusions

A series of Cr^{3+}-doped β-TCP powders was successfully synthesized by a wet co-precipitation method followed by high-temperature treatment. The dissolution of Cr^{3+} ions in the β-TCP crystal structure is limited. Single-phase materials were obtained with a doping level of up to 2 mol%, whereas the secondary Cr_2O_3 phase was detected with a 5 mol% doping level. EPR spectroscopy revealed the presence of multiple Cr^{3+}-related centers, which most likely arise from the same

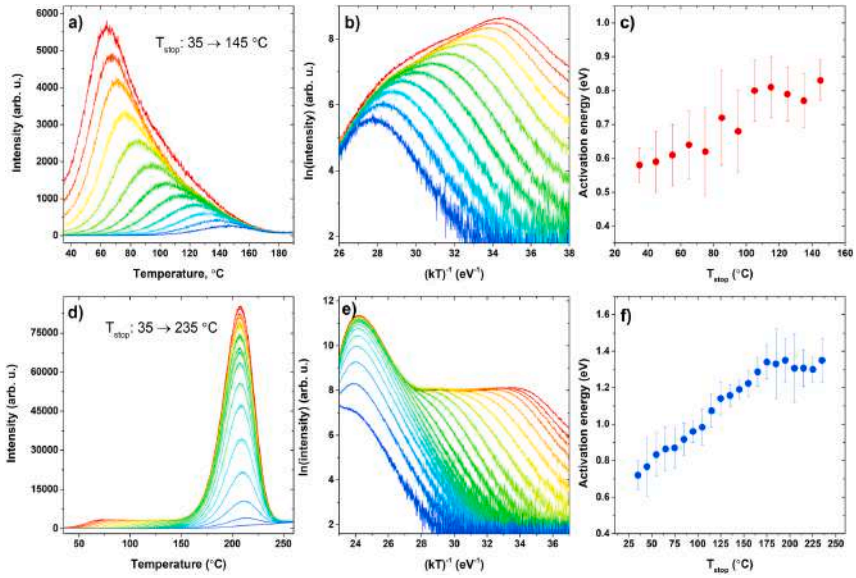

Fig. 6. TSL glow curves measured after preheating to different T_{stop} temperatures; IRA plots of the glow curves obtained from the T_{max}-T_{stop} experiments; E_a – T_{stop} plots obtained by IRA; (a), (b), (c) - 0.1 mol% Cr^{3+}-doped β-TCP sample; (d), (e), (f) - undoped β-TCP sample.

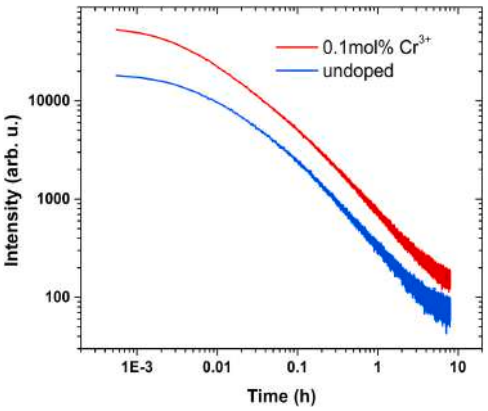

Fig. 7. The afterglow decay curves of the undoped and 0.1 mol% Cr^{3+}-doped β-TCP samples after irradiation for 5 min with X-rays.

crystallographic site but with different defects in the vicinity. All Cr^{3+}-doped β-TCP powders demonstrated broadband emission with a maximum wavelength of 760 nm. The highest intensity was achieved for the 0.1 mol% Cr^{3+} sample, most likely due to concentration quenching at higher Cr^{3+} concentrations. The TSL measurements demonstrated that Cr^{3+}-doped and undoped samples have fundamentally different trap structures. For both the undoped and Cr^{3+}-doped samples, the afterglow after irradiation with X-rays for 5 min can be detected for at least 8 h.

CRediT authorship contribution statement

Sapargali Pazylbek: Methodology, Investigation, Formal analysis, Data curation. **Jonas Stadulis:** Writing – original draft, Visualization, Methodology, Investigation, Formal analysis. **Guna Doke:** Writing – original draft, Visualization, Resources, Methodology, Investigation, Formal analysis. **Andris Antuzevics:** Writing – original draft, Visualization, Methodology, Investigation, Formal analysis. **Mariusz Sandomierski:** Investigation, Formal analysis. **Arturas Katelnikovas:** Writing – review & editing, Methodology, Investigation, Formal analysis. **Chen-Ying Su:** Resources, Investigation, Formal analysis, Data curation. **Hsu-Wei Fang:** Validation, Supervision, Resources, Conceptualization. **Aleksej Zarkov:** Writing – review & editing, Supervision, Resources, Methodology, Funding acquisition, Formal analysis, Conceptualization.

Declaration of competing interest

The authors declare that they have no known competing financial interests or personal relationships that could have appeared to influence the work reported in this paper.

Acknowledgements

This project has received funding from the Research Council of Lithuania (LMTLT), agreement No S-MIP-23-85. A.A. and G.D. acknowledge the donation of SIA "Mikrotikls" (MikroTik) administered by the University of Latvia Foundation, project No. 2326. Institute of Solid State Physics, University of Latvia, Latvia as the Center of Excellence has received funding from the European Union's Horizon 2020 Framework Programme H2020-WIDESPREAD-01-2016-2017-TeamingPhase2 under grant agreement No. 739508, project CAMART^2.

Appendix A. Supplementary data

Supplementary data to this article can be found online at https://doi.org/10.1016/j.optmat.2024.116569.

Data availability

Data will be made available on request.

References

[1] W. Habraken, P. Habibovic, M. Epple, M. Bohner, Calcium phosphates in biomedical applications: materials for the future? Mater. Today 19 (2) (2016) 69–87.
[2] H. Yook, J. Hwang, W. Yeo, J. Bang, J. Kim, T.Y. Kim, J.-S. Choi, J.W. Han, Design strategies for hydroxyapatite-based materials to enhance their catalytic performance and applicability, Adv. Mater. 35 (43) (2023) 2204938.
[3] F. Gao, Z. Wang, M. Fang, X. Tan, S.H. Xu, M. Liu, G.T. Fei, L.D. Zhang, Biological calcium phosphate nanorods for piezocatalytical extraction of U(VI) from water, Nano Res. 16 (11) (2023) 12772–12780.
[4] J. Qiao, J. Zhao, Z. Xia, A review on the Eu^{2+} doped β-$Ca_3(PO_4)_2$-type phosphors and the sites occupancy for photoluminescence tuning, Opt. Mater. X 1 (2019) 100019.
[5] C. Qi, J. Lin, L.-H. Fu, P. Huang, Calcium-based biomaterials for diagnosis, treatment, and theranostics, Chem. Soc. Rev. 47 (2) (2018) 357–403.
[6] M. Gu, W. Li, L. Jiang, X. Li, Recent progress of rare earth doped hydroxyapatite nanoparticles: luminescence properties, synthesis and biomedical applications, Acta Biomater. 148 (2022) 22–43.
[7] M. Bohner, B.L.G. Santoni, N. Döbelin, β-tricalcium phosphate for bone substitution: synthesis and properties, Acta Biomater. 113 (2020) 23–41.
[8] Z. Fan, Y. Wang, Z. Leng, G. Gao, L. Li, L. Huang, G. Li, Luminescence-monitored progressive chemical pressure implementation realized through successive Y^{3+} and Mg^{2+} doping into $Ca_{10.5}(PO_4)_7$:Eu^{2+}, J. Am. Chem. Soc. 146 (16) (2024) 11500–11506.
[9] M. Yashima, A. Sakai, T. Kamiyama, A. Hoshikawa, Crystal structure analysis of β-tricalcium phosphate $Ca_3(PO_4)_2$ by neutron powder diffraction, J. Solid State Chem. 175 (2) (2003) 272–277.
[10] L. Sinusaite, A. Popov, A. Antuzevics, K. Mazeika, D. Baltrunas, J.-C. Yang, J. L. Horng, S. Shi, T. Sekino, K. Ishikawa, A. Kareiva, A. Zarkov, Fe and Zn co-substituted beta-tricalcium phosphate (β-TCP): synthesis, structural, magnetic, mechanical and biological properties, Mater. Sci. Eng. C. 112 (2020) 110918.
[11] D.V. Deyneko, Y. Zheng, K. Barbaro, V.N. Lebedev, S.M. Aksenov, E.Y. Borovikova, M.R. Gafurov, I.V. Fadeeva, B.I. Lazoryak, G. Di Giacomo, C. Cicione, V. Tilotta, F. Russo, G. Vadalà, J.V. Rau, Dependence of antimicrobial properties on site-selective arrangement and concentration of bioactive Cu^{2+} ions in tricalcium phosphate, Ceram. Int. 49 (13) (2023) 21308–21323.
[12] S. Liu, Y. Liang, X. Ma, H. Li, W. Zhang, D. Tu, Y. Chen, Tunable photoluminescence and energy transfer efficiency in β-$Ca_3(PO_4)_2$-$Ca_9La(PO_4)_7$:Eu^{2+}, Mn^{2+} solid solution phosphors introduced by emptying site and structural confinement effect for solid-state lighting application, Inorg. Chem. 59 (6) (2020) 3596–3605.
[13] J.B. Vincent, New evidence against chromium as an essential trace element, J. Nutr. 147 (12) (2017) 2212–2219.
[14] M. Back, J. Ueda, H. Nambu, M. Fujita, A. Yamamoto, H. Yoshida, H. Tanaka, M. G. Brik, S. Tanabe, Boltzmann thermometry in Cr^{3+}-doped Ga_2O_3 polymorphs: the structure matters, Adv. Opt. Mater. 9 (9) (2021) 2100033.
[15] W. Bu, T. Wang, Y. Wang, W. Huang, L. Guo, Y. Yue, X. Zhu, J. Xiao, X. Yu, Near-Infrared Mechanoluminescence of $Gd_3Ga_5O_{12}$: Cr^{3+}, La^{3+} for Biological Stress Imaging, Laser Photonics Rev., 2024 2400893.
[16] Y. Zhang, Z. Peng, X. Chen, D. Gao, X. Sha, Y. Zhang, L. Wang, T. Liu, X. Zhang, J. Zhang, Y. Cao, Y. Wang, L. Li, X. Li, S. Xu, H. Yu, B. Chen, Cooling condition effect on spectral properties and smartphone-based anticounterfeiting application of $Zn_3Ga_2Ge_2O_{10}/Cr^{3+}$ phosphors, Inorg. Chem. 63 (30) (2024) 14152–14161.
[17] Z. Liao, M. Sójka, J. Zhong, J. Brgoch, Developing the $Na_2CaZr_2Ge_3O_{12}$:Cr^{3+} garnet phosphor for advanced NIR pc-LEDs in night vision and bioimaging, Chem. Mater. 36 (9) (2024) 4654–4663.
[18] M. Schamel, A. Bernhardt, M. Quade, C. Würkner, U. Gbureck, C. Moseke, M. Gelinsky, A. Lode, Cu^{2+}, Co^{2+} and Cr^{3+} doping of a calcium phosphate cement influences materials properties and response of human mesenchymal stromal cells, Mater. Sci. Eng. C. 73 (2017) 99–110.
[19] S. Tautkus, K. Ishikawa, R. Ramanauskas, A. Kareiva, Zinc and chromium co-doped calcium hydroxyapatite: sol-gel synthesis, characterization, behaviour in simulated body fluid and phase transformations, J. Solid State Chem. 284 (2020) 121202.
[20] I.V. Zatovsky, N.Y. Strutynska, V.N. Baumer, O.V. Shishkin, N.S. Slobodyanik, The whitlockite-related phosphate $Ca_9Cr(PO_4)_7$, Acta Crystallogr. E 63 (10) (2007) i180–i181.
[21] A.Z. Alshemary, Y.-F. Goh, I. Shakir, R. Hussain, Synthesis, characterization and optical properties of chromium doped β-Tricalcium phosphate, Ceram. Int. 41 (1, Part B) (2015) 1663–1669.
[22] F. Zhao, Z. Song, Q. Liu, Novel Cr^{3+}-activated far-red emitting phosphors with β-$Ca_3(PO_4)_2$-type structure for indoor plant cultivation, Int. J. Miner. Metall. Mater. 29 (6) (2022) 1286–1294.

[23] S.A. Alawsh, S.M.H. Qaid, M. Alkadi, N.N. Asemi, A.A.A. Ahmed, Chromium activated $Ca_9Al(PO_4)_7$ nanophosphors: synthesis, morphology and dosimetry characteristics, Phys. Scr. 99 (1) (2024) 015942.
[24] D. Griesiute, L. Sinusaite, A. Kizalaite, A. Antuzevics, K. Mazeika, D. Baltrunas, T. Goto, T. Sekino, A. Kareiva, A. Zarkov, The influence of Fe^{3+} doping on thermally induced crystallization and phase evolution of amorphous calcium phosphate, CrystEngComm 23 (26) (2021) 4627–4637.
[25] L. Sinusaite, A. Antuzevics, A.I. Popov, U. Rogulis, M. Misevicius, A. Katelnikovas, A. Kareiva, A. Zarkov, Synthesis and luminescent properties of Mn-doped alpha-tricalcium phosphate, Ceram. Int. 47 (4) (2021) 5335–5340.
[26] L. Sinusaite, I. Grigoraviciute-Puroniene, A. Popov, K. Ishikawa, A. Kareiva, A. Zarkov, Controllable synthesis of tricalcium phosphate (TCP) polymorphs by wet precipitation: effect of washing procedure, Ceram. Int. 45 (9) (2019) 12423–12428.
[27] L. Sinusaite, A. Kareiva, A. Zarkov, Thermally induced crystallization and phase evolution of amorphous calcium phosphate substituted with divalent cations having different sizes, Cryst. Growth Des. 21 (2) (2021) 1242–1248.
[28] A. Jillavenkatesa, R.A. Condrate Sr., The infrared and Raman spectra of β-and α-tricalcium phosphate ($Ca_3(PO_4)_2$), Spectrosc. Lett. 31 (8) (1998) 1619–1634.
[29] R.K. Singh, M. Srivastava, N.K. Prasad, S. Awasthi, A. Dhayalan, S. Kannan, Iron doped β-Tricalcium phosphate: synthesis, characterization, hyperthermia effect, biocompatibility and mechanical evaluation, Mater. Sci. Eng. C. 78 (2017) 715–726.
[30] C. Mellier, F. Fayon, V. Schnitzler, P. Deniard, M. Allix, S. Quillard, D. Massiot, J.-M. Bouler, B. Bujoli, P. Janvier, Characterization and properties of novel gallium-doped calcium phosphate ceramics, Inorg. Chem. 50 (17) (2011) 8252–8260.
[31] A. Antuzevics, G. Krieke, G. Doke, A. Zarins, L. Avotina, E. Sprugis, J. Stadulis, A. Beganskiene, A. Kareiva, A. Zarkov, Electron paramagnetic resonance and luminescence spectroscopy of transition metal ion impurities and X-ray-induced radicals in brushite, J. Alloys Compd. 996 (2024) 174779.
[32] C.R. Kesavulu, R.P.S. Chakradhar, R.S. Muralidhara, J.L. Rao, R.V. Anavekar, EPR, optical absorption and photoluminescence properties of Cr^{3+} ions in lithium borophosphate glasses, J. Alloys Compd. 496 (1) (2010) 75–80.
[33] F.S. De Vicente, F.A. Santos, B.S. Simões, S.T. Dias, M. Siu Li, EPR, optical absorption and luminescence studies of Cr^{3+}-doped antimony phosphate glasses, Opt. Mater. 38 (2014) 119–125.
[34] K. Kowalska, M. Kuwik, J. Polak, J. Pisarska, W.A. Pisarski, EPR and optical spectroscopy of Cr^{3+} ions in barium gallo-germanate glasses containing B_2O_3/TiO_2, J. Lumin. 245 (2022) 118775.
[35] P. Rodionovs, M. Kemere, A. Antuzevics, U. Rogulis, A. Sarakovskis, A. Fedotovs, Multi-site incorporation of Cr^{3+} in $CaAl_{12}O_{19}$, Materialia 32 (2023) 101927.
[36] G. Doke, A. Antuzevics, G. Krieke, A. Kalnina, A. Sarakovskis, Novel broadband near-infrared emitting long afterglow phosphor $MgGeO_3$: Cr^{3+}, J. Alloys Compd. 918 (2022) 165768.
[37] M. Back, J. Ueda, J. Xu, K. Asami, M.G. Brik, S. Tanabe, Effective ratiometric luminescent thermal sensor by Cr^{3+}-doped mullite $Bi_2Al_4O_9$ with robust and reliable performances, Adv. Opt. Mater. 8 (11) (2020) 2000124.
[38] Y. Katayama, B. Viana, D. Gourier, J. Xu, S. Tanabe, Photostimulation induced persistent luminescence in $Y_3Al_2Ga_3O_{12}$:Cr^{3+}, Opt. Mater. Express 6 (4) (2016) 1405–1413.
[39] S. Shionoya, W.M. Yen, H. Yamamoto, Phosphor Handbook, CRC press, 2018.
[40] Y. Tanabe, S. Sugano, On the absorption spectra of complex ions. I, J. Phys. Soc. Jpn. 9 (5) (1954) 753–766.
[41] Y. Tanabe, S. Sugano, On the absorption spectra of complex ions II, J. Phys. Soc. Jpn. 9 (5) (1954) 766–779.
[42] M. Back, E. Trave, J. Ueda, S. Tanabe, Ratiometric optical thermometer based on dual near-infrared emission in Cr^{3+}-doped bismuth-based gallate host, Chem. Mater. 28 (22) (2016) 8347–8356.
[43] B. Henderson, A. Marshall, M. Yamaga, K.P.O. Donnell, B. Cockayne, The temperature dependence of Cr^{3+} photoluminescence in some garnet crystals, J. Phys. C Solid State Phys. 21 (36) (1988) 6187.
[44] M. Yamaga, B. Henderson, K.P. O'Donnell, G. Yue, Temperature dependence of the lifetime of Cr^{3+} luminescence in garnet crystals, Appl. Phys. B 51 (2) (1990) 132–136.
[45] J. Ueda, M. Back, M.G. Brik, Y. Zhuang, M. Grinberg, S. Tanabe, Ratiometric optical thermometry using deep red luminescence from $^4T_2$ and ^2E states of Cr^{3+} in $ZnGa_2O_4$ host, Opt. Mater. 85 (2018) 510–516.
[46] T. Gao, R. Liu, Y. Liu, X. Chen, X. Ma, Spectral design in Cr^{3+}-doped NIR phosphors via crystal field modulation, J. Lumin. 246 (2022) 118799.
[47] A. Vedda, M. Fasoli, Tunneling recombinations in scintillators, phosphors, and dosimeters, Radiat. Meas. 118 (2018) 86–97.
[48] A.J.J. Bos, Theory of thermoluminescence, Radiat. Meas. 41 (2006) S45–S56.
[49] S. McKeever, Thermoluminescence of Solids, Cambridge University Press, 1985.
[50] C. Sunta, Unraveling Thermoluminescence, Springer, 2014.
[51] J. Azorín, Determination of thermoluminescence parameters from glow curves—I. A review, Int. J. Rad. Appl. Instr. D 11 (3) (1986) 159–166.
[52] K. Van den Eeckhout, A.J.J. Bos, D. Poelman, P.F. Smet, Revealing trap depth distributions in persistent phosphors, Phys. Rev. B 87 (4) (2013) 045126.
[53] V. Pagonis, G. Kitis, C. Furetta, Numerical and Practical Exercises in Thermoluminescence, Springer Science & Business Media, 2006.
[54] G. Doke, G. Krieke, A. Antuzevics, A. Sarakovskis, B. Berzina, Optical properties of red-emitting long afterglow phosphor $Mg_2Si_{1-x}Ge_xO_4$: Mn^{2+}/Mn^{4+}, Opt. Mater. 137 (2023) 113500.
[55] Y. Kitagawa, J. Ueda, S. Tanabe, Blue persistent phosphor of $YSiO_2N$:Ce^{3+} developed by codoping Sm^{3+} or Tm^{3+} ions and thermoluminescence analysis of their trap distributions, Phys. Status Solidi A 219 (5) (2022) 2100670.

3rd publication

Tunable broadband visible emission achieved by phase transformation-driven self-reduction of Eu^{3+} to Eu^{2+} in a calcium phosphate matrix

S. Pazylbek, J. Stadulis, G. Doke, A. Antuzevics, V. Pankratov, G. Merkininkaite, A. Katelnikovas, A. Zarkov

Dalton Transactions 54(21) **(2025)** 8625-8634
(https://doi.org/10.1039/D5DT00681C)

Dalton Transactions

ROYAL SOCIETY OF CHEMISTRY

PAPER

View Article Online
View Journal | View Issue

Check for updates

Cite this: *Dalton Trans.*, 2025, **54**, 8625

Tunable broadband visible emission achieved by phase transformation-driven self-reduction of Eu^{3+} to Eu^{2+} in a calcium phosphate matrix†

Sapargali Pazylbek,‡[a] Jonas Stadulis,‡[a] Guna Doke,[a,b] Andris Antuzevics,[b] Vladimir Pankratov,[b] Greta Merkininkaite,[a] Arturas Katelnikovas[a] and Aleksej Zarkov *[a]

Received 20th March 2025,
Accepted 19th April 2025

DOI: 10.1039/d5dt00681c

rsc.li/dalton

In this work, we report the synthesis of Eu^{2+}-doped alpha-tricalcium phosphate (α-TCP, α-$Ca_3(PO_4)_2$) *via* a phase transformation of Eu^{3+}-doped $CaHPO_4{\cdot}2H_2O$. The phase conversion accompanied by a reduction of Eu^{3+} to Eu^{2+} occurred during the annealing of the starting material in a vacuum. The optical properties of the obtained α-TCP:Eu^{2+} were investigated by photoluminescence (PL), thermally stimulated luminescence, and persistent luminescence decay measurements. The obtained material exhibited tunable broadband PL with FWHM values ranging from 87 to 142 nm at room temperature. The PL can be tuned in terms of emission maximum and FWHM by varying the excitation wavelength. The broadband emission was achieved due to the multi-site occurrence of Eu^{2+} ions in the complex α-TCP matrix. Three types of traps were determined with activation energy values of 0.80, 0.75, and 0.68 eV. After irradiation with X-rays, an afterglow characterizable by an Eu^{2+} broadband spectrum with a maximum at around 480 nm can be detected for at least 10 h.

Open Access Article. Published on 21 April 2025. Downloaded on 5/27/2025 4:15:04 PM.
This article is licensed under a Creative Commons Attribution 3.0 Unported Licence.

1. Introduction

The design of visible broadband emission phosphors is crucial for developing next-generation phosphor-converted white-light-emitting diodes (pc-WLEDs), which are considered efficient, green, and energy-saving light sources. Recent efforts have been focused on designing single-activator phosphors to overcome the disadvantages of combining phosphors with distinct emission colors.[1] As one of the most common and highly efficient activators, the Eu^{2+} ion possesses broadband absorption in the UV to blue regions and multicolor emission. The optical properties of Eu^{2+}-doped phosphors strongly depend on the local environment of Eu^{2+} ions.[2] Consequently, the emission of Eu^{2+}-doped materials can be tuned by site occupancy engineering, resulting in the emission maximum from blue to infrared,[2] while the multiple-site occupancy of Eu^{2+} ions in a single host favors broadband emission.[3] For this reason, a structural engineering strategy is often employed to develop single broadband white-emitting phosphors. Recently, broadband Eu^{2+} emission was achieved in various inorganic matrices such as $Ba_3ScB_3O_9$,[4] $Ca_3Sc_2Si_3O_{12}$,[5] $Ba_3GeO_4Br_2$,[6] $K_2BaSr(PO_4)_{2-x}(BO_3)_x$,[7] *etc.*

Different phosphate-based matrices, including those of the calcium phosphate (CP) family, are widely employed to prepare lanthanide-activated phosphors.[8–10] Recent works on β-$Ca_3(PO_4)_2$-type (β-TCP) materials demonstrated the feasibility of the design of Eu^{2+}-based broadband phosphors. For instance, Fan *et al.* achieved a broadband visible emission in Eu^{2+}-activated β-TCP by employing chemical pressure.[11] The occupation of Eu^{2+} ions in the crystal lattice and resulting emission were tuned through the co-substitution of Ca^{2+} by Y^{3+} and Mg^{2+}. Full-spectrum white-light emission from Eu^{2+} ions occupying 3 inequivalent crystallographic sites was demonstrated for the $Ca_{9-y}Mg_yNaGd_{0.667}(PO_4)_7$:$Eu^{2+}$ phosphor.[12] Ultra-broadband emission reaching an FWHM of 330 nm was realized by Liu *et al.*[1] in $Ca_9LiMg_{1-x}Al_{2x/3}(PO_4)_7$:$Eu^{2+}$; in this case, the Eu^{2+} ions occupied 4 different sites. β-TCP is a low-temperature polymorph with 5 inequivalent Ca sites, allowing multi-site doping. The crystal structure of the high-temperature α-TCP polymorph is more complicated, containing 18 Ca sites.[13] This structural feature makes the α-TCP matrix highly attractive for developing broadband phosphors.

Most commonly, Eu^{2+}-doped materials are synthesized in a reducing atmosphere;[14] nevertheless, some specific inorganic

[a]*Institute of Chemistry, Vilnius University, Naugarduko 24, LT-03225 Vilnius, Lithuania. E-mail: aleksej.zarkov@chf.vu.lt*
[b]*Institute of Solid State Physics, University of Latvia, Kengaraga 8, LV-1063 Riga, Latvia*

†Electronic supplementary information (ESI) available. See DOI: https://doi.org/10.1039/d5dt00681c

‡These authors contributed equally.

Open Access Article. Published on 21 April 2025. Downloaded on 5/27/2025 4:15:04 PM.
This article is licensed under a Creative Commons Attribution 3.0 Unported Licence.

matrices allow the stabilization of the Eu^{2+} oxidation state in air. The self-reduction phenomenon is typically observed in materials such as borates,[15–17] silicates,[18] and phosphates.[19–21] In this light, CPs can also be considered suitable hosts for observing the self-reduction phenomenon.

CPs are a family of materials that can be classified by various parameters, including crystal structure, Ca/P ratio, and the presence of different structural species. Under particular conditions, the transformation from one phase to another phase can be achieved, including, but not limited to, polymorphism.[22,23] Thermally induced phase transformations of different CP phases suggest the thermal treatment of the starting material at elevated temperatures. The Ca/P ratio in starting materials and final products is usually expected to be identical; however, recently, it was shown that the phase conversion between different CPs can occur with a drastic change in the Ca/P ratio from 1 : 1 ($Ca_2P_2O_7$) to 1.5 : 1 ($Ca_3(PO_4)_2$) under certain conditions due to the evaporation of the phosphate species.[24]

Some reports on the preparation and investigation of Eu^{2+}-doped α-TCP are already known; however, some contradictions can be found. For instance, the preparation of $Ca_3(PO_4)_2$:Eu^{2+} reported by Ji *et al.*[25] and Zhou *et al.*[26] required a reducing atmosphere, while the optical properties of the products were tuned by varying the material cooling conditions during the synthesis or the Eu content. In the works by Li *et al.*,[27,28] the partial self-reduction of Eu^{3+} to Eu^{2+} was observed in α-TCP synthesized by solid-state reaction under an air atmosphere; however, the emission spectra (λ_{ex} = 393 nm) of the obtained materials were clearly dominated by the emission from Eu^{3+} ions indicating a low degree of reduction.

In the present work, we employed a phase transformation approach for preparing Eu^{2+}-doped α-TCP from Eu^{3+}-doped $CaHPO_4{\cdot}2H_2O$ (DCPD). The highly efficient self-reduction of Eu^{3+} to Eu^{2+} occurred during the phase conversion, resulting in multi-site doping and broadband PL that covered the entire visible spectrum. The tunable luminescence in terms of emission maximum and FWHM was achieved by varying the excitation wavelength.

2. Experimental

2.1. Synthesis

The starting Eu^{3+}-doped DCPD powder was synthesized by the wet co-precipitation method modifying a previously reported procedure.[24,29] For the synthesis, calcium nitrate tetrahydrate ($Ca(NO_3)_2{\cdot}4H_2O$, Carl Roth, >99%), europium(III) nitrate hexahydrate ($Eu(NO_3)_3{\cdot}6H_2O$, 99.9%, Acros Organics), and diammonium hydrogen phosphate ($(NH_4)_2HPO_4$, Carl Roth, >98%) were used as starting materials. First, the metal nitrates were dissolved in deionized water, resulting in a 0.8 M solution, where the Eu-substitution level was adjusted to 0.1 mol% with respect to Ca^{2+} ions. The $(NH_4)_2HPO_4$ solution of the same concentration was prepared in parallel. The solution containing phosphate ions was rapidly poured into the solution of metal ions under constant stirring, forming white precipitates. The as-prepared precipitates were aged in the reaction mixture for 5 min, and afterward, were vacuum filtered, washed with deionized water and dried in an oven at 50 °C overnight. For the synthesis of Eu-doped α-TCP, the as-prepared precipitates were annealed in a tube furnace in a vacuum (7.8×10^{-2} mbar) at 1300 °C for 24 h. After the annealing procedure, the furnace was allowed to cool down naturally.

2.2. Characterization

Powder X-ray diffraction (XRD) analysis was performed using a Rigaku MiniFlex II diffractometer (Cu-Kα, λ = 1.5419 Å) working in Bragg–Brentano ($\theta/2\theta$) geometry. The data were collected within the 10–60° 2θ range with a step of 0.02° and a scanning speed of 5° min^{-1}.

The morphological features of the synthesized powder were analyzed by scanning electron microscopy (SEM) using a Hitachi SU-70 microscope.

A Bruker ELEXSYS-II E500 CW-EPR spectrometer was used for electron paramagnetic resonance (EPR) investigations of the sample. The spectral acquisition settings were: room temperature, 9.838 GHz (X-band) or 34.02 GHz (Q-band) microwave frequency, 10 mW microwave power, and 0.4 mT magnetic field modulation amplitude.

The photoluminescence excitation (PLE) and photoluminescence emission (PL) spectra were measured using an Edinburgh Instruments FLS980 spectrometer equipped with double excitation and emission monochromators, a 450 W Xe arc lamp, a cooled (−20 °C) single-photon counting photomultiplier (Hamamatsu R928P), and mirror optics for the powder samples. Emission spectra were recorded using a 0.5 nm emission slit width, a 3.5 nm excitation slit width, a step size of 0.5 nm, and an integration time of 0.2 s, and were averaged over three repetitions. Excitation spectra were acquired using a 1.5 nm emission slit width, a 0.5 nm excitation slit width, the same step size and integration time, and also averaged over three repetitions. The PL spectra were corrected by a correction file obtained from a tungsten incandescent lamp certified by the NPL (National Physics Laboratory, UK). The PLE spectra were corrected by a reference detector. PL decay curves were measured using the same Edinburgh Instruments FLS980 spectrometer. A 405 nm pulsed laser diode (Edinburgh Instruments, EPL-405) was used as an excitation source.

Thermally stimulated luminescence (TSL) and persistent luminescence decay measurements were performed using a Lexsyg research fully automated TSL/OSL reader from Freiberg Instruments GmbH equipped with a Hamamatsu R13456 photomultiplier tube. An Andor SR-303i-B spectrometer coupled with a DV420A-BU2 CCD camera was used to obtain a persistent luminescence spectrum. A VF-50 J/S X-ray tube (40 kV, 0.5 mA, W-anode) or Q-switched short-pulsed UV laser DTL-389QT (263 nm) from the Laser-compact Group was used as the irradiation source. The system was operated at a linear heating rate of 1 °C s^{-1}. The afterglow decay was measured at a temperature of 25 °C. To eliminate any effects of previously stored energy, the samples were preheated to 300 °C before each measurement.

 This journal is © The Royal Society of Chemistry 2025

Open Access Article. Published on 21 April 2025. Downloaded on 5/27/2025 4:15:04 PM.
This article is licensed under a Creative Commons Attribution 3.0 Unported Licence.

3. Results and discussion

The XRD pattern of the as-precipitated powder is shown in Fig. S1.† The major phase was identified as DCPD, in accordance with a previous study.[30] A secondary monetite (DCPA, $CaHPO_4$) phase was also detected; however, its presence is not considered critical since the Ca/P ratio in both DCPD and DCPA is the same (Ca/P = 1 : 1). Moreover, upon annealing in air, DCPD first decomposes exactly to DCPA with further transformation to $Ca_2P_2O_7$ (CPP) at higher temperatures.[31] The PL spectrum of the as-prepared Eu-doped DCPD exhibits several peaks ranging from approximately 520 to 720 nm (Fig. S2†). These peaks are ascribed to the Eu^{3+} radiation emitted by 4f–4f transitions, specifically $^5D_0 \rightarrow {}^7F_{0-4}$,[32,33] and there was no emission attributed to Eu^{2+}.

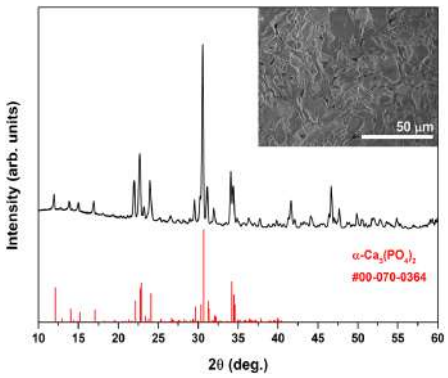

Fig. 1 XRD pattern of Eu-doped α-TCP obtained after annealing of Eu-doped DCPD in a vacuum at 1300 °C. Inset: SEM micrograph of Eu-doped α-TCP.

The XRD pattern of the material annealed in a vacuum at 1300 °C is given in Fig. 1. Evidently, the phase transformation to α-TCP occurred. The diffraction peaks matched very well with the standard XRD data of monoclinic $Ca_3(PO_4)_2$ (#00-070-0364). Such a transformation indicates the evaporation of phosphate species and formation of the CP phase with a significantly higher Ca/P ratio (Ca/P = 1.5 : 1). The SEM image (inset of Fig. 1) demonstrates the formation of monoliths with undefined shape and size varying in a microscopic range, which is typical for α-TCP prepared at high temperature.[34]

The normalized PLE spectra of Eu-doped α-TCP at emission wavelengths of 475 and 610 nm are shown in Fig. 2a. When monitored at λ_{em} = 475 nm, a broad band is seen, which is assigned to the $4f^7 \rightarrow 4f^65d^1$ transition of Eu^{2+} ions; however, for λ_{em} = 610 nm, the shape of the PLE spectrum changed significantly. The difference in the shape of the PLE spectra suggests that Eu^{2+} ions occupy at least 2 different sites. The sharp lines are associated with the presence of a minor Eu^{3+} amount and indicate incomplete reduction. These lines originate from $^7F_0 \rightarrow {}^5D_4$ (*ca.* 361.5 nm), $^7F_0 \rightarrow {}^5G_2$ (*ca.* 368.5 nm),

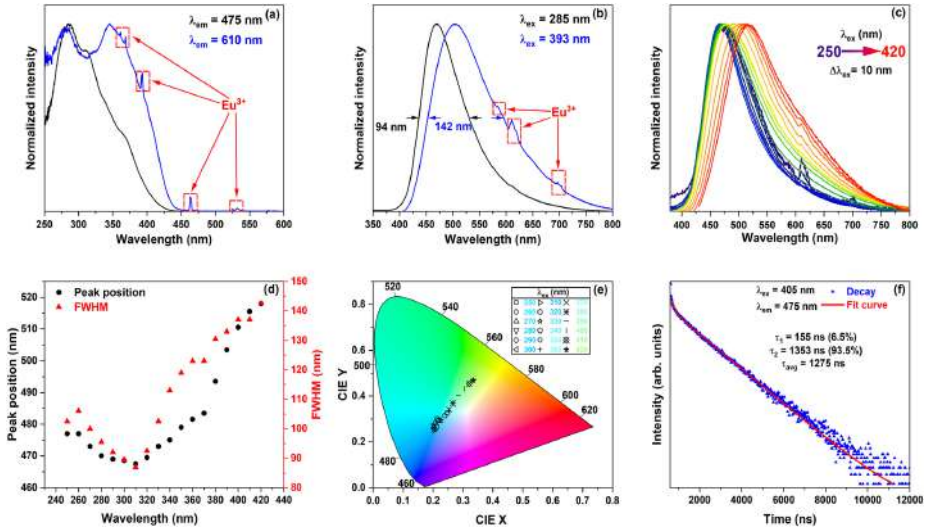

Fig. 2 Normalized PLE (λ_{em} = 475 and 610 nm) spectra (a); normalized PL (λ_{ex} = 285 and 393 nm) spectra (b); normalized PL spectra obtained under different excitation wavelengths (c); dependence of the emission maximum and FWHM on the excitation wavelength (d); dependence of the CIE 1931 chromaticity coordinates on the excitation wavelength (e); and the decay curve (λ_{ex} = 405 nm and λ_{em} = 475 nm) (f) for Eu-doped α-TCP.

Open Access Article. Published on 21 April 2025. Downloaded on 5/27/2025 4:15:04 PM.
This article is licensed under a Creative Commons Attribution 3.0 Unported Licence.

$^7F_0 \rightarrow {}^5L_6$ (*ca.* 393 nm), $^7F_0 \rightarrow {}^5D_2$ (*ca.* 464 nm), $^7F_0 \rightarrow {}^5D_1$ (*ca.* 525 nm), and $^7F_1 \rightarrow {}^5D_1$ (*ca.* 532 nm) intraconfigurational [Xe] $4f^6 \rightarrow$ [Xe]$4f^6$ transitions of Eu^{3+} ions.[35]

The PL spectrum obtained under 285 nm excitation exhibited a single broadband emission centered at 470 nm with an FWHM of 94 nm (4068 cm^{-1}), which is attributed to the $4f^65d^1 \rightarrow 4f^7$ transition typical of Eu^{2+} (Fig. 2b). The emission spectrum covers the entire range of visible light, while the asymmetric shape of the emission also suggests the presence of Eu^{2+} in multiple sites. In mixed-valent Eu-doped materials, the emission can be tuned by varying the excitation wavelength, which allows the observation of the emission of exclusively Eu^{2+} or Eu^{3+} ions or control of the intensity ratio of simultaneous emission.[19,36,37] Such an effect allowing for direct control of the luminescence color is achieved due to the overlap in the excitation spectra of Eu^{2+} and Eu^{3+} within the range of 250–450 nm.[18] Therefore, we also recorded the PL spectrum under an excitation wavelength of 393 nm. The emission lines associated with Eu^{3+} can be seen at *ca.* 590 nm ($^5D_0 \rightarrow {}^7F_1$), 610 nm ($^5D_0 \rightarrow {}^7F_2$), and 700 nm ($^5D_0 \rightarrow {}^7F_4$); however, the emission spectrum is still dominated by the broadband emission of Eu^{2+}. The Eu^{2+} emission maximum was red-shifted to 503 nm, and a significant increase in the FWHM value to 142 nm (5268 cm^{-1}) was observed. Considering these spectral changes, we investigated the dependence of emission spectra on the excitation wavelength, systematically changing λ_{ex} from 250 to 420 nm with a step of 10 nm (Fig. 2c). This variation allowed tuning of the emission spectra in terms of emission maximum and FWHM (Fig. 2d). Two opposite trends were observed depending on the excitation wavelength: the increase of the excitation wavelength from 250 to 310 nm led to a blue shift accompanied by the narrowing of the emission band, while in the range from 310 to 420 nm, the effect was opposite. Summarizing, under specific excitation, the emission maximum can be shifted from 467 to 517 nm, and FWHM values can be varied from 87 to 142 nm. Yu *et al.*[37] previously achieved similar spectral tuning in Eu^{2+}/Eu^{3+}-doped Ba_2InTaO_6. The authors associated the observed shift with the occupation of different crystallographic sites by Eu^{2+} ions. The observed dependence of the CIE 1931 chromaticity coordinates on the excitation wavelength was nearly linear (Fig. 2e), shifting from a blue to greenish-yellow region as the excitation wavelength increased from 310 to 420 nm. The exact coordinate values are summarized in Table S1.† Under specific excitation, a near-white emission can be obtained, demonstrating a color-adjustable emission. Fig. 2f shows the PL emission decay curve of Eu-doped α-TCP when the specimen was excited at 405 nm, and the emission was monitored at 475 nm. A two-exponential PL decay was observed with fast (τ = 0.16 μs) and slow (τ = 1.35 μs) components. The calculated effective PL lifetime value (τ_{eff}) was 1.27 μs. It has been previously reported that the appearance of the fast component could be linked to non-radiative energy migration between Eu^{2+} ions.[38]

The mechanism of Eu^{3+} self-reduction in the phosphates of divalent metals is usually explained by the formation of cationic vacancies due to substitution with aliovalent Eu^{3+} ions.[28,39] Negatively charged vacancies act as electron donors and reduce Eu^{3+} ions to the divalent state, being further protected from the oxidizing air atmosphere by the phosphate framework. In our case, such a mechanism is reasonably accepted; however, during the transformation of CPP to α-TCP in a vacuum, the charged phosphate species are evaporated, which also could influence the oxidation state of Eu ions in the matrix. Some reports on the Eu partial self-reduction in α-TCP synthesized by solid-state reaction are known.[27,28,40] The comparison of the emission spectra under 393 nm revealed that we achieved a significantly higher degree of reduction, which could be associated with the peculiarities of the synthetic approach.

The Eu-doped DCPD precursor was also annealed in air at an identical temperature for comparison. The XRD analysis (Fig. S3†) revealed that the major crystalline phase was α-CPP, which indicates that the Ca/P ratio in the as-prepared and annealed materials is nearly the same. A negligible amount of β-TCP was also identified as an impurity. The formation of α-CPP was expected since α-CPP is assumed to be a high-temperature CPP polymorph, and an annealing procedure was performed above the β- to α-CPP phase transition temperature.[29] The PL spectrum of this sample is dominated by sharp emission lines originating from Eu^{3+}, indicating that Eu ions mainly exist in the +3 oxidation state. Nevertheless, the emission band centered at *ca.* 412 nm was also observed, suggesting that the minor amount of Eu ions was reduced during the annealing. Previously, Doat *et al.*[41] reported the partial stabilization of Eu^{2+} ions in α-CPP synthesized under an air atmosphere and thermally quenched in liquid nitrogen. The emission band arising from Eu^{2+} was observed at 415 nm, which agrees well with our results.

Temperature-dependent PL spectra of Eu-doped α-TCP obtained under excitation wavelengths of 285 and 393 nm are depicted in Fig. 3. Under 285 nm excitation, the PL spectra changed in terms of intensity, spectral shape, and emission maximum (Fig. 3a). At 77 K, two emission peaks centered at 457 and 505 nm are clearly seen; however, with an increase in temperature, the spectral shape transforms into an asymmetric single-peak band. The position of the emission maximum was nearly stable at 470 nm in the temperature range from 150 to 350 K, followed by a red shift at higher temperatures. The FWHM value exhibited a multidirectional trend depending on the temperature: in the range from 77 to 300 K, it decreased, while in the range from 300 to 450 K, it increased (Fig. 3b). The maximum value of 114.5 nm (4761 cm^{-1}) was determined at 77 K. A nearly linear thermal quenching of integrated intensity was observed (Fig. 3b). At 400 K the integrated emission intensity constituted 51% of that at 300 K. The relatively strong thermal quenching of emission might be caused by thermal ionization (photoionization), thermally activated crossover to the ground state, multiphonon-relaxation, and energy transfer to quenching centers.[42–44] The thermal quenching that occurs might limit the phosphor from high-temperature applications. The CIE chromaticity coordinates were located in the cyan-white region (Fig. 3c).

This journal is © The Royal Society of Chemistry 2025

Open Access Article. Published on 21 April 2025. Downloaded on 5/27/2025 4:15:04 PM.
This article is licensed under a Creative Commons Attribution 3.0 Unported Licence.

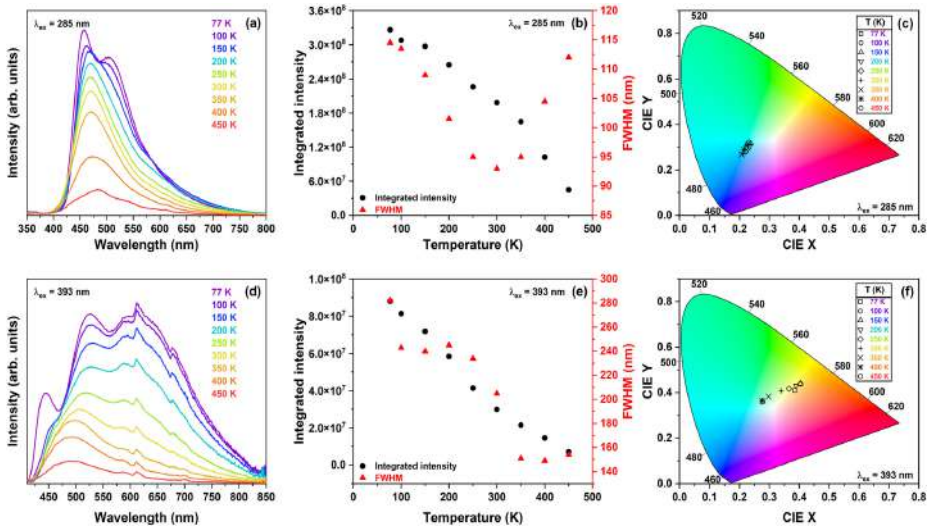

Fig. 3 Temperature-dependent PL spectra (a and d); dependence of integrated emission intensity and FWHM on temperature (b and e); dependence of the CIE 1931 chromaticity coordinates on temperature (c and f) for Eu-doped α-TCP excited at 285 nm (a–c) and 393 nm (d–f).

In the case of 393 nm excitation, the emission spectra obtained were significantly broader (Fig. 3d). The FWHM value demonstrated a decreasing trend in the temperature range from 77 to 350 K and nearly stabilized at higher temperatures (Fig. 3e). The highest value of 282 nm (8942 cm^{-1}) was also observed at 77 K. For the calculations of FWHM, only the emission of Eu^{2+} ions was involved; the emission of Eu^{3+} was ignored. The diversified dependence of FWHM values for both excitation wavelengths can be associated with the different behavior of Eu^{2+} ions occupying particular sites in the crystal lattice. The emission intensity decreased with the increasing temperature owing to the non-radiative decay at higher temperatures. The observed decrease was also nearly linear; in this case, at 400 K, it constituted 49% of that at 300 K. The thermal quenching in the red region was more pronounced, which is reflected in the gradual shift of CIE chromaticity coordinates from orange to greenish-white (Fig. 3f).

The deconvolution of broadband emission spectra with multiple peaks can ascribe the spectral components to the Eu^{2+} ions occupying specific crystallographic sites. For instance, such an approach was demonstrated by Liao *et al.*,[9] who investigated the PL spectra of Eu^{2+}-doped $Rb_{0.5}K_{1.5}CaPO_4$(F, Cl). The authors concluded that there are 3 suitable sites for Eu^{2+} substitution in the analyzed crystal structure; consequently, 3 components of the PL spectrum were specifically ascribed. In our case, the determination of Ca sites occupied by Eu^{2+} ions is extremely challenging due to the peculiarities of the α-TCP crystal structure. This compound crystallizes in a monoclinic crystal structure with a $P2_1/a$ space group having 18 inequivalent crystallographic Ca sites.[45] Considering the doping level investigated in this work, the commonly employed Rietveld refinement of the XRD data does not seem to be a reliable tool for determining the Eu^{2+} position in the crystal lattice.

The theoretical work by Matsunaga *et al.* investigated the thermodynamic equilibrium between TCP polymorphs substituted with divalent cations having different sizes.[46] One of the investigated ions was Sr^{2+}. Taking into account the nearly identical ionic radii of Eu^{2+} and Sr^{2+},[47] a simplified assumption can be made that the behavior of Eu^{2+} in the considered crystal structure could be identical to that of Sr^{2+}. It was shown that 4 specific Ca sites in the α-TCP structure are energetically more favorable for Sr^{2+}. The lowest defect formation energies of Sr^{2+} are in the Ca-5 (CN = 7), Ca-8 (CN = 7), Ca-14 (CN = 7), and Ca-17 (CN = 7) positions, having polyhedron volumes of 19.9, 19.9, 17.2, and 20.0 $Å^3$, respectively.[45]

The fitting of emission spectra obtained at 77 and 300 K under 285 and 393 nm excitation is shown in Fig. 4. Regardless of the excitation wavelength and temperature, all spectra can be fitted with 3 sub-spectra corresponding to Eu^{2+} ions in at least 3 different environments. Another approach for ascribing the sub-spectra proposed by van Uitert considers the calculations involving the coordination number, radius of the cation replaced by Eu^{2+}, and electron affinity of anion atoms.[48] In the case of α-TCP:Eu^{2+}, there is only one type of cation and anion in the matrix. If we assume the abovementioned calculations by Matsunaga *et al.*[46] for Eu^{2+}, the coordination number for all four positions is also the same. Thus, further

Open Access Article. Published on 21 April 2025. Downloaded on 5/27/2025 4:15:04 PM.
This article is licensed under a Creative Commons Attribution 3.0 Unported Licence.

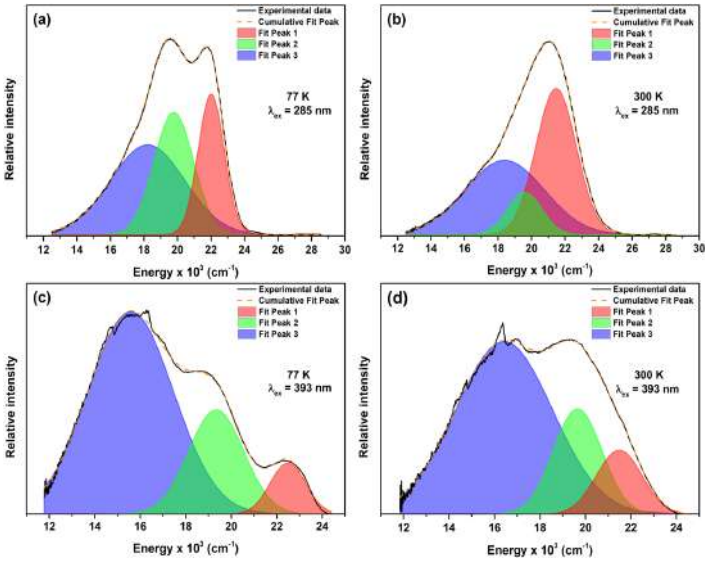

Fig. 4 PL spectra and Gaussian fitting curves of Eu-doped α-TCP for λ_{ex} = 285 nm (a and b) and λ_{ex} = 393 nm (c and d) at 77 K (a and c) and 300 K (b and d).

investigation is needed to attribute the emission of Eu^{2+} centers to specific crystallographic sites.

EPR spectroscopy was employed to confirm the multi-site occupancy of Eu^{2+} ions in α-TCP. The EPR spectra of the investigated α-TCP sample (Fig. 5) indicated the presence of Eu in the divalent state. The detected spectra consisted of many lines spread over a broad field range with maximum intensity at $g \approx 2.0$ (356 mT for the X-band; 1221 mT for the Q-band), typical for Eu^{2+} in various crystalline hosts.[49–52] The EPR spectrum of Eu^{2+} originates from zero-field splitting (ZFS) of the $^8S_{7/2}$ ground state, which results in seven allowed orientation-dependent ZFS transitions.[51,52] In powdered samples, the averaging across all possible single-crystal orientations and the overlap of signals from multiple possible sites generally lead

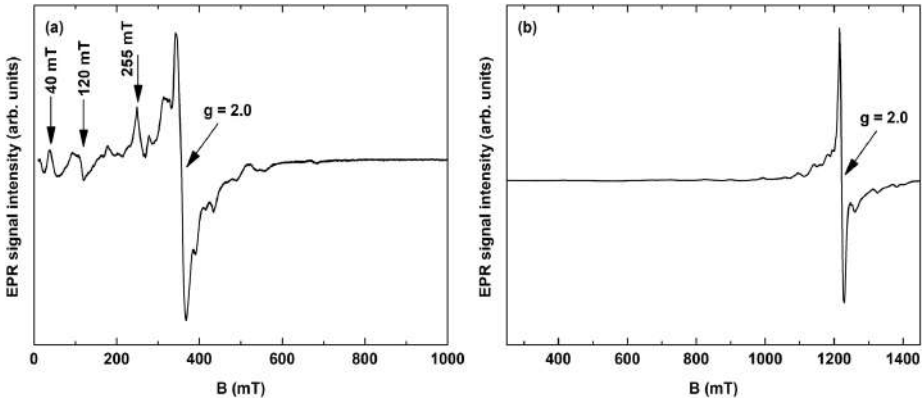

Fig. 5 X-band (a) and Q-band (b) EPR spectra of the Eu-doped α-TCP powder.

This journal is © The Royal Society of Chemistry 2025

Open Access Article. Published on 21 April 2025. Downloaded on 5/27/2025 4:15:04 PM.
This article is licensed under a Creative Commons Attribution 3.0 Unported Licence.

to complex spectra, which are problematic to interpret unambiguously. The "EPR-silent" Eu^{3+} ions do not contribute to the spectrum.[51]

The EPR spectra suggest the formation of several isolated Eu^{2+} centers in α-TCP. One component is quite symmetrically centered at $g \approx 2.0$ in the spectra acquired at both frequency bands, indicating an intermediate ZFS magnitude for this site. Additional signals at lower fields are visible in the X-band spectrum (40, 120, and 255 mT), implying at least one more Eu^{2+} site with larger ZFS values. The absence of broad, structureless signals typically associated with Eu^{2+} clustering effects[50] suggests that europium is sufficiently diluted to form isolated centers in α-TCP.

It was observed that when the Eu-doped α-TCP sample is exposed to ionizing radiation (X-rays and UV), the delocalized charge carriers are generated and subsequently trapped by several charge traps corresponding to different material defects. This effect is demonstrated by the TSL measurements shown in Fig. 6. The basic principle of the TSL method involves irradiation of the material with appropriate high-energy radiation at room or lower temperature; thus, some charge carriers will delocalize and become trapped. Then, the material is heated typically at a constant heating rate, and charges can be released if sufficient energy is accumulated. The luminescence signal may increase and decrease throughout all measuring processes, with increases corresponding to the traps with specific activation energy. In the end, a glow curve consisting of one or more glow peaks as $I = f(T)$ will be obtained.[53]

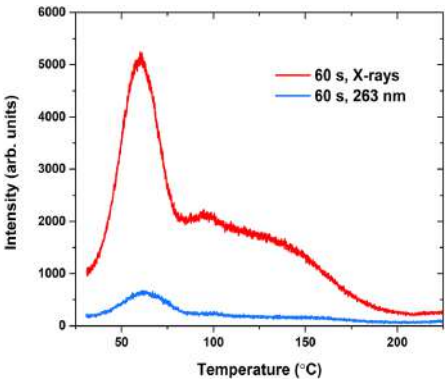

Fig. 6 TSL glow curves of the Eu-doped α-TCP sample after irradiation with X-rays or UV for 60 s, heating rate 1 °C s^{-1}.

Fig. 6 depicts the TSL glow curves of α-TCP:Eu^{2+} after irradiation with X-rays and UV at 263 nm. In both cases, the same structure of glow peaks remains; thus, the same traps are filled regardless of the irradiation source. On the other hand, after exposure to the X-rays, a much stronger TSL signal is detected; thus, there is a higher filled trap concentration. For further analysis, X-ray irradiation was selected. The glow curve consists of multiple glow peaks, with the most prominent one having a maximum at around 60 °C; at higher temperatures, there are indistinguishable numbers of overlapping glow peaks.

For further analysis, the well-established and extensively used T_{max}–T_{stop} and initial rise analysis (IRA) methods were applied.[54–56] For T_{max}–T_{stop}, a step of 5 °C from 35 to 150 °C was used. Measured TSL glow curves are shown in Fig. 7a, while Fig. 7b depicts IRA plots of the same glow curves. The data for Fig. 7c were obtained by analyzing these two plots. The T_{max}–T_{stop} plot reveals that charge traps can be divided into three groups. Similarly, trap depth or activation energy (E_a) values can be divided into groups with approximate values of 0.80, 0.75, and 0.68 eV. However, counterintuitively, lower E_a values correspond to higher T_{stop} values. This goes against

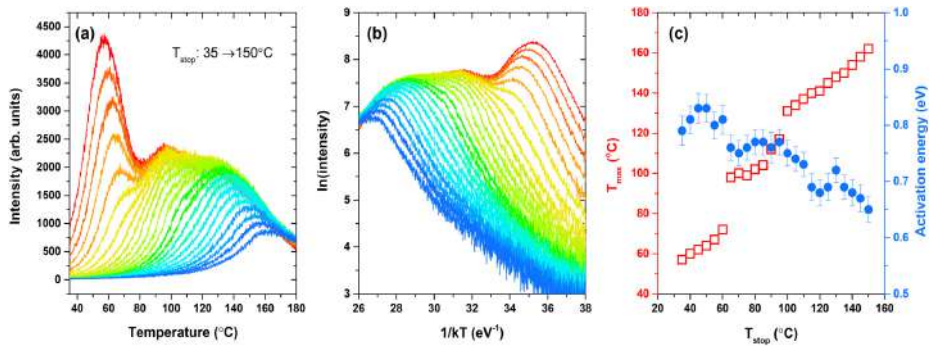

Fig. 7 TSL glow curves of the Eu-doped α-TCP sample after preheating up to different T_{stop} values between 35 and 150 °C with a 5 °C step. The sample was irradiated with X-rays for 60 s before each preheating (a); IRA plots of the glow curves obtained from the T_{max}–T_{stop} experiment (b); the T_{max}–T_{stop} plot and the E_a–T_{stop} plot (c).

Open Access Article. Published on 21 April 2025. Downloaded on 5/27/2025 4:15:04 PM.
This article is licensed under a Creative Commons Attribution 3.0 Unported Licence.

basic TSL theory, which predicts that glow peaks with maxima at higher temperatures correspond to deeper traps. Similar results have been observed previously but not explained indisputably.[57,58] False shallow trap depth value appearance in IRA plots could be linked to de-trapping *via* thermally assisted tunneling, where the obtained E_a value would stand not for the energy necessary to breach the gap between the trap and the band as in the classical TSL process but for the energy difference between the ground level and the tunneling level of a trap.[59,60] However, further investigation outside the scope of this research would be necessary for profound conclusions.

Previous studies have suggested that materials with trap depths of around 0.7 eV could lead to effective persistent luminescence at room temperature.[61] This is also true for the Eu-doped α-TCP sample. After irradiation with X-rays, an afterglow characterizable by an Eu^{2+} typical broadband spectrum[28,62,63] with maxima around 480 nm can be detected for at least 10 h (Fig. 8). The persistent luminescence spectrum is primarily associated with a single Eu^{2+} site. This further suggests tunneling as a key mechanism of persistent luminescence. The tunneling recombination process is highly sensitive to the spatial separation between traps and luminescent centers. Therefore, it is expected that persistent luminescence will be predominantly generated from Eu^2 ions in close proximity to traps.

The α-TCP crystal structure is known to be highly susceptible to the presence of impurities and the conditions of thermal treatment.[46,64] Moreover, thermal quenching is often used to prepare the phase-pure α-TCP; however, the annealing conditions are also closely related to the chemical purity. Unfortunately, we were not able to prepare α-TCP doped with a higher amount of Eu^{2+} due to the melting of the product. At the same time, the synthesis at lower temperatures resulted in the formation of β-TCP impurities. In exploring the self-reduction phenomenon, further attempts should be made to prepare Yb^{2+} and Sm^{2+}-doped α-TCP in a similar manner. Both these ions are redox active; however, their reduction potentials are significantly more negative.[65] Moreover, the distribution of Eu^{2+} ions within the α-TCP structure and, consequently, the optical properties could be tuned by partially substituting Ca^{2+} with Sr^{2+} or Ba^{2+}. While smaller cations are hardly adopted by the α-TCP structure, Sr^{2+} or Ba^{2+} ions can be easily dissolved by occupying particular Ca sites.

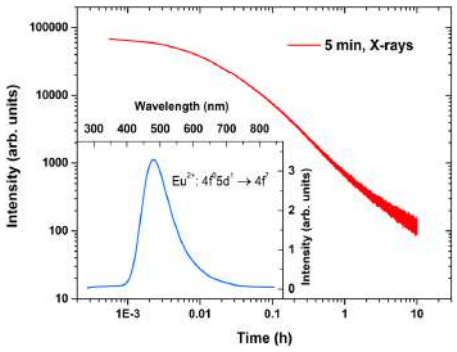

Fig. 8 The afterglow decay curve of the Eu-doped α-TCP sample after irradiation for 5 min with X-rays; inset: the corresponding Eu^{2+} spectrum.

4. Conclusions

In this work, Eu^{2+}-doped α-TCP was successfully synthesized *via* a phase transformation of Eu^{3+}-doped DCPD. The phase conversion, accompanied by a reduction of Eu^{3+} to Eu^{2+}, was achieved by annealing the starting material at 1300 °C in a vacuum. The initial Ca/P ratio of 1 : 1 characteristic of DCPD changed to *ca.* 1.5 : 1 due to the selective evaporation of phosphate species. The obtained material exhibited a broadband emission covering the entire visible spectrum. The emission tunability was achieved by varying the excitation wavelength, resulting in the shift of the emission maximum and FWHM values ranging from 87 to 142 nm at room temperature. The broadband emission was achieved due to the multi-site occupancy of Eu^{2+} ions in a complex α-TCP matrix. The deconvolution of emission spectra indicated that Eu^{2+} ions occupy at least 3 inequivalent crystallographic sites. TSL measurements revealed the presence of three types of traps with activation energy values of 0.80, 0.75, and 0.68 eV. After irradiation with X-rays, an afterglow of the Eu^{2+} broadband spectrum could be detected for at least 10 h. The high degree of reduction and multi-site occupancy of Eu^{2+} ions in α-TCP achieved by the selected synthetic approach opens new possibilities for the development of color-tunable broadband phosphors.

Data availability

The data supporting this study have been included within the article and the corresponding ESI.†

Conflicts of interest

There are no conflicts to declare.

Acknowledgements

This project has received funding from the Research Council of Lithuania (LMTLT), agreement no. S-MIP-23-85. A. A. and G. D. acknowledge the donation of SIA "Mikrotīkls" (MikroTik) administered by the University of Latvia Foundation, project no. 2326. V. P. acknowledges the LZP grant lzp-2023/1-0063.

This journal is © The Royal Society of Chemistry 2025

Open Access Article. Published on 21 April 2025. Downloaded on 5/27/2025 4:15:04 PM.
This article is licensed under a Creative Commons Attribution 3.0 Unported Licence.

References

1 S. Liu, L. Li, X. Qin, R. Du, Y. Sun, S. Xie, J. Wang, M. S. Molokeev, S. Xi, J. G. Bunzli, L. Zhou and M. Wu, *Adv. Mater.*, 2024, e2406164.
2 Z. Yang, Y. Zhao, Y. Zhou, J. Qiao, Y.-C. Chuang, M. S. Molokeev and Z. Xia, *Adv. Funct. Mater.*, 2022, **32**, 2103927.
3 Y. Zhu, X. Wang, J. Qiao, M. S. Molokeev, H. C. Swart, L. Ning and Z. Xia, *Chem. Mater.*, 2023, **35**, 1432–1439.
4 Z. Tang, Q. Zhang, Y. Cao, Y. Li and Y. Wang, *Chem. Eng. J.*, 2020, **388**, 124231.
5 C. Jiang, Q. Liu, K. Li, Y. Feng, Y. Fu, Y. Li, Y. Zhang, X. Qian, B. Wei and P. Du, *Chem. Eng. J.*, 2024, **496**, 154360.
6 Z. Tang, F. Du, L. Zhao, H. Liu, Z. Leng, H. Xie, G. Zhang and Y. Wang, *Laser Photonics Rev.*, 2023, **17**, 2200911.
7 G.-D. Xie, J.-Y. Si, G.-H. Li, G.-M. Cai, Z.-P. Wang and X.-J. Wang, *J. Mater. Chem. C*, 2024, **12**, 18066–18076.
8 H. Chen, Z. Zhang, R. Mi, M. S. Molokeev, Y. Liu, B. Wang, L. Mei, M. Fang, X. Wu, X. Min and Y.-g. Liu, *J. Lumin.*, 2024, **275**, 120795.
9 M. Liao, F. Wu, D. Zhu, X. Zhang, H. Dong, Z. Lin, M. Wen and Z. Mu, *Chem. Eng. J.*, 2022, **449**, 137801.
10 D. Wu, J. Si, G. Xie, J. Huang and G. Cai, *Ceram. Int.*, 2023, **49**, 34805–34813.
11 Z. Fan, Y. Wang, Z. Leng, G. Gao, L. Li, L. Huang and G. Li, *J. Am. Chem. Soc.*, 2024, **146**, 11500–11506.
12 Z. Luo, H. Zou, Z. Zheng, Y. Zhao, C. Wang, Q. Sun and Y. Song, *Inorg. Chem.*, 2024, **63**, 17449–17459.
13 R. G. Carrodeguas and S. De Aza, *Acta Biomater.*, 2011, **7**, 3536–3546.
14 M. Cao, J. Tian, W. Zhuang, R. Liu, Y. Liu, G. Chen, G. Zhou, L. Wang and J. Wang, *Inorg. Chem.*, 2022, **61**, 1805–1815.
15 Z. Meng, Y. Gao, J. a. Song, Z. Jiang, W. Lv, Q. Zeng, D. Wen and T. Hu, *Dalton Trans.*, 2023, **52**, 5443–5452.
16 P. Liang, W.-L. Lian and Z.-H. Liu, *Chem. Commun.*, 2021, **57**, 3371–3374.
17 M. Sójka, M. Runowski, T. Zheng, A. Shyichuk, D. Kulesza, E. Zych and S. Lis, *J. Mater. Chem. C*, 2022, **10**, 1220–1227.
18 W. Teng, H. Dong, C. Hu, X. Yang, J. Wang, X. Liang, B. Yang, J. Ru, B. Teng and D. Zhong, *J. Lumin.*, 2024, **269**, 120524.
19 H. Wang, K. Su, L. Mei, Q. Guo and L. Liao, *Inorg. Chem.*, 2023, **62**, 12468–12479.
20 H. Wang, K. Su, B. Ma, Y. Wang, L. Mei, Q. Guo and L. Liao, *Chem. Eng. J.*, 2023, **478**, 147361.
21 S. Li, Z. Qiu, Y. Mo, H. Zhang, H. Lian, J. Zhang and S. Lian, *Dalton Trans.*, 2022, **51**, 6622–6630.
22 L. Sinusaite, I. Grigoraviciute-Puroniene, A. Popov, K. Ishikawa, A. Kareiva and A. Zarkov, *Ceram. Int.*, 2019, **45**, 12423–12428.
23 L. Sinusaite, A. Popov, E. Raudonyte-Svirbutaviciene, J.-C. Yang, A. Kareiva and A. Zarkov, *Ceram. Int.*, 2021, **47**, 12078–12083.
24 D. Griesiute, E. Raudonyte-Svirbutaviciene, A. Kareiva and A. Zarkov, *CrystEngComm*, 2022, **24**, 1166–1170.
25 H. Ji, Z. Huang, Z. Xia, M. S. Molokeev, M. Chen, V. V. Atuchin, M. Fang, Y. g. Liu and X. Wu, *J. Am. Ceram. Soc.*, 2015, **98**, 3280–3284.
26 W. Zhou, J. Han, X. Zhang, Z. Qiu, Q. Xie, H. Liang, S. Lian and J. Wang, *Opt. Mater.*, 2015, **39**, 173–177.
27 D. Luo, C. Tong, Y. Zhu, C. Xu and Y. Li, *J. Lumin.*, 2020, **219**, 116863.
28 C. Tong, Y. Zhu, C. Xu and Y. Li, *Phys. B*, 2016, **500**, 20–23.
29 D. Griesiute, E. Garskaite, A. Antuzevics, V. Klimavicius, V. Balevicius, A. Zarkov, A. Katelnikovas, D. Sandberg and A. Kareiva, *Sci. Rep.*, 2022, **12**, 7116.
30 D. Griesiute, J. Gaidukevic, A. Zarkov and A. Kareiva, *Sustainability*, 2021, **13**, 7859.
31 A. Antuzevics, G. Krieke, G. Doke, A. Zarins, L. Avotina, E. Sprugis, J. Stadulis, A. Beganskiene, A. Kareiva and A. Zarkov, *J. Alloys Compd.*, 2024, **996**, 174779.
32 X. Han, C. Xin, S. Wang, J. Wu, Z. Ye, H. Yu and H. Zhang, *Inorg. Chem.*, 2023, **62**, 9679–9686.
33 S. N. Jayaramu, D. Janardhana, L. J. B. Erasmus, E. Coetsee, D. E. Motaung and H. C. Swart, *Dalton Trans.*, 2024, **53**, 16557–16576.
34 L. Sinusaite, A. Antuzevics, A. I. Popov, U. Rogulis, M. Misevicius, A. Katelnikovas, A. Kareiva and A. Zarkov, *Ceram. Int.*, 2021, **47**, 5335–5340.
35 Z. Hao, J. Zhang, X. Zhang and X. Wang, *Opt. Mater.*, 2011, **33**, 355–358.
36 X.-Y. Sun, X.-C. Le, Z. Xiao, X. Shi, W.-F. Wang, Z. Hu, Q.-M. Yang, R. Wei and H. Guo, *J. Am. Ceram. Soc.*, 2020, **103**, 3119–3125.
37 B. Yu, Y. Li, Y. Wang, N. Li, P. Xiao, D. Liu and L. Geng, *Inorg. Chem.*, 2022, **61**, 2463–2475.
38 W. Zhou, J. Han, F. Pan, J. Zhang, Q. Xie, S. Lian, L. Yu and J. Wang, *J. Am. Ceram. Soc.*, 2014, **97**, 3631–3635.
39 M. Peng, Z. Pei, G. Hong and Q. Su, *J. Mater. Chem.*, 2003, **13**, 1202–1205.
40 C. Tong, Y. Zhu, C. Xu, L. Yang and Y. Li, *Phys. B*, 2017, **521**, 153–157.
41 A. Doat, F. Pellé and A. Lebugle, *J. Solid State Chem.*, 2005, **178**, 2354–2362.
42 P. Dorenbos, *J. Phys.:Condens. Matter*, 2005, **17**, 8103.
43 G. Blasse and B. C. Grabmaier, *Luminescent Materials*, Springer-Verlag, Berlin, Heidelberg, 1994.
44 W. M. Yen and M. J. Weber, *Inorganic phosphors: compositions, preparation and optical properties*, CRC press, 2004.
45 M. Yashima and Y. Kawaike, *Chem. Mater.*, 2007, **19**, 3973–3979.
46 K. Matsunaga, T. Kubota, K. Toyoura and A. Nakamura, *Acta Biomater.*, 2015, **23**, 329–337.
47 R. D. Shannon, *Acta Crystallogr., Sect. A*, 1976, **32**, 751–767.
48 L. G. van Uitert, *J. Lumin.*, 1984, **29**, 1–9.
49 M. Buryi, T. Salamakha, V. Babin, J. Paterek, F. Hájek, Z. Remeš, L. Landová, E. Trusova and Y. Tratsiak, *Ceram. Int.*, 2021, **47**, 29232–29252.

Open Access Article. Published on 21 April 2025. Downloaded on 5/27/2025 4:15:04 PM.
This article is licensed under a Creative Commons Attribution 3.0 Unported Licence.

50 L. Havlák, J. Bárta, M. Buryi, V. Jarý, E. Mihóková, V. Laguta, P. Boháček and M. Nikl, *J. Phys. Chem. C*, 2016, **120**, 21751–21761.
51 D. K. Patel, B. Rajeswari, V. Sudarsan, R. K. Vatsa, R. M. Kadam and S. K. Kulshreshtha, *Dalton Trans.*, 2012, **41**, 12023–12030.
52 A. Antuzevics, M. Kemere, G. Krieke and R. Ignatans, *Opt. Mater.*, 2017, **72**, 749–755.
53 S. W. McKeever, *Thermoluminescence of solids*, Cambridge university press, 1985.
54 S. W. S. McKeever, *Phys. Status Solidi A*, 1980, **62**, 331–340.
55 V. Pagonis, G. Kitis and C. Furetta, *Numerical and practical exercises in thermoluminescence*, Springer Science & Business Media, 2006.
56 G. Doke, G. Krieke, P. Rodionovs, D. Nilova and A. Antuzevics, *J. Rare Earths*, 2025, **43**, 676–683.
57 S. Akca, M. Oglakci, Z. G. Portakal, N. Kucuk, M. Bakr, M. Topaksu and N. Can, *Radiat. Phys. Chem.*, 2019, **160**, 105–111.
58 K. H. Gavhane, M. S. Bhadane, A. S. Bhoir, P. P. Kulkarni, B. J. Patil, V. N. Bhoraskar, S. D. Dhole and S. S. Dahiwale, *J. Alloys Compd.*, 2020, **817**, 152805.
59 A. Vedda, M. Nikl, M. Fasoli, E. Mihokova, J. Pejchal, M. Dusek, G. Ren, C. R. Stanek, K. J. McClellan and D. D. Byler, *Phys. Rev. B:Condens. Matter Mater. Phys.*, 2008, **78**, 195123.
60 M. Kitaura, A. Sato, K. Kamada, A. Ohnishi and M. Sasaki, *J. Appl. Phys.*, 2014, **115**, 083517.
61 K. Van den Eeckhout, A. J. J. Bos, D. Poelman and P. F. Smet, *Phys. Rev. B:Condens. Matter Mater. Phys.*, 2013, **87**, 045126.
62 J. Qiao, J. Zhao and Z. Xia, *Opt. Mater.:X*, 2019, **1**, 100019.
63 M. Leimane, K. Krizmane, I. Bite, J. Grube and V. Vitola, *Materials*, 2023, **16**, 4416.
64 L. Sinusaite, A. Kareiva and A. Zarkov, *Cryst. Growth Des.*, 2021, **21**, 1242–1248.
65 M. R. MacDonald, J. E. Bates, J. W. Ziller, F. Furche and W. J. Evans, *J. Am. Chem. Soc.*, 2013, **135**, 9857–9868.

This journal is © The Royal Society of Chemistry 2025

4th publication

Luminescence and Electron–Hole-Trapping Centers in α-$Ca_2P_2O_7$-Mn

T.N. Nurakhmetov, T.T. Alibay, K.B. Zhangylyssov, A.S. Nurpeissov, **S. Pazylbek**, D. Griesiute, A. Zarkov, A. Kareiva

Crystals 14(5) **(2024)** 406
(https://doi.org/10.3390/cryst14050406)

crystals

MDPI

Article

Luminescence and Electron–Hole-Trapping Centers in α-$Ca_2P_2O_7-Mn$

Turlybek N. Nurakhmetov [1], Temirulan T. Alibay [1], Keleshek B. Zhangylyssov [1], Aibek S. Nurpeissov [1,*], Sapargali Pazylbek [2], Diana Griesiute [2], Aleksej Zarkov [2] and Aivaras Kareiva [2]

[1] L.N. Gumilyov Eurasian National University, st. Satpaev-2, Astana Z01A3D7, Kazakhstan; keleshek92@yandex.ru (K.B.Z.)
[2] Institute of Chemistry, Faculty of Chemistry and Geosciences, Vilnius University, Naugarduko 24, LT-03225 Vilnius, Lithuania
* Correspondence: lord_sukre@mail.ru

Abstract: The mechanisms of formation of induced intrinsic and impurity radiative states, which consist of intrinsic and impurity electron–hole-trapping center states in irradiated $Ca_2P_2O_7-Mn$ and $Ca_2P_2O_7$ phosphates, were investigated using thermoactivation and vacuum-ultraviolet spectroscopy methods. These centers are excited at photon energies of 4.0 eV and 4.5 eV, which are within the matrix's transparency region. New radiative-induced states at 3.06 eV and 2.92 eV are demonstrated to be generated upon the excitation of anions by photons with energies of 5.0 and 5.64 eV. This process is due to charge transfer from the ion to the impurities, specifically $Mn^{2+}(O^{2-}-Mn^{2+})$ and the neighboring ion $O^{2-}-(P_2O_7)^{4-}$. Furthermore, upon the excitation of matrix anions with photon energies exceeding the band gap (8.0–8.25 eV), electron-trapping by impurities such as Mn^{2+} and $(P_2O_7)^{4-}$ ions results.

Keywords: electrons and holes; trapping center; luminescence; XRD; SEM; emission spectra; excitation spectra

check for updates

Citation: Nurakhmetov, T.N.; Alibay, T.T.; Zhangylyssov, K.B.; Nurpeissov, A.S.; Pazylbek, S.; Griesiute, D.; Zarkov, A.; Kareiva, A. Luminescence and Electron–Hole-Trapping Centers in α-$Ca_2P_2O_7-Mn$. *Crystals* **2024**, *14*, 406. https://doi.org/10.3390/cryst14050406

Academic Editor: Bertrand Poumellec

Received: 1 March 2024
Revised: 29 March 2024
Accepted: 23 April 2024
Published: 26 April 2024

Copyright: © 2024 by the authors. Licensee MDPI, Basel, Switzerland. This article is an open access article distributed under the terms and conditions of the Creative Commons Attribution (CC BY) license (https://creativecommons.org/licenses/by/4.0/).

1. Introduction

Calcium phosphates constitute a diverse family of materials that find widespread use in a variety of fields, including as medicine for bone regeneration, catalysis, sensor technology, and as foundational matrices for the development of optical materials. In the study of these materials' optical properties, special emphasis is placed on examining the luminescent characteristics of doped phosphates. These luminescent properties are pivotal in the creation of white light sources, which are achieved by coating blue near-ultraviolet-emitting LED chips with phosphors [1]. Furthermore, the enduring phosphorescence and thermoluminescence exhibited by phosphates hold promise for a range of applications across the energy sector, lighting, and optical visualization in the red and infrared spectral ranges [2].

To advance the applications mentioned above, numerous studies have been conducted on the luminescent properties of phosphates. For instance, the research conducted by authors [3] demonstrated the luminescent characteristics of $KSrPO_4$ activated by Eu^{3+} following irradiation with synchrotron radiation. It was revealed that Eu^{2+} ions are formed in the excited state as a result of charge transfer from the matrix to the impurities $(O^{2-}-Eu^{3+})$. The charge transfer from O^{2-} to Eu^{3+} requires an energy of 4.6 eV. During the relaxation process from the excited state back to the ground state, recombination emission occurs at 2.9 eV, corresponding to the $4f^6 5d - 4f^7$ transition. Additionally, the energy gap from the excited electronic state of Eu^{2+} to the bottom of the conduction band is estimated to be 0.4 eV.

The nature of impurity emission centers in phosphates activated by Mn^{2+} ions was the focus of investigations by the authors of [3,4]. In $Ca_2P_2O_7-Mn$, it was discovered that

broad emission bands at 2.17 eV, 2.08 eV, and 2.14 eV are excited by several bands at 2.48 eV, 3.1 eV, 2.95 eV, and 3.44–3.65 eV. According to the hypothesis presented by the authors in [4], these excitation spectra are indicative of forbidden intra-center transitions of Mn^{2+} ions situated at the cationic sites of the crystal lattice. Further, authors in [3] identified that emission at 1.93 eV, which is not only excited by intracenter bands but also efficiently by UV emission at 5.9 eV, can be attributed to charge transfer from the matrix, $Ca_5Mn\ (PO_4)_7$, to the Mn^{2+} impurities $(O^{2-} - Mn^{2+})$. Additionally, the observation of thermoluminescence at 240 K and between 400 and 477 K, along with phosphorescence, is linked to the creation of trap centers during X-ray excitation.

The formation of electron–hole-trapping centers in phosphates was observed during photon irradiation, with energies surpassing the band gap, leading to the creation of free electron–hole pairs. In the research conducted by authors [5], thermoluminescence (TL) was studied in YPO_4 doped with Ce^{3+} and Ln^{3+} (where Ln represents Nd^{3+}, Er^{3+}, Ho^{3+}, Dy^{3+}). During the irradiation of $YPO_4:\ Ce^{3+},\ Ln^{3+}, Ln^{2+}$ electron-trapping centers are formed by the trapping of free electrons. Simultaneously, the trapping of holes by the Ln^{3+} ground state leads to the formation of Ln^{4+} hole trapping centers. TL is observed because of the recombination decay of these electron–hole–trapping centers.

Phosphors doped with Eu^{2+} impurities are utilized as sources of green radiation, which is instrumental in exciting hole-trapping centers, thereby generating stable red and infrared radiation. The photoluminescence, radioluminescence, and phosphorescence properties of these phosphors, when doped with rare earth ions, have been extensively studied by the authors in references [6–16].

In reviews and summary articles [17–19], the optical properties of non-rare-earth ions Mn^{4+} and Mn^{2+} have been investigated by the authors. Their properties were compared with the known properties of Eu^{2+} light-emitting diodes, which emit red light in various materials. It has been demonstrated that from an economic standpoint, Mn^{4+} ions, not being rare-earth ions, surpass Eu^{2+} ions in terms of red-light intensity. The main comparative properties of Mn^{4+} and Eu^{2+} ions in various host materials have been considered. Spectral differences in emission between Mn^{4+} and Eu^{2+} activator ions have been demonstrated, which can provide green and orange-red emissions depending on their practical application.

In the studies by authors [20,21], the mechanisms for the accumulation of intrinsic and impurity electron–hole-trapping centers were explored in both pure and Mn^{2+}-activated $CaSO_4$ and $BaSO_4$. It was demonstrated that intrinsic $SO_4^{3-} - SO_4^-$ and impurity $Mn^+ - SO_4^-$ trapping centers form as a result of free electrons localizing on the SO_4^{2-} anion and Mn^{2+} impurities, through the reactions $SO_4^{2-} + e^- \rightarrow SO_4^{3-}$ and $Mn^{2+} + e^- \rightarrow Mn^+$.

From a brief review of the literature, several conclusions can be drawn: During the irradiation of excited anion complexes, impurity electron-trapping centers form below the conduction band; when free electrons and holes localize on rare-earth ions, electron- and hole-trapping centers are generated, whose recombination leads to thermoluminescence (TL) and phosphorescence.

This work will discuss the mechanisms of the formation of electron- and hole-trapping centers upon the excitation of the $Ca_2P_2O_7 - Mn$ phosphor across a broad spectral (from 4 eV to 12 eV) and temperature range (15–300 K). By analyzing the excitation spectra of impurity emission from Mn^{2+} and the newly created recombination or tunneling emissions comprising electron–hole trapping centers, the study investigates the relaxation processes that facilitate energy transfer to impurities.

2. Objects and Research Methods

Undoped and Mn-doped $Ca_2P_2O_7$ powders were synthesized using the wet co-precipitation method, as described in [4,7]. The Mn substitution rate was set at 1 mol.% relative to Ca^{2+}. The obtained precipitates were annealed at 1200 °C, with a heating rate of 5 °C/min and a holding time of 10 min.

Characterization

X-ray diffraction analysis (XRD) of the powders was carried out using Ni-filtered Cu-Kα radiation on a Rigaku MiniFlex II diffractometer, operating in the Bragg–Brentano (θ/2θ) geometry. Data were collected over a 2θ range from 10 to 60°, with a step size of 0.02° and a scanning speed of 1°/min.

The morphology of the synthesized products was examined using a Hitachi SU-70 (Tokyo, Japan) field emission scanning electron microscope (FE-SEM).

Measurements of emission and excitation spectra in the spectral range from 6.2 eV to 12.4 eV (100–200 nm) were carried out using a vacuum monochromator assembled according to the Seiya–Namioka scheme with a recording monochromator Solar M-266 (Solar LS, Minsk, Belarus) and a PMT detector Hamamatsu H11890-01 (Hamamatsu Photonics, Shizuoka Pref, Japan). A hydrogen lamp is used for excitation in the VUV range of the spectrum. Cooling up to 15 K is provided by a cryostat with helium cooling equipment of a closed cycle.

To measure emission spectra in the range of 1.5–6.2 eV, a Solar SM 2203 (Solar LS, Minsk, Belarus) spectrofluorometer was used. Low-temperature studies (77 K) using a cryostat with a vacuum of 10^{-4} Pa cooling were carried out using liquid nitrogen.

The samples were irradiated using a BSV-23 X-ray tube with a copper anode, operating at a tube current of 10 mA and a voltage of 40 kV. The energy range of the X-ray photons was between 10 and 15 keV, and a 150 W xenon lamp XBO (OSRAM GmbH, Garching, Germany) with a photon energy of 1.5−6.2 eV (200–830 nm) was utilized.

3. Experimental Results

In order to determine the nature of intrinsic, impurity, and recombination emissions at trapping centers in $Ca_2P_2O_7$ and $Ca_2P_2O_7 - Mn$ phosphors, excitation, and emission spectra were studied upon excitation by ultraviolet and X-ray radiation over a wide temperature range from 15 K to 300 K.

The crystallinity and purity of the synthesized powders were assessed using X-ray diffraction analysis. The X-ray diffraction pattern of the $Ca_2P_2O_7$ sample doped with Mn, after annealing at 1200 °C, is depicted in Figure 1. The diffraction peaks closely match the standard pattern for α-$Ca_2P_2O_7$ (PDF #073-0440), confirming the successful formation of the target material. A minor presence of the adjacent phase, α-$Ca_3(PO_4)_2$, was also observed, likely resulting from the evaporation of phosphate particles during the process.

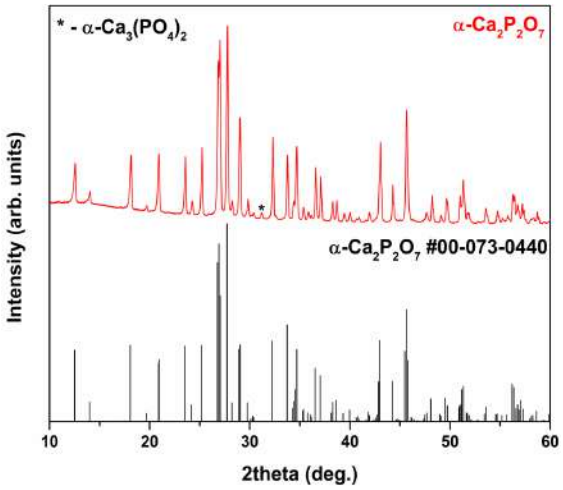

Figure 1. X-ray diffraction pattern of α-$Ca_2P_2O_7 : Mn$ powder alongside the standard sample.

The morphological characteristics of the synthesized powders were examined through scanning electron microscopy (SEM). Representative SEM images of the Mn-doped $Ca_2P_2O_7$ sample, displayed in Figure 2, reveal that the powders are composed of a mix of plate-like and irregularly shaped particles. Notably, the plate-like particles exhibit grains ranging in size from micrometers to sub-micrometers.

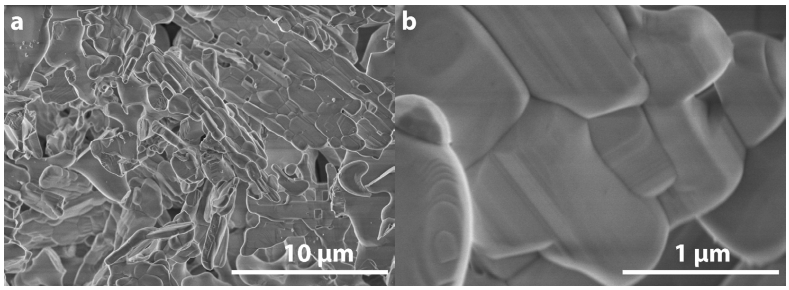

Figure 2. SEM micrographs of $Ca_2P_2O_7 : Mn$ powder. (**a**) general view at 10 µm; (**b**) at magnifications up to 1 µm.

In Figure 3, the emission spectra of the $Ca_2P_2O_7 - Mn$ phosphor, upon irradiation with 6.2 eV photons at 300 K, is depicted as curve 1. Additionally, the emission spectra measured at 77 K in a cryostat, following excitation with 6.2 eV (200 nm) photons, are shown as curve 2. The analysis of Figure 3 reveals that at 300 K, there is an intracenter emission band at 2.06 eV (602 nm), attributed to the Mn^{2+} ion within the phosphor (curve 1), alongside the emergence of new emission bands at 3.06 eV (405 nm) and 2.92 eV (425 nm) (curve 1). Notably, at 77 K, the Mn^{2+} emission band markedly diminishes, whereas the intensity of the newly observed emission bands at 3.06 eV (405 nm) and 2.92 eV (405 nm) experiences a 1.5-fold increase.

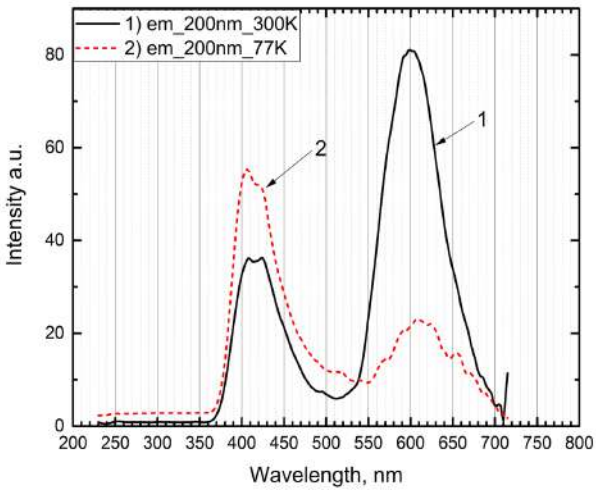

Figure 3. Emission spectra of the $Ca_2P_2O_7 - Mn$ phosphor upon excitation with 6.2 eV (200 nm) photons (1—at 300 K, 2—at 77 K).

In Figure 4, the excitation spectrum for the main intracenter emission of Mn^{2+} at 2.06 eV (602 nm), 300 K (curve 1), and 77 K (curve 2) is presented. The analysis of the graph

indicates that at 77 K, the emission band is excited at discrete energies of approximately 2.5 eV (496 nm), 3.0 eV (413 nm), 3.5 eV (354 nm), 4.0 eV (310 nm), 4.5 eV (275 nm), and within the range of 6.2 to 5.0 eV. Conversely, at 300 K, these emission bands also occur but exhibit lower intensity, particularly within the narrower range of 4.0 eV (310 nm) to 4.5 eV (275 nm).

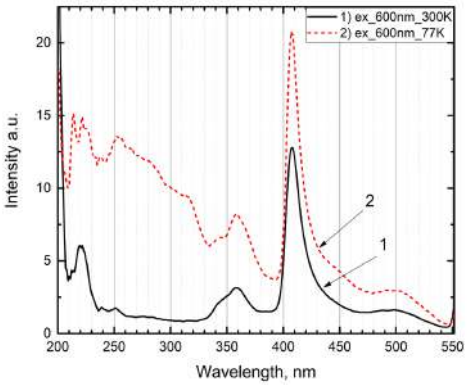

Figure 4. Excitation spectra of the intracenter emission for the 2.06 eV (602 nm) band, irradiated $Ca_2P_2O_7 - Mn$ (1—at 300 K, 2—at 77 K).

In Figure 5, the excitation spectra for the newly identified bands at 3.06 eV (405 nm) and 2.92 eV (425 nm), following pre-irradiation of the phosphor at 6.2 eV (200 nm), are displayed at both 300 K and 77 K. Excitation bands are identified within the ranges of 3.94–4.0 eV (310–314 nm), 4.5–4.6 eV (269–275 nm), and broadly from 6.2 eV (200 nm) to 5.5 eV (225 nm). Notably, these bands are prominently observed at 77 K, indicating a stronger response to excitation at this lower temperature. Conversely, at 300 K, these same bands manifest as weak excitation bands, suggesting a diminished excitation efficiency at higher temperatures.

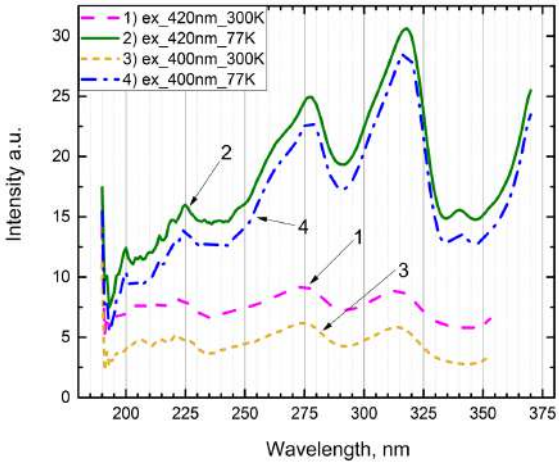

Figure 5. Excitation spectra of the pre-irradiated phosphor: 1—for the emission band at 2.92 eV (425 nm) at 300 K; 2—for the emission band at 2.92 eV (425 nm) at 77 K; 3—for the emission band at 3.06 eV (405 nm) at 300 K; 4—for the emission band at 3.06 eV (405 nm) at 77 K.

When measuring the excitation spectra for the intracenter emission of the Mn^{2+} ion at 2.06 eV (602 nm), emission bands similar to those identified by authors in [2] were observed at 2.5 eV (496 nm), 3.1 eV (400 nm), 3.0 eV (413 nm), and between 3.5 eV (354 nm) and 3.6 eV (344 nm). Additionally, alongside the main intracenter emission at 2.06 eV (602 nm) for Mn^{2+}, the excitation spectrum revealed bands for the newly identified emissions at 3.06 eV (405 nm) and 2.92 eV (419 nm), specifically within the ranges of 3.94–4.0 eV (310–314 nm) and 4.5–4.6 eV (269–275 nm). Furthermore, excitation bands at 5.0 eV (248 nm) and 5.64 eV (220 nm) were also detected. Consequently, these newly emerged emission bands are excited by photon energies of 3.94–4.0 eV (310–314 nm), 4.5–4.6 eV (269–275 nm), 5.0 eV (248 nm), and 5.64 eV (220 nm).

Similar experiments were carried out using pure $Ca_2P_2O_7$ phosphor. The emission spectrum of this phosphor, when irradiated with photons at energies of 6.2 eV (200 nm) (curves 1 and 2) and 5.64 eV (220 nm) (curves 3 and 4) at temperatures of 77 K and 300 K, is depicted in Figure 6. It is observed that emission bands at 2.92 eV (425 nm) and 3.06 eV (344 nm) appear at both 77 K and 300 K, mirroring those in the $Ca_2P_2O_7 - Mn$ phosphor.

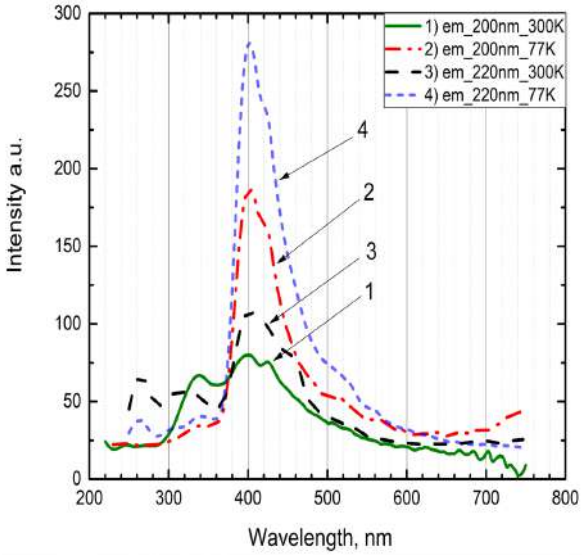

Figure 6. Emission spectrum of the phosphor $Ca_2P_2O_7$ when excited by photons at 6.2 eV (200 nm) (1—at 300 K, 2—at 77 K) and when excited by photons at 5.64 eV (220 nm) (3—at 300 K, 4—at 77 K).

Figure 7 presents the excitation spectra of the pre-irradiated $Ca_2P_2O_7$ phosphor with UV photons at an energy of 6.2 eV (200 nm) for the recombination emission bands at 2.92 eV (292 nm) (curves 1 and 2) and 3.06 eV (405 nm) (curves 3 and 4), at 300 K and 77 K respectively. In alignment with observations from the $Ca_2P_2O_7 - Mn$ phosphor, excitation bands are identified at 3.94–4.0 eV (310–314 nm) and 4.5–4.6 eV (269–275 nm), along with a band at 5.64 eV (220 nm). Additionally, in pure phosphates, emissions at 2.92 eV are also excited by photon energies of 4.0 eV (310 nm) and within the range of 4.45–4.6 eV (269–278 nm), occurring within the matrix's transparency region.

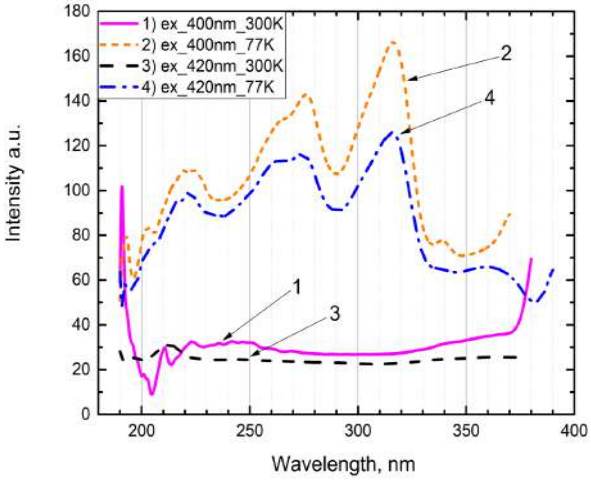

Figure 7. Excitation spectra of pre-irradiated phosphor: for the emission band at 2.95 eV (420 nm): 1—at 300 K; 2—at 77 K; for the emission band at 3.1 eV (400 nm): 3—at 300 K; 4—at 77 K.

Figure 8 illustrates the temperature-dependent behavior of emission intensity for bands at 2.95 eV (420 nm) (curve 1), 3.1 eV (400 nm) (curve 2), and 2.06 eV (602 nm) (curve 3). The data reveal that the intensity of the recombination emissions at 2.95 eV and 3.1 eV shows a gradual decline starting from 77 K. Moreover, it is observed that the intensity of the intracenter emission associated with the Mn^{2+} impurity at 2.06 eV (602 nm) decreases in a monotonic fashion until reaching 350 K, beyond which it experiences a sharp increase up to 450 K.

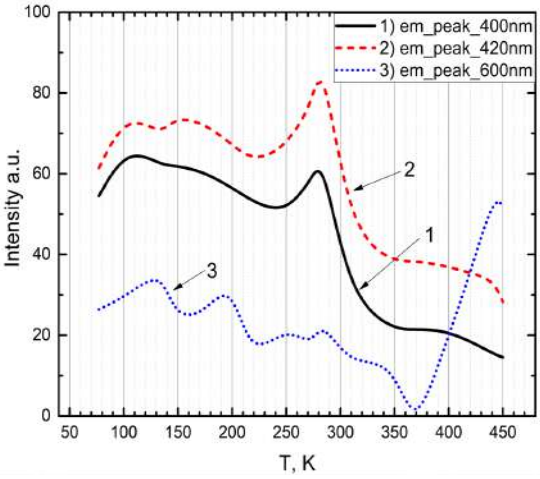

Figure 8. Temperature dependence of emission intensity at 1—at 2.95 eV (420 nm); 2— at 3.1 eV (400 nm); and 3— at 2.06 eV (600 nm).

Figure 9 illustrates the TL curve of $Ca_2P_2O_7 - Mn$. In the $Ca_2P_2O_7 - Mn$ phosphor irradiated with X-rays at 77 K, TL peaks appear at 200–270 K, 350 K, and 400–440 K. TL

peaks appear in the temperature range where the intensity of the emission 2.92 eV (425 nm) and 3.06 eV of the combined radiative state of the phosphor $Ca_2P_2O_7 - Mn$ changes.

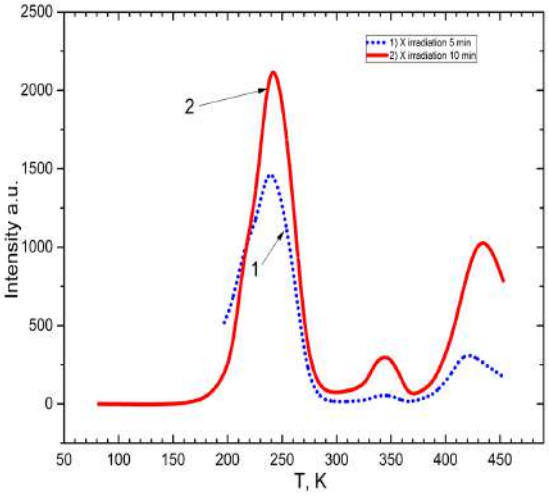

Figure 9. TL curve of $Ca_2P_2O_7 - Mn$ irritated by X irradiation: 1—5 min; 2—10 min.

In our forthcoming research, we aim to delve into the formation of electron- and hole-trapping centers upon excitation within the vacuum-ultraviolet region, specifically at photon energies ranging from 6.2 eV to 12.4 eV (100–200 nm). This range is critical as it encompasses the energies at which free electron–hole pairs are predominantly formed, particularly above 8 eV (155 nm), as highlighted in the studies by authors [22].

The findings reported by [22] reveal that long-lasting phosphorescence and thermally stimulated luminescence are primarily linked to the creation of electron–hole-trapping centers. These centers emerge through charge transfer from the oxygen anion to the valence band during the excitation of the 3*d* state of Mn^{2+} and the 5*d* states of rare-earth ions, specifically in transitions involving $O^{2-} - Mn^{2+}$ and $O^{2-} - Re^{3+}$ complexes. Furthermore, reference [22] correlates the fundamental absorption band observed in matrices such as $CaBPO_5 - Ce^{3+}$, $LiCaPO_4 - Ce^{3+}$, and $Li_2CaSiO_4 - Ce^{3+}$ with electron transitions from the anionic groups PO_4^{3-} and SiO_4^{4-} to the conduction band.

In Figure 10, the emission spectrum of the α-$Ca_2P_2O_7 - Mn$ phosphor, excited by photons at energies of 8.26 eV (150 nm) and 7.75 eV (160 nm), is presented for temperatures of 300 K and 15 K. At 300 K, emissions are observed at 2.06 eV, corresponding to the intracenter emission of the Mn^{2+} ion (curves 1 and 3). When the temperature is lowered to 15 K, the intensity of the 2.06 eV (600 nm) emission from Mn^{2+} decreases by a factor of 2 to 2.5, and new emission bands emerge at 2.92 eV (425 nm) and 3.06 eV (405 nm) (curves 2 and 4 in Figure 10). This pattern of emissions is consistent with the observations made under UV irradiation at 6.2 eV (200 nm) photon energy at 77 K. The reduction in the Mn^{2+} emission band leads to the formation of new electronic trapping centers as a result of the reaction $Mn^{2+} + e^- \rightarrow Mn^+$, in conjunction with localized holes in $(P_2O_7)^{3-}$, forming $Mn^+ - (P_2O_7)^{3-}$ complexes.

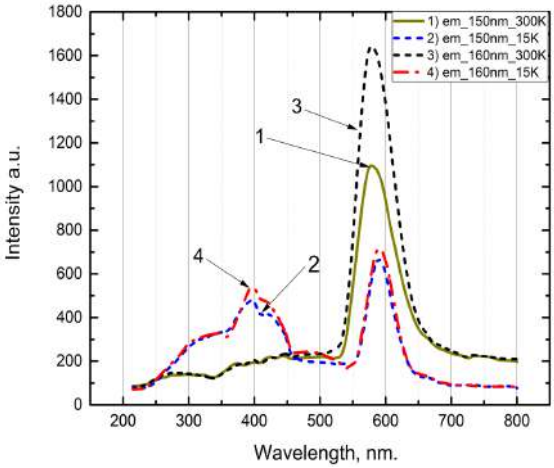

Figure 10. Emission spectra of α-$Ca_2P_2O_7$ phosphor under excitation by photons at 8.26 eV (150 nm) (1—at 300 K, 2—at 15 K) and under excitation by photons at 7.75 eV (160 nm) (3—at 300 K, 4—at 15 K).

Figure 11 shows the excitation spectrum of α-$Ca_2P_2O_7 - Mn$ emission for the 2.0 eV (620nm) and 2.1 eV (590 nm) bands at 300 and 15 K. Figure 11 shows that the emission of the Mn^{2+} ion is excited at photon energies of 7.85 eV (158 nm). This value is the band gap for the phosphor α-$Ca_2P_2O_7 - Mn$.

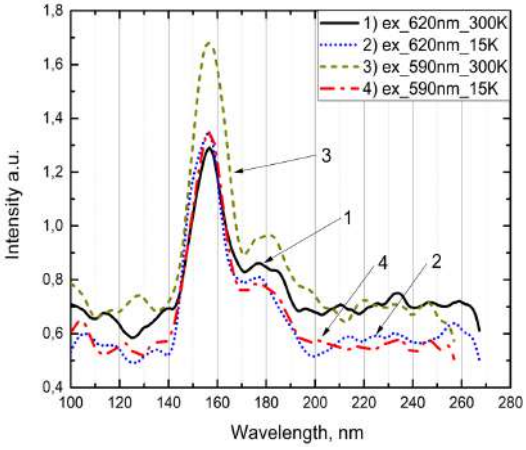

Figure 11. Excitation spectra of $Ca_2P_2O_7 - Mn$ for the emission band at 2.0 eV (620 nm): 1—at 300 K; 2—at 15 K, and for the emission band at 2.1 eV (590 nm): 3—at 300 K; 4—at 15 K.

4. Discussion

The experimental results highlight the following processes occurring in the $Ca_2P_2O_7 - Mn$ phosphor upon excitation with 6.2 eV (200 nm) ultraviolet photons:

1. The occurrence of impurity intracenter emissions at 2.06 eV (600 nm) from the Mn^{2+} ion, observable at both 300 K and 77 K.

2. The generation of new induced recombination emissions at 2.95 eV (420 nm) and 3.1 eV (405 nm), resulting from charge transfer between excited matrix anions and impurities, specifically between $(O^{2-} - Mn^{2+})$ and $O^{2-} - (P_2O_7)^{4-}$.

To further elucidate the characteristics of the intracenter emission at 600 nm and the newly induced emissions at 2.95 eV (420 nm) and 3.1 eV (405 nm), the excitation spectra of these emissions were meticulously measured.

1. Intracenter emission at 2.06 eV (600 nm) are excited:
   - At 3.65 eV (340 nm) and 3.4 eV (335 nm), as shown by the authors of [5], corresponding to intra-center excitations of the Mn^{2+} ion.
   - At 5.64 eV (220 nm) and 4.96 eV (251 nm) because of charge transfer from the excited anion to impurities and neighboring anions $(O^{2-} - Mn^{2+})$ and $O^{2-} - (P_2O_7)^{4-}$.
   - ~2.5 eV (496 nm) excitation of trap centers near the Mn^{2+} ion.
   - 4.0 eV (310 nm) and 4.5 eV (275 nm) emissions arising in the transparency region of the $Ca_2P_2O_7 - Mn$ matrix.
2. The newly created induced emissions at 2.95 eV (496 nm) and 3.1 eV (400 nm) are excited at photon energies of 4.0 eV (310 nm) and 4.5 eV (275 nm), as well as in the spectral range of 4.96 eV (256 nm) and 5.64 eV (220 nm), where these new induced emissions are mainly created at low temperatures of 77 K.

Next, to clarify the correlation between the above-mentioned regularities with the processes in the pure matrix $Ca_2P_2O_7$, similar experimental studies on the $Ca_2P_2O_7$ phosphor were conducted.

- When the pure $Ca_2P_2O_7$ phosphor was excited with photon energies ranging from 5.9 to 6.2 eV (200–210 nm), emissions at 2.95 eV (496 nm) and 3.1 eV (400 nm) were detected at both 77 K and 300 K.
- These induced emissions are excited at photon energies of 4.0 eV (310 nm) and 4.5 eV (275 nm) in the transparency region of the pure $Ca_2P_2O_7$ matrix and more intensively so at 77 K.

The emission bands for matrix samples of $Ca_2P_2O_7$ and with an admixture of Mn are listed in Table 1.

Table 1. Emission spectra.

Sample	Temperature	Excitation Energy	Emission Peaks	Interpretation
$Ca_2P_2O_7 - Mn$	300 K	6.2 eV (200 nm)	2.06 eV (600 nm), 3.06 eV (405 nm), 2.92 eV (425 nm)	Mn^{2+}
	77 K		2.06 eV (600 nm)—low intensity 3.06 eV (405 nm), 2.92 eV (425 nm)—high intensity	Mn^{2+}
$Ca_2P_2O_7$	300 K	6.2 eV (200 nm)	2.92 eV (425 nm), 3.06 eV (405 nm),	matrix
		5.64 eV (220 nm)	2.92 eV (425 nm), 3.06 eV (405 nm),	matrix
	77 K	6.2 eV (200 nm)	2.92 eV (425 nm), 3.06 eV (405 nm),	matrix
		5.64 eV (220 nm)	2.92 eV (425 nm), 3.06 eV (405 nm),	matrix

Excitation bands of the type for samples of the matrix and with an admixture of Mn are indicated in Table 2.

Table 2. Excitation spectra.

Sample	Temperature	Emission Peaks	Excitation Energy	Interpretation
$Ca_2P_2O_7 - Mn$	300 K	2.06 eV (600 nm)	4.0–4.5 eV (275–310 nm)	Mn^{2+}
	77 K	2.06 eV (600 nm)	2.5 eV (496 nm), 3.0 eV (413 nm), 3.5 eV (354 nm), 4.0 eV (310 nm), 4.5 eV (275 nm), 5.0–6.2 eV (200–248 nm)	Mn^{2+}
	300 K	3.06 eV (405 nm), 2.92 eV (425 nm),	3.94–4.0 eV (310–314 nm), 4.5–4.6 eV (269–275 nm), 5.5–6.2 eV (200–225 nm)—weak intensity	matrix
	77 K	3.06 eV (405 nm), 2.92 eV (425 nm),	3.94–4.0 eV (310–314 nm), 4.5–4.6 eV (269–275 nm), 5.5–6.2 eV (200–225 nm)—strong intensity	
$Ca_2P_2O_7$	300 K	2.92 eV (425 nm), 3.06 eV (405 nm),	3.94–4.0 eV (310–314 nm), 4.5–4.6 eV (269–275 nm), 5.64 eV (220 nm).	matrix
	77 K	2.92 eV (425 nm), 3.06 eV (405 nm),	3.94–4.0 eV (310–314 nm), 4.5–4.6 eV (269–275 nm), 5.64 eV (220 nm).	

The main question of these studies is the formation of induced or combined radiative states in pure and doped phosphors in the same manner as a result of charge transfer from the matrix to impurities and neighboring anions $(O^{2-} - Mn^{2+})$ and $O^{2-} - (P_2O_7)^{4-}$. As a result, intrinsic and impurity electron-trapping centers Mn^+ and $(P_2O_7)^{5-}$, complementary to hole-trapping centers $(P_2O_7)^{3-}$ near Mn^{2+} impurities, are formed. During the excitation of the anion $(P_2O_7)^{4-}$, due to the charge transfer of Mn^{2+} impurities, Mn^+ should be created, and the hole component $(P_2O_7)^{3-}$ is mainly localized near Mn^{2+} impurities.

It is assumed that similar induced and combined radiative states at 2.95 eV (420 nm) and 3.1 eV (400 nm) should be created upon trapping free electrons and holes by Mn^{2+} impurities and $(P_2O_7)^{4-}$ anions. We conducted experimental research in the vacuum ultraviolet spectral range from 12.4 eV (100 nm) to 4.96 eV (250 nm), where free electron–hole pairs are created. When irradiated with photons with energies of 8.26 eV (150 nm) and 7.75 eV (160 nm) at temperatures of 300 K and 15 K, intracenter emissions of Mn^{2+} at 2.15 eV (577 nm) and new induced or combined radiative states at 2.95 eV (420 nm) and 3.1 eV (400 nm) are created. Impurity emissions of Mn^{2+} at photon energies of 8.0 eV (155 nm) are excited by free electrons. It is known that the band gap of $CaBPO_5$ and $LiCaPO$ phosphors are 8.26 eV (150 nm) and 7.65 eV (162 nm), respectively [22].

The primary focus of these studies is to understand the formation of induced or combined radiative states in both pure and doped phosphors, facilitated by charge transfer from the matrix to impurities and neighboring anions, specifically $O^{2-} - Mn^{2+}$ and $O^{2-} - (P_2O_7)^{4-}$. This process results in the formation of intrinsic and impurity electron-trapping centers (Mn^+ and $((P_2O_7)^{5-})$ that complement hole-trapping centers $(P_2O_7)^{3-}$ located near Mn^{2+} impurities. It is proposed that during the excitation of the anion $(P_2O_7)^{4-}$, charge transfer from Mn^{2+} impurities should lead to the creation of Mn^+, with the hole component $(P_2O_7)^{3-}$ primarily localized near Mn^{2+} impurities. Consequently, it is hypothesized that similar induced and combined radiative states at 2.95 eV (420 nm) and 3.1 eV (400 nm) are formed by the trapping of free electrons and holes by Mn^{2+} impurities and $(P_2O_7)^{4-}$ anions.

The estimated band gap of $Ca_2P_2O_7$ is approximately 8.0 eV (155 nm).

Thus, the new combined radiative states are created as a result of charge transfer from the excited ion P_2O_7 to Mn^{2+} impurities and ions $(P_2O_7)^{4-}$.

These radiative states are generated when electrons are captured by impurities and intrinsic centers, specifically through the reactions $Mn^{2+} + e^- \rightarrow Mn^+$ and $(P_2O_7)^{4-} + e^- \rightarrow (P_2O_7)^{3-}$. This results in the formation of impurity $Mn^+ - (P_2O_7)^{3-}$ and intrinsic $(P_2O_7)^{5-}$–$(P_2O_7)^{3-}$ electron–hole-trapping centers. The trapping of electrons by Mn^{2+}

ions and $(P_2O_7)^{4-}$ anions lead to the creation of these specific centers, facilitating the observed radiative states.

The temperature-dependent measurements of the new radiative states at 2.95 eV (420 nm) and 3.1 eV (400 nm) reveal a distinct pattern: their intensity steadily decreases from 77 K to 250 K, experiences a surge between 250 K and 300 K, and then undergoes a sharp decline from 300 K to 400 K. Concurrently, the intensity of the intracenter emission at 2.06 eV Mn^{2+} shows a slight decrease over the same temperature range, followed by a significant increase between 370 K and 450 K.

The experimental results, as illustrated in Figures 3, 6 and 8, confirm the temperature dependence of the intensity for the newly induced emissions at 2.95 eV (420 nm) and 3.1 eV (400 nm). Notably, the efficiency of generating these induced emissions at lower temperatures, specifically at 15 K and 77 K, is found to be twice as high compared to that at higher temperatures ranging from 300 K to 350 K.

The observed temperature-dependent behavior of the radiative states at 2.95 eV (420 nm) and 3.1 eV (400 nm), particularly the flaring up and subsequent rapid decrease in intensity between 250 K and 300 K, can be attributed to ionization processes: $Mn^{+} \rightarrow Mn^{2+} + e^{-}$; $(P_2O_7)^{3-} \rightarrow (P_2O_7)^{4-} + e^{-}$. This ionization leads to the generation of free electrons in the conduction band, which then recombine with localized holes near the Mn^{2+} impurity, specifically $(P_2O_7)^{3-}$. The energy released during this recombination is transferred to the impurities, resulting in an observed increase in the intensity of intracenter emission at 2.06 eV (600 nm) for Mn^{2+}. Consequently, this process facilitates energy transfer from the matrix to the impurities. In analogous research conducted by authors [3] on $KSrPO_4 - Eu^{3+}$, electron ionization from the Eu^{2+} ion into the conduction band was observed with an activation energy of 0.4 eV, illustrating a similar charge transfer mechanism.

The decrease in the intensity of the combined radiative state of 2.92 eV (425 nm) and 3.0 eV (413 nm) is associated with the decay of electron-trapping centers and the implementation of electron recombination with a hole-trapping center, which is confirmed by the appearance of TL peaks in this temperature range in the irradiated phosphor $Ca_2P_2O_7 - Mn$ at 80 K (Figure 9). The presence of TL peaks confirms the formation of electron- and hole-trapping centers during irradiation with UV (6.2 eV (200 nm)) photons.

The formation of induced or combined radiative states, which include the electronic configurations of electron–hole-trapping centers $Mn^{+} - (P_2O_7)^{3-}$ and $(P_2O_7)^{5-} - (P_2O_7)^{3-}$, is supported by experimental evidence. Specifically, new induced emissions at 2.95 eV (420 nm) and 3.1 eV (400 nm), stimulated by the irradiation of trapping centers, are excited at photon energies of 4.0 eV (310 nm) and 4.5 eV (275 nm) within the transparency region of the matrix, as shown in Figures 5 and 6. Similarly, intracenter emissions from the Mn^{2+} ion are excited at these same photon energies, as demonstrated in Figures 4, 5 and 7.

The experimental evidence solidly supports that induced states arise from the electronic configurations of both intrinsic and impurity-trapping centers. Specifically, the radiative decay and relaxation processes involving the excited state $Mn^{+} - (P_2O_7)^{3-}$ commence from a singular energy level as the temperature increases. This behavior underscores the dynamic interaction between these trapping centers under thermal variation. Figure 12 presents a model illustrating the presumed arrangement of electronic- and hole-trapping centers, providing a visual representation of these complex interactions.

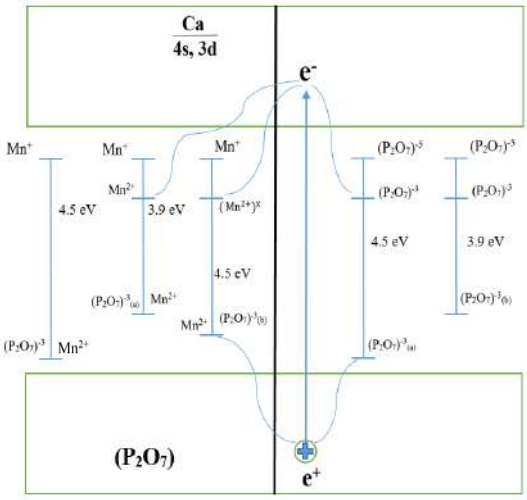

Figure 12. Model depicting the arrangement of electronic- and hole-trapping centers.

Here is the explanation of the model describing electronic transitions in irradiated $Ca_2P_2O_7 - Mn$ at temperatures of 300 K and 77 K.

At a temperature of 300 K, irradiated $Ca_2P_2O_7$ with photons of 6.2 eV (200 nm) generates electron–hole pairs $e^+(P_2O_7)^{3-}$- e^-. Upon the transition from $6A_1$ to $4T_1$ in the Mn^{2+} ion, an emission band occurs at 2.06 eV (600 nm). At temperatures of 77 K and 300 K, a free electron occurs:

Upon capture by Mn^{2+} impurities: $Mn^{2+} + e^- \rightarrow Mn^+$;

Upon capture by the matrix anions $(P_2O_7)^{4-} + e^- \rightarrow (P_2O_7)^{5-}$.

As a result, electronic Mn^+ and hole $(P_2O_7)^{3-}$ capture centers arise, i.e., Mn^+-$(P_2O_7)^{3-}$. Hybrid or combined electronic states arise beneath the conduction band consisting of the electronic state Mn^+ and $(P_2O_7)^{5-}$.

Parallel to this process, a hole localized above the valence band near the ground state of the Mn^{2+} ion is localized above the valence band $(P_2O_7)^{3-}$. Due to the anisotropic nature of the compound, the holes formed with unpaired electrons in different crystallographic directions localize above the valence band ceiling at different energy positions: $(P_2O_7)^{3-}(a)$ and $(P_2O_7)^{3-}(b)$.

The experimental data obtained by analyzing the photoluminescence decay curves of the samples reveal distinct decay times for different emission bands (Figure 13). Specifically, the decay time for the intracenter emission at 2.06 eV (corresponding to 600 nm or 2 bands) is measured at 55 μs. In contrast, the decay time for the induced emission at 3.1 eV (corresponding to 400 nm or 1 band) is significantly shorter at 22 μs. The induced photoluminescence from Mn^{2+} emissions is notably observed following cascade recombination processes, highlighting the complex dynamics of electron–hole recombination in these materials.

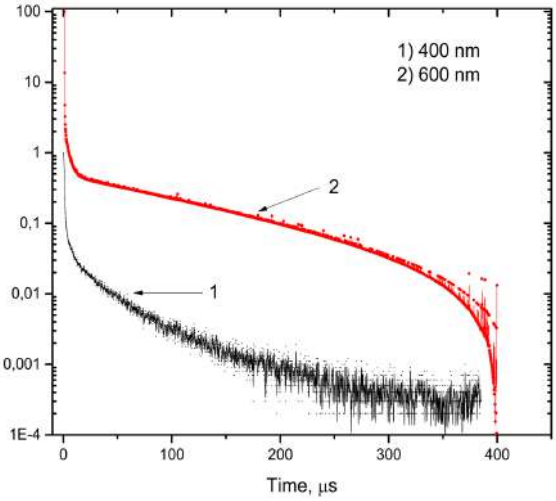

Figure 13. Decay curves for emission bands at (1) 3.1 eV (400 nm); (2) 2.06 eV (600 nm).

The photon energies of 4.0 eV (310 nm) and 4.5 eV (275 nm), responsible for exciting the intrinsic and impurity radiative states at 2.95 eV (420 nm) and 3.1 eV (400 nm), correspond to the absorption and excitation energies bridging the ground and excited states of both intrinsic and impurity electron–hole-trapping centers. This relationship is detailed in the band model illustrated in Figure 12. The model elucidates how these specific photon energies facilitate transitions that result in the observed radiative states, providing a comprehensive understanding of the energy dynamics within the phosphor.

5. Conclusions

In irradiated $Ca_2P_2O_7 - Mn$ phosphors, new induced emissions at 2.95 eV (420 nm) and 3.1 eV (400 nm) have been detected, which are excited at photon energies of 4.0 eV (310 nm) and 4.5 eV (275 nm) in the transparency range of the matrix. The new radiative states at 2.95 eV (420 nm) and 3.1 eV (400 nm) are created upon excitation of anions by photons with energies of 5.0 eV (548 nm) and 5.64 eV (220 nm), resulting from charge transfer from the $(P_2O_7)^{4-}$ ion to the Mn^{2+} impurities and neighboring ions according to the reaction $(O^{2-} - Mn^{2+})$ and $O^{2-} - (P_2O_7)^{4-}$.

It is shown that the radiative states at 2.95 eV and 3.1 eV are also created upon excitation of anions with photon energies of 8.0 eV and 8.25 eV exceeding the band gap, due to electron-trapping by impurities and neighboring ions according to reactions $Mn^{2+} + e^- \rightarrow Mn^+$ and $(P_2O_7)^{4-} + e^- \rightarrow (P_2O_7)^{5-}$.

Based on the measurement of the excitation spectra of the recombination emission at 2.95 eV (420 nm) and 3.1 eV (400 nm) and the impurity emission at 2.06 eV (600 nm), it has been shown that they are simultaneously excited at photon energies of 4.0 eV (310 nm) and 4.5 eV (275 nm). These values represent the excitation spectrum of the new induced electron radiative states at 2.95 eV (420 nm) and 3.1 eV (400 nm), consisting of intrinsic and impurity electronic trapping center states.

Author Contributions: T.N.N.: Supervision, Writing—original draft, Writing—review & editing; T.T.A.: Investigation, Visualization. K.B.Z.: Writing—review & editing, Correspondence; A.S.N.: Investigation, Correspondence; S.P.: Formal analysis, Methodology; D.G.: Investigation; A.Z.: Conceptualization, Methodology; A.K.: Conceptualization, Resources. All authors have read and agreed to the published version of the manuscript.

Funding: This research was funded by the Science Committee of The Ministry of Science and Higher Education of the Republic of Kazakhstan (Grant No: AP23488657).

Data Availability Statement: Available on request from the authors.

Conflicts of Interest: The authors declare no conflict of interest.

References

1. Cao, R.; Wang, W.; Zhang, J.; Ye, Y.; Chen, T.; Guo, S.; Xiao, F.; Luo, Z. Luminescence properties of $Sr_2Mg_3P_4O_{15}$:Mn^{2+} phosphor and the improvement by co-doping Bi^{3+}. *Opt. Mater.* **2018**, *79*, 223–226. [CrossRef]
2. Lecointre, A.; Benhamou, R.A.; Bessiére, A.; Wallez, G.; Elaatmani, M.; Viana, B. Red long-lasting phosphorescence (LLP) in β-TCP type $Ca_{9\cdot5}Mn(PO_4)_7$ compounds. *Opt. Mater.* **2011**, *34*, 376–380. [CrossRef]
3. Zhou, R.; Lin, L.; Liu, C.; Dorenbos, P.; Tao, Y.; Huang, Y.; Liang, H. Insight into Eu redox and Pr^{3+} 5d emission in $KSrPO_4$ by VRBE scheme construction. *Dalton Trans.* **2018**, *47*, 306–313. [CrossRef] [PubMed]
4. Griesiute, D.; Garskaite, E.; Antuzevics, A.; Klimavicius, V.; Balevicius, V.; Zarkov, A.; Katelnikovas, A.; Sandberg, D.; Kareiva, A. Synthesis, structural and luminescent properties of Mn-doped calcium pyrophosphate ($Ca_2P_2O_7$) polymorphs. *Sci. Rep.* **2022**, *12*, 7116. [CrossRef] [PubMed]
5. Lecointre, A.; Bessière, A.; Bos, A.J.J.; Dorenbos, P.; Viana, B.; Jacquart, S. Designing a red persistent luminescence phosphor: The example of YPO_4:Pr^{3+},Ln^{3+} (Ln = Nd, Er, Ho, Dy). *J. Phys. Chem. C* **2011**, *115*, 4217–4227. [CrossRef]
6. Zhou, R.; Ma, F.; Su, F.; Ou, Y.; Qi, Z.; Zhang, J.; Huang, Y.; Dorenbos, P.; Liang, H. Site Occupancies, VUV-UV–vis photoluminescence, and X-ray radioluminescence of Eu^{2+}-doped $RbBaPO_4$. Inorganic Chemistry. *Inorg. Chem.* **2020**, *59*, 17421–17429. [CrossRef] [PubMed]
7. Wang, Y.; Brik, M.G.; Dorenbos, P.; Huang, Y.; Tao, Y.; Liang, H. Enhanced green emission of Eu^{2+} by energy transfer from the 5D3 level of Tb^{3+} in $NaCaPO_4$. *J. Phys. Chem. C* **2014**, *118*, 7002–7009. [CrossRef]
8. Lecointre, A.; Viana, B.; LeMasne, Q.; Bessière, A.; Chanéac, C.; Gourier, D. Red long-lasting luminescence in clinoenstatite. *J. Lumin.* **2009**, *129*, 1527–1530. [CrossRef]
9. Tang, Q.; Tang, H.; Luo, D.; Zhang, C.; Guo, J.; Wu, H. Thermoluminescence spectra and dose responses of $SrSO_4$ phosphors doped with rare earths (Eu, Dy, Tm) and phosphorus. *Radiat. Prot. Dosim.* **2019**, *187*, 164–173. [CrossRef]
10. Song, H.J.; Yim, D.K.; Roh, H.-S.; Cho, I.S.; Kim, S.-J.; Jin, Y.-H.; Shim, H.-W.; Kim, D.-W.; Hong, K.S. $RbBaPO_4$:Eu^{2+}: A new alternative blue-emitting phosphor for UV-based white light-emitting diodes. *J. Mater. Chem. C* **2013**, *1*, 500–505. [CrossRef]
11. Zhao, C.; Xia, Z.; Yu, S. Thermally stable luminescence and structure evolution of (K, Rb)$BaPO_4$:Eu^{2+} solid-solution phosphors. *J. Mater. Chem. C* **2014**, *2*, 6032–6039. [CrossRef]
12. Hussain, T.; Asfora, V.K.; da Nobrega, B.P.; de Barros, V.S.; de Azevedo, W.M.; Khoury, H.J. Thermoluminescence properties of nanocrystalline $BaSO_4$ doped with Eu^{2+} produced by solid state combustion synthesis. *Radiat. Phys. Chem.* **2021**, *186*, 109531. [CrossRef]
13. Zhai, B.-G.; Liu, D.; He, Y.; Yang, L.; Huang, Y.M. Tuning the photoluminescence of Eu^{2+} and Eu^{3+} co-doped $SrSO_4$ through post annealing technique. *J. Lumin.* **2018**, *194*, 485–493. [CrossRef]
14. Guckan, V.; Altunal, V.; Nur, N.; Depci, T.; Ozdemir, A.; Kurt, K.; Yu, Y.; Yegingil, I.; Yegingil, Z. Studying $CaSO_4$: Eu as an OSL phosphor. *Nucl. Instrum. Methods Phys. Res. Sect. B Beam Interact. Mater. At.* **2017**, *407*, 145–154. [CrossRef]
15. Annalakshmi, O.; Jose, M.T.; Madhusoodanan, U. Synthesis and characterisation of $BaSO_4$:Eu thermoluminescence phosphor. *Radiat. Prot. Dosim.* **2012**, *150*, 127–133. [CrossRef] [PubMed]
16. Sun, L. Photoluminescence investigation of Eu^{2+}-doped $BaSO_4$. *Exp. Theor. Nanotechnol.* **2022**, 387–394. [CrossRef]
17. Adachi, S. Mn^{4+} vs Mn^{2+}—A comparative study as efficient activator ions in phosphor materials: A review. *J. Lumin.* **2023**, *263*, 119993. [CrossRef]
18. Adachi, S. Review—Photoluminescence Spectroscopy of Mn^{2+}-Activated Phosphors: Part I. Fundamentals. *ECS J. Solid State Sci. Technol.* **2023**, *12*, 126003. [CrossRef]
19. Adachi, S. Review—Photoluminescence Spectroscopy of Mn^{2+}-Activated Phosphors: Part II. Some Representative Phosphors. *ECS J. Solid State Sci. Technol.* **2023**, *12*, 126004. [CrossRef]
20. Yussupbekova, B.N.; Nurakhmetov, T.N.; Salikhodzha, Z.M.; Zhunusbekov, A.M.; Kainarbay, A.Z.; Daurenbekov, D.H.; Sadykova, B.; Zhangylyssov, K.B. Intrinsic and impurity emission and formation mechanism of trapping centers in $LiKSO_4$-Cu crystals. *Nucl. Instrum. Methods Phys. Res. Sect. B Beam Interact. Mater. At.* **2020**, *481*, 19–23. [CrossRef]
21. Nurakhmetov, T.N.; Alibay, T.T.; Zhangylyssov, K.B.; Daurenbekov, D.H.; Zhunusbekov, A.M.; Kainarbay, A.Z.; Sadykova, B.M.; Tolekov, D.A.; Shamiyeva, R.K. Specific Features of Formation of Electron and Hole Trapping Centers in Irradiated $CaSO_4$-Mn and $BaSO_4$-Mn. *Crystals* **2023**, *13*, 1054. [CrossRef]
22. Dorenbos, P.; Pierron, L.; Dinca, L.; Van Eijk, C.W.E.; Kahn-Harari, A.; Viana, B. 4f–5d spectroscopy of Ce^{3+} in $CaBPO_5$, $LiCaPO_4$ and Li_2CaSiO_4. *J. Phys. Condens. Matter* **2003**, *15*, 511–520. [CrossRef]

Disclaimer/Publisher's Note: The statements, opinions and data contained in all publications are solely those of the individual author(s) and contributor(s) and not of MDPI and/or the editor(s). MDPI and/or the editor(s) disclaim responsibility for any injury to people or property resulting from any ideas, methods, instructions or products referred to in the content.

NOTES

Vilniaus universiteto leidykla
Saulėtekio al. 9, III rūmai, LT-10222 Vilnius
El. p. info@leidykla.vu.lt, www.leidykla.vu.lt
bookshop.vu.lt, journals.vu.lt
Tiražas 20 egz.